

# Observational asteroseismology

A Dissertation Presented to  
the Faculty of Science at the University of Aarhus  
in Partial Fulfillment of the Requirements for the  
Degree of Doctor of Philosophy

by  
Christoffer Karoff  
5 May 2008



# Abstract

This dissertation is submitted to the Faculty of Science at the University of Aarhus, Denmark, in partial fulfillment of the requirements for the PhD degree in Astronomy. The work presented has been performed under the supervision of Dr Hans Kjeldsen and Dr Torben Arntoft. The work was mainly carried out at the Department of Physics and Astronomy, University of Aarhus and at the Deutsches Zentrum für Luft- und Raumfahrt, Berlin (1 April to 1 October, 2005).

The dissertation contains two parts where the first is a general review of the current status of observational asteroseismology; the second contains five papers that have been produced during the PhD project.

The review in the first part of this dissertation describes the main observational methods and techniques in asteroseismology and discusses recent scientific results from asteroseismology of solar-like stars and low-degree helioseismology of the Sun, including results from seismic studies of e.g. abundances, flares, dynamos, granulation and rotation. The second part of this dissertation includes four published refereed papers on: variable stars in the *COROT* fields; slowly pulsating B stars in the NGC 371; flare driven global oscillations in the Sun; high-frequency modes in solar-like stars, and one yet unpublished paper on mixed modes in  $\beta$  Hydri.

The four most significant results obtained in this PhD project are: the discovery of a strong correlation between the energy at high frequency in the solar acoustic spectrum and flares, which suggest that flares drive global oscillations in the Sun in the same way that the entire Earth is set ringing for several weeks after a major earthquake such as the 2004 December Sumatra-Andaman one; the discovery that the Sun is not the only solar-like star that has oscillations with frequencies higher than the atmospheric acoustic cut-off frequency; the discovery of 29 candidate slowly pulsating B stars in the Small Magellanic Cloud which could, if confirmed, contradict stellar theory which predicts that slowly pulsating B stars should not be present in the low-metallicity Small Magellanic Cloud; and the development of techniques for data reduction of space-based asteroseismic data.



# Acknowledgements

I would like to thank my supervisor Hans Kjeldsen for his continuous support and enthusiasm toward my project. For always asking critical questions. But mostly for all his passing remarks that led me to come up with new ideas. I am also very grateful to Torben Arentoft who has guided me through most of the studies in this dissertation and always shown patience in going through and correcting my work.

I wish to thank Jørgen Christensen-Dalsgaard and Douglas Gough for teaching me the theoretical aspects of astero- and helioseismology and for answering a great part of the millions of questions that I had.

Thanks goes to Heike Rauer and her group at the Deutsches Zentrum für Luft- und Raumfahrt, Berlin for making our collaborations both pleasant and fruitful, and for taking care of me during my visit in 2005.

I also wish to thank Tim Bedding, Hans Bruntt, Dennis Stello, Brandon Tingley, Frank Grundahl, Søren Frandsen, Jonas Debosscher, Petr Kabath, Bill Chaplin and Lars Glowienka for fruitful collaborations, friends and colleagues at the University of Aarhus for providing a comfortable and interesting environment to work in and Conny Aerts for sticking up for me at a few conferences.

Thanks also goes to Anette Skovgaard and Torben Arentoft for reading the draft version of this dissertation and correcting a host of misspellings.

My deepest gratitude goes to my wonderful family and my beloved wife Helle Skovbjerg Karoff, who has always been a great support. Without their endless love and never-dwindling belief in me, this project would not have been what it is.

Last, but not least, I would like to acknowledge the financial support for this work from the Danish National Science Research Council through the Danish AsteroSeismology Centre (DASC) and the Instrument Center for Danish Astrophysics (IDA).

*Christoffer Karoff,  
Århus, 5 May 2008.*



# List of Publications

## Refereed papers

Kjeldsen, H., Bedding, T. R., Arentoft, T., Butler, R. P., Dall, T., **Karoff, C.**, Kiss, L. L., Tinney, C. G., Chaplin, W. J., 2008, The amplitudes of solar oscillations using stellar techniques, *The Astrophysical Journal*, accepted

**Karoff, C.**, Kjeldsen, H., 2008, Evidence that solar flares drive global oscillations in the Sun, *The Astrophysical Journal Letters*, 678, L73

**Karoff, C.**, Arentoft, T., Glowienka, L., Coutures, C., Nielsen, T. B. Dogan, G., Grundahl, F., Kjeldsen, H., 2008, SPB stars in the open SMC cluster NGC 371, *Monthly Notices of the Royal Astronomical Society*, 386, 1085

**Karoff, C.**, 2007, High-frequency modes in solar-like stars, *Monthly Notices of the Royal Astronomical Society*, 381, 1001

Bedding, T.R., Kjeldsen, H., Arentoft, T., Bouchy, F., Brandbyge, J., Brewer, B.J., Butler, R.P., Christensen-Dalsgaard, J., Dall, T., Frandsen, S., **Karoff, C.**, Kiss, L.L., Monteiro, M.J.P.F.G., Pijpers, F.P., Teixeira, T.C., Tinney, C.G., Baldry, I.K., Carrier, F., O'Toole, S.J., 2007, Solar-like oscillations in the G2 subgiant  $\beta$  Hydri from dual-site observations, *The Astrophysical Journal*, 663, 1315

Kabath, P., Eigmüller, P., Erikson, A., Hedelt, P., Rauer, H., Titz, R., Wiese, T., **Karoff, C.**, 2007, Characterization of *COROT* target fields with BEST: Identification of periodic variable stars in the IR01 field, *The Astronomical Journal*, 134, 1560

**Karoff, C.**, Rauer, H., Erikson, A., Voss, H., Kabath, P., Wiese, T., Deleuil, M., Moutou, C., Meunier, J.C., Deeg, H., 2007, Identification of variable stars in *COROT*'s first main observing field (LRc1), *The Astronomical Journal*, 134, 766

**Karoff, C.**, Bruntt, H., Kjeldsen, H., Bedding, T.R., Buzasi, D., 2007, Detection of p-mode oscillations in  $\beta$  Hydri from photometric observations with *WIRE*, *Communications in Asteroseismology*, 150, 147

**Karoff, C.**, 2007, High-frequency interference peaks in solar-like stars, *Communications in Asteroseismology*, 150, 145

## Refereed papers near completion

**Karoff, C.**, Bruntt, H., Kjeldsen, H., Bedding, T.R., Buzasi, D.L., 2008, Combining observations from ground and space: mixed modes in the subgiant  $\beta$  Hydri, *Monthly Notices of the Royal Astronomical Society*, near submission

Kabath, P., Eig Müller, P., Erikson, A., Hedelt, P., Kirste S., von Paris, P., Rauer, H., Renner, S., Titz, R., Wiese, T., **Karoff, C.**, 2007, Characterization of *COROT* target fields with BEST: Identification of periodic variable stars in the LRA1 field, *The Astronomical Journal*, near submission

Arentoft et al. (48 authors including **Karoff, C.**), 2008, Multi-site Doppler Spectroscopy of Procyon A. I. Observations and Data Reduction, *The Astrophysical Journal*, near submission

## Papers without referee

Hekker et al. (48 authors including **Karoff, C.**), 2008, Oscillations in Procyon A: First results from a multi-site campaign, *Journal of Physic*

Nørmark, D., Andreassen, L., **Karoff, C.**, 2008, Regndans - eller en virkelig ubekvem sandhed, AU-gustus, 1

Nørmark, D., Andreassen, L., **Karoff, C.**, 2008, Regndans eller videnskab, Jyllands-Posten, 07.02.08

**Karoff, C.**, Rauer, H., Erikson, E., Voss, H., 2006, Milli-Magnitude Time-Resolved Photometry with BEST, *Astronomical Society of the Pacific*, 349, 261

**Karoff, C.**, Arentoft, T., Kjeldsen, H., 2006, Noise Originating from Intra-pixel Structure and Satellite Attitude Jitter on *COROT*, *Astronomical Society of the Pacific*, 349, 393

**Karoff, C.**, Pedersen, M.S.S., Jensen, H.R., 2005, DTUusatII - An Asteroseismic CubeSat, *DTUusat: Payload Conference*

# Contents

<b>Abstract</b>	<b>v</b>
<b>Acknowledgements</b>	<b>vii</b>
<b>List of Publications</b>	<b>ix</b>
Refereed papers . . . . .	ix
Refereed papers near completion . . . . .	x
Papers without referee . . . . .	x
<b>I Overview</b>	<b>1</b>
<b>1 Introduction</b>	<b>3</b>
<b>2 Methods of Observational Asteroseismology</b>	<b>5</b>
2.1 Ground-based Photometry . . . . .	5
2.1.1 Introduction . . . . .	5
2.1.2 Data Reduction . . . . .	6
2.1.3 Data Analysis . . . . .	8
2.2 Space-based Photometry . . . . .	8
2.2.1 Introduction . . . . .	8
2.2.2 Data Reduction . . . . .	10
2.2.3 Data Analysis . . . . .	12
2.3 Ground-based Radial-velocity Observations . . . . .	13
2.3.1 Introduction . . . . .	13
2.3.2 Data Reduction . . . . .	14
2.3.3 Data Analysis . . . . .	16
2.4 Fourier Analysis . . . . .	17
2.4.1 Introduction . . . . .	17
2.4.2 The Least-squares Spectrum . . . . .	17
2.4.3 The Fast-Fourier Transform (FFT) . . . . .	20
2.4.4 The Power-density Spectrum . . . . .	23
2.4.5 Iterative-Sine-Wave-Fitting . . . . .	24
2.4.6 Simultaneous-Iterative-Sine-Wave-Fitting . . . . .	25
2.4.7 Filtering . . . . .	26

<b>3</b>	<b>Scientific Results from Asteroseismology</b>	<b>27</b>
3.1	The Surface . . . . .	27
3.1.1	The Problem with the Solar Abundances . . . . .	27
3.1.2	Excitation of $\beta$ Cep and SPB Stars at Low-metallicity . . . . .	29
3.1.3	Spots and Dynamos . . . . .	30
3.1.4	Excitation of Global Oscillation by Flares . . . . .	32
3.2	The Granulation Zone . . . . .	35
3.2.1	Granulation Background in the Acoustic Spectrum . . . . .	35
3.2.2	Oscillation Amplitudes in Velocity and Photometry . . . . .	38
3.2.3	Structure in The Echelle Diagram . . . . .	44
3.2.4	Modeling Acoustic Spectra . . . . .	46
3.2.5	Rotation Splitting, Differential Rotation . . . . .	48
3.3	The Core . . . . .	50
3.3.1	g Modes in the Sun . . . . .	50
3.3.2	Avoided Crossing in $\beta$ Hydri . . . . .	51
<b>II</b>	<b>Papers</b>	<b>53</b>
<b>4</b>	<b>Variable Stars in the <i>COROT</i> Fields</b>	<b>55</b>
4.1	Introduction . . . . .	57
4.2	Observation . . . . .	59
4.3	Data Reduction . . . . .	60
4.3.1	Image Subtraction . . . . .	61
4.3.2	Photometry . . . . .	62
4.3.3	Astrometry and Calibration . . . . .	63
4.4	Data Analysis . . . . .	64
4.4.1	Identification of Suspected Variable Stars . . . . .	64
4.4.2	Identification of Periodic Variable Stars and Period Determination . . . . .	64
4.5	Variable Star Catalog . . . . .	67
4.6	Data Completeness . . . . .	73
4.7	Conclusions . . . . .	74
<b>5</b>	<b>SPB Stars in NGC 371</b>	<b>77</b>
5.1	Introduction . . . . .	79
5.2	The Target Cluster: NGC 371 . . . . .	80
5.3	The Data and the Data Reduction . . . . .	80
5.3.1	Analysis of Differential Light Curves . . . . .	82
5.4	Eclipsing Binaries . . . . .	83
5.5	Be Stars . . . . .	83
5.6	Pulsating Stars in the Upper Part of the Main Sequence . . . . .	85
5.6.1	Color-magnitude-diagram of NGC 371 . . . . .	87
5.6.2	Period Distribution in NGC 371 . . . . .	89
5.6.3	Amplitude Ratio and Phase Difference . . . . .	90
5.6.4	Multimode Pulsation . . . . .	91
5.7	Summary and Conclusions . . . . .	91

<b>6</b>	<b>Flare Driven Global Oscillations in the Sun</b>	<b>95</b>
6.1	Introduction . . . . .	97
6.2	Frequency/Time Diagrams . . . . .	98
6.3	Correlation at Different Frequencies . . . . .	100
6.4	Correlation at High Frequency . . . . .	102
6.5	Discussion . . . . .	102
<b>7</b>	<b>High-frequency Modes in Solar-like Stars</b>	<b>105</b>
7.1	Introduction . . . . .	107
7.2	Data . . . . .	109
7.2.1	The Sun . . . . .	109
7.2.2	$\beta$ Hydri . . . . .	110
7.2.3	$\alpha$ Cen A . . . . .	110
7.2.4	$\alpha$ Cen B . . . . .	110
7.3	Data Analysis . . . . .	111
7.4	Theory . . . . .	115
7.5	Discussion . . . . .	119
<b>8</b>	<b>Mixed Modes in the <math>\beta</math> Hydri</b>	<b>121</b>
8.1	Introduction . . . . .	123
8.2	Observations and Data Reduction . . . . .	125
8.3	Power Excess . . . . .	126
8.4	Modelling the Power-Density Spectrum . . . . .	128
8.5	Results and Analysis . . . . .	132
8.5.1	Mode Frequencies . . . . .	132
8.5.2	Mode Lifetime . . . . .	134
8.5.3	Echelle Diagram and Avoided Crossings . . . . .	135
8.6	Summary . . . . .	136
8.7	Appendix . . . . .	137
8.7.1	Decorrelation of Photometric Light Curves . . . . .	137
8.7.2	Adjusting Statistical Weights . . . . .	139
	<b>Conclusions</b>	<b>143</b>
	<b>Bibliography</b>	<b>xv</b>



Part I  
Overview



# Chapter 1

## Introduction

*ASTEROSEISMOLOGY: The study of the interior of stars by the observation and analysis of oscillations at their surface. n.*  
— Oxford English Dictionary

*HELIOSEISMOLOGY: The study of the sun's interior by the observation and analysis of oscillations at its surface. n.*  
— Oxford English Dictionary

Observations of oscillations in the Sun and other stars enable us to understand the physics that takes place inside a star. Fortunately most stars oscillate, some at many different frequencies, some at a few, some with large amplitudes and some with small. This dissertation is devoted to the study of oscillations in solar-like stars and especially the ones that oscillate like the Sun, i.e. have solar-like oscillations.

The first part of this dissertation follows Gizon & Birch (2005) by starting with describing the main techniques of asteroseismology of solar-like stars in Chapter 2 and then reviews and discusses recent scientific results from asteroseismology of solar-like stars and low-degree helioseismology in Chapter 3.

The second chapter in this dissertation describes the main observational methods and techniques used in asteroseismology of solar-like stars, i.e. ground-based photometry and spectroscopy and space-based photometry. Here we focus on observations made in the time domain and not on observational methods that can be used to estimate the stars' color, temperature, chemical composition, etc. from photometry and spectroscopy. Also helioseismic observations of the Sun are often made with observation methods and techniques not described in this dissertation such as for instance observations with a resonant-scattering solar spectrometer (Brookes et al., 1978).

Traditional observations of oscillations in stars have been made with ground-based photometry, in the beginning with photo-multipliers and during the last two decades with CCDs. Though ground-based photometry is an excellent tool for studying oscillations in classical pulsators including  $\delta$  Scuti,  $\gamma$  Dor, SPB and  $\beta$  Cep stars it is not appropriate for studying solar-like oscillations. Today asteroseismology is therefore mainly made with space-based photometry and ground-based spectroscopy, using dedicated satellites such as *COROT* (Baglin

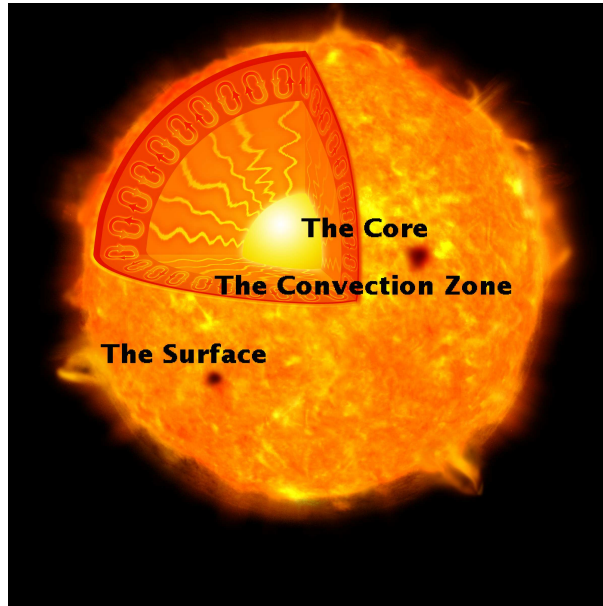


Figure 1.1: Schematic drawing of the Sun with the three regions that will be discussed in this dissertation marked. In Chapter 3 we will review and discuss recent scientific results from helio- and asteroseismology in relation to these three regions. From: NASA/CXC/M.Weiss

et al., 2002) and state-of-the-art spectrographs such as UVES, HARPS and UCLES (see Section 2.3.1).

The second chapter also includes an introduction to the tools used in time-series analysis of asteroseismic data.

The third chapter in this dissertation is a review and a discussion of recent scientific results from asteroseismology of solar-like stars and low-degree helioseismology. Here special attention is given to methods and tools that have been used with success in low-degree helioseismology and that have the potential of providing scientific results in asteroseismology, though data for doing this are not available today.

In order to place the different results in asteroseismology and low-degree helioseismology in a general context the different results have been categorized according to where in the stars they take place. In this dissertation the star has been separated into: the surface; the convection zone and the core (see Fig. 1.1). This categorization has been adopted from Kjeldsen & Bedding (2007) as it serves well for a categorization of the scientific results.

The purpose of the second and third chapter in this dissertation is to provide a general context for the papers in the fourth chapter. Therefore special attention is given to phenomena such as spots and flares in chapter three as these phenomena are related to some of the major discoveries in this PhD dissertation.

# Chapter 2

## Methods of Observational Asteroseismology

In this chapter we introduce the three most used methods in observational asteroseismology, i.e. ground-based photometry and spectroscopy and space-based photometry. We evaluate the ups and downs of the different methods and give a review of recent results that have been obtained with the different methods. We also give an introduction to the tools used in time-series analysis of asteroseismic data.

### 2.1 Ground-based Photometry

#### 2.1.1 Introduction

Though it is not possible to make photometric observations of solar-like oscillations from ground, because of noise from scintillation from the Earth's atmosphere, ground-based photometry is still one of the main observation methods used in asteroseismology in general. Ground-based photometry is mainly used in asteroseismology for heat-engine pulsators such as  $\delta$  Scuti,  $\gamma$  Dor, SPB and  $\beta$  Cep stars, and white dwarfs.

The ground-based campaign with the highest precision per exposure to date was done by Gilliland et al. (1993) who obtained a precision per exposure as high as 0.25 mmag. As nobody else has been able to go higher than this (to our knowledge) this value properly sets the limit for photometric precision from ground.

The fact that best precision was obtained 15 years ago does not mean that ground-based photometry has not improved since then. It means that ground-based photometry is limited to a precision around 0.25 mmag per exposure because of scintillation from the Earth's atmosphere. The improvements in ground-based photometry during the last 15 years have therefore not been in the precision, but mainly in the number of stars that can be monitored simultaneously and in the duration of the observations. During the last decade a large number of programs dedicated to detecting transiting hot Jupiters have been born, e.g. STARE, Vulcan, WASP, SuperWASP, PSST, HAT, APT, PASS, TEST and BEST (see Voss, 2006, for a recent review of these large field-of-view (FOV) surveys). These projects all monitor a large FOV containing many thousands of stars for periods of a few months (some of them over more than

one season). The problem with these surveys is that the point-spread functions (PSF) of the images become heavily under-sampled and crowding becomes a problem. On the other hand the hunt for transiting hot Jupiters have encouraged developments of new software for photometry in crowded fields. This means that the precision in the ground-based large FOV surveys is now not too far from the precision obtained by Gilliland et al. (1993). In fact the main problem for the ground-based large FOV surveys might not be the precision, but the sampling and the fact that all transiting hot Jupiter surveys are only done in a single filter. Another reason why asteroseismology has not really been done on data from the large FOV surveys is that these surveys observe field stars where no additional information is available for the stars other than the information in the light curves.

Additional information for the stars can be obtained by observing stars in stellar clusters. In a stellar cluster all the stars have roughly the same age and the same chemical composition. This means that we have two important constraints to use when modeling the observed stars. Therefore a large number of programs have been made during the last three decades dedicated to observing stellar clusters. These studies can be separated into three different types: Studies of mostly SPB and  $\beta$  Cep stars in young open clusters (age 5 to 25 Myr); studies of  $\delta$  Scuti and  $\gamma$  Doradus stars in older open clusters and studies of mainly RR Lyrae stars in globular clusters (see Pigulski, 2006, for a recent review).

There have also been attempts to detect solar-like oscillations in main-sequence stars in stellar clusters (for instance Gilliland et al., 1993) though unsuccessful. Lately two studies have tried to use ground-based photometry to detect solar-like oscillations in red giants in stellar clusters (Stello et al., 2007; Frandsen et al., 2007), where the first one was successful.

### 2.1.2 Data Reduction

The reduction of ground-based photometry data normally consists of making photometry on a number of CCD frames, one exception is the Whole Earth Telescope (WET) campaigns which are often made with photon-multipliers.

The first steps in the reduction of CCD frames consist of making bias and sky background subtraction and of correcting the sensitivity of the CCD with a flat-field. This is done by standard procedures for bias and background subtraction and flat-fielding (Kjeldsen & Frandsen, 1992).

The next step is to make photometry on the CCD frames. If there is only a limited number of stars on the CCD frames, this is best done with aperture photometry, where an (mostly circular) aperture window is selected around the target star. Then the flux of the star is measured in this aperture and the background around the aperture (star) is measured and subtracted. If the frames on the other hand suffer from a given amount of crowding then more sophisticated methods need to be used. Some of the most popular photometry packages are the Dominion Astrophysical Observatory Photometry packages, DAOPHOT (Stetson, 1987), the MultiObject MultiFrame Photometry packages, MOMF

(Kjeldsen & Frandsen, 1992) and the Image Subtraction packages, ISIS (Alard, 2000)

### **DAOPHOT**

DAOPHOT performs PSF photometry, this means that it fits a PSF to the brightest stars on the frame, calculates the magnitude and position of all other stars and then subtracts them from the frame. DAOPHOT is known to perform well in highly crowded fields, but in less crowded fields it has lower precision than MOMF and ISIS (Handler, 2003; Karoff et al., 2006b)

### **MOMF**

MOMF performs a combination of aperture and PSF photometry. This means that it first subtracts all the stars from the frame and makes a determination of the background; it then goes back to the original frame, subtracts the background and makes a re-determination of the PSF; it then uses the new PSF to measure the magnitude and the position of the stars before it subtracts the stars. Then the program makes aperture photometry on the subtracted frames and uses these results to correct the original magnitudes. The difference between DAOPHOT and MOMF is that MOMF subtracts the stars on the frame star by star whereas DAOPHOT subtracts all the stars simultaneously. Generally MOMF is believed to be the most precise photometry program (Handler, 2003) especially for the brightest stars, though it has problems with heavily crowded under-sampled frames (Karoff et al., 2006b).

### **ISIS**

The general idea behind image subtraction is to obtain a master frame and use this frame to subtract the background and all the constant stars from the other frames. There are two critical steps in image subtraction: first to align all the frames and second to match the seeing between the master frame and the frames to subtract. The last step is done by convolving the master frame with a convolution kernel in order to match the seeing in the master frame to the seeing in the frames that are going to be subtracted.

After having subtracted the master frame from all the frames that are going to be subtracted ISIS, performs PSF-weighted photometry on all the subtracted frames. The result is a number of differential light curves of all the non-constant stars in the frames. ISIS is only capable of making differential photometry.

The master frame can be either the best seeing frame of the observing run or it can be obtained by stacking a number of best seeing frames from the whole observing run.

ISIS is one of the few programs that performs well in crowded under-sampled frames. Therefore ISIS (and other difference images analysis packages) are often used in the large FOV surveys. ISIS is also capable of handling large PSF variations over the FOV as it divides each frame into a number of sub-frames and analyzes these sub-frames separately. This is a feature that DAOPHOT and MOMF are lacking.

### 2.1.3 Data Analysis

The analysis of ground-based photometric data consists of identifying pulsation periods in the observed stars and attaching a mode identification to these modes. The pulsation periods are mostly found in the acoustic spectrum as will be described in Section 2.4, though an increasing number of studies also uses the method introduced by Schwarzenberg-Czerny (1996) which fits a set of periodic orthogonal polynomials to the observations and evaluates the quality of the fit with the use of an analysis-of-variance statistic.

The stars are often observed in different filters, which makes it possible to compare the amplitudes and the phases of the variability seen in different colors. For a transient phenomena the amplitude ratios between different colors should be close to unity, as a transient event such as an eclipse is a purely geometric phenomena, whereas for oscillations the surface of the star changes and therefore the amplitude ratios are expected to be different from unity. This is also the case for the phase differences between the oscillations observed in different filters though a general expression is difficult to calculate (see De Cat et al., 2007, for discussion).

Generally the oscillation amplitudes decrease for increasing wavelength, and the decrease is generally largest for radial modes and becomes smaller with increasing angular degree  $l$  (Heynderickx et al., 1994). Dupret et al. (2003) have improved these calculations by Heynderickx et al. (1994) by including a more precise determination of the non-adiabatic eigenfunctions in the outer layers of the stellar atmospheres and have extended the model to include also SPB stars. The calculations by Dupret et al. (2003) have been extensively used by for instance De Cat et al. (2005, 2007), who also used the amplitude ratios to determine if the variability that is seen originates from transient events or from oscillations.

The radial order  $n$  can in principle be found by using Eddington's formulation to obtain frequency for  $n = 0$  mode and assuming constant frequency spacing between radial modes of higher order  $n$ :

$$\log Q = \log P + 1/2 \log(M/M_{\odot}) - 3/4 \log(L/L_{\odot}) + 3 \log(T/T_{\odot}), \quad (2.1)$$

where  $P$  is the period of the oscillation and  $Q$  is the pulsation constant which can be obtained either theoretically or observationally (For  $\delta$  Scuti, SPB and  $\beta$  Cep stars  $Q$  equals 0.033 Breger, 2000; Stankov & Handler, 2005). But in practice the distribution of oscillation modes in  $\delta$  Scuti, SPB and  $\beta$  Cep stars is too random for this to work, i.e. not all modes are excited to visible amplitudes. Therefore identification of the radial order  $n$  in  $\delta$  Scuti, SPB and  $\beta$  Cep stars remains one of the most problematic tasks in asteroseismology.

## 2.2 Space-based Photometry

### 2.2.1 Introduction

Photometric observations of solar-like oscillation in main-sequence stars have to be done from space to avoid scintillation from the Earth's atmosphere. So

far four missions have tried to observe solar-like oscillation in photometry, i.e. *WIRE* (Buzasi et al., 2000), *SMEI* (Tarrant et al., 2007, only red giants), *MOST* (Walker et al., 2003), *COROT* (Baglin et al., 2002) and for the future we expect great results from *KEPLER* (Borucki et al., 2003). Observations of solar-like oscillations in solar-like stars have thus only been obtained with *WIRE* (Schou & Buzasi, 2001; Bruntt et al., 2005; Karoff et al., 2008b) and *COROT* (ESA, 2007). Contradicting results have been reported for observations of solar-like oscillations in solar-like stars with *MOST* (Matthews et al., 2004; Christensen-Dalsgaard & Kjeldsen, 2004; Bedding et al., 2005; Régulo & Roca Cortés, 2005; Lambert et al., 2006; Guenther et al., 2007; Baudin et al., 2008; Marchenko, 2008; Walker, 2007), and in general the noise limit in the *MOST* data seems to be too high to detect solar-like oscillations in solar-like stars. One exception might be the new *MOST* data from 2007 obtained with an improved observation method (Walker, 2007). Both *WIRE* and *MOST* have observed solar-like oscillations in a number of red giants (Buzasi et al., 2000; Retter et al., 2003; Stello et al., 2008; Barban et al., 2007; Kallinger et al., 2008a,b). The two satellites have also conducted a number of successful observations of oscillations in  $\beta$  Cep and SPB stars (Cuypers et al., 2002; Walker et al., 2005; Aerts et al., 2006a,b; Saio et al., 2006) and  $\delta$  Scuti stars (Poretti et al., 2002; Buzasi et al., 2005; King et al., 2006; Rowe et al., 2006; Bruntt et al., 2007; Matthews, 2007).

An important reason to make observations of solar-like oscillations from space is to ensure continuous observations in order to avoid sidebands in the acoustic spectra. This has been a huge problem for ground-based observations, as it is here only possible to observe at night. Gaps in the time series with a period of 1 day cause sidebands in the acoustic spectra with a spacing of  $11.6\mu\text{Hz}$ , which complicates the mode determination. For the first space-base data that we have received from *WIRE*, gaps in the time series are also a problem (Poretti et al., 2002; Karoff et al., 2008b). Here the gaps are caused either by the Earth getting into the line-of-sight or from stray light. This problem is also seen in the *MOST* data (Reegen et al., 2006). For a satellite in low-earth orbit as *WIRE*, *MOST* and *COROT*, the gaps appear with a period of around 100 minutes causing sidebands in the acoustic spectra with a spacing of  $167\mu\text{Hz}$ . This is a huge problem for many solar-like stars as e.g. Procyon where a spacing of  $167\mu\text{Hz}$  equals three times the large separation (Roca Cortés et al., 1999).

A spacing of  $167\mu\text{Hz}$  is so large that it does not shift the individual frequencies, but it makes the acoustic spectra more noisy as energy from the low-frequency part of the spectrum will trail into the high-frequency part. It also makes the analysis more difficult as the different frequencies are no longer independent of each other.

The capability of a given mission to detect solar-like oscillations is best evaluated in the acoustic spectrum, by measuring the noise level at high frequency. The capability of different missions to detect for instance solar-like oscillations can be compared either by calculating the noise level over the total length of the observations or by calculating the noise level for time intervals of the same length. *WIRE* and *MOST* have observed targets for up to a month. *COROT* has and will observe the same targets for 150 days and *KEPLER* will observe

Table 2.1: Precision in space-based observation of oscillation in solar-like stars

Instrument	Precision	Duration	Reference
<i>WIRE</i>	1.8 ppm	9.5 d	Bruntt et al. (2005)
<i>MOST</i>	2 ppm	38 d	Walker (2007)
<i>COROT</i>	0.4 ppm	60 d	ESA (2007)
<i>KEPLER</i>	0.7 ppm	30 d	Kjeldsen (private communication)

Table 2.2: Precision and S/N in space-based observation after observing a bright target for at month.

Instrument	Precision	S/N
<i>WIRE</i>	1.0 ppm	10
<i>MOST</i>	2.3 ppm	4
<i>COROT</i>	0.6 ppm	18
<i>KEPLER</i>	0.7 ppm	14

the same field for more than 3.5 years, though some of the individual stars might not be observed for the complete duration of the mission.

Table 2.1 gives the noise level at high frequency in the amplitude spectra obtained with *WIRE*, *MOST* and *COROT* as well as the expected noise level for *KEPLER*.

Table 2.2 gives the noise level at high frequency in the amplitude spectra for a month of observation obtained by scaling the values given in Table 2.1. The S/N, which has been obtained by assuming an average stellar signal of 10 ppm, in agreement with Kjeldsen & Bedding (1995) is also given.

We should also mention the projects that will try to do asteroseismic observations with pico and nano class satellites. A pico satellite is a satellite which has a volume of one liter, a mass of one kg and a power budget of one W. Asteroseismic observations with such a satellite was first suggested by Karoff et al. (2005). A similar concept is now under development in the *BRITE* Constellation project (Weiss, 2008), which is a group of four nano-satellites (mass from one to ten kg) whose purpose is to photometrically measure stellar oscillations in bright stars. The *BRITE* Constellation satellites are under construction at the University of Vienna (in collaboration with Canadian Space Agency) and scheduled for launch in early 2009.

## 2.2.2 Data Reduction

It is not possible to download entire CCD frames from satellites such as *WIRE*, *MOST*, *COROT* and *KEPLER* because of limited down-link capability. Therefore, the only available data are a number of windows around selected targets, or pure intensity measurements performed onboard (see Fig. 2.1 for an example of such a window from *WIRE*).

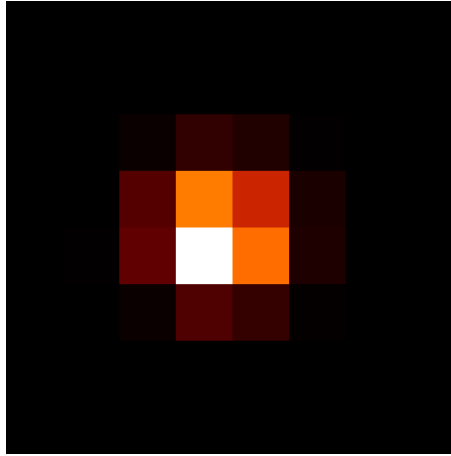


Figure 2.1:  $8 \times 8$  pixel window of  $\beta$  Hydri from the startracker on the *WIRE* satellite.

With just one window with one star, it is not possible to perform differential photometry. Therefore, the best solution is to use simple unit-weighted aperture photometry with a more or less sophisticated estimation of the background.

Bruntt et al. (2005) estimated the background in the *WIRE* data as a mean of the 12 pixels in the corners of the windows (3 pixels in each corner).

Reegen et al. (2006) use the background pixels in the *MOST* data to correct the value of the pixels inside the aperture, before measuring the intensity inside the aperture, instead of calculating the intensity in the aperture and in the background separately. This is done by plotting the value of a background pixel as a function of a target pixel and then correcting the value of the target pixel with the slope of this plot, in order to remove any correlation between background and target pixels (see Reegen et al., 2006, for details of how this is done). This correction is based on the assumption that the stray-light sources superpose for a given pixel as individual point sources.

As the total number of pixels is 841 in the *MOST* windows and the number of target pixels is larger than 50, this correction between background and target pixels can be done a significant number of times. Reegen et al. (2006) show some examples where each target pixel has been corrected by 95 to 300 background pixels – though it is not clear how many times the target pixels in Procyon and  $\eta$  Boo have been corrected (Matthews et al., 2004; Guenther et al., 2005). This is important, as Reegen et al. (2006) show that correcting the target pixels with 300 background pixels will lower the amplitudes in the oscillations to half of the real value.

Another way to estimate the background which has been used on both *WIRE* and *MOST* data (Karoff, 2005), is to calculate the background as a weighted mean of the background pixels, where the weights are assigned according to the variations in different groups of background pixels. This approach is only possible when a sufficient number of background pixels are available. The background is then calculated as a weighted mean of all the background pixels,

where the weights are calculated based on the variance assigned to a number of predefined groups of background pixels:

$$B_{l+1} = \frac{\sum_i G_i \cdot w_i}{\sum_i w_i} \quad (2.2)$$

where  $G_i$  is the mean of all the pixels in the  $i$ th group of background pixels and  $w_i$  is the weight of the group of background pixels, calculated as:

$$w_i = \frac{1}{\exp\left(\frac{G_i - B_l}{\sigma(G_i)}\right)} \quad (2.3)$$

where  $B$  is the background and  $\sigma(G_i)$  is the variance of all the pixels in the  $i$ th group of background pixels.

The background can for instance be calculated with 4 ( $l = 3$ ) interactions where  $B_0$  is set to the mean of all the background pixels.

For *COROT* and *KEPLER* the photometry algorithms will have a different approach as many stars are observed here on the same CCD and as separate windows are downloaded for estimating the background. This means that the background and the stellar flux are not estimated from the same windows. Also the windows are not squared. Instead choices of individual windows are made at the beginning of each observation. In fact *WIRE* was capable of downloading five windows of five different stars simultaneously, but it has not been possible to use this to improve the photometry.

### 2.2.3 Data Analysis

After the raw time series are produced the next step is to correct the time series for any systematic effects. For *WIRE* and *MOST* the most important effect is stray light which has a strong effect on the background.

For *WIRE* the correction has either been done simply by removing all the data points affected by stray light (Bruntt et al., 2005) or by decorrelating the time series with the orbital phase, using a distance-weighted mean (Karoff et al., 2008b). The last approach has the advantage that it does not use the signal in the data point that is corrected.

For *MOST*, stray-light noise is removed by the algorithm described in Section 2.2.2. In other words the correction is done at pixel level (Reegen et al., 2006), but the problem is that the stellar signal is affected by the correction. This means that removing the stray light will also remove some of the stellar signal. Therefore, though the noise level in the acoustic spectrum can be heavily reduced by this approach, the S/N is not improved as the stellar signal is also reduced.

For *COROT* and *KEPLER* the most important effect to correct for is the satellite jitter which causes small movements of the stars on the CCD. This means on one hand that parts of the star can move outside the aperture mask and on the other hand that different parts of the PSF are placed differently within a given pixel. The later will have an effect as the CCDs are not equally sensitive across a pixel (Jordan et al., 1994; Karoff, 2005; Karoff et al., 2006a).

Satellite jitter can also be corrected for by using distance-weighted means as described in Karoff et al. (2008b) (see also Section 8.7.1). Drummond et al. (2006) use a similar approach for correcting the time series from *COROT*, but here the correction is made by calculating a correction map. This can be done either beforehand knowing the PSF and the aperture masks or afterwards by use of the data themselves.

As in all other aspects of time-series analysis it is important to have the complete time series checked for bad data points. Therefore it is important to have a reliable measurements of the quality of each data point (the uncertainty of each data point). When simple unit-weighted aperture photometry is performed then the uncertainties cannot be calculated without using the measured intensity of the star. Instead the uncertainty can be calculated as the RMS of all data points separated by a given time. Here it is important that the time intervals are significantly smaller than the stellar oscillation period (Karoff et al., 2008b). Or the uncertainties can be calculated as the residuals of the time series where the stellar signal has been removed. This is done by selecting a frequency band in the acoustic spectrum where there is no stellar signal and apply an inverse band-pass filter to the time series in this frequency band (Arentoft et al., 2008)

In order to ensure the right absolute values of the uncertainties the uncertainties can be scaled by Parseval's theorem as described in Butler et al. (2004).

It has also proved highly useful to ensure that the uncertainties are Gaussian distributed as is done by Butler et al. (2004) (see also Karoff et al., 2008b, and Section 8.7.2 for a more detailed discussion). The main goal of this is to remove bad data points with unrealistic uncertainties, which in most cases mean less than 5% of the data points.

## 2.3 Ground-based Radial-velocity Observations

### 2.3.1 Introduction

Driven by the hunt for exoplanets ground-based radial-velocity measurements have within the last 13 years succeeded in obtaining the high precision needed not solely for finding exoplanets, but also for detecting solar-like oscillations in stars. This precision is typically close to 1 m/s per exposure (or even below). Anyway the first detection of solar-like oscillation in a star was in fact not made with radial-velocity observation. These were made by measuring fluctuations in the temperature of the star via their effect on the equivalent widths of the Balmer lines' line-widths (Kjeldsen et al., 1995).

The general idea in measuring precise radial velocities with spectroscopy is to measure small Doppler shifts in the spectral lines. If one wants to measure a 1 m/s shift in a spectrum with a resolution of 0.025 Å per pixel then this demands that a shift in the spectral lines of the order of 0.001 pixel is identified. In order to do this many spectral lines are measured at the same time and some kind of reference is used to ensure the stability over time.

Table 2.3: Summary of the Procyon campaign (from Arentoft et al., 2008). Ref: 1. Rupprecht et al. (2004); 2. Bouchy & Carrier (2002); 3. Endl et al. (2005); 4. Butler et al. (1996); 5. Kambe et al. (2008); 6. Hatzes et al. (2003); 7. Mosser et al. (2008); 8. Bouchy et al. (2002); 9. Claudi et al. (2005); 10. Frandsen et al. (1995)

Instrument	Technique	Nights	Eff. obs.	Spectra	$f_{\text{Nyq}}$	Noise Level	Noise / min.	Ref.
		Allocated	time (h)		(mHz)	( $\text{cm s}^{-1}$ )	( $\text{m s}^{-1}$ )	
HARPS	ThAr	8	52.0	5698	13.8	2.0	0.64	1
CORALIE	ThAr	5	27.0	936	4.0	9.8	2.2	2
McDonald	iodine	6	16.2	1719	15.6	14.4	2.5	3
Lick	iodine	14	95.4	1900	2.1	10.9	4.7	4
UCLES	iodine	12	41.4	2451	8.2	6.6	1.9	5
Okayama	iodine	20	83.4	1997	3.1	8.0	3.2	6
Tautenburg	iodine	21	14.6	494	4.0	22.8	3.8	7
SOPHIE	ThAr	9	35.1	3924	9.7	4.7	1.2	8
EMILIE	Fabry-Perot	4	25.7	1631	7.8	10.1	2.2	9
SARG	iodine	4	15.2	693	5.9	12.6	2.1	10
FIES	ThAr	$5 \times 1/2$	12.6	1087	7.9	21.7	3.4	11

Today a number of spectrographs around the globe are capable of measuring precise radial velocities with this methods, and fortunately they all (except UVES) participated in the 2006 Procyon campaign (Arentoft et al., 2008). This resulted in not just a unique data set of Procyon, but also in the possibility of comparing the different spectrographs, the different observation method and different telescope. A summary of the observations is given in Table 2.3. Here it is seen that the instruments dedicated to radial-velocity observations (HARPS, CORALIE, UCLES, SOPHIE) are generally also the instruments that provide the best precision.

The main reason for making an asteroseismic campaign is to be able to observe 24 hours a day. When observing with a single telescope it is only possible to observe at night. This means that the time series will have gaps of between 8 to 16 hours and these gaps will cause sidebands to rise in the acoustic spectrum which complicates the frequency analysis (as discussed in Section 2.2.1). Only a small number of stars with solar-like oscillations have been observed by a multi-site campaign (see Bedding & Kjeldsen, 2007a, for a recent review). Though the frequency analysis is complicated by the sidebands in single-site observations these observations can still teach us many things about the physics that takes place in these stars. Knowledge can be gained about the mean mode amplitude and the central frequency of the excess power (see Stello et al., 2008, for an example of how to use these parameters).

### 2.3.2 Data Reduction

All the instruments in the Procyon campaign construct an echelle spectrum of the stars where the spectra are cut into a number of echelles which are stacked



Figure 2.2: HARPS echelle spectrum of Procyon

vertically on the CCD. An example of an echelle spectrum is shown in Fig. 2.2. The first step in the data reduction is to calculate a calibrated one dimensional spectrum from these CCD images. An example of a one dimensional spectrum is shown in Fig. 2.3. When this is done the next step is to obtain the line-spread-function (LSF), which is a function of the instrument. This can be done either with the use of ThAr or with the use of iodine.

The instruments that use ThAr as a reference all use a fiber to transport the light from the telescope to the spectrograph. In practice the spectrograph is then fed with two fibers: one from the telescope and one from a ThAr lamp. This means that two separate spectra are exposed on the CCD: one from the star and one from the ThAr lamp separated by the distance between the two fibers.

The idea of using an iodine cell for reference is different from using ThAr, as the light from the star passes through the iodine cell before it is exposed on the CCD. In this way a spectrum containing both iodine and stellar lines ( $I_{obs}$ ) is obtained. By comparing the observed spectrum ( $I_{obs}$ ) with a high-precision or theoretical iodine spectrum ( $I_{I_2}$ ) and a high-precision or theoretical stellar spectrum ( $I_s$ ) the LSF and the Doppler line shifts can be obtained:

Numerical this is done by modeling the combined spectrum as (Butler et al., 1996):

$$I_{obs}(\lambda) = k[I_{I_2}(\lambda) \cdot I_s(\lambda + \Delta\lambda)] * LSF \quad (2.4)$$

where  $k$  is a normalization factor,  $\Delta\lambda$  is the Doppler shift and  $*$  represents convolution. The iodine spectrum ( $I_{I_2}$ ) can be known beforehand either as a theoretical iodine spectrum or as a high-precision iodine spectrum taken by a dedicated instrument. Information about the stellar spectrum ( $I_s$ ) can also

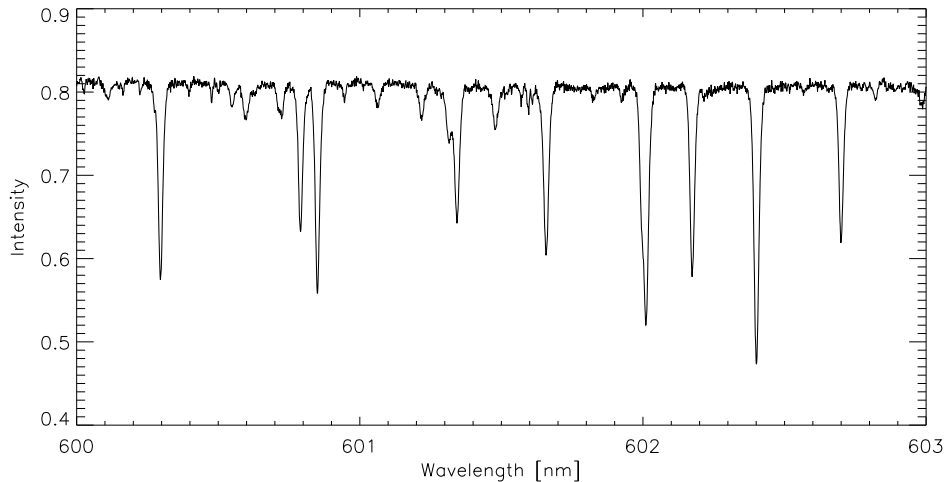


Figure 2.3: Part of the HARPS spectrum of Procyon

be gained beforehand, either by making some assumption about the spectrum based on the stellar type or by having the stars observed with another telescope.

The difference between the ThAr and the iodine method is that the LSF and the Doppler line shifts are obtained in the same spectrum with the iodine method whereas two different spectra are used in the ThAr method. This means that in principle it is possible to monitor changes in the LSF better with the iodine method. On the other hand the most precise radial-velocity observations are made with ThAr, except from the VLT UCLES (Dekker et al., 2000) observations of  $\alpha$  Cen B (Kjeldsen et al., 2005). Both the ThAr and the iodine method has proven capable of producing radial velocities with a precision better than 1 m/s, but in general the precision obtained on a given object will not only depend on the method used, but also on the telescope size, duty cycle, guiding, etc.

The recent development of a laser frequency comb for radial-velocity measurements (Li et al., 2008) suggests that the precision and stability of this method exceeds both the ThAr and the iodine method. The laser frequency comb method could therefore very well be the method to use on future spectrographs, but we will have to await the first successful real observations of stellar radial velocities before this can be settled.

### 2.3.3 Data Analysis

The main part of the data analysis of ground-based radial-velocity observation is to down-weight bad data points and to optimize the window function. The bad data points are down weighted the same way as it is done for space-based photometry (see Section 2.2.3), but here the advantage is that realistic uncertainties can be obtained in the data reduction as radial velocities from many different echelle orders are obtained simultaneously.

The idea behind optimizing the window function is that the best sites in a multi-site campaign will get the highest weights in the time series and therefore cause sidebands to rise in the acoustic spectrum even if the observations are made 24 hours a day. This means that the weighted spectrum with the lowest noise level will have sidebands. These sidebands can be lowered by optimizing the weights (Bedding et al., 2004). In this way the weights are iteratively changed to lower the energy in the sidebands compared to the energy in the main peak. This procedure lowers the sidebands, but it also raises the noise level; therefore the frequency analysis is normally performed in both the noise optimized and in the window-function optimized spectrum. The analyses of the two spectra are then compared.

## 2.4 Fourier Analysis

### 2.4.1 Introduction

An asteroseismic analysis always includes analyzing a time series in the frequency domain. This is done in an acoustic spectrum when the frequency or period is plotted on the horizontal axis and amplitude or power on the vertical. This amplitude or power spectrum can be calculated in many ways where the most well-known are the Fast-Fourier Transform (FFT) (Gauss, 1866; Press et al., 1992) and the discrete Fourier transform (mostly known as the Lomb-Scargle periodogram, Lomb, 1976; Scargle, 1982). These spectra converge to the same spectrum for evenly sampled data without gaps, but the definition of the amplitudes is not always the same, which is a problem when comparing data that have been analyzed with different methods. Here we derive the least-squares spectrum that is defined so that a sine wave with an amplitude of 1 in the time domain has a peak with an amplitude of 1 in the amplitude spectrum and an area of 1 in the power-density spectrum.

The least-squares spectrum we present here differs only slightly from the discrete Fourier transform or the Lomb-Scargle periodogram (Lomb, 1976; Scargle, 1982), i.e. the only difference is in the normalization.

A popular tool for calculating amplitude and power spectra is `Period04` (Lenz & Breger, 2005). `Period04` produces amplitude spectra identical to least-squares spectra, but it does not have an option to calculate power-density spectra. `Period04` has an option for subtracting a number of sine waves from the time series, but the approach is different from the approach presented here, which is the approach used in the stellar group at the University of Aarhus for the last 15 years.

### 2.4.2 The Least-squares Spectrum

For a set of observations  $x_0, \dots, x_{N-1}$  with zero mean obtained at times  $t_n$  we can set up a model of the observations:

$$x_n = \alpha \cdot \cos(\nu t_n) + \beta \cdot \sin(\nu t_n), \quad (2.5)$$

that assumes that the time series consists of a single sine wave. Representing a sine wave as it is done here is equal to representing it as  $A \cdot \sin(\nu t + \delta)$  where we have  $A = \sqrt{(\alpha^2 + \beta^2)}$  and  $\delta = \tan^{-1}(\alpha/\beta)$ .

$\alpha$  and  $\beta$  can be calculated by minimizing the following equation:

$$R(\nu_k) = \sum_{n=0}^{N-1} \{x_n - [\alpha \cdot \cos(\nu_k t_n) + \beta \cdot \sin(\nu_k t_n)]\}^2. \quad (2.6)$$

The minimum of the equation is found where:

$$\frac{\partial R}{\partial \alpha} = \frac{\partial R}{\partial \beta} = 0. \quad (2.7)$$

By adopting the notation:

$$YC = \sum_{n=0}^{N-1} x_n \cdot \cos(\nu_k t_n), \quad (2.8)$$

$$YS = \sum_{n=0}^{N-1} x_n \cdot \sin(\nu_k t_n), \quad (2.9)$$

$$CC = \sum_{n=0}^{N-1} \cos^2(\nu_k t_n), \quad (2.10)$$

$$SS = \sum_{n=0}^{N-1} \sin^2(\nu_k t_n), \quad (2.11)$$

$$CS = \sum_{n=0}^{N-1} \cos(\nu_k t_n) \cdot \sin(\nu_k t_n), \quad (2.12)$$

we obtain the following normal equation:

$$\begin{bmatrix} CC & CS \\ CS & SS \end{bmatrix} \begin{bmatrix} \alpha(\nu_k) \\ \beta(\nu_k) \end{bmatrix} = \begin{bmatrix} YC \\ YS \end{bmatrix}, \quad (2.13)$$

which can be denoted as

$$\mathbf{Xa} = \mathbf{y}. \quad (2.14)$$

The solution for  $\mathbf{a}$  will then be:

$$\mathbf{a} = \mathbf{X}^{-1}\mathbf{y}, \quad (2.15)$$

i.e.

$$\begin{bmatrix} \alpha(\nu_k) \\ \beta(\nu_k) \end{bmatrix} = \begin{bmatrix} CC & CS \\ CS & SS \end{bmatrix}^{-1} \begin{bmatrix} YC \\ YS \end{bmatrix} = \begin{bmatrix} SS/D & -CS/D \\ -CS/D & CC/D \end{bmatrix} \begin{bmatrix} YC \\ YS \end{bmatrix}, \quad (2.16)$$

where  $D = CC \cdot SS - CS^2$ . This can also be written as:

$$\alpha(\nu_k) = \frac{SS \cdot YC - CS \cdot YS}{CC \cdot SS - CS^2}, \quad (2.17)$$

$$\beta(\nu_k) = \frac{CC \cdot YS - CS \cdot YC}{CC \cdot SS - CS^2}. \quad (2.18)$$

The least-squares spectrum can then be obtained as:

$$A(\nu_k) = \sqrt{\alpha(\nu_k)^2 + \beta(\nu_k)^2} \quad (2.19)$$

One of the two greatest advantages of the least-squares spectrum over the FFT spectrum is that it can be calculated using statical weights (the other is that it can be used on unevenly sampled data). This is done by assigning a statical weight  $w_n$  to each data point  $x_n$ , so that Eq. 2.6 will read:

$$R(\nu_k) = \sum_{n=0}^{N-1} \frac{w_n}{\bar{w}} \{x_n - [\alpha \cdot \cos(\nu_k t_n) + \beta \cdot \sin(\nu_k t_n)]\}^2. \quad (2.20)$$

Eq. 2.20 can then be solved in the same way as Eq. 2.6 by changing the notation in Eqs 2.8–2.12 to:

$$YC = \sum_{n=0}^{N-1} w_n x_n \cdot \cos(\nu_k t_n), \quad (2.21)$$

$$YS = \sum_{n=0}^{N-1} w_n x_n \cdot \sin(\nu_k t_n), \quad (2.22)$$

$$CC = \sum_{n=0}^{N-1} w_n \cdot \cos^2(\nu_k t_n), \quad (2.23)$$

$$SS = \sum_{n=0}^{N-1} w_n \cdot \sin^2(\nu_k t_n), \quad (2.24)$$

$$CS = \sum_{n=0}^{N-1} w_n \cdot \cos(\nu_k t_n) \cdot \sin(\nu_k t_n), \quad (2.25)$$

as in Frandsen et al. (1995) .

We note again that the only difference between the least-squares spectrum and the Lomb-Scargle periodogram is the normalization. In the normalization of the Lomb-Scargle periodogram the focus is on calculating the significance of a given peak in the spectrum, whereas the focus here is on ensuring that a sine wave with an amplitude of 1 in the time domain also has an amplitude of 1 in the frequency domain. In order to evaluate when a peak is significant we use the  $4\sigma$  criteria given by Breger et al. (1993). This criteria is an empirical criteria, which have proven its usefulness in the analysis of many, especially ground-based, data sets (Breger et al., 1993).

It is important to note the difference between the Fourier transform and the least-squares spectrum. In the Fourier transform a sequence of observations  $x_0, \dots, x_{N-1}$  with zero mean is transformed into a sequence of frequencies  $X_0, \dots, X_{N-1}$  by:

$$X_k = \sum_{n=0}^{N-1} x_n e^{-\frac{2\pi i}{N} kn} \quad (2.26)$$

for real-valued  $X(\omega_k)$ . The Fourier transform fulfills Parseval's theorem:

$$\sum_{n=0}^{N-1} |x_n|^2 = \frac{1}{N} \sum_{k=0}^{N-1} |X_k|^2 \quad (2.27)$$

This means that we can transform data from the time to the frequency domain and vice versa without losing any information. But this can only be done because we have a given number of natural frequencies, i.e.

$$\nu_n = 2\pi n/T, \quad n = -N/2, \dots, +N/2. \quad (2.28)$$

where  $N$  is the total number of data points and  $T$  is the duration of the observations.

As the natural frequencies are only given for evenly sampled data, it follows that Parseval's theorem is not fulfilled for unevenly sampled data and that unevenly sampled data do not have a well defined Nyquist frequency or a set of natural frequencies (Eyer & Bartholdi, 1999). This also includes data with gaps.

This means that for unevenly sampled data the acoustic spectra (least squares or FFT) are not  $\chi^2$  distributed with two degrees of freedom. This again includes data with gaps. This gives us some problems with the use of statistics when modeling power spectra of solar-like stars; we will revert to this in Section 3.2.4.

### 2.4.3 The Fast-Fourier Transform (FFT)

In helioseismology the amplitude spectrum is traditionally calculated by use of FFT. This can of course only be done on evenly sampled data and therefore special care is taken in many observations such as GONG and BiSON to have evenly sampled data. Gaps in the data are most easily removed by filling the gaps with zeros and then scaling the amplitudes with the fill factor, i.e. the inverse of the duty cycle. Consider a time series of  $N$  regular sampled measurements, but with gaps. By including the gaps the time series has  $M$  points. The FFT of  $M$  points can then be calculated where the  $(M - N)$  points that have no measurements have been set to zero. In order to get the right amplitudes the FFT amplitudes need to be multiplied by  $2\frac{M}{N}$ . This will ensure that a sine wave with an amplitude of 1 in the time domain has a peak with an amplitude of 1 in the FFT spectrum. It is also seen that if we have an evenly sampled time series without gaps we need to multiply the FFT amplitudes by

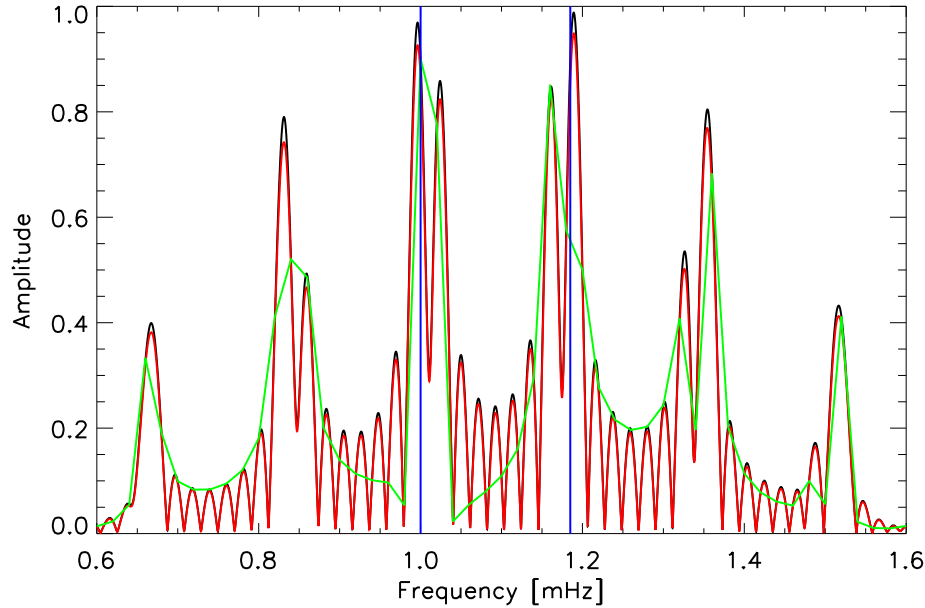


Figure 2.4: Comparison between the least-squares spectrum (black) and the FFT spectrum at the natural frequencies (green) and over-sampled (red). The simulated time series mimic a short 16 h *WIRE* time series, i.e. observations are made only 40 minutes during each 100 minutes orbit. The time-series includes only two frequencies, one at 1.000 mHz and one at 1.185 mHz. Both with an amplitude of one.

2 in order to ensure amplitude normalization. The reason for this is that we are only interested in half of the frequencies calculated in the FFT spectrum.

Zeros can also be added to the beginning or end of the time series before calculating the FFT spectrum in order to over-sample the spectrum. This is called zero-padding:

$$X_k = \sum_{n=0}^{M-1} x_n e^{-\frac{2\pi i}{M}kn} \quad (2.29)$$

where  $M > N$ . As  $x_n = 0$  for  $n > N$  this does not change  $X_k$ , but the amplitudes still need to be normalized by  $2\frac{M}{N}$ .

In Figs 2.4 & 2.5 we have compared the least-squares spectrum of a noise free time series that included two frequencies at 1.000 mHz and 1.185 mHz. It is seen how critical it is to not just calculate the spectrum at the natural frequencies.

Another approach for analyzing data with gaps is to fill the gaps with some kind of interpretation. The art of interpreting the data in the gapes is known as gap-filling and has been used with some success on solar data (see for example

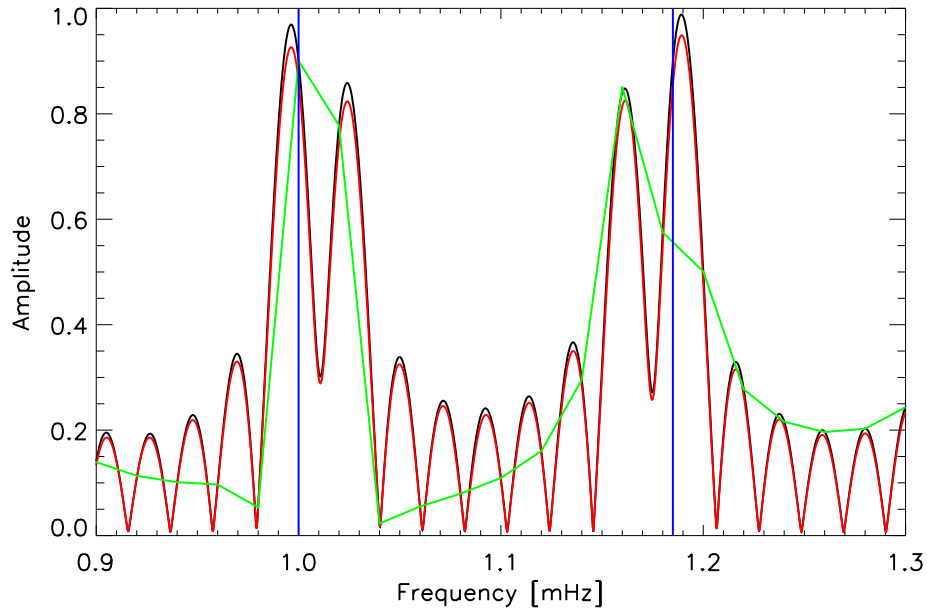


Figure 2.5: The same as Fig. 2.4, but with a zooming in on the simulated frequencies in the time series. It is seen that none of the peaks in neither the least squares nor the FFT spectrum are located on the simulated frequencies. In fact the top of the peak at 1.185 mHz in the FFT spectrum sampled at the natural frequencies is not located on true frequency, but on the orbital harmonics of the peak at 1.000 mHz (1.167 mHz). As there is no noise in the time series the two frequencies and the right amplitudes are easily found by using a CLEAN algorithm, both in the least-squares and in the FFT spectrum

Fahlman & Ulrych, 1982; Brown & Christensen-Dalsgaard, 1990; Fossat et al., 1999).

The art of gap-filling is the art of predicting how the stars behave when we are not observing them. Needless to say this is not possible and data should therefore not be gap-filled.

The least-squares spectrum has two great advantages over the FFT spectrum: Firstly, it is possible to assign weights to each data point (Frandsen et al., 1995). This is necessary for multi-site ground-based data where data from different telescopes will not have the same quality, but it is also highly useful for space-based data in order to down-weight data obtained over the South-Atlantic Anomaly or data with a significant fraction of stray light (Karoff et al., 2008b). Secondly, the least-squares spectrum can be calculated on unevenly sampled data.

The setback from working on unevenly sampled data is that the spectrum is not a transform as the Fourier transform, and therefore the least-squares spectrum can in principle not be used as a representation of the data as the Fourier transform can. This means that the spectrum calculated on unevenly

sampled data cannot (in principle), as opposed to the Fourier transform, be used for filtering.

An argument for using FFT has been that it is much faster to calculate an FFT spectrum than a least-squares spectrum. This is of course true, but it is not a real problem with today's computers. We routinely calculate least-squares spectra of 12 years of *SOHO* data – indeed more than 6 millions data points, and it does not take more than half an hour.

#### 2.4.4 The Power-density Spectrum

If the sampling of a data set is uneven and/or finite then there will be more than one peak in the spectrum (sidebands). For a regular well sampled (observed over many periods), but finite time series a sine wave in the time domain will produce a window function in the frequency domain which is approximately given by (Christensen-Dalsgaard, 2003):

$$A(\nu) \propto T \operatorname{sinc} \left[ \frac{T}{2}(\nu - \nu_0) \right], \quad (2.30)$$

where  $\nu_0$  is the frequency of the sine function in the time domain and

$$\operatorname{sinc}(x) = \frac{\sin x}{x} \quad (2.31)$$

is the sinc function. If the time series contains periodic gaps separated by a given time  $\tau$ , then the window function is approximately given by (Christensen-Dalsgaard, 2003):

$$A(\nu) \propto T \cos \left[ \frac{\tau}{2}(\nu - \nu_0) \right] \operatorname{sinc} \left[ \frac{T}{2}(\nu - \nu_0) \right]. \quad (2.32)$$

In both cases the window function reduces to a  $\delta$  function in the unlikely case of infinite sampling.

In order to have a spectrum that is independent of the sampling we therefore define the power-density spectrum so that a sine wave with an amplitude of 1 in the time domain produces a window function with an area of 1 in the frequency domain. This is done by defining the power-density spectrum as the multiple of the amplitude spectrum and the effective observing length. The effective observing length can be calculated as the reciprocal of the area under the spectral window (Kjeldsen et al., 2005).

The power-density spectrum can be obtained as:

$$PDS(\nu_k) = \frac{A(\nu_k)^2}{\int_0^{\nu_{\text{Nq}}} W(\nu) d\nu} \quad (2.33)$$

where the spectral window function  $W$  is obtained as the least-squares spectrum of a single sine wave with the amplitude of 1 and integrated from zero to the Nyquist frequency ( $\nu_{\text{Nq}}$ ). This is of course not possible as the Nyquist frequency is not defined for unevenly sampled data, but in practice it works as the Nyquist frequency will go to zero at high frequency. As the area under the window function is the same for any frequency the integral in Eq. 2.33 can be

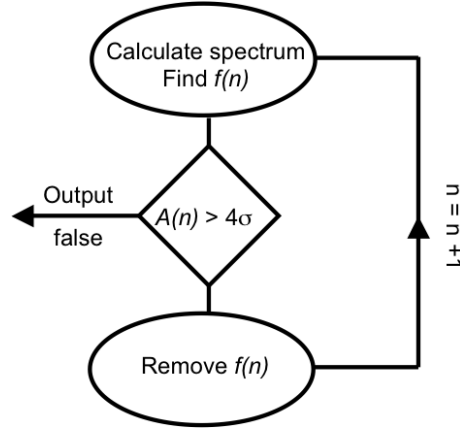


Figure 2.6: Schematic illustration of ISWF. The diamonds represent (while) loops and the ellipses represent operations.

calculated for any frequency, but it is important that the frequency sampling is the same in the calculated power-density spectrum and the spectral window function.

The power-density spectrum has the advantage that the amplitudes are independent of the sampling. This means that noise sources in observations with different sampling and duration can be compared directly in the power-density spectrum.

The power-density spectrum has been used to obtain the amplitude per oscillation mode of a number of solar-like stars (Kjeldsen et al., 2005, 2008) as will be discussed in Section 3.2.2.

### 2.4.5 Iterative-Sine-Wave-Fitting

The algorithms that we present here as iterative-sine-wave-fitting (ISWF) and simultaneous-iterative-sine-wave-fitting (SISWF) are similar to the original CLEANing algorithm used in radio interferometry (Högbom, 1974).

When we know the amplitude and phase (or equivalent  $\alpha$  and  $\beta$ ) of a given frequency in the data we can easily remove it from the data.

$$cx_n = x_n - A_0 \cdot \sin(\nu_0 t_n + \delta_0), \quad (2.34)$$

or equivalent:

$$cx_n = x_n - \alpha(\nu_0) \cdot \cos(\nu_0 t_n) - \beta(\nu_0) \cdot \sin(\nu_0 t_n). \quad (2.35)$$

This can be done for an arbitrary number of frequencies, i.e. it can be done iteratively. This means that we start by removing the wave associated with the highest peak in the spectrum, then we calculate the spectrum again and remove the wave associated with the highest peak in the new spectrum, until there are no more peaks with an S/N higher than 4 (see Fig. 2.6).

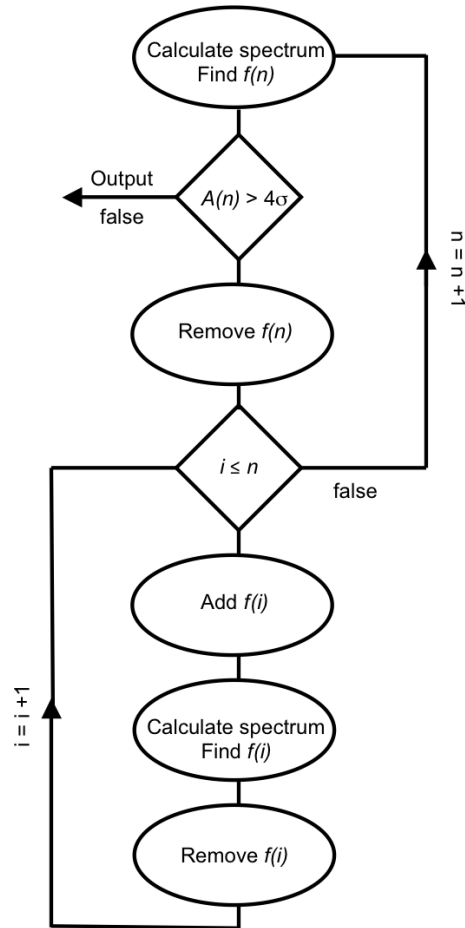


Figure 2.7: Schematic illustration of SISWF. The diamonds represents (while) loops and the ellipses represents operations.

### 2.4.6 Simultaneous-Iterative-Sine-Wave-Fitting

Another approach to finding a large number of waves in a data set is to use SISWF. Here we draw on techniques used in radio interferometry (Högbom, 1974) and define a loop gain  $\gamma$  by which we want to remove a given wave.

SISWF is performed as explained in Fig. 2.7, i.e. we start by removing  $\gamma$  times the oscillation with the highest amplitude and then find the oscillation with the highest amplitude in the new spectrum, then remove  $\gamma$  times this oscillation, we then find the first oscillation again, remove  $\gamma$  times this oscillation and so on and so forth.

SISWF takes into account spectral leakage when evaluating the amplitude and phase of a wave. This means that it can find waves that are closely separated in frequency as long as all the waves have a main peak with an S/N higher than 4.

The loop gain can be chosen to be anything between 0 and 1. We have used 0.5 with success.

SISWF has been used intensively with great success on a number of ground-based multi-site campaigns on solar-like stars (see for example Bedding et al., 2004; Kjeldsen et al., 2005; Bedding et al., 2007). As SISWF can work on many oscillation modes at the same time it has a larger probability compared to ISWF of selecting the right frequency for a given mode instead of one of the sidebands. But SISWF is not appropriate for space-based data where the duration of the observation is much longer than the mode lifetime.

In the case where the observed object oscillates at many different modes simultaneously, SISWF has a great advantage over the way in which the modes are estimated in for example Period04 (Lenz & Breger, 2005). In Period04 a solution for the amplitude, frequency and phase of all the modes is found simultaneously, whereas the solution is found iteratively with SISWF. In this way SISWF can avoid problems with singularities, i.e. two modes with infinite amplitude, the same frequency and phases that are separated by  $\pi$ .

### 2.4.7 Filtering

Any evenly sampled time series can be filtered for any signal in a given frequency range. This can to some extent also be done for an unevenly sampled time series or weighted time series by assuming that the least-squares spectrum is a representation of the time series in the frequency domain. Then a set of observations  $x_n$  can be filtered in the frequency range  $\nu_f$  and thereby producing a new time series  $cx_n$ :

$$cx_n = x_n - \frac{\sum_{\nu=\nu_f} \alpha(\nu) \cdot \cos(\nu t_n) - \beta(\nu) \cdot \sin(\nu t_n)}{\sum_{\nu=\nu_f} W(\nu)} \quad (2.36)$$

Although this formulation relies on an assumption that is mathematical wrong it will work on most time series as long as the sampling in the frequency domain is reasonable high and as long as the band-pass that is filtered is large compared to the window function.

A more correct way to filter an unevenly sampled time series or weighted time series is to use ISWF or SISWF as a filter. When using ISWF or SISWF as a filter one has to choose a given threshold (e.g. S/N=0.001) and then keep removing waves in the frequency range that needs to be filtered until there are no more peaks above the given threshold. This filter does not assume that the least-squares spectrum is a representation of the time series. It only removes a given periodic signal from the time series one after another. But this filter is very ineffective with respect to computing power and it can therefore not be used on 12 years of SOHO data for example. Therefore there are places where it is preferred to use the least-squares spectrum filter even though it relies on an assumption that is mathematical wrong.

# Chapter 3

## Scientific Results from Asteroseismology

This chapter is a review of recent scientific results from asteroseismology of solar-like stars and low-degree helioseismology. The subjects that are discussed are: Solar abundances; Spots and dynamos; Flares; Granulation; Excitation; Oscillation amplitudes; Structure in the echelle diagram; Rotation; Stellar cores; g modes; and Avoided crossing. The aim of this chapter is to provide a general context for the papers in the next chapter.

### 3.1 The Surface

Without the use of seismic techniques we are only able to see the surface of the Sun and other stars which can only provide us with information about the luminosity, the temperature and the chemical abundances of the stars. Measurements of these three parameters can thus be used together with observed oscillation frequencies to test stellar models. For the Sun, where we are able to resolve the surface, we can also observe some of the phenomena that take place there, such as spots and flares.

#### 3.1.1 The Problem with the Solar Abundances

It is important to have a reliable estimate of the abundances of different elements in the Sun as the abundances are an important ingredient in helioseismic models and therefore the abundances can be used as a test of helioseismology and vice versa. This is also the case for stellar abundances and asteroseismology.

The solar abundances have been under heavy debate during the last decade as new improved solar abundances are in conflict with results from helioseismology (see Basu & Antia, 2008, for an excellent review). But the solar abundances are in fact not just important for modeling the Sun, they are also important for modeling other stars as the abundances of these stars are often calculated based only on scaling the solar abundances with the stars' positions in the Hertzsprung-Russell diagram. The solar abundances are also important for astrophysics in general as the abundances of a given object are mostly given relative to the solar abundances. As we will see in Section 3.1.2 changes in the solar abundances can lead to changes in the theoretical prediction of excitation of pulsation in SPB,  $\beta$  Cep and subdwarf B stars. These stars can therefore

be seen as examples of cases where we can use the abundances to test stellar models and vice versa.

The solar abundances can be obtained not only from spectroscopy, but also from the solar wind, from solar energetic particles and most importantly from meteorites (Anders & Grevesse, 1989). Independent measurements can be made of some of the solar abundances, which can be used as a consistency check of the way that the solar abundances are calculated from spectroscopy.

The standard solar abundances were compiled by Anders & Grevesse (1989) (with updated versions by Grevesse & Noels, 1993; Grevesse & Sauval, 1998). These abundances mainly rely on meteoritic data, but adjustments were made according to spectral analysis. The problem here was that the spectral analysis was done using a 1D hydrostatic model of the solar atmosphere. Therefore the line-broadening of the spectral lines had to be calculated by making assumptions about free parameters in the model, i.e. the micro- and macro-turbulence.

Asplund et al. (2005) were the first to calculate the solar abundances by use of a 3D hydrodynamical model of the solar atmosphere. This changed the solar abundances dramatically. The largest changes were seen in carbon, nitrogen, oxygen and iron (which were lowered 35 to 45%) and consequently also in the metallicity  $Z/X$  (which was lowered by 28%) compared to Grevesse & Sauval (1998).

The helioseismic problem with the new solar abundances is that the models calculated with these abundances match the observations much worse than the models calculated with the old abundances (see Fig. 3.1). This is especially the case around the bottom of the convection zone ( $\sim 0.7 R_{\odot}$ ).

The three most important things that have changed in the solar models by using the new solar abundances are: the helium abundance; the position of the base of the convection zone; and the nuclear energy generation rate.

The helium abundance cannot be measured in the photosphere by spectroscopy as it is a noble gas. Therefore the helium abundance is considered a free parameter in the solar models (together with the mixing length parameter  $\alpha$ ), though general constraints are given from the helium abundance in prominence and flare spectra and in the giant planets (Basu & Antia, 2008). When the metallicity is lowered the Sun becomes more blue and more luminous, but as we know the color (temperature) of the Sun one of the free parameters need to be changed. In this way the helium abundance is lowered by 6% in models using the new abundances (Bahcall et al., 2005).

The base of the convection zone is defined as the place where the heat flux from the solar core is no longer transported by radiation, but instead by convection and this depends on the opacity there. The effect of lowering the metallicity is to lower the opacities. This means that the base of the convection zone moves away from the center (Bahcall et al., 2005).

The nuclear generation rate in the solar core is affected by the reduction of the elements in the CNO cycle, but the energy produced by the CNO cycle is less than 1% of the energy produced by the  $p-p$  chain. The reduced metallicity could also reduce the opacity in the solar core (Bahcall et al., 2005).

At this stage there are no clear answers to the disagreement between the new solar abundances and seismic solar models and it is therefore not clear if

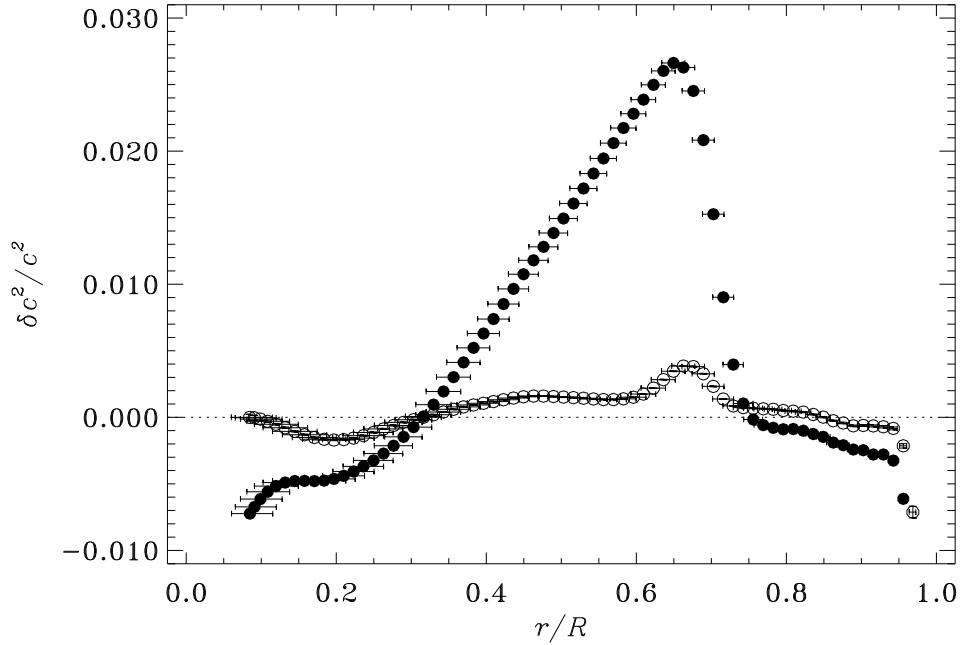


Figure 3.1: Relative differences in squared sound speed, in the sense (Sun) - (model), against fractional distance  $r/R$  to the solar center. The open symbols are for Model S (which uses the abundances from Anders & Grevesse, 1989). The filled symbols are for a model with the revised abundances presented by Asplund et al. (2005). The figure has been prepared by J. Christensen-Dalsgaard.

the answers should be found in the models of the solar atmosphere used in the calculation of the abundances or in the models of the solar interior used in the seismic models. Anyway we can expect that once we have found an answer to the disagreement we have also improved the models of the solar atmosphere, of the solar interior or of both.

### 3.1.2 Excitation of $\beta$ Cep and SPB Stars at Low-metallicity

One place where the values of the solar abundances have a large effect is in the models of  $\beta$  Cep and SPB stars. Pulsation in these stars is driven by the heat-engine or  $\kappa$  mechanism which is due to the opacity bump caused by the iron ionization zone. Changing the abundances alters both the opacities and the amount of iron in the stars and this can therefore have a dramatic effect on the way in which the oscillations are excited in  $\beta$  Cep and SPB stars.

One of the problems with  $\beta$  Cep and SPB stars is that though pulsation is generally believed not be present in stars with metallicity much lower than the solar metallicity, an increasing number of  $\beta$  Cep and SPB stars are seen in the low-metallicity Magellanic Clouds (see Karoff et al., 2008a, or Chapter 5 for discussion)

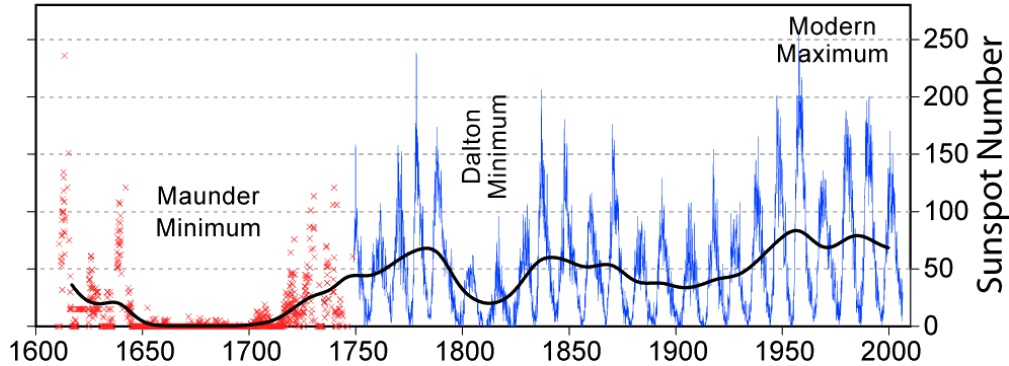


Figure 3.2: Monthly average number of Sunspots. From: Global Warming Art.

Miglio et al. (2007a,b) have shown that the instability strip in the Hertzsprung-Russell diagram is enlarged by using the new abundances together with new opacities. Especially it is shown by Miglio et al. (2007a,b) that the new abundances and the new opacities can drive radial oscillations in stars with a metallicity as low as 0.01 which cannot be done with the old abundances and opacities. It is also seen that the new abundances have the effect of extending the excited frequencies towards higher overtones.

Though there are contradicting interpretations of the effect of the new abundances on the excitations of  $\beta$  Cep and SPB stars (see for example Pamyatnykh & Ziomek, 2007) it might be possible to test the new abundances and opacities on oscillations in low-metallicity  $\beta$  Cep and SPB stars.

If the result by Karoff et al. (2008a) is confirmed and it really appears that  $\beta$  Cep and SPB stars are common in low-metallicity environments then we will be left with the same kind of problem that asteroseismology of white dwarfs was facing 12 years ago. Here a new class of pulsating subdwarf B stars were found and to begin with the oscillations in these stars were believed to be driven by the He II – He II convection zone; however, it was soon realized that the driving was negligible in the He II – He II convection zone as this region contains only very little mass, and therefore it carries practically no weight in terms of driving. Instead it was shown by Charpinet et al. (1997) that pulsation in subdwarf B stars could be driven by an opacity bump due to a local enhancement of the iron abundance in the envelopes of these stars. The enhancement was shown to be caused by gravitational settling and radial levitation of heavy elements. A similar driving mechanism has been investigated for  $\beta$  Cep and SPB stars in low-metallicity environments by Miglio et al. (2007c), but it is still not clear if this is the solution to the possible low-metallicity  $\beta$  Cep and SPB stars.

### 3.1.3 Spots and Dynamos

Sunspots are regions on the surface of the Sun that are a few thousand degrees colder than the surroundings. The sunspots therefore appear black on the solar surface. The first records of sunspots were made by Galileo in 1612 and they have been continuously recorded ever since. These observations have revealed

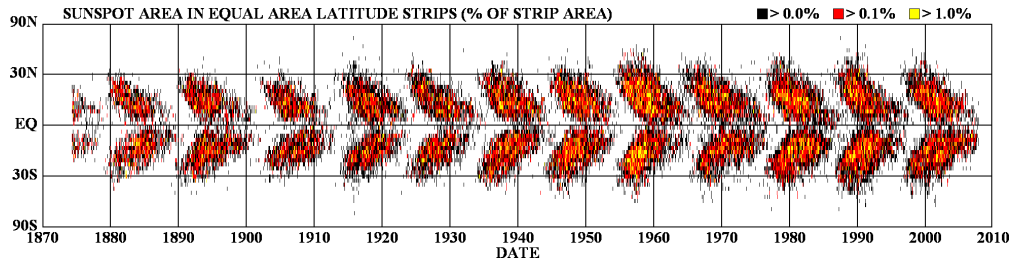


Figure 3.3: The sunspot butterfly diagram, showing the size of sunspots as a function of solar latitude and time. From: NASA/MSFC/NSSTC/HATHAWAY

both the 11 year cycle of the sunspots known as the solar dynamo and also temporal changes on a longer scale as is seen in Fig. 3.2

The sunspots are believed to originate from magnetic flux tubes that rise through the convection zone and emerge at the photosphere (Charbonneau, 2005). This can be seen from the fact that sunspots always appear in pairs with opposite magnetic polarity. The sign for the leading sunspot changes from cycle to cycle. The magnetic flux tubes rise through the convection zone as they are wound up by the differential rotation of the Sun; therefore the sunspots only appear in a 60 degree wide latitudinal band around the equator as can be seen in the butterfly diagram (Fig. 3.3). The butterfly diagram also shows that in a cycle the sunspots emerge closer and closer to the equator, in agreement with the models of the Sun's internal magnetic field.

All cool stars with outer convection zones are expected to have spots and stellar dynamos. As the dynamos are closely related to the rotation, young stars that tend to rotate faster will have a stronger dynamo, more spots and more activity. Spots can be observed on stellar surfaces with the use of photometry, spectroscopy, interferometry and microlensing (see Berdyugina, 2005, for discussion). For solar-like stars the spots can be seen in the time-series of white-light photometry (as has been done for HD49933 ESA, 2007) or radial velocity (as has been done for Procyon by Arentoft et al., 2008). These observations can be compared with the same kind of observations of the Sun, this being either VIRGO observations in photometry or GOLF observations in radial velocity. These observations have only been made recently as they demand high absolute precision. Another way to observe spots and stellar cycles is to monitor the stars in CA II H & K emission (Wilson, 1978). The variations caused by the spots are much stronger in the ultraviolet than in the visual, therefore observations in the ultraviolet do not demand as high a precision as observations in the visual or of radial velocities. In this way stellar cycles have been monitored in around 100 stars in the Mount Wilson Observatory HK Project (Baliunas et al., 1995) since 1966.

Stellar cycles can also be observed using asteroseismology, which has been proven by helioseismic observations of small frequency shifts of the p modes (Chaplin et al., 2007) and in amplitudes changes of the p modes (Chaplin et

al., 2000a). The frequency shifts are believed to originate from changes in the near surface sound speed caused by changes in the internal magnetic field or from changes in the radial-velocity component of the granulation (Metcalf et al., 2007). The frequency shifts rise from around  $0.2 \mu\text{Hz}$  at low frequency to just below  $1 \mu\text{Hz}$  at high frequency, and they are expected to scale with stellar rotation (Metcalf et al., 2007). The shifts are positive at maximum magnetic activity and vice versa.

Metcalf et al. (2007) provide a way to calculate the shifts based on the mass and radius of the star and on the mode inertia of the oscillation. Using this method Metcalf et al. (2007) calculate the expected frequency shifts for  $\beta$  Hydri which are significantly lower than those seen in the Sun (mean value of  $0.1 \mu\text{Hz}$  due to the slow rotation of  $\beta$  Hydri). Metcalf et al. (2007) also identified these shifts in  $\beta$  Hydri, but the error bars on the used frequencies were too large to make the identified shifts statistically significant.

Fletcher et al. (2006) have detected a mean change in the frequencies in  $\alpha$  Cen A of  $0.6 \pm 0.3 \mu\text{Hz}$  between ground- and space-based observations separated by 19 months, when correcting for the Earth's orbit.

The peak amplitudes of the solar p modes show a decrease of  $46 \pm 5\%$  from solar minimum to solar maximum (Chaplin et al., 2000a); this decrease is believed to originate mainly from an increase in the mode line-widths, which is caused by increased mode damping around solar maximum. This can be seen from the relation between the excitation of the modes as a function of frequency  $F$ , the amplitude of the mode  $A$  and the damping time of the mode  $\eta$  (Chaplin et al., 2000a):

$$A \propto \frac{F}{\eta^2}, \quad (3.1)$$

which gives:

$$\frac{\delta A}{A} = \frac{\delta F}{F} - 2 \frac{\delta \eta}{\eta}. \quad (3.2)$$

As Chaplin et al. (2000a) measure  $\delta A/A$  to  $-0.46 \pm 0.05$  and  $\delta \eta/\eta$  to  $-0.24 \pm 0.03$  they conclude that the excitation of the modes must be constant.

The changes in the damping rates is believed to originate from changes in the horizontal length scale of the flow in the upper part of the convection zone (Houdek et al., 2001). The theory is supported by observations by Muller (1988) which show that the horizontal granule size becomes smaller by 5% from solar minimum to solar maximum and by numerical simulation of convection in magnetic fields which shows that the presents of magnetic field can modify the horizontal length scale of the convective flow (Moore & Weiss, 1973).

p-mode amplitude changes have not yet been observed in other stars, but it is our hope that we will be able to do this with data from *KEPLER*.

### 3.1.4 Excitation of Global Oscillation by Flares

Flares are huge explosions on the Sun's surface. They are believed to originate from reconnection of magnetic field lines in corona loops. The flares release energy at all wave lengths and they also accelerate electrons, protons and ions.

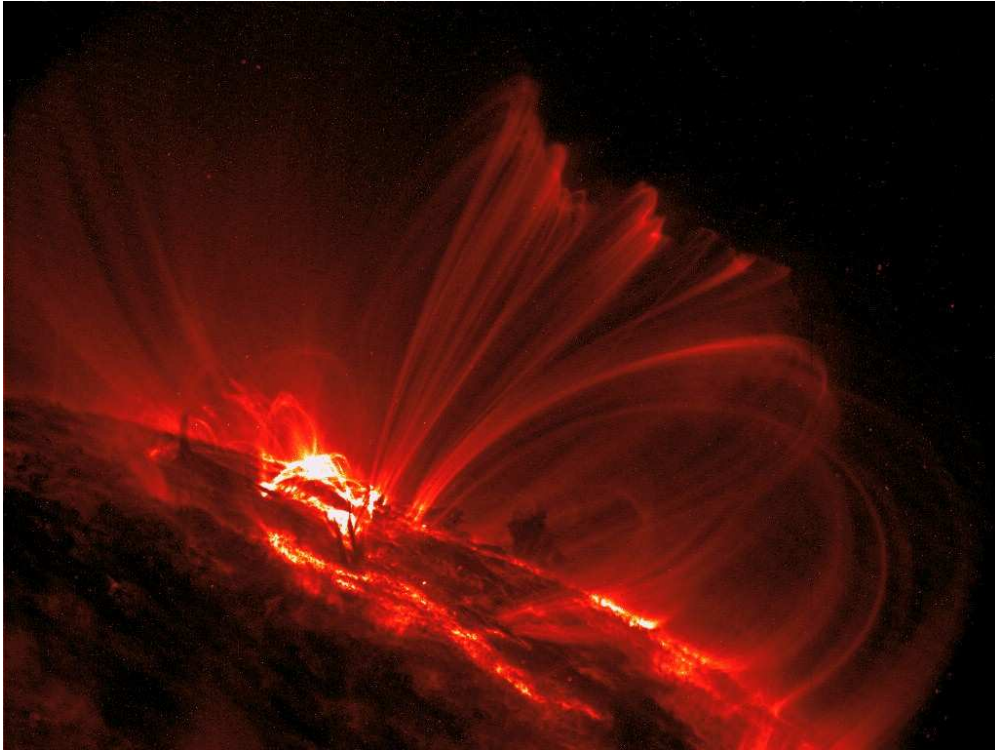


Figure 3.4: Image of the active regions AR 9628 and AR 9632 taken by the Transition Region and Coronal Explorer (TRACE) at 23:59 UT on the October 1, 2001. These active regions produced several flares during their disk passage, including one at 23:40 UT that is seen in this image (From: NASA).

Though the released energy is huge the flares cannot easily be detected above the solar background at all wavelengths - they are best detected in X-rays.

The energy released by flares are known to generate a number of different wave-like phenomena on and inside the Sun. In the corona flares can generate super-fast alfvénic shock waves known as Moreton waves (Moreton & Ramsey, 1960). These waves which can propagate distances comparable to the solar radius with speeds of  $1000 - 2000 \text{ km s}^{-1}$  have some similarities with the circularly expanding bubble-like shocks following an atomic bomb explosion (Ballai, 2007). The Moreton waves are best seen in  $H\alpha$ . Some flares also generate local short-lived high-degree oscillations in the active regions in which they are produced (Kosovichev & Zharkova, 1998). These waves can propagate  $100 - 200 \text{ Mm}$  with speeds of  $200 - 300 \text{ km s}^{-1}$ . The detection of these waves was made using time-distance helioseismology where the wave excited by the flare can be followed with a circular mask propagating away from the flare.

Before the detection of the 5-minute oscillation in the Sun it was suggested by Wolff (1972) that flares could drive free global oscillations in the Sun. The nature of these waves differs from the waves detected by Kosovichev & Zharkova (1998) because they have low-angular degree and therefore needs to travel

through the whole Sun before they are reflected. Although it is generally accepted that the p modes are excited by the near-surface convection a number of studies have investigated if some part of the excitation of the p modes was caused by for example flares. These studies have come out with contradicting results. Gavryusev & Gavryuseva (1999) found a high correlation between temporally varying p-mode power measured at low degree in GONG data and the coronal mass ejection event number, but because of the way they normalized the correlation coefficient and because of the selective selection of the events it is not possible to make a qualitative evaluation of the correlation coefficient obtained by Gavryusev & Gavryuseva (1999) nor is it possible to compare there value of the correlation coefficient with values obtained in other data sets. Ambastha & Antia (2006) on the other hand found no correlation between a longer disk-integrated GONG data set and flare and coronal mass ejection indices. In this study the correlation coefficient was properly normalized and there was no selection of events.

Analysis of BiSON data has also revealed that though the strength of the p modes follows the distribution expected from stochastic excitation by near-surface convection, there is evidence of a few more very large events than what is predicted by the theory, but these events show only a poor correlation with flares (Chaplin et al., 1995).

Karoff & Kjeldsen (2008) were therefore the first to clearly prove the prediction by Wolff (1972). This was done by using a wavelet-like technique on data from the VIRGO instrument on *SOHO* and by looking at the high-frequency part of the acoustic spectrum instead of at the p modes as these waves are much more sensitive to the acoustic background than the p modes.

The reason for this is that the observed power of p modes at high frequency are significantly lower than the power observed at the peak (3 mHz). According to Stein & Nordlund (2001) one finds the p-mode power to decrease inversely to the fourth power of the frequency (above 3 mHz) simply as a consequence of the granulation power decreasing as  $\nu^{-4}$ . Therefore a single event like a flare that excites a mode will have a larger relative effect at high frequencies because the other excitation sources are much smaller.

Related to this, one should also note that the high-frequency background (between the p modes) also shows an increased correlation with flare activity. One may therefore argue that the background noise from granulations correlate with flare activity and that the increased background transfer more power into the high-frequency modes via the stochastic excitation.

Another explanation to why the flare-generated global waves are seen in the high-frequency part of the acoustic spectrum could be that flares would excite oscillations in the chromosphere rather than inside the photosphere. Observations of oscillations in absorption lines in the ultraviolet part of the spectrum have shown that the oscillations here have a characteristic period of 3 minutes rather than the 5-minute period of the p modes (Deubner, 1995). In the acoustic spectrum the oscillations in the chromosphere are known to show a few mHz broad envelope of energy rather than distinct peaks. This means that the chromosphere shows just as much energy at the frequencies in between the p mode as on them (Deubner, 1995). These two phenomena agree with the nature of

the high-frequency waves in which the signature of the flares is seen (Karoff & Kjeldsen, 2008).

## 3.2 The Granulation Zone

The energy generated in the stellar cores can be transported to the surface of the stars by either radiation or convection. The condition for the energy to be transported by convection is that the radiative temperature gradient is larger than the adiabatic temperature gradient (Christensen-Dalsgaard, 2008):

$$\nabla_{\text{R}} > \nabla_{\text{ad}}. \quad (3.3)$$

The radiative temperature gradient can be estimated as (Christensen-Dalsgaard, 2008):

$$\nabla_{\text{R}} \propto \kappa \frac{L(r)}{m(r)} \frac{\rho}{T^3}, \quad (3.4)$$

where  $\kappa$  is the opacity,  $L(r)$  is the total amount of energy transported through a sphere of radius  $r$ ,  $m(r)$  is the mass inside the sphere of radius  $r$ ,  $\rho$  is the density and  $T$  is the temperature.

In general the energy is transported by convection: in the outer parts of stars less massive than the Sun as these stars are relatively cool and therefore the term  $\frac{\rho}{T^3}$  is large; in the outer parts of stars with mass similar to the Sun as the opacity  $\kappa$  is large there; and in the core of stars more massive than the Sun as the energy generation is large and therefore the term  $\frac{L(r)}{m(r)}$  is large (Christensen-Dalsgaard, 2008).

When energy is transported by convection in the outer parts of the stars it means that hot matter rises to the surface and cool matter sinks in convection currents. The convection currents are made of granules which are typically 1000 km in diameter and have lifetimes of 6 to 12 minutes (Müller et al., 2001).

Stars with an outer convection zone are interesting for asteroseismology because the granulation can excite global oscillations and because we can see the effect of the granulation in the background of the acoustic spectrum in these stars.

### 3.2.1 Granulation Background in the Acoustic Spectrum

The granules can be seen in high-resolution images of the Sun, but we can also see granulation in the acoustic spectrum of the Sun and other stars with near-surface convection. This was first done by Harvey (1985), who modeled the background in the solar acoustic spectrum as a drifting system, where the distribution of the intensities or velocities on the solar surface decays with a slope of  $-2$  in power. In this way the background in the solar acoustic spectrum is given as:

$$P(\nu) = \frac{4\sigma^2\tau}{1 + (2\pi\nu\tau)^2}, \quad (3.5)$$

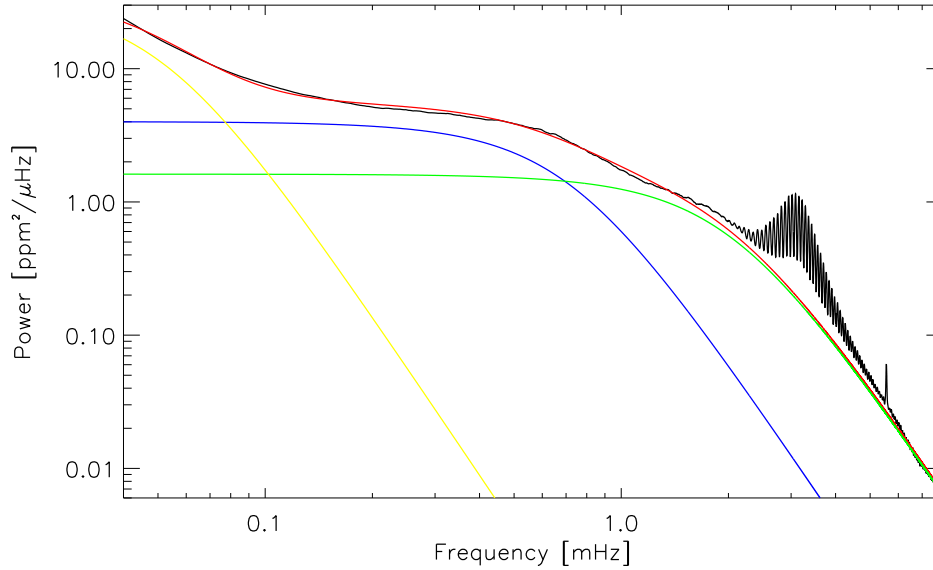


Figure 3.5: The solar acoustic background. The black line shows the smoothed version of the solar acoustic spectrum from Fig. 6.1 and the red line is the extended Harvey model (Eq. 3.6). The yellow line shows the contribution from activity, the blue from granulation and the green from faculae.

where  $\sigma$  is the rms intensity or velocity of the granules and  $\tau$  is the characteristic lifetime of the granules. But granulation is not the only phenomenon in the background of the solar acoustic spectrum, in order to get a good agreement between the models and the observations the models should also include: faculae ( $\tau \sim 70$  s); mesogranulation ( $\tau \sim 10^4$  s); supergranulation ( $\tau \sim 10^5$  s); and active regions ( $\tau \sim 10^6$  s). The faculae are the bright points seen on visual solar images often close to the dark sunspots. The faculae are due to changes in the opacity caused by a strong magnetic field which means that we see into the granulation cells rather than seeing the surface of the granulation cells and as the temperature is higher inside the granulation cells than at their surfaces the faculae appear brighter than their surroundings. (Keller et al., 2004). Meso- and supergranulation are larger granulation cells (7,000 and 30,000 km in diameter, respectively) and their origin remains largely unknown.

Unfortunately, the original model by Harvey (1985) fails to reproduce the background in the observed acoustic spectrum for frequencies higher than the atmospheric cut-off frequency. The reason for this is that granulation cannot be modeled with turbulent cascades (Nordlund et al., 1997) as it is done in the drift model. Turbulence shows a distribution with a slope of  $-2$  in power, convection on the other hand has a lower limit in the time domain on which changes can take place. This means that on small time-scales (or at high frequency) convection is not noisy whereas turbulence is. Therefore the background of the acoustic spectrum decays with a slope of  $-4$  at frequencies higher than

Table 3.1: Background Parameters for the extended Harvey model

Type	Parameters	Value
Faculaes	$\tau$ (s)	78.1
	$\sigma$ (ppm)	0.067
Granulation	$\tau$ (s)	221.4
	$\sigma$ (ppm)	0.072
Activity	$\tau$ (s)	3096
	$\sigma$ (ppm)	0.052

the atmospheric cut-off frequency. Taking this into account the Harvey model extends to:

$$P(\nu) = \sum_n \frac{4\sigma_n^2 \tau_n}{1 + (2\pi\nu\tau_n)^2 + (2\pi\nu\tau_n)^4}, \quad (3.6)$$

Fig. 3.5 shows the smoothed version of the solar acoustic spectrum from Karoff & Kjeldsen (2008) with the extended Harvey model overlaid. The parameters used in the Harvey model are given in Table. 3.1. The one thing that can easily be compared with other observations is the characteristic lifetime of the granules which is found to be 221.4 s. This is around half the lifetime of around 7 minutes found by Müller et al. (2001) by means of a time-slice analysis of 1400 white-light images of the Sun with high-spatial resolution from the Swedish Vacuum Solar Telescope on La Palma. A reason for this difference could be that the solar acoustic background cannot know the difference between when a granule is born and when it dies. This would mean that the time scale observed in the acoustic spectrum should be half the value found in the white-light images. The results presented here are in agreement with the results obtained by (Vázquez Ramió et al., 2005) using the original Harvey model.

A number of studies have used a simple power law relation for fitting the solar acoustic background (Harvey et al., 1993; Aigrain et al., 2003) where the slope differs from the values of  $-2$  and  $-4$ . Though such a model fits the background nicely it is not justified physically. In order to test the effect of using a simple power law instead of the physical Harvey model on  $\sigma$  and  $\tau$  we have tried to model the acoustic background with the original Harvey model, but where the slope of the granulation and the bright points was changed to  $-4$ :

$$P(\nu) = \sum_n \frac{4\sigma_n^2 \tau_n}{1 + (2\pi\nu\tau_n)^4}, \quad (3.7)$$

It is seen in Fig. 3.6 that the power law model generally matches the observations better, but as is seen in Table. 3.2 there are no significant changes in the obtained parameters. That the power law model matches the observations better than the extended Harvey model does not mean that the power law model is better, as there are no physical reflections behind this model. It could mean however that there are phenomena (especially around 1mHz) that remain

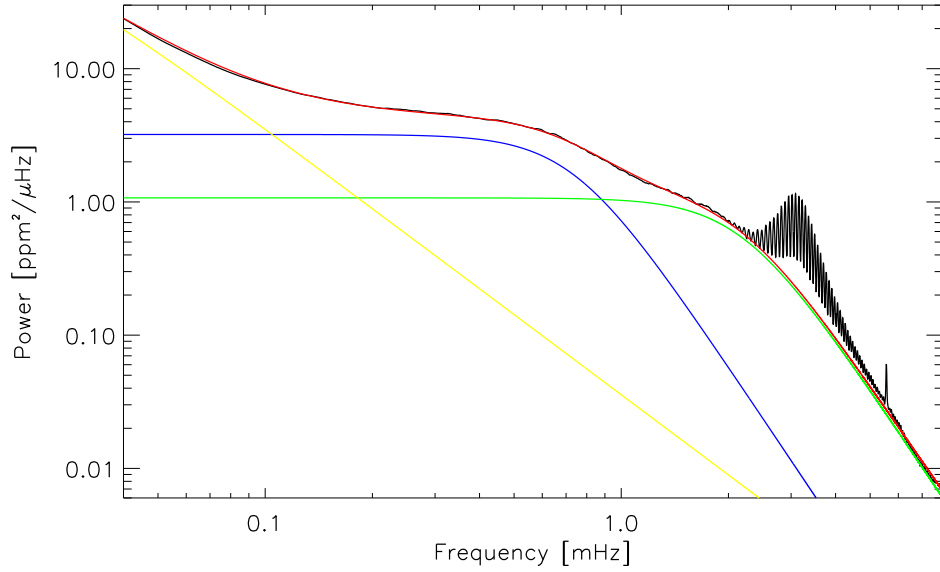


Figure 3.6: The same as Fig. 3.5, but this time the background has been modeled with a power-law model in Eq. 3.7.

to be fully understood, though the general properties of the background in the solar acoustic spectrum seem to be well understood.

A good understanding of the acoustic background spectrum in solar-like stars is important as it is used when calculating the mode amplitude of the p-mode oscillations as done in the method developed by Kjeldsen et al. (2005). This can be done by using the scaling relations in Kjeldsen & Bedding (in prep.). Here it is found that the rms intensity of the granules and the characteristic lifetime of the granule scale as:

$$\sigma \propto \frac{\sqrt{L}}{T_{\text{eff}} M}, \quad (3.8)$$

and

$$\tau \propto \frac{L}{T_{\text{eff}}^{3.5} M} \quad (3.9)$$

where  $L$  is the luminosity,  $M$  the mass and  $T_{\text{eff}}$  the effective temperature of the stars.

### 3.2.2 Oscillation Amplitudes in Velocity and Photometry

The first estimates of the amplitudes of solar-like (convection driven) oscillations were given by Kjeldsen & Bedding (1995). They found that the velocity amplitudes predicted in the models by Christensen-Dalsgaard & Frandsen (1983)

Table 3.2: Background Parameters for the power law model

Type	Parameters	Value
Faculaes	$\tau$ (s)	72.7
	$\sigma$ (ppm)	0.061
Granulation	$\tau$ (s)	216.9
	$\sigma$ (ppm)	0.061
Activity	$\tau$ (s)	10752
	$\sigma$ (ppm)	0.062

were well fitted by the relation:

$$\frac{\delta V}{V} \propto \left( \frac{L}{M} \right)^s, \quad (3.10)$$

where  $L$  is the luminosity and  $M$  is the mass of a given star. The value of  $s$  was found to be 1 by Kjeldsen & Bedding (1995). Later Houdek et al. (1999) and Samadi et al. (2007) have redone the exercise of Kjeldsen & Bedding (1995) and obtained rather different values of  $s$  ranging from 0.7 to 1.47. Houdek et al. (1999) included convection in the stellar models by using a nonlocal, time-dependent mixing-length model and found that the scaling law was well satisfied for  $M/M_\odot \leq 1.4$ . For higher masses the amplitudes were generally larger than the predictions by the scaling law. Samadi et al. (2007) used numerical 3D simulations of surface convective zones to characterize the turbulent spectra and found that  $s$  should be between 0.7 and 1.0 depending on which form was used for the convection eddy time-correlation.

Scaling relations can also be obtained for the intensity oscillation amplitudes, by assuming (Kjeldsen & Bedding, 1995):

$$T_{\text{eff}}^2 \frac{\delta V}{V} \propto \frac{\delta L}{L}. \quad (3.11)$$

This gives:

$$\frac{\delta L}{L} \propto \frac{L}{T_{\text{eff}}^2 M}. \quad (3.12)$$

As the Sun is assumed to have a black-body spectrum the intensity oscillation amplitudes will also depend on the wavelength in which the oscillations are observed, so that the oscillation amplitudes will decrease linearly with increasing wavelength (Kjeldsen & Bedding, 1995). All the observations of stellar oscillation amplitudes are performed without a filter in front of the CDD which we assume corresponds to the observation of the solar oscillation in the green channel on the VIRGO instrument on *SOHO* and therefore we do not include the wavelength dependency in the equations.

In recent years it has become possible to test these scaling relations due to the increasing number of stars where solar-like oscillations have been observed. When comparing oscillation amplitudes it is important to have a general definition of how the amplitudes are measured. Such a definition has been given

by Kjeldsen et al. (2008) based on the way that the amplitudes are calculated in Kjeldsen et al. (2005) (see also Section 2.3.1 in this dissertation). Here the first parameter that needs to be defined is the width of the Gaussian used for smoothing. Kjeldsen et al. (2008) suggest to use  $4\Delta\nu$ , where  $\Delta\nu$  is the large separation. This works well for most of the solar-like stars, especially for the stars observed by *WIRE* where the width needs to be larger than the satellite orbital harmonic – 179  $\mu\text{Hz}$ , but for stars where the excess power is at low frequency, for example Procyon, this approach does not work without problems, as the dip in the power at frequencies lower than the excess power is reduced as a cause of the heavily smoothing in the radial-velocity measurements. Also for K giants the width of  $4\Delta\nu$  becomes problematic, as  $\Delta\nu$  here is comparable to the frequency of the excess power. The reason for scaling the width with  $\Delta\nu$  is that the excess power then becomes independent of the width of the excess power envelope, i.e. the number of continual radial orders that are excited in the stars. For the estimation of the mode amplitudes done by Arentoft et al. (2008) the width is therefore set to  $4\Delta\nu$  at the frequency of the power excess (1 mHz) and then adjusted on a logarithm scale with frequency; this ensures that the dip below the excess is not reduced, but it only produces half a solution to the problem as there is no longer a physical argument of the choice of width.

The amplitudes are normalized by multiplying the PDS by  $\Delta\nu/c$  where  $c$  is a factor that measures the effective number of modes per order. Originally Kjeldsen et al. (2005) used  $c = 3$  based on the simple argument that on average we see 3 modes per radial order  $n$ , but these numbers of course need to be calculated as it is done by Kjeldsen et al. (2008). Such a calculation is based on the spatial filters  $S_l$  (Christensen-Dalsgaard, 1989), which quote the spatial response of the observations (wavelength) to modes with degree  $l$ , i.e.:

$$c = \sum_{l=0}^4 (S_l/S_0)^2. \quad (3.13)$$

This gives  $c = 4.09$  for radial velocities obtained by Doppler shifts and 3.13 for photometry obtained at 500 nm (Kjeldsen et al., 2008).

Table 3.3 lists the number of stars in which solar-like oscillations have been observed. For the majority of these stars the amplitudes have been calculated as outlined above, but for some of the stars (i.e. HD49933, 70 Oph A,  $\eta$  Boo,  $\beta$  Vir and  $\delta$  Eri) the original measurements were not available and therefore we have relied on numbers published in the literature. In the studies by Carrier et al. the amplitudes are quoted as the peak values, but in a range. As these peaks are generally higher than the amplitude per mode calculated the way it is outlined here (because of the stochastic excitation) we have therefore always used the lower value in this range.

The velocity amplitudes per mode of the stars in Table 3.3 are plotted in Fig. 3.7 as a function of  $L/M$ . By fitting a straight line to the data in the log-log plot we can give an estimate of the parameter  $s$  in the scaling relation (Eq. 3.10); here we obtain  $s = 0.64 \pm 0.23$  which is in agreement with Samadi et al. (2007), in marginal agreement with Kjeldsen & Bedding (1995) and not in agreement with Houdek et al. (1999). The uncertainties on  $s$  has been estimated

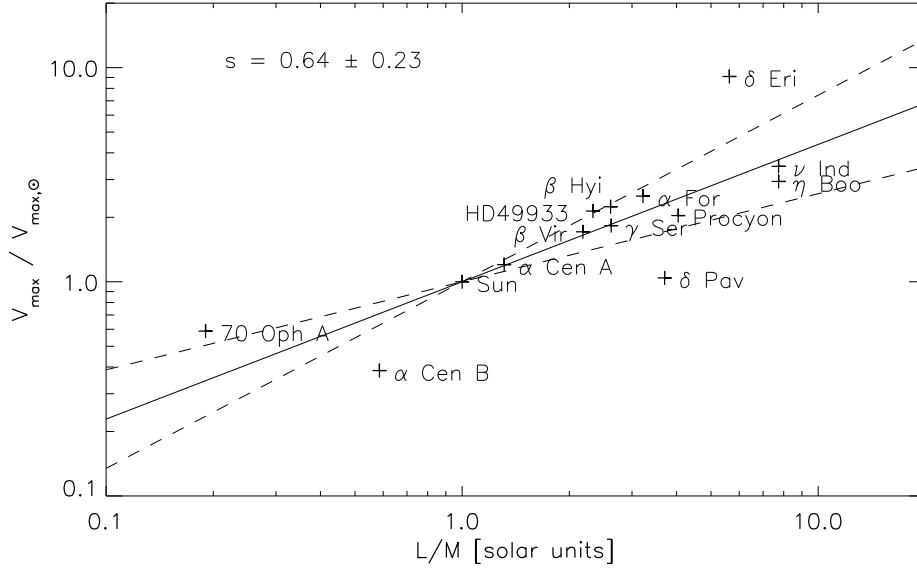


Figure 3.7: The radial-velocity amplitude per mode of the stars in which we have observed solar-like oscillations, as a function of  $L/M$ . The solid line gives the best fit to the scaling law relations (Eq. 3.9). The dotted lines marks the uncertainties in the fit based on estimates of the uncertainties in the mode amplitudes as explained in the text.

by assuming uncertainties of 3 cm/s on the amplitude per mode for all the stars except the Sun where we used the value of 0.7 from (Kjeldsen et al., 2008). The reason that the uncertainties cannot be estimated with higher authenticity is that most of the uncertainties in the estimation of the amplitude per mode are in the way that the background in the acoustic spectra are modeled. In other words the uncertainties are not in the observations, but in the model that we use.

Based on the divergence between the scaling relation by Kjeldsen & Bedding (1995) and some of the observations in Fig. 3.9 Kjeldsen & Bedding (in prep.) have suggested a new scaling relation which is based on the Harvey model of the background granulation (as discussed in the previous section):

$$\frac{\delta V}{V} \propto \frac{L\sqrt{\tau_{\text{life}}}}{T_{\text{eff}}^{2.25}M^{1.5}}, \quad (3.14)$$

and:

$$\frac{\delta L}{L} \propto \frac{L\sqrt{\tau_{\text{life}}}}{T_{\text{eff}}^{4.25}M^{1.5}}. \quad (3.15)$$

These relations are plotted for velocity in Fig. 3.8 and intensity in Fig. 3.9 assuming constant mode lifetime

This improved version of the scaling relation is seen to agree well with the observations for the velocity amplitudes, but it is not possible to determine

Table 3.3: Parameters for stars showing solar like oscillations. The temperatures, surface gravities, luminosities and masses are from Pijpers (2003), except HD 49933 which is from Bruntt et al. (2004). The radial-velocity amplitudes are from Kjeldsen et al. (2008) and the photometric amplitudes are from Karoff et al. (2008b), except for HD49933 where the radial-velocity amplitude is from Mosser et al. (2005) and the photometric amplitude is from ESA (2007) and Procyon, 70 Oph A,  $\eta$  Boo,  $\beta$  Vir and  $\delta$  Eri where the radial-velocity amplitudes are from Arentoft et al. (2008), Carrier & Eggenberger (2006), Carrier et al. (2005b), Carrier et al. (2005a) and Carrier et al. (2003), respectively.

name	$T_{\text{eff}}$ [K]	$\log g$ [cm/s <sup>2</sup> ]	$L$ [ $L_{\odot}$ ]	$M$ [ $M_{\odot}$ ]	$V$ [cm/s]	$I$ [ppm]
Sun	5770	4.44	1.00	1.00	18.7	4.25
$\beta$ Hydri	5860	4.05	4.00	1.53	41.9	13.5
$\alpha$ For	6000	4.00	4.00	1.24	47.0	–
$\delta$ Eri	4884	3.40	3.39	0.60	170.0	–
Procyon	6500	4.04	7.00	1.73	38.1	6.0
$\beta$ Vir	6109	4.20	3.59	1.64	32.0	–
$\eta$ Boo	6003	3.62	9.20	1.19	55.0	–
$\alpha$ Cen B	5255	4.51	0.54	0.92	7.2	–
$\alpha$ Cen A	5830	4.34	1.58	1.20	22.5	6.0
$\gamma$ Ser	6249	4.16	3.02	1.15	34.2	–
70 Oph A	5260	5.00	0.80	4.20	11.0	–
$\delta$ Pav	5538	3.80	1.33	0.36	19.5	–
$\nu$ Ind	5381	3.43	6.70	0.87	64.7	–
HD49933	6557	4.30	3.50	1.50	40.0	4.6

whether the old scaling relation with  $s=0.63$  or the new scaling relation agrees best with the observation for the velocity amplitudes.

By using stellar models to obtain a relation between luminosity, mass and temperature Kjeldsen & Bedding (in prep.) find that Eq. 3.14 reduces to the  $L/M$  scaling relation in Eq. 3.10 where  $s$  is equal to 0.5 for zero main sequence stars, 0.8 for main sequence stars without convective cores and 0.7 for evolved main sequence stars with convective cores. This agrees very well with the results presented in Fig. 3.8 for the velocity amplitudes. This also shows why the original scaling relation seems to work, though there are some outliers.

As far as the intensity amplitudes are concerned the agreement in Fig. 3.9 is not so good. Though the number of stars with measured intensity oscillation amplitude is limited the observations can be used to test if the relation between the velocity and intensity amplitudes given by the scaling relation is correct. Both Kjeldsen & Bedding (1995) and Kjeldsen & Bedding (in prep.) assume that the intensity scales with  $T_{\text{eff}}^2$  times the velocity amplitudes. This assumption is based on the models by Christensen-Dalsgaard & Frandsen (1983). In order to test this assumption we have plotted the ratio of the intensity and the velocity amplitudes as a function of temperature. By fitting a straight line to



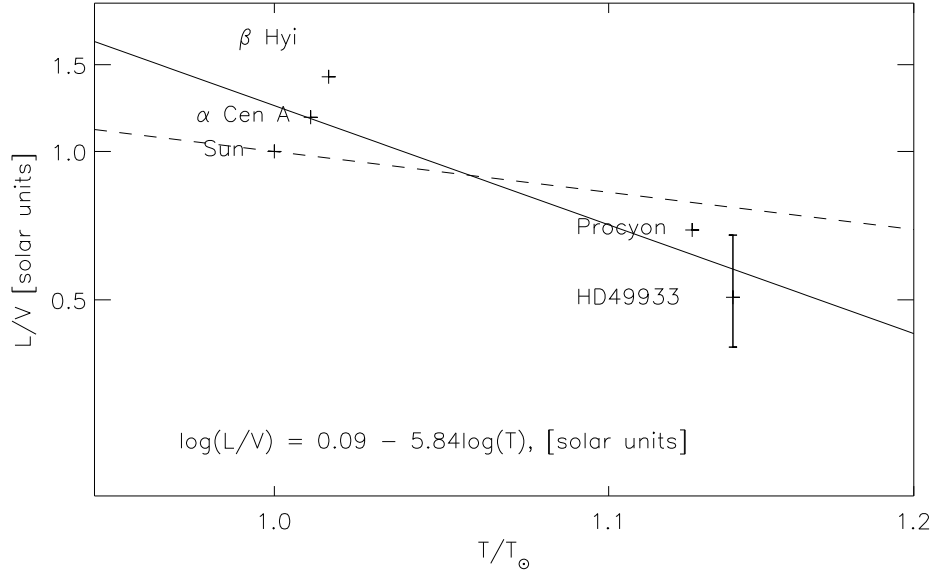


Figure 3.10: The ratio between the intensity and the velocity amplitudes as a function of temperature in a log-log plot. The solid line shows the best fitted straight line and the dotted line shows a straight line with a slope of  $-2$  as assumed by Kjeldsen & Bedding (1995) and Kjeldsen & Bedding (in prep.). As discussed in the text we have no reliable estimates of the uncertainties of the data points, but a hint can be found for HD49933 using the upper and lower limits of the radial-velocity amplitudes obtained by Mosser et al. (2005).

the points in this figure we obtain:

$$T_{\text{eff}}^{5.84} \frac{\delta V}{V} \propto \frac{\delta L}{L}. \quad (3.16)$$

which differs significantly from the assumption by Kjeldsen & Bedding (1995) and Kjeldsen & Bedding (in prep.). Anyway we do not think that the observations are precise enough to claim that 5.84 is the value to use (as we only have 5 data points with high scatter and no reliable estimates of the uncertainties), but only that the value seems to be larger than 2.

### 3.2.3 Structure in The Echelle Diagram

The frequencies of the p modes with different radial order  $n$  and angular degree  $l$  are related through the asymptotic relation (Tassoul, 1980):

$$\nu_{nl} \simeq \left( n + \frac{l}{2} + \varepsilon \right) \Delta\nu - \frac{l(l+1)}{6} \delta\nu \quad (3.17)$$

where

$$\Delta\nu = \nu_{n+1,l} - \nu_{n,l} \quad (3.18)$$

is the large separation and

$$\delta\nu = \nu_{n+1,0} - \nu_{n,2} \quad (3.19)$$

is the small separation and  $\varepsilon$  is a phase constant determined by the reflection properties near the surface (which in general is a function of frequency).

To illustrate the relationship between observed p modes and the simplified asymptotic relation, the frequencies are often plotted in an echelle diagram. Here the mode frequencies are plotted on the vertical axis and the mode frequencies modulo  $\Delta\nu$  are plotted on the horizontal axis.

The large frequency separation is given as:

$$\Delta\nu = \left( 2 \int_0^R \frac{dr}{c} \right)^{-1} \quad (3.20)$$

where  $c$  is the sound speed. Following Kjeldsen & Bedding (1995) the square of the adiabatic sound speed scales with the temperature ( $c^2 \propto T$ ) and the temperature can be estimated as  $T \propto M/R$  so:

$$\Delta\nu \propto \left( \frac{M}{R^3} \right)^{1/2}. \quad (3.21)$$

The small frequency separation is given as:

$$\delta\nu \simeq -(4l + 6) \frac{\Delta\nu}{4\pi^2\nu} \int_0^R \frac{dc}{dr} \frac{dr}{r}. \quad (3.22)$$

The small separation depends on the gradient in the sound speed instead of the sound speed, as was the case for the large separation. The gradient in the sound speed of the Sun depends on changes in the chemical composition in the center of the Sun. As the chemical composition changes as the Sun ages, the small frequency separation can be used to determine the age of the Sun, while the large separation can be used to determine the mass and the radius or the density.

The asymptotic relation is of course never completely fulfilled, this is partly because the assumptions in the approximation are too simple, but also because second order effects are not taken into account. These second order effects can be studied by investigating the second frequency differences of the p modes (Gough, 1990):

$$\Delta_2\nu_{n,l} \equiv \nu_{n-1,l} + \nu_{n+1,l} - 2\nu_{n,l} \quad (3.23)$$

These second frequency differences will be sensitive to any rapid variation in the sound speed in the star. This could be at for instance the bottom of the convective zone (Monteiro et al., 1994), at the convective core (has not yet been done for solar-like stars as the Sun does not have a convective core) or it could be at the helium ionization zone (Houdek & Gough, 2007). Such rapid variations in the sound speed will induce an oscillating component in  $\Delta_2\nu$  (or in the echelle diagram). This oscillating component will have a cyclic frequency that is approximately equal to twice the acoustic depth of the variation in the

sound speed and an amplitude that depends on the amplitude of the variation in the sound speed (Houdek & Gough, 2007).

In this way the low-degree second frequency differences of the Sun is a sum of four components: oscillating components from the ionization of He I and He II and from the bottom of the convection zone and a slow drift that is believed to originate from the too simple assumption in the asymptotic approximation (Houdek & Gough, 2007).

The amplitudes of the second frequency differences in the Sun are around 1  $\mu\text{Hz}$  so if we want to measure the depth of the ionization and convection zone we need to measure the mode frequencies with a precision better than 0.1  $\mu\text{Hz}$ , and in order to do that the stars need to be observed for more than a hundred days.

Another interesting way in which the asymptotic relation can be violated which was noted by Soriano et al. (2007) is that in the presence of a convective helium-rich core the small separation  $\delta\nu$  may become negative. A possible explanation for why the small separation becomes negative is that the integral in Eq. 3.22 should not be evaluated from 0 to  $R$ , but from the inner turning point  $r_t$  to  $R$ . And, it is exactly in the region between 0 and  $r_t$  that the sound speed changes dramatically in a helium-rich convective core.

### 3.2.4 Modeling Acoustic Spectra

The p-mode frequencies can be obtained by using SISWF as described in Section 2.4.6 and plotting the frequencies in the echelle diagram, but in order to obtain more information about the stellar oscillations it is convincing to make a model of the acoustic spectrum. Such a model will have a number of free parameters, e.g. mode frequencies and amplitudes, mode lifetimes, stellar rotation, inclination and also mode asymmetry, which will have to be adjusted in order to have the best match between the observed acoustic spectrum and the model. Of course such a model can also be made in the time domain instead of in the frequency domain (Brewer et al., 2007), but for space-based observations the number of data points in the time domain can be a few million whereas not much more than a few thousand data points are needed in the frequency domain (an example could be to model 1 mHz with 0.1  $\mu\text{Hz}$  resolution).

The model is most often matched with the observed acoustic spectrum by minimizing a logarithmic-likelihood function  $l$  (Toutain & Appourchaux, 1994):

$$l = - \sum_{k=1}^N \ln f(\nu_k, \lambda), \quad (3.24)$$

where  $f$  is the probability distribution of the observed power spectrum  $S(\nu_k)$  and the model spectrum  $S_0(\nu_k)$  which is a function of the frequencies  $\nu_k$  and of  $p$  modeled parameters  $\lambda = (\lambda_1, \lambda_2, \dots, \lambda_p)$ :

$$f(\nu, \lambda) = \frac{1}{S_0(\nu, \lambda)} e^{-\frac{S(\nu_k)}{S_0(\nu, \lambda)}}. \quad (3.25)$$

This probability distribution assumes that the power spectrum of p-mode oscillations is distributed around a mean Lorentzian profile with a  $\chi^2$  distribution with two degrees of freedom (Toutain & Appourchaux, 1994). Combining Eq. 3.24 and Eq. 3.25 gives:

$$l = \sum_{k=1}^N \left( \ln S_0(\nu_k) + \frac{S(\nu_k)}{S_0(\nu_k)} \right) \quad (3.26)$$

The uncertainties to a given parameter  $\lambda_p$  can be obtained as the diagonal elements in the inverse of the Hessian matrix:

$$h_{ij} = \sum_{k=1}^N \frac{\partial^2}{\partial \lambda_i \partial \lambda_j} f(\nu_k, \lambda) \quad (3.27)$$

The assumption that is made here is that the hyper-surface of  $l$  near a maximum value of  $\lambda_p$  is approximately Gaussian and this is only the case if all the frequency bins are independent, i.e. when the data are obtained with high duty cycle. If the observations are not made with high duty cycle it can be an advantage to calculate the non-logarithmic likelihood function instead of the logarithmic one, thereby lowering the effect of low-amplitude noise relative to the high-amplitude signal as it is done by Karoff et al. (2008b). A way to calculate the uncertainties without making assumptions about the shape of the hyper-surface of  $l$  is to model different substrings of the complete time series and then compare the obtained parameters  $\lambda_p$  in the different substring or by use of Monte Carlo simulations. In fact the assumption that the hyper-surface of  $l$  is approximately Gaussian has only been shown for the frequencies (Duvall & Harvey, 1986) and as see in Karoff et al. (2008b) it is not valid for the mode lifetime. Therefore the uncertainties should not only be based on the Hessian matrix.

The logarithmic-likelihood function is normally minimized by a more or less standard hill-climbing routine such as the Powell algorithm (Press et al., 1992), but of course more sophisticated algorithms can be used such as genetic algorithms (Fletcher et al., 2003, 2004) or simulated annealing algorithms (Press et al., 1992). The advantage of these algorithms is that they have a higher chance of finding the global minimum of the logarithmic-likelihood function and not just a local minima. This is important as there will be local minimums when the number of free parameters in the model is between 50 to 100 as it is for the solar-like oscillations.

For asteroseismic targets with moderate to low S/N the following parameters are reasonable (see Fletcher et al., 2006; Karoff et al., 2008b):

- A frequency for each  $n, l$  mode.
- An amplitude for each  $n, l$  mode.
- A mean mode lifetime.
- A mean rotation rate.

- An inclination.
- A background component.

This gives  $2N + 4$  free parameters where  $N$  is the number of  $n, l$  modes. The frequencies and amplitudes of the  $m > 0$  modes are given by the rotation rate and the inclination (see Gizon & Solanki, 2003). This model can be made even more simple if the inclination is known as is the case in the  $\alpha$  Cen A & B system (Fletcher et al., 2006) or if the  $v \sin i$  and radius are known, in which case constraints are made on the relation between the rotation rate and the inclination (Karoff et al., 2008b). On the other hand the model can also be made arbitrarily more complex by including additional parameters as (see for instance Fletcher et al., 2004, 2008):

- A line width for each  $n, l$  mode.
- A rotational splitting for each  $n, l$  mode (though not for  $l=0$ ).
- A peak asymmetry parameter for each  $n, l$  mode.

which gives around  $5N$  free parameters. Though this has been done in the solar case by fitting pairs of modes, it remains to be proven that such a model can be used in global modeling of other stars.

### 3.2.5 Rotation Splitting, Differential Rotation

One of the most exciting parameters that can be obtained from the acoustic spectra is the rotational splitting which can inform us about not just the mean rotation rate of the stars, but, with sufficient data, also about the differential rotation rates of the stars, i.e. the rotation rate as a function of distance to the center and latitude.

The rotational splitting as a function of  $n, l, m$  that is given as:

$$\nu_{nlm} = \nu_{nl} + \delta\nu_{nlm} \quad (3.28)$$

can be approximated by (Schou et al., 1994):

$$\delta\nu_{nlm} = \frac{m}{2\pi} \int_0^R \int_0^\pi K_{nlm}(r, \theta) \Omega(r, \theta) r dr d\theta \quad (3.29)$$

where the kernels  $K_{nlm}$  are functions of the mode eigenfunction of the non-rotation stars which are symmetric around  $m$  and therefore only depend on  $|m|$ .  $\Omega(r, \Theta)$  is the rotation profile of the star as a function of distance to the center and latitude which we want to obtain. In the solar case this has been done to high precision with the use of different inversions techniques, but for solar-like stars where we only observe  $l < 2$ , we will not be able to make such a high-resolution map (Gizon & Solanki, 2004). What might be possible to measure instead is the difference in the rotation rate between the convective and the radiative zones and between the equator and the poles. Observations of the Sun suggest that the inner parts of the Sun have rigid rotation though

the uncertainties are large here. This is one of the things that we hope to be able to test in the future, if other solar-like stars also have rigid rotation in the center. As the measurements of the rotation rates in the central parts of the stars are mainly constrained by the low-degree modes this is one of the places where the measurements are not degenerate by not being able to resolve the stellar surfaces.

Stellar models suggest that the differences in the rotation rates between the equator and the poles should scale with the depth of the convection zone. This can be tested with asteroseismology if we are able to measure the depth of the convection zone (as discussed in Section 3.2.3) and the difference in the rotation between the equator and the poles. This will be important as differential rotation is also expected to be the origin of stellar cycles.

In general the behavior of the rotation splitting as a function of  $n$  depends on the rotation profile as a function of distance from the center whereas the behavior as a function of  $l$  depends on the rotation profile as a function of latitude.

The stellar rotation has traditionally been studied by analyzing the widths of the absorption lines, but this method only provides a measurement of  $v \sin i$ , where  $v$  is the equatorial rotation and  $i$  is the inclination angle. By analyzing the amplitudes of the different modes as a function of  $l$  and  $m$  the inclination can be obtained independently of the rotation rates (Gizon & Solanki, 2003). This can be done as the visibility of modes with different  $l$  and  $m$  changes as a function of the inclination. In order to do this the mean rotation splitting needs to be larger than the broadening of the modes caused by the finite mode lifetime and small enough so that the excitation is not affected by the rotation. In practice this means that the rotation rate has to be between 2 and 10 times the solar rotation rate.

Measurements of the inclination are needed if one wants to calculate the true mass of an exoplanet observed with radial velocity. For the exoplanets observed with radial velocities it is only possible to measure  $M_p \sin i$  without the use of asteroseismology, where  $M_p$  is the mass of the planet. In fact such asteroseismic measurements are highly desired as current planet-search surveys are mostly based on low-activity targets as these provide the best radial-velocity precision (Udry & Santos, 2007). But in general stars with large inclinations show lower activity than stars with small inclinations. In fact a star with 90 degrees inclination will not show activity as it will not rotate as seen from the Earth. Also, as most spots are believed to be positioned close to the equator which will be the regions on the stars with the lowest visibility, these stars will have the lowest observed activity at an inclination of 90 degrees. If it is the case that a selection criteria based on activity is the same as a selection criteria based on inclination, then it means that in general the exoplanet masses  $M_p$  will be larger than what is assumed from normal statistical distribution of inclinations.

### 3.3 The Core

The stellar cores are in principle best studied with g modes instead of p modes as the g modes have large eigenfunction in the central part of the stars whereas the eigenfunctions of the p modes are largest in the outer part of the stars. The g modes are driven by gravitation and the driving force is therefore buoyancy. As is the case for the p mode the g modes also obey an asymptotic relation, but here the spacing between modes of different radial order  $n$  is constant in period and not in frequency (Tassoul, 1980):

$$\Pi_{nl} = \frac{\Pi_0}{\sqrt{l(l+1)}}(n + \epsilon) \quad (3.30)$$

where

$$\Pi_0 = 2\pi^2 \left( \int \frac{N}{r} dr \right). \quad (3.31)$$

The intergral is from the inner to the outer turning points.  $N$  is the buoyancy frequency:

$$N^2 = g \left( \frac{1}{\Gamma_1 p} \frac{dp}{dr} - \frac{1}{\rho} \frac{d\rho}{dr} \right) \quad (3.32)$$

where  $\Gamma_1$  is the adiabatic exponent:

$$\Gamma_1 = \left( \frac{\partial \ln p}{\partial \ln \rho} \right)_{\text{ad}} \quad (3.33)$$

As discussed in Section 3.2.3 the stellar cores are of particular interest because energy can be transported by both radiation and convection in this part of the stars. In the solar core the energy is transported by radiation, but it is believed that the physical structure will vary significantly in more masive stars with convective cores and observations of g modes will be the best tool for revealing this.

Because the eigenfunctions of the g modes are largest in the central parts the g modes are expected to be particularly useful for measuring the rotation of the stellar cores. Therefore a number of studies have tried to detect g modes in the Sun.

#### 3.3.1 g Modes in the Sun

A number of studies have announced detection of g modes in the Sun. One of the most recent of such studies were made by García et al. (2007) who looked for a periodic structure in the acoustic spectrum in agreement with the asymptotic relation for g modes in Eq. 3.30. This was done by calculating the power spectrum for the power-density spectrum of 10 years of data from the GOLF instrument on *SOHO*. This analysis revealed a  $6.5\sigma$  (in power) peak around a constant spacing of 24 minutes. It was also shown that the observed power spectrum of the power-density spectrum was in agreement with predictions from solar models. Though the study seems auspicious it has to be remembered that

a  $6.5\sigma$  peak in power (2.5 in amplitude) is not a significant detection. To cite a remark made by D.W. Kurtz to the early detection of p modes in solar-like stars:

”The solar oscillations have a restricted range in frequency space, so Fourier transforms of sections of Fourier Transforms were made until  $4\sigma$  peaks were found and the discovery of solar-like oscillators was announced ... over and over again. Dream on – for decades each time the result was only over-interpreted noise. After all, you expect  $3\sigma$  peaks 1 out of 200 times in data with Gaussian noise; if you search thousands of frequencies and enough Fourier Transforms of sections of Fourier Transforms, eventually you do find  $4\sigma$  peaks. The statistics guarantee that.” (Kurtz, 2004)

Detection of individual g modes have also been claimed by Garcia et al. (2008) who saw a  $1.6\sigma$  peak at  $220.7\ \mu\text{Hz}$  in the GOLF data. A  $1.6\sigma$  peak can of course not be claimed as a detection, but the peak was also seen in VIRGO data and with lower  $\sigma$  in MDI and GONG data (Garcia et al., 2008), but not in the BiSON data (Chaplin, private communication). For the VIRGO data wavelet analysis found that the peak was coherent over the 10 years of observation, though this was not the case in the other data sets.

Generally it is believed that observations of solar g modes would benefit from being observed over decades as the g modes are believed to have mode lifetimes of the order of millions of years (Christensen-Dalsgaard et al., 1974). This is of course not in agreement with the fact that signal from the possible g mode at  $220.7\ \mu\text{Hz}$  is only coherent in the VIRGO data and the reason for this discrepancy might be that the g modes do not have such long mode lifetimes, though it seems most likely that the peak at  $220.7\ \mu\text{Hz}$  is not a g mode. Dintrans et al. (2005) have used 2D simulation of convection to show that if the g modes are excited at the base of the convection zone, then they will have mode lifetimes comparable to the oscillation periods. If this is the case it will (according to Eq. 3.2) also lower the height of the peaks in the acoustic spectrum below the detection threshold. On the other hand g modes would not be expected to be significantly damped by the outer convection zone as the g modes have low mode mass in these regions.

### 3.3.2 Avoided Crossing in $\beta$ Hydri

The observations by Bedding et al. (2007) and the observations by Karoff et al. (2008b) indicate that the p modes in  $\beta$  Hydri show avoided crossing (also associated with the terms ”mode bumping” and ”mixed modes”). Though the frequencies of the mixed modes identified by Bedding et al. (2007) and Karoff et al. (2008b) are not the same, the results are still very interesting as mixed modes are the key to understanding the stellar interior beneath the convection zone.

It was shown by Osaki (1975) that g modes could be trapped in the stellar cores of evolved stars. These g modes are trapped behind the gradient in

the mean molecular weight and therefore separated from the p modes. This gradient in the mean molecular weight is largest in evolved massive stars where it develops as the convective core retreat, but it is also expected to be present in evolved solar mass stars where it develops from the nuclear burning of H into He (Guenther, 1991). The p modes for which frequencies overlap the frequencies of the trapped g modes will be affected by this through avoided crossing. The signature of avoided crossing is clearly seen in the echelle diagram where the regular spacing of the modes given by the asymptotic relation is lost for the affected modes.

Though avoided crossings have not been observed, signatures have been seen in the echelle diagram of  $\eta$  Boo (Christensen-Dalsgaard et al., 1995), Procyon (Martić et al., 2004) and  $\beta$  Hydri (Bedding et al., 2007; Karoff et al., 2008b). As described by Guenther (2004) the mixed modes can be used to fine tune the estimates of the stellar ages, but this demands that a sufficient number of modes are detected in the stars. The problem is that avoided crossings complicate the mode identification as the asymptotic relation can no longer be used as a confident guide. Therefore it is desirable if mode identification can be made without using the asymptotic relation when analyzing the effect of avoided crossing. The mode identification could for example be made based on the rotation splitting by using the amplitude ratio of the different  $m$  components as the amplitudes of different  $m$  components change as a function of  $l$  and the rotation. If this could be accomplished for stars with solar-like oscillation then the obtained mode frequencies could be compared with frequencies from models of a given angular degree where the ridges of the avoided crossing could be followed. The ridges of the avoided crossing can easily be identified in an age versus mode frequency plot (see for example Guenther, 2004) of a given angular degree.

Another way to distinguish the mixed modes from the ordinary p modes could be based on their mode lifetimes. As discussed in Section 3.3.1 g modes probably have mode lifetimes of the order of millions of years whereas p modes only have mode lifetimes of a couple of days. As the mixed modes have both g- and p-mode character they are expected to have significantly longer mode lifetimes than the ordinary p modes (Moreira et al., 2005, suggest  $\eta \gg 150$  days). On the other hand if the g modes only have mode lifetimes a few times longer than their periods (Dintrans et al., 2005) then we would expect the mixed modes to have smaller mode lifetimes than the ordinary p modes. As shown in Eq. 3.2 the amplitude of a mode in the acoustic spectrum is proportional to the mode lifetime; so if the g modes have significantly longer mode lifetimes than the p modes then the mixed modes would be expected to have higher and narrower peaks in the acoustic spectra than the ordinary p modes.

Part II  
Papers



# Chapter 4

## Variable Stars in the *COROT* Fields

The paper *Identification of Variable Stars in COROT's first main observing field (LRc1)* presented in this chapter has been published in:

Karoff et al. (2007) Christoffer Karoff, Heike Rauer, Anders Erikson, Petr Kabath, Tino Wiese, Magali Deleuil, Claire Moutou, Jean-Charles Meunier & Hans Deeg, *AJ*, 134, 766 , 2007

The paper is the first in a series of papers (see also Kabath et al., 2007, 2008) describing the results from the Berlin Exoplanet Search Telescope (BEST) stellar variability survey in the target fields of the *COROT* space mission. The aim of the survey is to minimize false-alarm rates and to identify potential targets for the additional science program. This paper also gives a detailed description of the data reduction and analysis of the BEST data. The data reduction makes use of the ISIS packages (Bertin & Arnouts, 1996). The choice of ISIS was made based on a comparative test of different photometry algorithms described in Karoff et al. (2006b).



## Identification of Variable Stars in *COROT*'s first main observing field (LRc1)

Christoffer Karoff\*, Heike Rauer\*, Anders Erikson\*,  
Petr Kabath†, Tino Wiese\*, Magali Deleuil†,  
Claire Moutou†, Jean-Charles Meunier† & Hans Deeg‡

### Abstract

The *COROT* space mission will monitor several target fields for up to 150 days to perform asteroseismology and to search for extrasolar planets by photometric transits. Variable stars in the target fields are important objects for additional scientific studies but can also disturb the search for planetary transits. A variability characterization of the target fields prior to *COROT* observations is therefore important for two reasons: to find interesting variable stars to monitor further and to make an analysis of the impact of the variable stars on detecting extrasolar planet transits with *COROT*.

The Berlin Exoplanet Search Telescope (BEST) is a small wide-angle telescope dedicated to high-precision photometry. It has observed a  $9 \text{ deg}^2$  field of view centered at  $(\alpha, \delta) = (19^{\text{h}}00^{\text{m}}00^{\text{s}}0, +00^{\circ}01'55''.2)$  (J2000.0) over 98 nights to search for variable stars in the surroundings of the first long-run target field (LRc1) of the *COROT* space mission. In this data set we identified 92 periodic variable stars, 86 of which are new discoveries and 6 of which are known from the General Catalogue of Variable Stars (GCVS). For five of the GCVS stars, variability could not be confirmed. Forty-three of the 92 detected periodic variable stars are identified as eclipsing binaries. We have evaluated the completeness of our survey for eclipsing binaries by comparing it to the expected fraction of eclipsing binaries based on *HIPPARCOS* observations. From this evaluation we show that the BEST data set presented here has a completeness of 20% – 30% for periods longer than 1 day and is complete relative to *HIPPARCOS* for short-period binaries.

## 4.1 Introduction

Small wide-angle telescopes such as the Berlin Exoplanet Search Telescope (BEST; Rauer et al., 2004) offer a unique possibility of identifying stellar variability in a large number of stars. Apart from giving us important information

---

\*Institut für Planetenforschung, Deutsches Zentrum für Luft- und Raumfahrt, Rutherfordstrasse 2, D-12489 Berlin, Germany. E-mail: karoff@phys.au.dk

†Laboratoire d'Astrophysique de Marseille, CNRS - Université de Provence, BP 8, 13376 Marseille Cedex 12, France

‡Instituto de Astrofísica de Canarias, E-38200 La Laguna, Spain

on the individual targets, these kinds of wide-field data also contain information on the statistical distribution of variable stars, which can be used not only to understand the structure and evolution of the Galaxy, but also to analyze the expected false-alarm rates for transiting extrasolar planet searches (Brown, 2003). For space missions searching for extrasolar planets by photometric transits, knowledge of the variable stars in the target fields helps reduce the number of false alarms, thereby reducing the amount of follow-up observation needed. In addition, the variable stars provide interesting targets for additional science.

The *COROT* space mission (Baglin et al., 2002; Bordé et al., 2003), launched on 2006 December 27, will observe a number of target fields for up to 150 days in order to perform asteroseismic studies of the target stars and to search for extrasolar planets by photometric transits. The observation of the first 150 day "long-run" field (LRc1) started in spring 2007. This field has been observed with BEST in order to identify variable stars. *COROT* is expected to obtain a precision of 0.66 ppm in 5 days of observation in the asteroseismic channel and 700 ppm in 1 hr of observation in the exoplanet channel (Baglin et al., 2002). This is an order of magnitude better than what can be obtained with BEST, because *COROT* benefits from not having to observe through the atmosphere. Therefore, many of the transits that are expected to be detected with *COROT* will not be visible in the BEST data, but despite this order-of-magnitude gap the BEST data will be highly valuable to the *COROT* mission.

In the exoplanet channel of the *COROT* satellite, stars have a large point-spread function (PSF) due to a prism installed in front of the detectors to obtain the colors of each star. The color information will help to distinguish stellar activity from exoplanet transits. In dense target fields, however, the resulting relatively large PSFs of the stellar spectra can overlap. Prior knowledge of variables overlapping the PSFs of interesting target stars will therefore be helpful to avoid misinterpretation.

In addition to searching exoplanetary transits, additional science programs will be performed in the *COROT* fields on selected targets. Some of these additional programs are interested in variable stars, e.g., binaries. To be able to place integration windows in the satellite field on such targets, their position has to be known before observing the field with *COROT*. A search for variable stars in the *COROT* fields is therefore also helpful for the additional science program of the mission by detecting previously unknown variables in the field and confirming or rejecting the variability of the stars mentioned in variable star catalogs.

A variability characterization like the one presented here of the target fields prior to *COROT* observations is therefore important for two reasons: to find interesting variable stars to monitor further by preselecting windows and to make an analysis of the impact of the variable stars on detecting extrasolar planet transits with *COROT*.

The present paper is arranged as follows: Section 4.2 describes the observations, Section 4.3 summarizes the data reduction procedure, Section 4.4 describes the data analysis, including search and detection of periodic variable stars, Section 4.5 contains the variable star catalog of the observed field, and

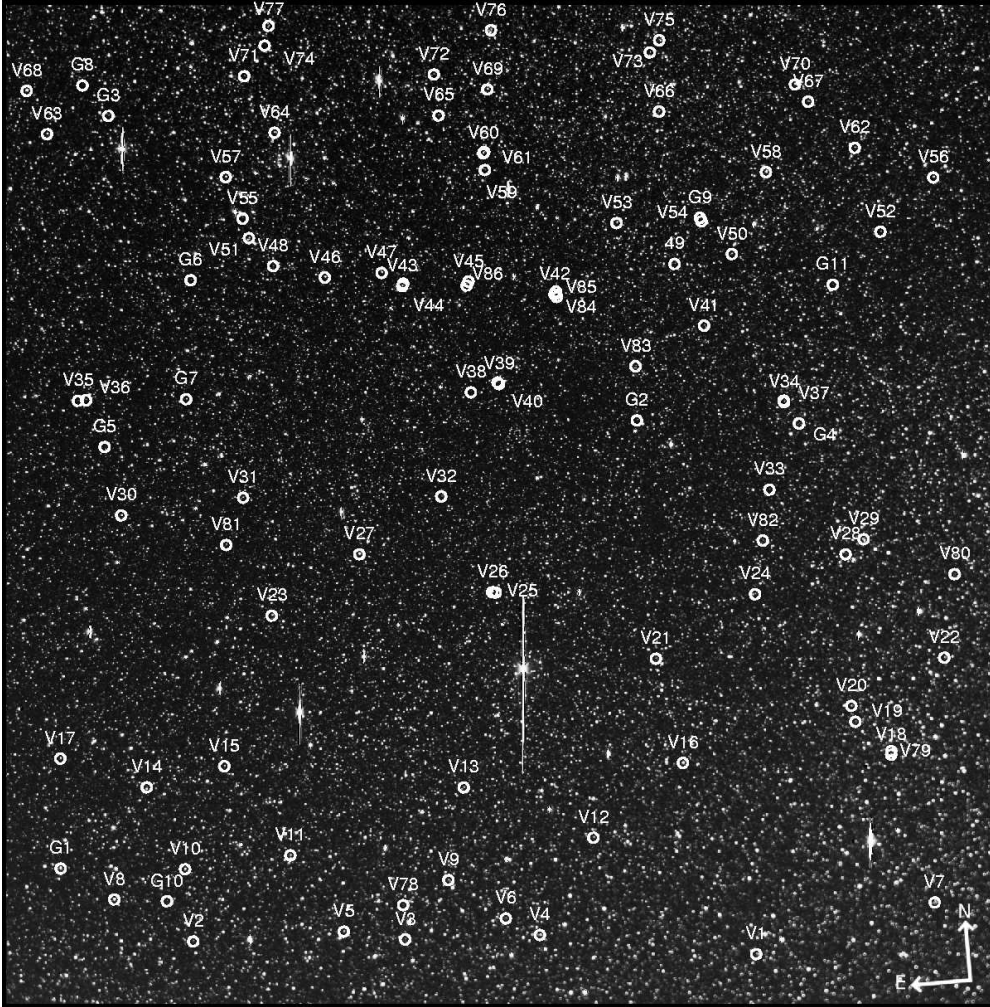


Figure 4.1: The reference frame. The newly identified periodic variable stars are marked (V) as well as the stars from the GCVS (G).

Section 4.6 describes the analysis of the completeness of the data set. Concluding remarks are found in Section 4.7.

## 4.2 Observation

BEST is a small wide-angle telescope operated by the Institut für Planetenforschung of the Deutsches Zentrum für Luft- und Raumfahrt (DLR) and is located at the Observatoire de Haute-Provence (OHP), France. It consists of a Schmidt telescope with a 20 cm effective aperture, an  $f/2.7$  focal ratio, and an AP-10 CCD camera, with  $2048 \times 2048$  pixels of  $14 \mu\text{m}$  size (Rauer et al., 2004). The result is a  $3.1^\circ \times 3.1^\circ$  field of view (FOV) with a pixel scale of  $5''.5$ . This is comparable to *COROT*, which has a pixel scale of  $2''.3$  and a FOV for each of the four CCDs of  $1.3^\circ \times 1.3^\circ$ .

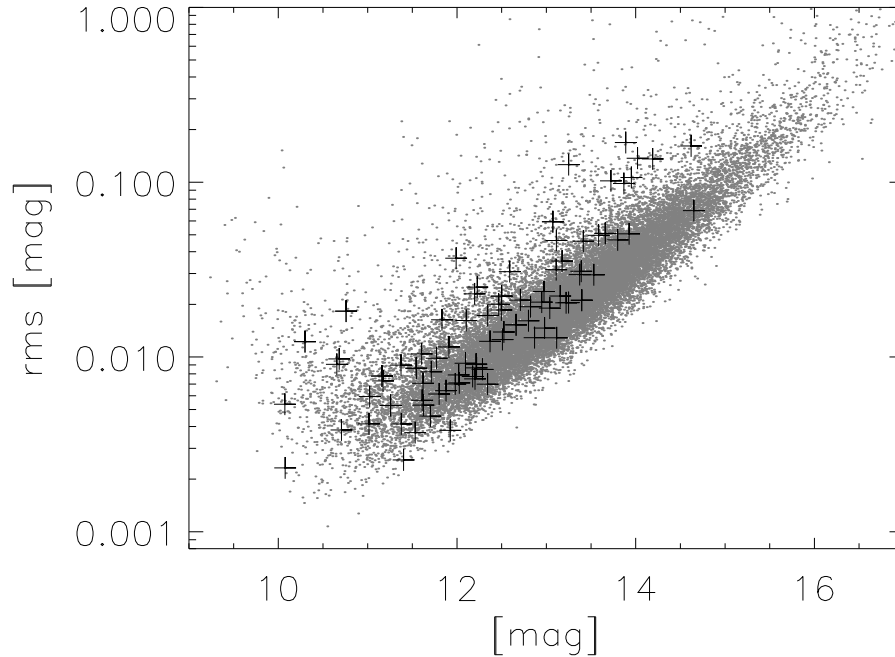


Figure 4.2: The rms scatter of all the light curves (*gray dots*) and of the identified periodic variable stars (*crosses*).

We present the results from a monitoring program of the *COROT* field LRc1 in the Galactic center direction centered at  $(\alpha, \delta) = (19^{\text{h}}00^{\text{m}}00^{\text{s}}.0, +00^{\circ}01'55''.2)$  (J2000.0) obtained from 2005 June 6 to September 7. The data set consists of a total of 35 nights of observations spread out over 98 nights in summer 2005. No data were obtained on nights with bad weather, around midsummer, or around full Moon. The observations were made without a filter in front of the CCD (the spectral response of the CCD corresponds to a wide *R* bandpass) in order to detect as many photons as possible and to provide a maximum sampling rate. An equal number of frames were obtained with 40, 120, and 240 s integration times in order to observe stars in a large magnitude range and to analyze the effect of crowding in the frames. We only present data from the 240 s integration frames here, corresponding to 727 frames in total. Fig. 4.1 shows the  $3.1^{\circ} \times 3.1^{\circ}$  FOV observed.

### 4.3 Data Reduction

The reduction of the data was performed as described by Karoff et al. (2006b). Based on a comparative test of three different photometry algorithms (SExtractor (Bertin & Arnouts, 1996), MOMF (Kjeldsen & Frandsen, 1992) and ISIS (Alard, 2000)) a data reduction pipeline was built (Karoff et al., 2006b) in order to reduce noise originating from the stellar background, extending the data

Table 4.1: Parameters used in ISIS

sub_x:	10	Sub_y	10
deg_bg:	3	deg_spatial:	2
ngause:	3		
sigma_gauss1:	0.7	deg_gauss1:	6
sigma_gauss2:	2.0	deg_gauss2:	4
sigma_gauss3:	4.0	deg_gauss3:	3
nstamps_x:	10	nstamps_y:	10
half_mesh_size:	9	half_stamp_size:	15

pipeline of BEST data, which was optimized for less crowded fields observed at its previous location at the Thüringer Landessternwarte, Germany (Rauer et al. 2004). We outline the different steps in the pipeline below.

The frames are calibrated from night to night by standard procedures as described in (Rauer et al., 2004). Hereafter, the reduction generally follows the method given in the ISIS package (Alard, 2000).

### 4.3.1 Image Subtraction

Image subtraction is performed in order to remove both the sky and the stellar background. This is done by subtracting a reference frame from all the frames, which removes the sky background and all the constant stars. When image subtraction is performed in the right way it will produce uncrowded frames where only the variable stars are present. The noise will then be dominated by the photon noise from the target stars and from the stellar background.

Before image subtraction can be made all the frames need to be transformed into the same  $(x, y)$ -coordinate grid. The frame with the best seeing from the middle of the observation run was selected as the template frame for this transformation. Then ISIS produced a reference frame by combining a number of best-seeing frames. The reference frame was then subtracted from all the other frames with the ISIS parameters listed in Table 4.1. This means that the reference frame is convolved with a convolution kernel in order to match all the stars in the frames.

Having subtracted the reference frame from all the other frames, ISIS constructs a frame that is the mean of the absolute normalized deviations of all the subtracted frames. This frame only contains nonconstant stars, as all the constant stars have been removed by the subtraction. Unfortunately, this only works for nonconstant stars that have a large amplitude, as is discussed below.

The ISIS package also includes a photometry routine that performs PSF-weighted photometry on the variable stars detected, thereby producing light curves of the differential fluxes of the stars. For different reasons, discussed below, we did not use this routine. We used the output of ISIS to distinguish between true periodic variable stars and stars that showed variability because of contamination from another nearby variable star.

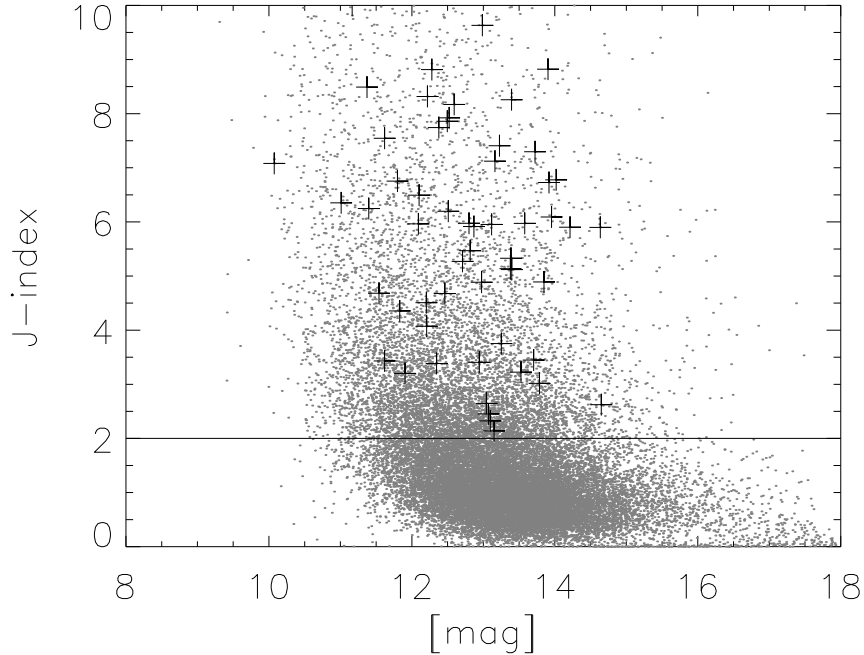


Figure 4.3: The variability index  $J$  vs.  $R$  magnitude. The gray dots represents all the observed stars while the crosses represents the periodic variable stars that we have identified. The 9112 stars above the line with a index  $J$  larger than 2.0 were selected as suspected variable stars.

### 4.3.2 Photometry

There are three reasons why we do not use the photometry algorithm in ISIS. The first is that ISIS only produces light curves of differential fluxes; in order to convert these into magnitudes, photometry needs to also be performed on the reference frame in the same way as on the subtracted frames. The second reason, which has been noted by Mochejska et al. (2002) and Hartman et al. (2004), is that the detection of variables in ISIS works best for variables with an amplitude of at least 0.1 mag, since small-amplitude variables tend to get washed out in the overall noise in the subtracted frames. The last reason is that in order to do PSF-weighted photometry, the stars need to have a well-defined PSF; this is not always true if the stars are undersampled. We therefore preferred to perform simple unit-weight aperture photometry on the subtracted frames. Hartman et al. (2005) analyzed differences in performing PSF-weighted and unit-weighted aperture photometry on the subtracted frames and concluded that PSF-weighted photometry works best for the relatively faint stars, while unit-weighted aperture photometry works best for the relatively bright stars, but also that PSF-weighted photometry gives rise to a constant error term in the light curves. In addition, it is important that the transformation from differential fluxes to magnitudes is correct when evaluating the rms noise level

obtained by different photometry algorithms and when comparing the noise level for ground-based transit surveys like BEST to that of space-based transit surveys like *COROT*. By using the same unit-weighted aperture photometry algorithm on the subtracted frames, as well as on the reference frame, we are confident that this transformation is correct.

Hartman et al. (2004) note that if they use an aperture radius below 7 pixels for stars with a FWHM of the order of 3 pixels, the amplitude of the light curves is artificially reduced. As the FWHMs of the stars we analyze here are in the range from 1 to 3 pixels, depending on the seeing on different nights, we use an aperture radius of 7 pixels. We did try to reduce the aperture radius, which resulted not only in reduced amplitudes of the light curves but also reduced rms noise level in the light curves, as expected because of a decrease in the amount of background noise. In other words it might be possible to increase the precision by using smaller or nonconstant apertures, but then the amplitude and noise determination would not be as reliable. It is also noted here that although the PSFs in the nonsubtracted frames may be small, there may be large non-Gaussian residuals in the subtracted frames that require large apertures in order to ensure flux preservation. It is important to note here that the aperture radius of 7 pixels is only used on the subtracted frames where all the constant stars are removed. Therefore, using an aperture radius of 7 pixels does not mean that we are not able to resolve stars separated by less than 7 pixels (as long as they are not variables). Figure 4.2 shows the rms scatter in a single night (June 29) of all the light curves as a function of stellar luminosity, with the identified periodic variable stars marked. The figure shows that periodic variable stars are found roughly equally distributed over stellar luminosity. The obtained precision is comparable to what has been obtained by other small wide-angle telescopes (Hartman et al., 2004; Kane et al., 2004, 2005a,b).

### 4.3.3 Astrometry and Calibration

As noted by Hartman et al. (2005) the light curves need to be calibrated for systematic changes in the zero points. This is done by selecting a number of nonsaturated stars with low rms noise in the light curves and then calculating the mean change of the light curves. We selected 2182 stars for calculating these zero-point changes and found that the corrections from frame to frame were below 0.02 mag, except for a few bad frames which contained clouds or airplane tracks.

Even after the zero-point correction, residuals of systematic trends in the light curves caused by, e.g., air mass, cloud cover, and temperature variations were still present in the data (these residuals are sometimes referred to as "red noise"). We therefore applied the algorithm introduced by Tamuz et al. (2005) in order to correct for systematic effects. This clearly improved the rms noise level, in particular in the brightest stars. A detailed discussion of the photometric limitations of the BEST survey will be presented in a forthcoming paper.

The astrometric calibration was performed by matching the 1500 brightest stars in the stellar catalog obtained from the reference frame with the 2000 brightest stars (magnitude limit 11.4) of the USNO-A2.0 catalog (Monet et al., 1998). The problem of matching the observed stars to stellar catalogs is not trivial. The main reason for this is the large image scale of BEST ( $5''.5 \text{ pixel}^{-1}$ ). This means that stars in a crowded part of the frame will have multiple matches in the stellar catalogs. The astrometric calibration was performed using MATCH (Valdes et al., 1995). MATCH finds a linear, quadratic, or cubic transformation between two stellar catalogs. We used a cubic transformation to calculate the transformation from the  $(x, y)$ -coordinates of the CCD to right ascension and declination. We note that a linear transformation does not work because of the large FOV.

Out of the brightest 1500 stars in the stellar catalog obtained from the reference frame it was possible to match 902 with a matching radius of  $2 \cdot 10^{-4}$  degree. From these 902 stars we calculated an absolute magnitude difference between the observations and the USNO-A2.0 catalog  $R$  band. We note that we do not intend to perform a real absolute photometric calibration of the stars, since only relative magnitudes are needed to identify variables.

## 4.4 Data Analysis

### 4.4.1 Identification of Suspected Variable Stars

We used the variability index  $J$  defined by Stetson (1996) to identify stars as suspected variable stars. The index  $J$  is defined as the normalized sum of the deviation of each data point (or pair of data points with small separations in time) in the light curve compared to the expected noise level for that star (the expected noise level is calculated based on the signal-to-noise ratio of the star). We considered data points to be pairs if they were separated by less than 0.03 day. Fig. 4.3 shows the index  $J$  as a function of magnitude.

We classified all 9112 stars with an index  $J$  greater than 2 as suspected variables, as all these stars show some kind of variability. Most of these stars are clearly variable stars, but either the period cannot be properly determined because of an imperfect duty cycle or the stars are nonperiodic or multiperiodic variable stars. In this paper we concentrate on the periodic variable stars.

### 4.4.2 Identification of Periodic Variable Stars and Period Determination

All the stars classified as suspected variables were searched for periodicity with the method introduced by Schwarzenberg-Czerny (1996). This method fits a set of periodic orthogonal polynomials to the observations and evaluates the quality of the fit with the use of an analysis-of-variance statistic. All the suspected variable stars were fitted with two polynomials, and all objects with a fit quality better than 0.9 were examined visually.

In the visual examination we selected stars as periodic variable stars if they showed a clear periodicity between 0.286 and 120 days. We rejected light curves

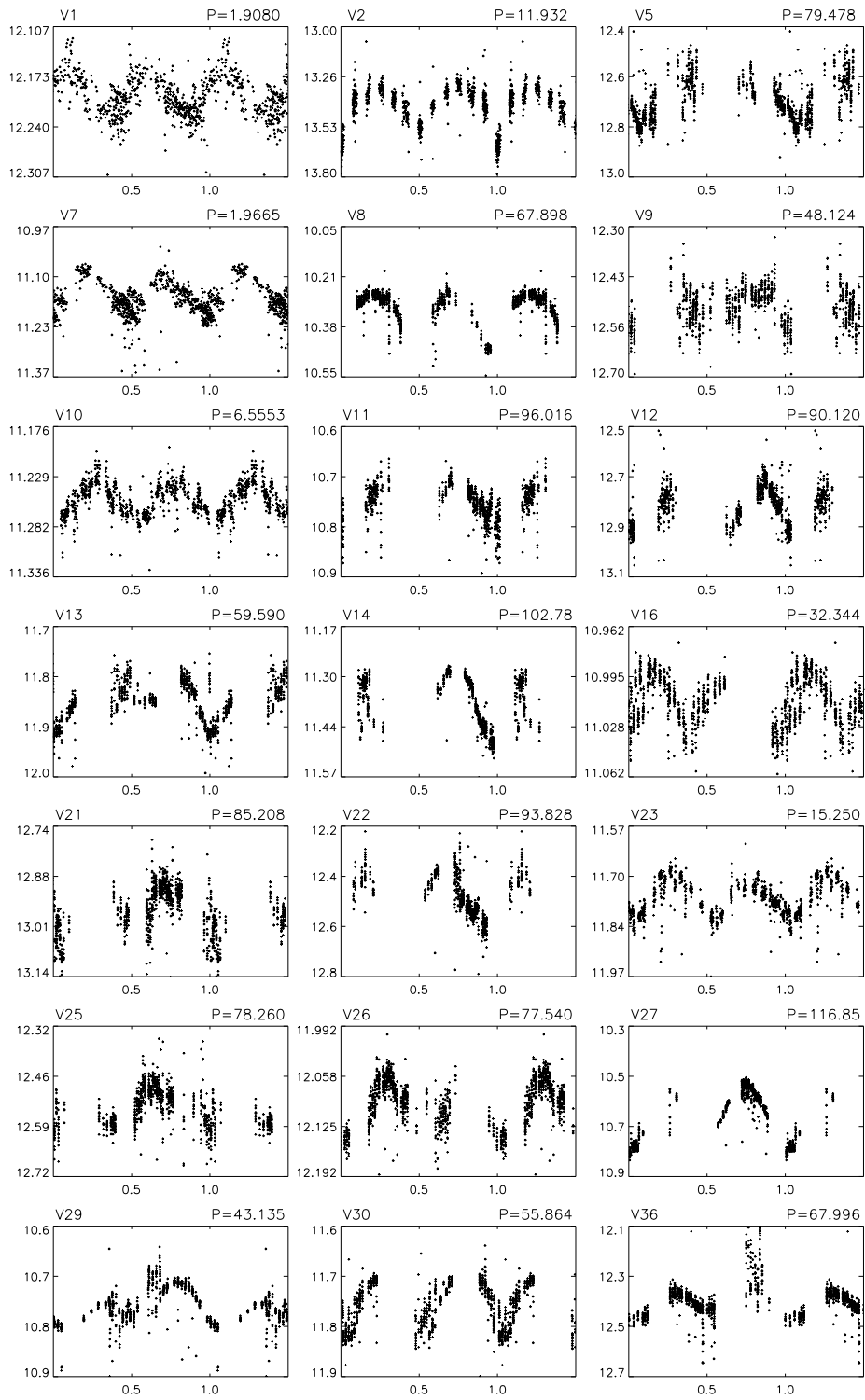


Figure 4.4: Light curves of 43 periodic pulsating stars in  $R$ . Magnitude is shown versus phase. The period is given in the upper right of each diagram is days.

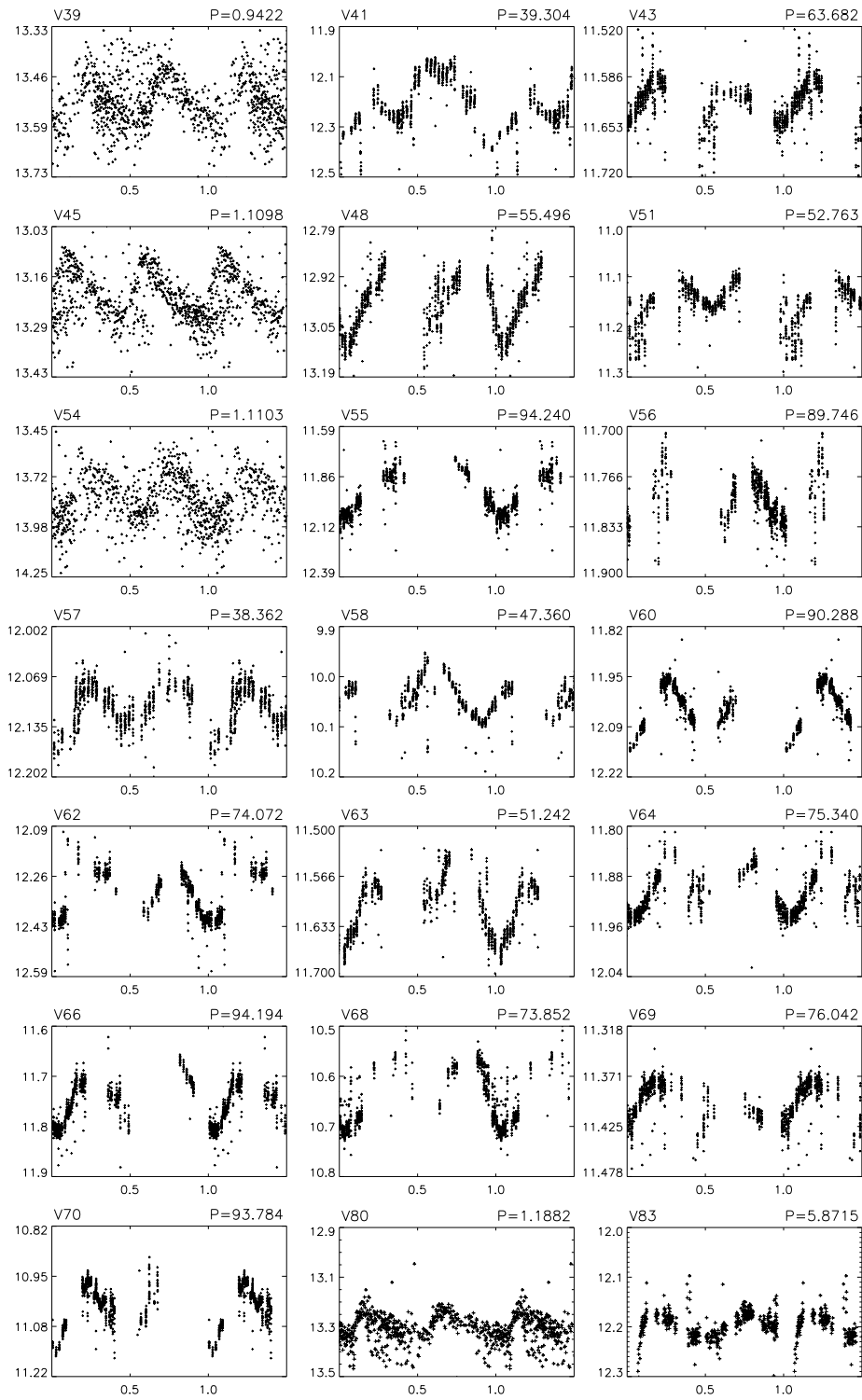


Figure 4.4: Continued

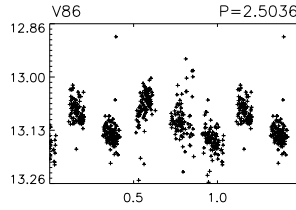


Figure 4.4: Continued

with periods close to 1 day, or harmonics of 1 day, because the periodicities in these light curves are likely to be caused by periodic changes in background level, temperature, air mass, etc.

We have identified 92 periodic variable stars in the data set (Tables 4.2 and 4.3). It is seen in Fig. 4.1 that the periodic variable stars are detected all over the CCD, although the density depends on the stellar density in that part of the field.

## 4.5 Variable Star Catalog

The GCVS (Kholopov et al., 1998) contains 60 variable stars in the field, 11 of which have periods less than 120 days. We have identified all 11 stars in the BEST data set. The phased light curves are shown in Fig. 4.4, and the corresponding parameters are given in Table 4.3. By looking at the light curves and comparing them with the index  $J$  we were able to confirm variability in six cases (G1, G2, G8, G9, G10, and G11). None of the 11 stars were detected by the algorithm we had set up to search for periodicity. G8, G9, and G11 are RR Lyrae stars with such a characteristic light curve that they should have been detected by the algorithm. By going back in the analysis to see why these stars were not detected, we see that they were all excluded during the visual inspection. There are three reasons for this exclusion. First, the method introduced by Schwarzenberg-Czerny (1996) provides a period that is equal to half the true period. This means that the phased light curves mainly show a falling trend. Second, the method introduced by Schwarzenberg-Czerny (1996) provides a period offset from the true period (the period of G8 is off by 5%, G9 by 0.2%, and G11 by 33%), thereby making the phased light curve look a lot more noisy. Third, G8 and G11 have periods very close to 1 day. G1, G2, and G10 do not show strongly periodic signals, and detection was not expected.

We were not able to confirm variability in five cases (G3, G4, G5, G6, and G7). There are three possible reasons why we were not able to confirm variability in these three stars: (1) the identification as variable stars in the GCVS is wrong, (2) the stars are not variable anymore, and (3) the variability of the stars is below the noise level in the BEST data. In Table 4.3 it is seen that all three stars should have amplitudes larger than 1 mag, and in Fig. 4.4 it is seen that the observed variability in the light curves is well below 1 mag. This rules out the third possibility.

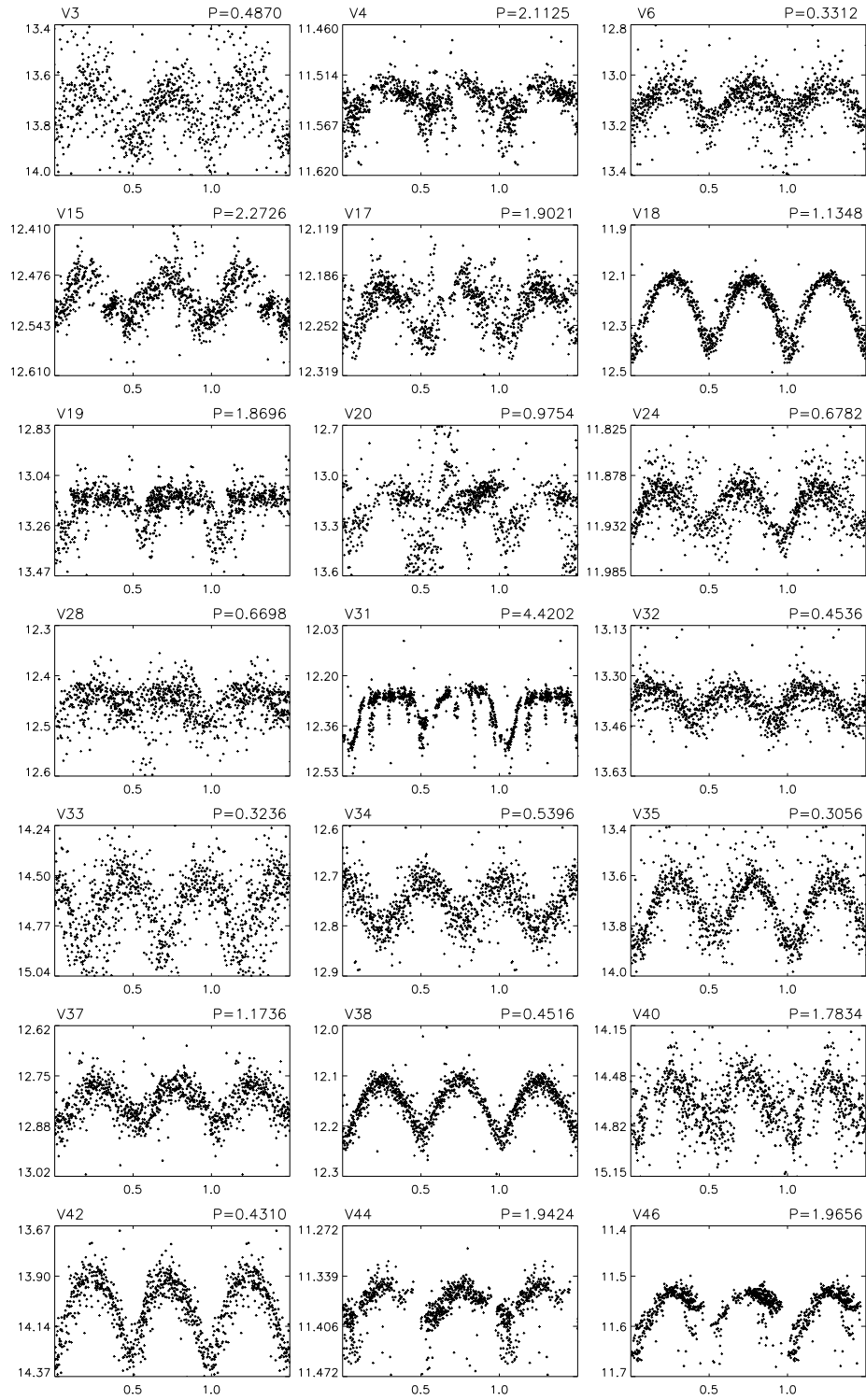


Figure 4.5: Light curves of 43 eclipsing binaries in *R*. See caption in Fig. 4.4.

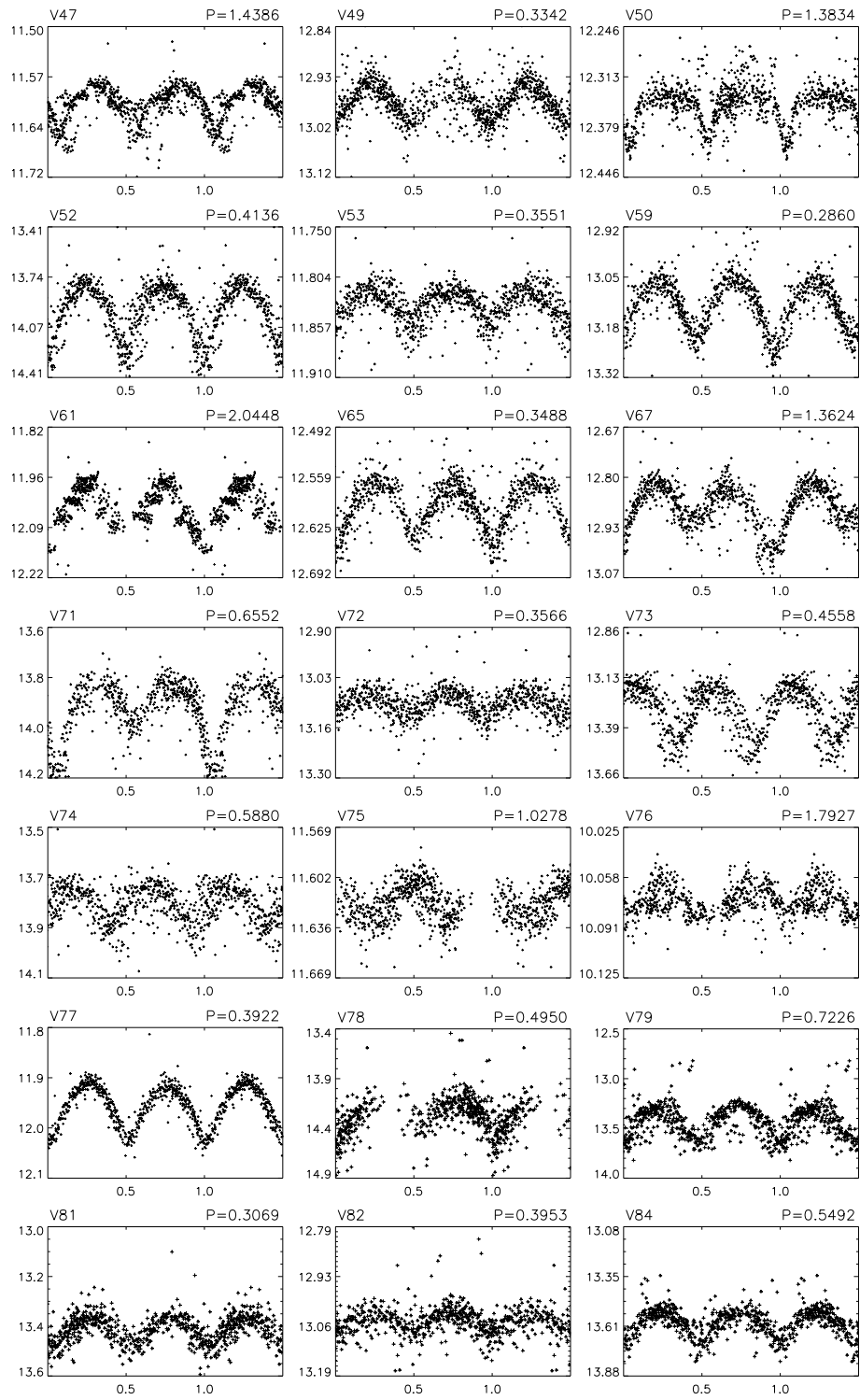


Figure 4.5: Continued

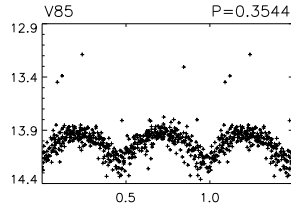


Figure 4.5: Continued

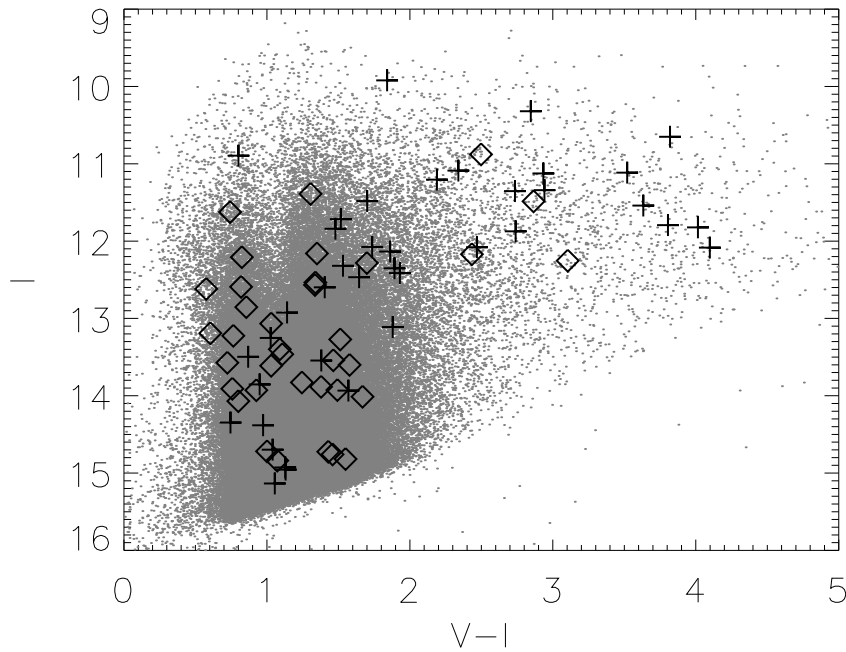


Figure 4.6: Color-magnitude diagram for stars in the *COROT* center field. The gray dots are stars from the ExoDat catalog, the crosses are 49 pulsating periodic variable stars and the diamonds are 43 eclipsing binaries found by BEST and identified in the ExoDat catalog.

We have divided the periodic variable stars identified by our search into two groups: periodic pulsating variables and eclipsing binaries. The two groups each contain 43 stars. For most of the stars it is easy to make this classification, but for some stars the classification may not be unique. The light curves of the periodic variable stars are shown in Figs 4.5 and 4.6, and the parameters are listed in Table 4.2.

The detected periodic variable stars were cross-identified with the USNO-A2.0 catalog. For each star we checked that the cross-identification was unique. If there were multiple or no identifications we did not assign a USNO-A2.0 ID to the star. The USNO-A2.0 IDs are given in Table 4.2. We also looked up all

the detected periodic variable stars in the SIMBAD catalog but were only able to identify one of the periodic variable stars, i.e., V66 = V1225 Aql.

Some of the stars show problems with blending. This means that the stars next to the variable stars also show variability. For each case where we had two or more stars showing the same kind of variability within the radius of the aperture (7 pixels) we have only identified one of the stars as a periodic variable. It is difficult to verify from the light curves alone which star is the true variable, because a faint star next to a bright variable star can show larger relative variability than the true bright variable star. In order to overcome this problem we identified all the variable stars that were affected by blending in the variability frame of our ISIS pipeline (the frame that was the mean of the absolute normalized deviations of all the subtracted frames), because this frame will only show truly variable stars. This approach only works well if the relative amplitudes in the variable stars are high.

A few stars, such as V20, V31, and V50, seem to show some additional variability apart from the periodic signal. By inspecting the light curves we found that the additional variability originated from a few nights where the noise level was unusually high. It is therefore most unlikely that this additional variability is of stellar origin.

Forty of the 92 identified periodic variable stars are in the LRc1 FOV of one of the two *COROT* CCDs dedicated to the planet program. These are V3, V4, V6, V9, V11, V12, V13, V15, V21, V23, V25, V26, V27, V32, V38, V39, V40, V41, V42, V43, V44, V45, V47, V49, V50, V53, V54, V58, V59, V60, V61, V65, V69, V78, V83, V84, V85, V86, G2, and G9. Some of the remaining identified periodic variable stars are expected to be in the FOV of some of the future pointings.

We have identified all the periodic variable stars in the ExoDat catalog (Deleuile et al., 2006). The ExoDat catalog is part of the preparation of *COROT* and has been made in order to select which stars to observe with *COROT*, taking into account spectral type, luminosity class, variability, and contamination (overlapping PSF on the focal plane). It contains, among other things, *BVRI* photometry of the field observed with the 2.5 m Isaac Newton Telescope at La Palma.

We cross-identify the periodic variable stars from BEST with the ExoDat catalog using a matching radius of  $1 \cdot 10^{-3}$  deg. In this way we obtain 81 matches out of the 86 periodic variable stars. More identifications could have been obtained by increasing the matching radius, but that would have also increased the number of mismatches.

Fig. 4.7 shows a color-magnitude diagram of the ExoDat catalog, with the discovered periodic variable stars marked. The stars in the  $V - I$  versus  $I$  diagram follow two branches: to the left the main-sequence stars and to the right the giant stars. For the faint stars there is a mismatch between stars on the main sequence and stars on the giant branch, since we do not know anything about the distance to the stars and therefore cannot provide their absolute luminosity. There is also a mismatch for nearby late main-sequence stars, which are bright with red colors and fall within or to the right of the giant branch. The diamonds in the figure represent eclipsing binaries, and the crosses

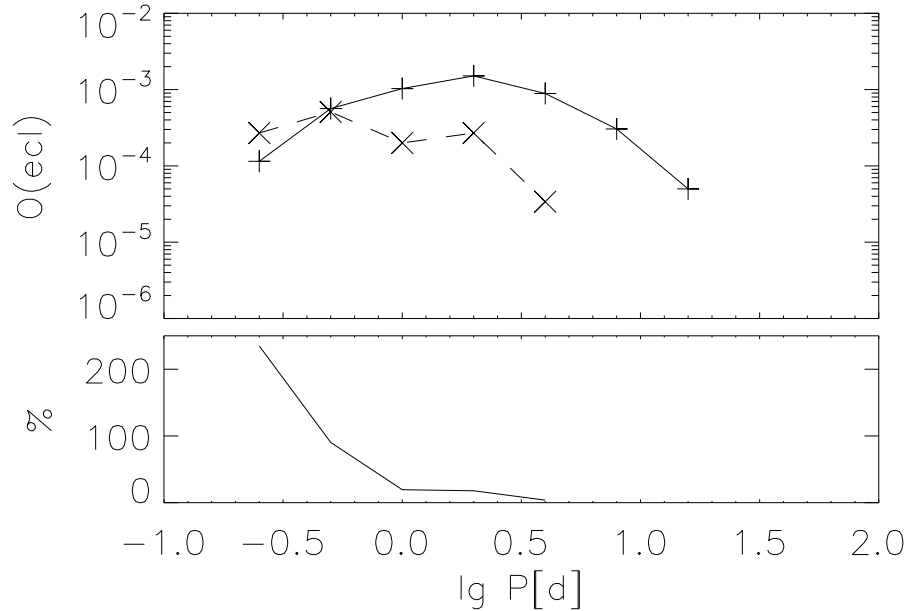


Figure 4.7: Top: Relative number of detected eclipsing binaries as a function of period. The solid line shows relative number of eclipsing binaries in the *HIPPARCOS* data – relative to the total number of stars observed by *HIPPARCOS* (from Söderhjelm & Dischler (2005)) and the dashed line shows relative number of detected eclipsing binaries in the BEST observations – relative to the total number of stars observed in the field by BEST. Bottom: The relative difference between the relative number of detected eclipsing binaries in the BEST data set and in the *HIPPARCOS* data set – i.e. the relative difference between the two lines in the upper plot. The *HIPPARCOS* data were obtained as the mean value of Fig. 14 and Fig. 4.15 in Söderhjelm & Dischler (2005).

represent periodic pulsating stars. A vague tendency for eclipsing binaries to fall mainly on the main sequence can be seen (15 out of 43; 35%), compared to the number of periodic pulsating stars that fall on the main sequence (7 out of 49; 14%). This is in agreement with what we expect, since most of the periodic pulsating stars we have found are Cepheids, Miras, or RR Lyrae stars, and none of these stars fall on the main-sequence branch in the  $V - I$  versus  $I$  diagram.

Due to their short periodicity, the identified eclipsing binaries cannot be comprised of giant stars. Hence, from their location in Fig. 4.7, they range from solar-type stars (at the typical main-sequence field star distance of *COROT* fields) to later but more nearby main-sequence stars.

## 4.6 Data Completeness

A way to evaluate the capability of ground-based surveys to detect variable stars is to compare the number of eclipsing binaries detected with a certain system with the expected number of eclipsing binaries in general. Evaluating the capability of ground-based surveys this way has the advantage that it includes not only the photometric precision of the data in the evaluation but also the phase coverage and the detection algorithms.

Fig. 4.8 shows the number of eclipsing binaries in the BEST data compared with the *HIPPARCOS* data (Söderhjelm & Dischler, 2005). A description of how the eclipsing binaries are detected in the *HIPPARCOS* data can be found in (Söderhjelm & Dischler, 2005).

The *HIPPARCOS* stars have been separated into two different absolute magnitude bins ( $M_v = -2.2$  to  $0.9$ ) and ( $M_v = 0.3$  to  $4.0$ ). This separation corresponds to a separation into two different parallax bins ( $(\pi > 4.5$  and  $\pi = 1.0 - 4.5)$  Söderhjelm & Dischler, 2005). As we do not know the parallaxes for the stars observed with BEST, we do not know the absolute magnitudes. We have tried to compare the BEST data with the *HIPPARCOS* data from both bins with more or less the same result, although the close *HIPPARCOS* sample seems to fit the BEST data slightly better than the distant sample.

Fig. 4.8 shows that BEST detected more eclipsing binaries at low periods, which is caused by the higher sampling rate of BEST compared to *HIPPARCOS*. The fact that BEST detected more eclipsing binaries than *HIPPARCOS* at low periods indicates that *HIPPARCOS* may not be perfect at low periods. At higher periods ( $\log P = 0.0$  to  $0.5$ ) BEST only detected 20% – 30% of the number of eclipsing binaries detected by *HIPPARCOS*. Söderhjelm & Dischler (2005) have calculated the relative number of eclipsing binaries as a function of period in three different amplitude bins ( $\Delta m > 0.1, 0.4$  and  $0.7$  mag). As almost all the eclipsing binaries we have detected have amplitudes between 0.1 and 0.4 mag, we only discuss the results from the first bin here, i.e., the bin with the largest eclipse probabilities. This statistical analysis shows that the BEST data set presented here has a completeness of 20% – 30% compared with the *HIPPARCOS* data set for periods longer than 1 day and is complete compared with the *HIPPARCOS* data set for short-period binaries.

As there were six periodic variable stars in the GCVS that we did not detect with our periodic variable star detection algorithm, there is reason to believe that our algorithm is not perfect. This means that by improving the algorithm more periodic variable stars would be detected and the completeness of the data set would increase. In particular, it is seen that we detect a lower number of eclipsing binaries with periods around 1 day than what is expected. This might mean that we have been too conservative with excluding periodic variable stars that have a period close to 1 day.

## 4.7 Conclusions

BEST has observed the first long-run field (LRc1) of the *COROT* mission for 35 nights. We have found 92 periodic variable stars in the data: 43 eclipsing binaries and 49 periodic pulsating stars.

Data reduction has been performed using image subtraction. Astrometric and photometric calibration were made by matching stars to the USNO-A2.0 catalog. We used the index  $J$  defined by Stetson (1996) to identify suspected variable stars and searched these stars for periodicity with the method introduced by Schwarzenberg-Czerny (1996). In this way we have identified 92 periodic variable stars, compared to the already known 11 variable stars in the GCVS with periods less than 120 days.

The periodic variable stars have been identified in the ExoDat catalog, and the color-magnitude diagram of the stars in the field shows that the eclipsing binaries have a slight tendency to lie on the main sequence compared to the periodic pulsating stars. This reflects that most of the periodic pulsating stars detected in the data are Cepheids, Miras, or RR Lyrae stars.

We also present a new tool to evaluate the completeness of a survey data set by comparing the number of eclipsing binaries detected in the data set with statistical estimates of the relative number of eclipsing binaries. The analysis shows that this BEST data set has a completeness of 20% – 30% compared with the *HIPPARCOS* data set for periods greater than 1 day and is complete relative to *HIPPARCOS* for shorter periods.

## Acknowledgments

We would like to thank T. Arentoft for helpful discussions and careful reading of the manuscript and the referee, B. S. Gaudi, for many useful suggestions and comments. We thank the Observatoire de Haute-Provence for great support of the BEST survey. C. K. gratefully acknowledges financial support by the Danish National Science Research Council through the Danish AsteroSeismology Centre (DASC) and the Instrument Center for Danish Astrophysics (IDA). This research has made use of the SIMBAD database, operated at CDS, Strasbourg, France.

Table 4.2: Periodic variable stars in the field.  $R_{mean}$  is the mean magnitude obtained with BEST,  $A_r$  is the amplitude of the periodic variability in the stars (corresponding to the deeper dip for eclipsing binaries) and the variability type is given as either periodic pulsating variables (PPV) or eclipsing binaries (EB).

ID	USNO	$\alpha$ (J2000)	$\delta$ (J2000)	$P$ (days)	$R_{mean}$	$A_R$	Type
V1	U0825_15631497	19 <sup>h</sup> 23 <sup>m</sup> 50 <sup>s</sup> .63	-00°34'53''.9	1.908	12.21	0.05	PPV
V2	U0825_16062830	19 <sup>h</sup> 30 <sup>m</sup> 46 <sup>s</sup> .56	-00°26'26''.0	11.932	13.40	0.16	PPV
V3	U0825_15906821	19 <sup>h</sup> 28 <sup>m</sup> 09 <sup>s</sup> .70	-00°28'21''.7	0.487	13.70	0.15	EB
V4	U0825_15803107	19 <sup>h</sup> 26 <sup>m</sup> 29 <sup>s</sup> .85	-00°28'59''.0	2.113	11.54	0.04	EB
V5	U0825_15951762	19 <sup>h</sup> 28 <sup>m</sup> 54 <sup>s</sup> .77	-00°26'13''.9	79.478	12.66	0.09	PPV
V6	U0825_15828621	19 <sup>h</sup> 26 <sup>m</sup> 54 <sup>s</sup> .41	-00°25'32''.8	0.331	13.07	0.09	EB
V7	U0825_15479782	19 <sup>h</sup> 21 <sup>m</sup> 36 <sup>s</sup> .79	-00°27'18''.2	1.967	11.17	0.06	PPV
V8	U0825_16122557	19 <sup>h</sup> 31 <sup>m</sup> 43 <sup>s</sup> .22	-00°17'50''.6	67.898	10.30	0.12	PPV
V9	U0825_15871361	19 <sup>h</sup> 27 <sup>m</sup> 35 <sup>s</sup> .18	-00°17'49''.5	48.124	12.50	0.07	PPV
V10	U0825_16065804	19 <sup>h</sup> 30 <sup>m</sup> 49 <sup>s</sup> .50	-00°12'59''.4	6.555	11.26	0.02	PPV
V11	U0825_15987353	19 <sup>h</sup> 29 <sup>m</sup> 31 <sup>s</sup> .05	-00°11'33''.6	96.016	10.76	0.06	PPV
V12	U0825_15757192	19 <sup>h</sup> 25 <sup>m</sup> 46 <sup>s</sup> .21	-00°11'33''.5	90.120	12.80	0.15	PPV
V13	...	19 <sup>h</sup> 27 <sup>m</sup> 19 <sup>s</sup> .88	-00°00'52''.6	59.590	11.87	0.15	PPV
V14	U0900_15449170	19 <sup>h</sup> 31 <sup>m</sup> 14 <sup>s</sup> .35	00°02'33''.5	102.780	11.37	0.10	PPV
V15	U0900_15370565	19 <sup>h</sup> 30 <sup>m</sup> 15 <sup>s</sup> .97	00°05'37''.6	2.273	12.51	0.03	EB
V16	U0900_14944293	19 <sup>h</sup> 24 <sup>m</sup> 36 <sup>s</sup> .78	00°01'16''.5	32.344	11.01	0.29	PPV
V17	U0900_15533956	19 <sup>h</sup> 32 <sup>m</sup> 17 <sup>s</sup> .06	00°08'47''.7	1.902	12.22	0.05	EB
V18	U0900_14773005	19 <sup>h</sup> 22 <sup>m</sup> 02 <sup>s</sup> .23	00°00'30''.4	1.135	12.22	0.13	EB
V19	U0900_14801088	19 <sup>h</sup> 22 <sup>m</sup> 27 <sup>s</sup> .37	00°06'59''.9	1.870	13.15	0.05	EB
V20	U0900_14803632	19 <sup>h</sup> 22 <sup>m</sup> 29 <sup>s</sup> .64	00°09'57''.4	0.975	13.16	0.18	EB
V21	U0900_14963651	19 <sup>h</sup> 24 <sup>m</sup> 52 <sup>s</sup> .18	00°20'50''.3	85.208	12.94	0.09	PPV
V22	...	19 <sup>h</sup> 21 <sup>m</sup> 18 <sup>s</sup> .72	00°17'50''.8	93.828	12.51	0.12	PPV
V23	U0900_15317860	19 <sup>h</sup> 29 <sup>m</sup> 34 <sup>s</sup> .44	00°32'54''.9	15.250	11.77	0.08	PPV
V24	U0900_14875071	19 <sup>h</sup> 23 <sup>m</sup> 36 <sup>s</sup> .07	00°31'39''.4	0.678	11.91	0.04	EB
V25	U0900_15102073	19 <sup>h</sup> 26 <sup>m</sup> 47 <sup>s</sup> .78	00°34'47''.2	78.260	12.52	0.07	PPV
V26	U0900_15105221	19 <sup>h</sup> 26 <sup>m</sup> 50 <sup>s</sup> .33	00°34'53''.4	77.540	12.09	0.11	PPV
V27	U0900_15227975	19 <sup>h</sup> 28 <sup>m</sup> 26 <sup>s</sup> .95	00°43'19''.9	116.850	10.64	0.12	PPV
V28	U0900_14801012	19 <sup>h</sup> 22 <sup>m</sup> 27 <sup>s</sup> .34	00°38'02''.4	0.670	12.46	0.02	EB
V29	U0900_14785145	19 <sup>h</sup> 22 <sup>m</sup> 13 <sup>s</sup> .39	00°40'37''.7	43.135	10.71	0.04	PPV
V30	U0900_15459522	19 <sup>h</sup> 31 <sup>m</sup> 21 <sup>s</sup> .44	00°53'04''.3	55.864	11.70	0.07	PPV
V31	U0900_15338939	19 <sup>h</sup> 29 <sup>m</sup> 50 <sup>s</sup> .48	00°55'01''.6	4.420	12.28	0.04	EB
V32	U0900_15147997	19 <sup>h</sup> 27 <sup>m</sup> 23 <sup>s</sup> .94	00°53'07''.7	0.454	13.38	0.08	EB
V33	U0900_14857685	19 <sup>h</sup> 23 <sup>m</sup> 20 <sup>s</sup> .96	01°50'48''.6	0.324	14.64	0.19	EB
V34	U0900_14842306	19 <sup>h</sup> 23 <sup>m</sup> 06 <sup>s</sup> .29	01°06'49''.3	0.549	12.71	0.06	EB
V35	...	19 <sup>h</sup> 31 <sup>m</sup> 48 <sup>s</sup> .52	01°14'41''.7	0.306	13.72	0.13	EB
V36	U0900_15489834	19 <sup>h</sup> 31 <sup>m</sup> 42 <sup>s</sup> .44	01°14'44''.2	67.996	12.38	0.07	PPV
V37	U0900_14842441	19 <sup>h</sup> 23 <sup>m</sup> 06 <sup>s</sup> .42	01°07'06''.8	1.174	12.82	0.09	EB
V38	U0900_15096269	19 <sup>h</sup> 26 <sup>m</sup> 42 <sup>s</sup> .91	01°11'48''.7	0.452	12.20	0.07	EB
V39	U0900_15088039	19 <sup>h</sup> 26 <sup>m</sup> 36 <sup>s</sup> .27	01°13'15''.5	0.942	13.53	0.10	PPV
V40	U0900_15245627	19 <sup>h</sup> 26 <sup>m</sup> 37 <sup>s</sup> .33	01°13'33''.9	1.783	14.65	0.10	EB
V41	U0900_14903885	19 <sup>h</sup> 24 <sup>m</sup> 02 <sup>s</sup> .05	01°21'50''.2	39.304	12.18	0.20	PPV
V42	U0900_15033451	19 <sup>h</sup> 25 <sup>m</sup> 51 <sup>s</sup> .33	01°29'12''.5	0.431	14.02	0.18	EB
V43	U0900_15172322	19 <sup>h</sup> 27 <sup>m</sup> 43 <sup>s</sup> .57	01°32'23''.8	63.682	11.62	0.03	PPV
V44	U0900_15110355	19 <sup>h</sup> 27 <sup>m</sup> 42 <sup>s</sup> .76	01°32'50''.7	1.942	11.37	0.03	EB
V45	U0900_15171348	19 <sup>h</sup> 26 <sup>m</sup> 54 <sup>s</sup> .39	01°32'32''.1	1.110	13.23	0.10	PPV
V46	U0900_15245627	19 <sup>h</sup> 28 <sup>m</sup> 40 <sup>s</sup> .54	01°34'50''.4	1.966	11.53	0.06	EB
V47	U0900_15190277	19 <sup>h</sup> 27 <sup>m</sup> 58 <sup>s</sup> .26	01°35'04''.1	1.439	11.61	0.07	EB
V48	U0900_15295393	19 <sup>h</sup> 29 <sup>m</sup> 18 <sup>s</sup> .23	01°37'29''.9	55.496	12.99	0.10	PPV
V49	U0900_14925806	19 <sup>h</sup> 24 <sup>m</sup> 21 <sup>s</sup> .19	01°33'31''.7	0.334	12.98	0.04	EB
V50	U0900_14877836	19 <sup>h</sup> 23 <sup>m</sup> 38 <sup>s</sup> .36	01°34'44''.0	1.383	12.35	0.06	EB
V51	U0900_15318544	19 <sup>h</sup> 29 <sup>m</sup> 34 <sup>s</sup> .91	01°42'55''.4	52.763	11.17	0.05	PPV
V52	U0900_14757657	19 <sup>h</sup> 21 <sup>m</sup> 47 <sup>s</sup> .43	01°37'15''.3	0.414	13.91	0.18	EB
V53	U0900_14975844	19 <sup>h</sup> 25 <sup>m</sup> 02 <sup>s</sup> .35	01°41'43''.0	0.355	11.83	0.04	EB
V54	...	19 <sup>h</sup> 23 <sup>m</sup> 59 <sup>s</sup> .33	01°41'30''.1	1.110	13.85	0.18	PPV
V55	U0900_15323691	19 <sup>h</sup> 29 <sup>m</sup> 38 <sup>s</sup> .78	01°46'35''.4	94.240	11.99	0.19	PPV
V56	U0900_14715405	19 <sup>h</sup> 21 <sup>m</sup> 05 <sup>s</sup> .86	01°46'41''.9	89.746	11.80	0.06	PPV
V57	U0900_15337670	19 <sup>h</sup> 29 <sup>m</sup> 49 <sup>s</sup> .43	01°54'27''.4	38.362	12.10	0.02	PPV
V58	U0900_14845601	19 <sup>h</sup> 23 <sup>m</sup> 09 <sup>s</sup> .52	01°49'30''.9	47.360	10.07	0.10	PPV
V59	...	19 <sup>h</sup> 26 <sup>m</sup> 37 <sup>s</sup> .45	01°52'57''.2	0.286	13.11	0.08	EB
V60	U0900_15090051	19 <sup>h</sup> 26 <sup>m</sup> 37 <sup>s</sup> .87	01°56'02''.9	90.288	12.02	0.10	PPV

Table 4.2: Continued.

ID	USNO	$\alpha$ (J2000)	$\delta$ (J2000)	$P$ (days)	$R_{\text{mean}}$	$A_R$	Type
V61	U0900_15089049	19 <sup>h</sup> 26 <sup>m</sup> 37 <sup>s</sup> .11	01 <sup>°</sup> 56′17″.0	2.045	12.02	0.06	EB
V62	U0900_14770477	19 <sup>h</sup> 22 <sup>m</sup> 02 <sup>s</sup> .70	01 <sup>°</sup> 53′01″.5	74.072	12.34	0.11	PPV
V63	U0900_15513261	19 <sup>h</sup> 32 <sup>m</sup> 00 <sup>s</sup> .07	02 <sup>°</sup> 04′19″.9	51.242	11.60	0.06	PPV
V64	U0900_15286457	19 <sup>h</sup> 29 <sup>m</sup> 11 <sup>s</sup> .40	02 <sup>°</sup> 02′07″.5	75.340	11.92	0.06	PPV
V65	U0900_15129182	19 <sup>h</sup> 27 <sup>m</sup> 08 <sup>s</sup> .90	02 <sup>°</sup> 04′04″.2	0.349	12.59	0.05	EB
V66	U0900_14931322	19 <sup>h</sup> 24 <sup>m</sup> 25 <sup>s</sup> .96	02 <sup>°</sup> 01′51″.4	94.194	11.70	0.08	PPV
V67	U0900_14809956	19 <sup>h</sup> 22 <sup>m</sup> 35 <sup>s</sup> .19	02 <sup>°</sup> 02′04″.5	1.362	12.87	0.09	EB
V68	U0900_15529595	19 <sup>h</sup> 32 <sup>m</sup> 13 <sup>s</sup> .30	02 <sup>°</sup> 12′33″.4	73.852	10.69	0.08	PPV
V69	U0900_15083048	19 <sup>h</sup> 26 <sup>m</sup> 32 <sup>s</sup> .09	02 <sup>°</sup> 07′48″.6	76.042	11.40	0.03	PPV
V70	U0900_14819436	19 <sup>h</sup> 22 <sup>m</sup> 44 <sup>s</sup> .20	02 <sup>°</sup> 05′24″.1	93.784	11.02	0.10	PPV
V71	U0900_15313364	19 <sup>h</sup> 29 <sup>m</sup> 31 <sup>s</sup> .49	02 <sup>°</sup> 12′54″.6	0.655	13.92	0.05	EB
V72	U0900_15131911	19 <sup>h</sup> 27 <sup>m</sup> 11 <sup>s</sup> .01	02 <sup>°</sup> 11′09″.9	0.357	13.10	0.14	EB
V73	U0900_14936196	19 <sup>h</sup> 24 <sup>m</sup> 30 <sup>s</sup> .18	02 <sup>°</sup> 12′53″.3	0.456	13.26	0.18	EB
V74	U0900_15290990	19 <sup>h</sup> 29 <sup>m</sup> 14 <sup>s</sup> .99	02 <sup>°</sup> 18′20″.5	0.588	13.77	0.10	EB
V75	U0900_14927833	19 <sup>h</sup> 24 <sup>m</sup> 22 <sup>s</sup> .78	02 <sup>°</sup> 15′02″.3	1.028	11.62	0.01	EB
V76	U0900_15076715	19 <sup>h</sup> 26 <sup>m</sup> 26 <sup>s</sup> .80	02 <sup>°</sup> 18′43″.4	1.793	10.07	0.02	EB
V77	U0900_15286206	19 <sup>h</sup> 29 <sup>m</sup> 11 <sup>s</sup> .29	02 <sup>°</sup> 21′55″.2	0.392	11.99	0.06	EB
V78	U0825_15906838	19 <sup>h</sup> 28 <sup>m</sup> 09 <sup>s</sup> .62	-00 <sup>°</sup> 21′58″.2	0.495	14.21	0.4	EB
V79	U0900_14772878	19 <sup>h</sup> 22 <sup>m</sup> 02 <sup>s</sup> .07	00 <sup>°</sup> 01′07″.5	0.723	13.39	0.2	EB
V80	U0900_14716806	19 <sup>h</sup> 21 <sup>m</sup> 07 <sup>s</sup> .48	00 <sup>°</sup> 33′09″.9	1.188	13.25	0.07	PPV
V81	U0900_15357089	19 <sup>h</sup> 30 <sup>m</sup> 05 <sup>s</sup> .04	00 <sup>°</sup> 46′28″.7	0.307	13.40	0.1	EB
V82	...	19 <sup>h</sup> 23 <sup>m</sup> 28 <sup>s</sup> .00	00 <sup>°</sup> 41′29″.1	0.395	13.04	0.05	EB
V83	U0900_14966595	19 <sup>h</sup> 24 <sup>m</sup> 54 <sup>s</sup> .54	01 <sup>°</sup> 15′03″.3	5.872	12.20	0.04	PPV
V84	U0900_15033451	19 <sup>h</sup> 25 <sup>m</sup> 49 <sup>s</sup> .73	01 <sup>°</sup> 28′43″.2	0.549	13.95	0.12	EB
V85	...	19 <sup>h</sup> 25 <sup>m</sup> 50 <sup>s</sup> .12	01 <sup>°</sup> 29′43″.5	0.354	13.95	0.2	EB
V86	U0900_15116292	19 <sup>h</sup> 26 <sup>m</sup> 55 <sup>s</sup> .97	01 <sup>°</sup> 31′47″.0	2.504	13.11	0.6	PPV

Table 4.3: Periodic variable stars in the field from GCVS.

ID	GCVS	$\alpha$ (J2000)	$\delta$ (J2000)	Type	$P$ (days)	$V_{\text{max}}$	$V_{\text{min}}$	$R_{\text{mean}}$
G1	ES Aql	19 <sup>h</sup> 32 <sup>m</sup> 21 <sup>s</sup> .50	-00 <sup>°</sup> 11′31″.8	SR	101.1	13.2	15.1	10.80
G2	V0362 Aql	19 <sup>h</sup> 24 <sup>m</sup> 55 <sup>s</sup> .67	01 <sup>°</sup> 05′00″.6	RV	68.	13.1	14.7	14.09
G3	V0381 Aql	19 <sup>h</sup> 31 <sup>m</sup> 13 <sup>s</sup> .68	02 <sup>°</sup> 07′03″.4	RV	54.8	12.7	15.4	12.90
G4	V0919 Aql	19 <sup>h</sup> 22 <sup>m</sup> 55 <sup>s</sup> .75	01 <sup>°</sup> 02′39″.7	EB/KE	0.797102	13.0	14.0	13.98
G5	V0920 Aql	19 <sup>h</sup> 31 <sup>m</sup> 30 <sup>s</sup> .75	01 <sup>°</sup> 05′53″.9	RRAB	0.4955033	13.3	14.3	12.97
G6	V0291 Aql	19 <sup>h</sup> 30 <sup>m</sup> 19 <sup>s</sup> .93	01 <sup>°</sup> 35′47″.1	RRAB	0.482889	13.5	15.0	13.91
G7	V0922 Aql	19 <sup>h</sup> 30 <sup>m</sup> 28 <sup>s</sup> .35	01 <sup>°</sup> 13′50″.9	RRAB	0.458874	16.3	17.5	12.99
G8	V0978 Aql	19 <sup>h</sup> 31 <sup>m</sup> 31 <sup>s</sup> .57	02 <sup>°</sup> 12′57″.3	RRAB	0.520935	14.6	15.9	14.37
G9	V1127 Aql	19 <sup>h</sup> 24 <sup>m</sup> 00 <sup>s</sup> .04	01 <sup>°</sup> 41′46″.1	RRAB	0.356005	14.8	16.0	13.42
G10	V1135 Aql	19 <sup>h</sup> 31 <sup>m</sup> 04 <sup>s</sup> .27	-00 <sup>°</sup> 18′42″.6	EA/SD	3.14546	15.5	16.6	14.69
G11	V1215 Aql	19 <sup>h</sup> 22 <sup>m</sup> 24 <sup>s</sup> .69	01 <sup>°</sup> 27′55″.4	RR	0.5013	15.3	16.0	15.20

# Chapter 5

## SPB Stars in NGC 371

The paper  *$\beta$  Cep and SPB stars in the young open SMC cluster NGC 371* presented in this chapter has been published in:

Karoff et al. (2008a) Christoffer Karoff, Torben Arentoft, Lars Glowienka, Christian Coutures, Tine Bjørn Nielsen, Gülnur Dogan, Frank Grundahl & Hans Kjeldsen, 2008, MNRAS, 386, 1085

This paper presents a list of 29 short period B type variables in the upper part of the main sequence, many of which are probably SPB stars. This is an interesting result as stellar models of stars in low-metallicity environments such as the SMC do not predict pulsation in  $\beta$  Cep stars and a heavily reduced rate of SPB stars compared to the Galaxy. If there are of the order of 29 SPB stars in the NGC371 then this means that this low-metallicity cluster has more SPB stars than any other known cluster and this would clearly contradict the theoretical predictions, namely that the excitation rate of pulsation by the  $\kappa$  mechanism would be lower in low-metallicity environments. A possible extension to the standard stellar models to account for this discrepancy could be to include local iron enhancement by diffusion and radiative accelerations (Miglio et al., 2007c) in the stellar models. Therefore this study shows how studies of B type variables in clusters are excellent tools for testing and improving stellar models.



## SPB stars in the open SMC cluster NGC 371

Christoffer Karoff\*, Torben Arentoft\*, Lars Glowienka\*,  
Christian Coutures†, Tine Bjørn Nielsen\*, Gülnur Dogan\*,  
Frank Grundahl\* & Hans Kjeldsen\*

### Abstract

Pulsation in  $\beta$  Cep and SPB stars are driven by the  $\kappa$  mechanism which depends critically on the metallicity. It has therefore been suggested that  $\beta$  Cep and SPB stars should be rare in the Magellanic Clouds which have lower metallicities than the solar neighborhood. To test this prediction we have observed the open SMC cluster NGC 371 for 12 nights in order to search for  $\beta$  Cep and SPB stars. Surprisingly, we find 29 short-period B-type variables in the upper part of the main sequence, many of which are probably SPB stars. This result indicates that pulsation is still driven by the  $\kappa$  mechanism even in low-metallicity environments. All the identified variables have periods longer than the fundamental radial period which means that they cannot be  $\beta$  Cep stars. Within an amplitude detection limit of 5 mmag no stars in the top of the Hertzsprung-Russell diagram show variability with periods shorter than the fundamental radial period. So if  $\beta$  Cep stars are present in the cluster they oscillate with amplitudes below 5 mmag, which is significantly lower than the mean amplitude of  $\beta$  Cep stars in the Galaxy. We see evidence that multimode pulsation is more common in the upper part of the main sequence than in the lower. We have also identified 5 eclipsing binaries and 3 periodic pulsating Be stars in the cluster field.

### 5.1 Introduction

$\beta$  Cep and slowly pulsating B stars (SPB) pulsate due to the  $\kappa$ -mechanism activated by the metal opacity bump (Cox et al., 1992). This give rise to p-mode pulsation in  $\beta$  Cep stars and g-mode pulsation in SPB stars. However the theoretical standard models do not predict the presence of pulsation in  $\beta$  Cep and SPB stars in low-metallicity environments such as the Magellanic Clouds.

Analysis of OGLE data have indeed shown that  $\beta$  Cep and SPB stars exist in the Magellanic Clouds (Pigulski & Kołaczkowski, 2002; Kołaczkowski et al., 2004, 2006) though it is not clear if the rate of  $\beta$  Cep and SPB stars is lower than or equal to the rate in the Galaxy. We have therefore observed the open

---

\*Department of Physics and Astronomy, University of Aarhus, Ny Munkegade, Building 1520, DK 8000 Aarhus C.E-mail: karoff@phys.au.dk

†Institut d'Astrophysique de Paris, CNRS, Universite Pierre et Marie Curie UMR7095, 98bis Boulevard Arago, 75014 Paris, France.

SMC cluster NGC 371 for 12 nights in order to search for  $\beta$  Cep and SPB stars. Observing a single cluster instead of the the entire SMC has a number of advantages, – e.g. the age and metallicity of the cluster can be constrained from fitting isochrones to the Hertzsprung-Russell diagram.

The metallicity of the SMC has been measured to between  $Z = 0.001$  and  $Z = 0.004$  (see Maeder et al., 1999, and references therein), while Miglio et al. (2007a,b) have calculated instability domains of  $\beta$  Cep and SPB stars using improved opacities and metal abundances which do not predict pulsation in  $\beta$  Cep and a heavily reduced rate of SPB stars compared to the Galaxy for  $Z < 0.005$ . We should therefore not expect to find any  $\beta$  Cep and only a limited number of SPB stars in the SMC, if any.

In order to test this prediction we have chosen to observe the cluster NGC 371 as this cluster has been observed before by Kjeldsen & Baade (1994) who saw some signs of variability, though no clear evidence of pulsation was seen.

The observations presented in this paper have been made with a single telescope. This means that clear mode and frequency determination can not be obtained and the frequencies can not be used for modeling. Instead this work presents a number of candidate SPB stars for followup observations with at least dual-side photometry and with spectroscopy.

The paper is arranged as follows. Section 5.2 presents the cluster. Section 5.3 describes how we obtained, reduced and analyzed the data. The identified eclipsing binaries are presented in Section 5.4, the Be stars in Section 5.5 and the pulsating stars in the upper part of the main sequence in Section 5.6. A summary and concluding remarks are found in Section 5.7.

## 5.2 The Target Cluster: NGC 371

NGC 371 ( $\alpha_{2000}, \delta_{2000} = 11^{\text{h}}03^{\text{m}}25^{\text{s}}.0, -72^{\circ}04'40''.0$ ) is a young open cluster in the SMC. Wisniewski & Bjorkman (2006) estimated a  $\log(\text{age})$  of 6.7 based on isochrone fitting to OGLE data assuming a metallicity of  $Z = 0.002$ . As there are no high-resolution spectra available for NGC 371 it has not been possible to estimate the metallicity autonomously.

The field of the cluster is shown in Fig. 5.1 with the identified variable stars marked.

## 5.3 The Data and the Data Reduction

The observations were obtained with the DFOSC instrument at the Danish 1.54-m telescope at ESO, La Silla during 12 nights in August and September 2005. 763 frames were collected in  $I$  and 623 in  $B$ . The same pointing was maintained during the observations, i.e., the stars were kept at fixed positions on the CCD (within a few pixels) during the observing run. Because of the crowding in the field the observations were always made in focus and the exposure times were then adjusted according to the seeing so that only the brightest 5% of the stars were saturated. This resulted in exposure times of approximately 20 s in  $I$  and

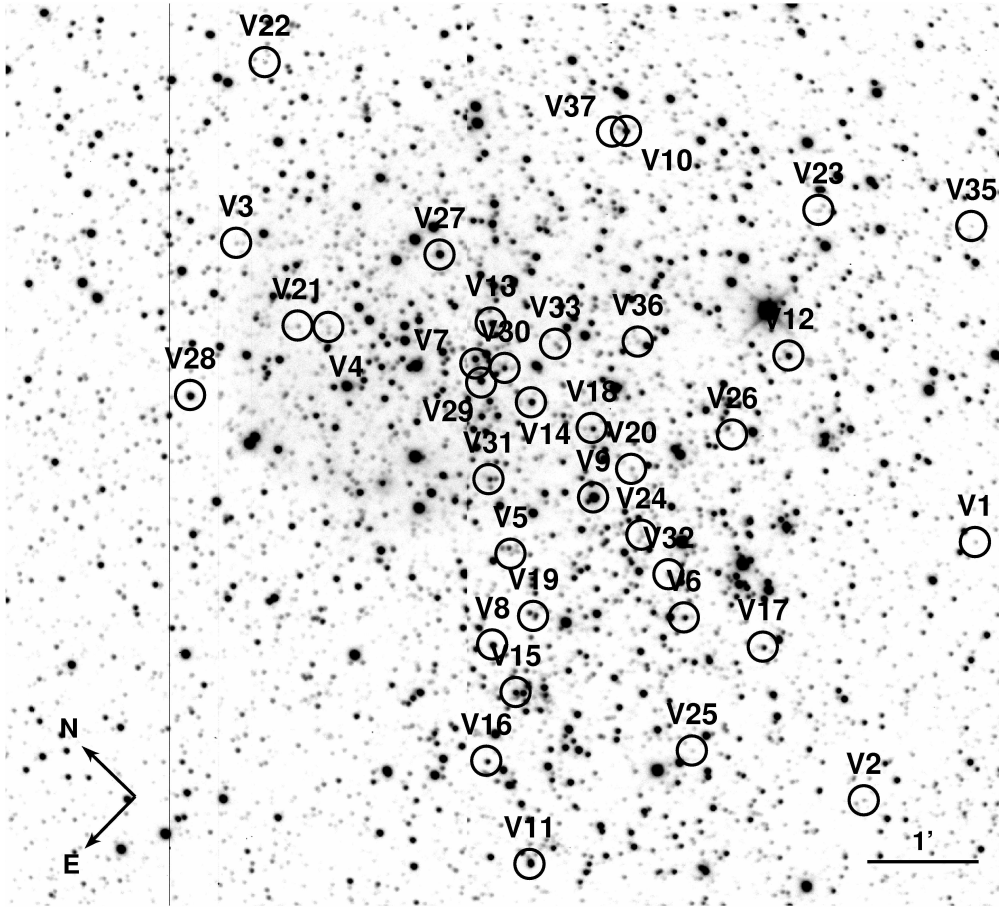


Figure 5.1: DFOSC image of NGC371, with the variables marked.

60 s in  $B$ . In Fig. 5.2 all the data are shown for one of the bright stars in NGC 371, illustrating the time distribution of the data set.

The CCD images were calibrated using standard procedures, i.e. a master BIAS was subtracted from each frame before the frames were divided by a master sky-flat in each filter. The master BIAS was obtained from a large number of frames from the whole observing run and the master sky-flats were obtained as the median of a large number of evening and morning sky-flats. We checked that both the BIAS and the flat-fields were indeed stable over the length of the observing run.

The photometric reductions were done using the software package MOMF (Kjeldsen & Frandsen, 1992). MOMF applies a very robust algorithm combining PSF and aperture photometry in semi-crowded fields.

Some of the light curves showed residuals of systematic trends caused by, e.g., air mass, cloud cover, and temperature variations (these residuals are sometimes referred to as "red noise"). We therefore applied the algorithm introduced by Tamuz et al. (2005) in order to correct for systematic effects. This clearly improved the rms noise level, in particular in the brightest stars.

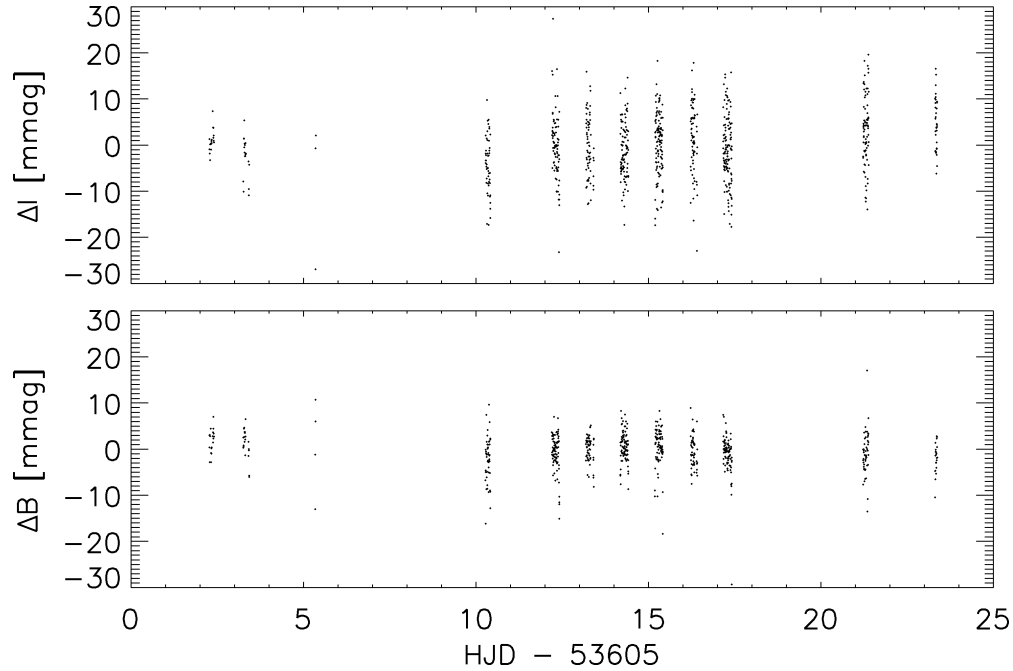


Figure 5.2: Light curves of one of the bright stars in NGC 371 showing the precision level and data sampling.

The resulting light curves had rms noise levels over the whole observing run ranging from a few mmag in the bright end and up to 50 mmag in the faint end. Some of the light curves showed night-to-night drifts, which means that the rms noise level in the individual nights was lower than over the whole observing run. Fig. 5.2 shows the precision in a typical bright star.

### 5.3.1 Analysis of Differential Light Curves

We obtained differential light curves of 6842 stars in the  $13.5' \times 13.5'$  FOV and we searched for variability in all these light curves. The light curves were kept in the instrumental system, but calibrated *UBVI* photometry was obtained from Zaritsky et al. (2002).

We used two complementary algorithms to search for variability; the analysis of variance periodograms (Schwarzenberg-Czerny, 1996) and simultaneous iterative sine wave fitting (Frandsen et al., 1995) based on the Lomb periodogram (Lomb, 1976). We searched for variability both with and without using statistical weights (Frandsen et al., 1995). The statistical weights were assigned as the standard deviation of all data points separated by less than 15 minutes from a given data point. For the analysis of variance approach we made visual examination of all light curves which had fit qualities better than 0.9 and for the Lomb periodogram approach we made visual examination of all light curves where the same peak in the periodogram was present in both *B* and *I* with a

Table 5.1: Stellar parameters for 5 eclipsing binaries in NGC 371. Periods are in days.

ID	$\alpha_{2000}$	$\delta_{2000}$	$B$	$B - I$	$P$
V1	01 03 04.1	-72 08 04	18.74	0.07	1.348
V2	01 03 34.9	-72 08 60	18.64	2.68	1.045
V3	01 03 40.5	-72 01 26	18.86	-0.17	0.556
V4	01 30 40.0	-72 02 33	19.14	-0.22	0.463
V5	01 03 43.5	-72 05 11	18.64	-0.23	0.609

S/N higher than 4 in amplitude (Breger et al., 1993). In total we ended up with a list of a little over a hundred stars that were selected for further analysis.

In the visual examination, stars were rejected mainly because of one of the following three causes: stars were placed outside the cluster region, stars were placed close to a hot pixel or a bad column, or the variability was not the same in the two filters. This gave us the list of the 37 stars presented in this paper. Light curves of all the variable stars will be added to CDS.

It is not possible to determine if a star is a true cluster member or not, as we only have two dimensional images available. To determine if a star is likely to be a true cluster member in three dimension a spectroscopic analysis is needed. Therefore we can not give a reliable estimate of the number of cluster members and some of the identified variable stars could turn out not to be clusters members.

## 5.4 Eclipsing Binaries

We have detected 5 eclipsing binaries (phased light curves are shown in Fig. 5.3). V1, V2 and V3 are located on the edge of the cluster, which means that they might not be cluster members. V4 and V5 are located safely inside the cluster and these stars could be important in determining the precise distance and age of the cluster. This information will again be important when trying to model the excitation mechanisms of  $\beta$  Cep and SPB stars based on data from this cluster.

V2 also shows some signs of pulsation with a frequency of 6.2 c/d, which suggest that this could be a binary system with one of the members being a pulsating star. But more photometry will be needed in order to evaluate the phenomenon properly – i.e removing the eclipse from the light curve before analyzing the pulsation.

## 5.5 Be Stars

Three of the detected variable stars match with the stars identified as Be stars by Wisniewski & Bjorkman (2006). They have identified 118 Be stars and 11 candidate Be stars in NGC371 based on two-color diagrams of  $B$ ,  $V$ ,  $R$  and  $H\alpha$  photometry. Though the nature of the variability of Be stars is believed to be transient, Be stars might also exhibit g- or p-mode pulsation. It

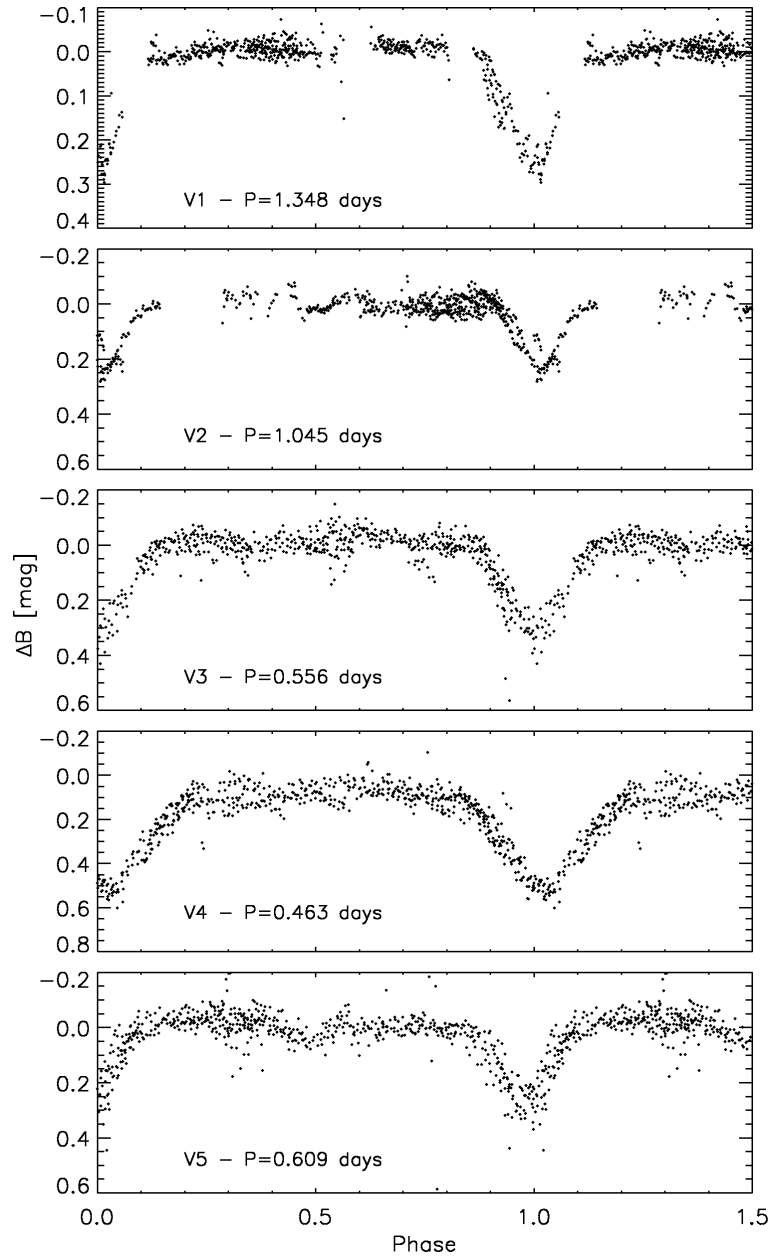


Figure 5.3: Phase light curves of the 5 eclipsing binaries identified in NGC 371.

is therefore clear that these three stars can be used to gain understanding of the relation between g- and p-mode pulsation and the variability of Be stars in low-metallicity environments. The amplitude spectra of the three Be stars are shown in Fig. 5.4. The light curves of the three Be stars all show coherent variability, which indicates that the variability originates from pulsation and not from transient events like activity.

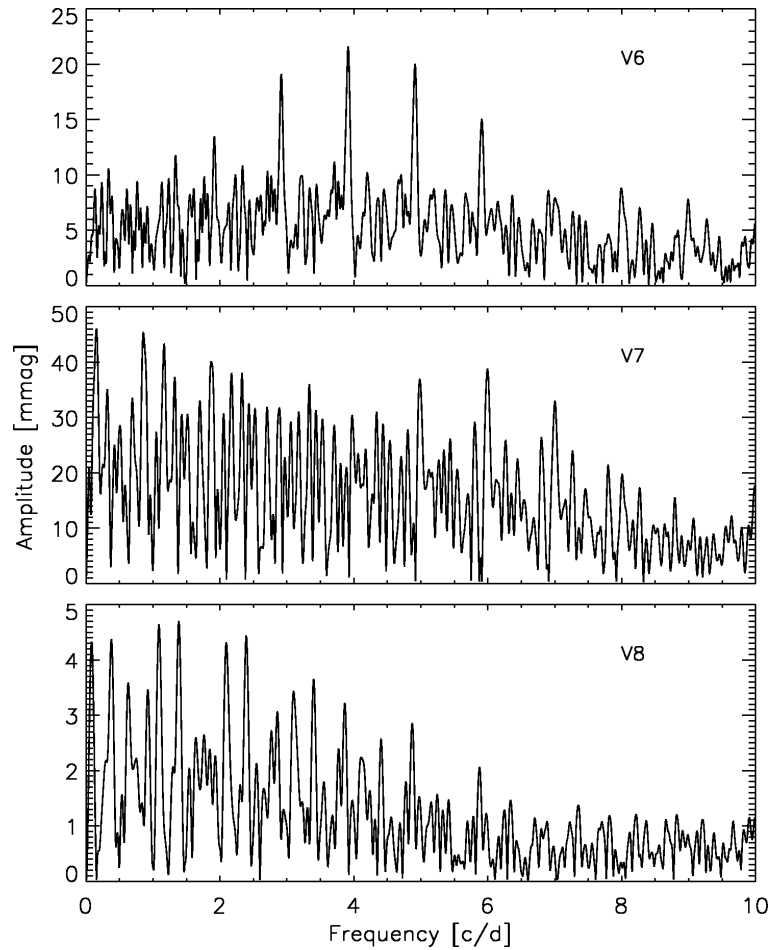


Figure 5.4: Amplitude spectra for 3 Be stars in NGC371. Note that the scale on the y-axis is different for the three stars.

## 5.6 Pulsating Stars in the Upper Part of the Main Sequence

The frequency analysis of the variable stars in the upper part of the main sequence followed Arentoft et al. (2007). This means that we made a simultaneous least-squares fit to all the frequencies with a S/N higher than 4 in the amplitude spectra of both the *I* and the *B* filter data. For each frequency we manually inspected the amplitude spectra, in order to find the frequency value that best described the variation in both filters. This step could not be made completely objective as daily aliases were present in the amplitude spectra because the observations were made from a single site. Therefore some of the detected frequencies might be shifted 1–2 c/d from the true oscillation frequencies. The uncertainties on the amplitudes and phases were calculated based on the error matrix in the least-squares fitting procedure, though we also used Monte Carlo simulations to check the consistency of these uncertainties [this

Table 5.2: Stellar parameters for 3 Be stars in NGC 371. The id's in the second column (ID II) are from Wisniewski & Bjorkman (2006).

ID	ID II	$\alpha_{2000}$	$\delta_{2000}$	$B$	$B - I$
V6	WBBe 43	01 03 34.5	-72 06 42	16.65	0.35
V7	WBBe 110	01 03 30.5	-72 03 46	17.99	-0.34
V8	WBBe 18	01 03 52.6	-72 05 39	15.73	0.21

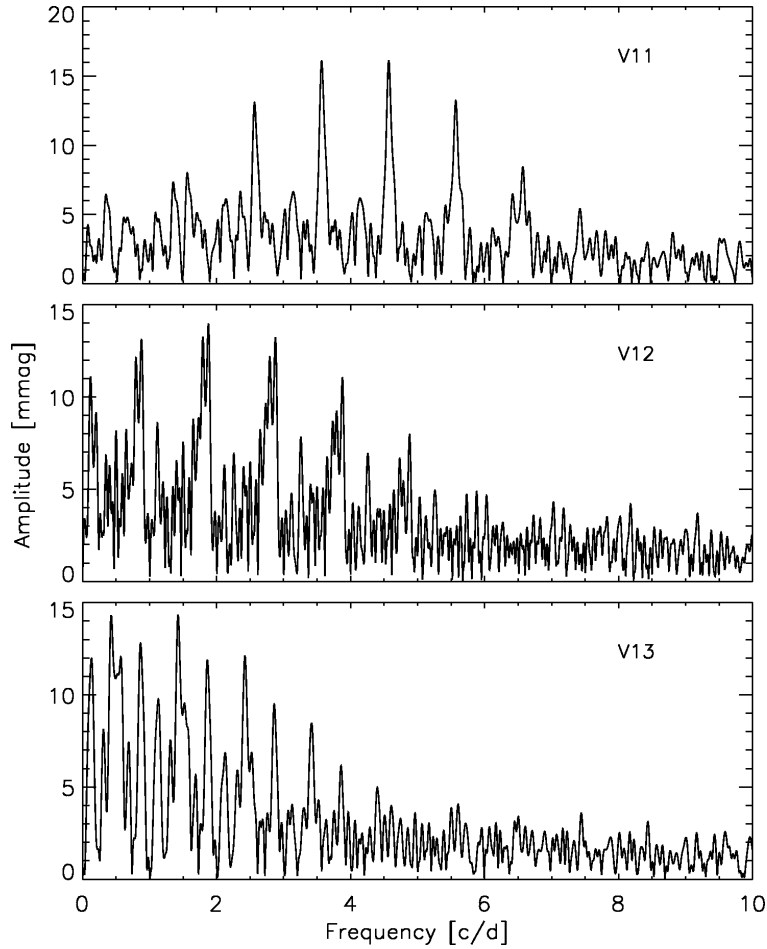


Figure 5.5: Amplitude spectra for three pulsating stars in the upper part of the main sequence of NGC 371.

was done with the use of Period04 (Lenz & Breger, 2005)]. This procedure for calculating the uncertainties assumes that we know the frequencies – i.e. that we know which peak reflect the oscillation mode. The calculated uncertainties does therefore not reflect the uncertainty originating from mismatch between the true oscillation mode and the daily aliases.

All the detected frequencies for the pulsating stars are given in Table 3 together with color, amplitude and phase information, three examples of am-

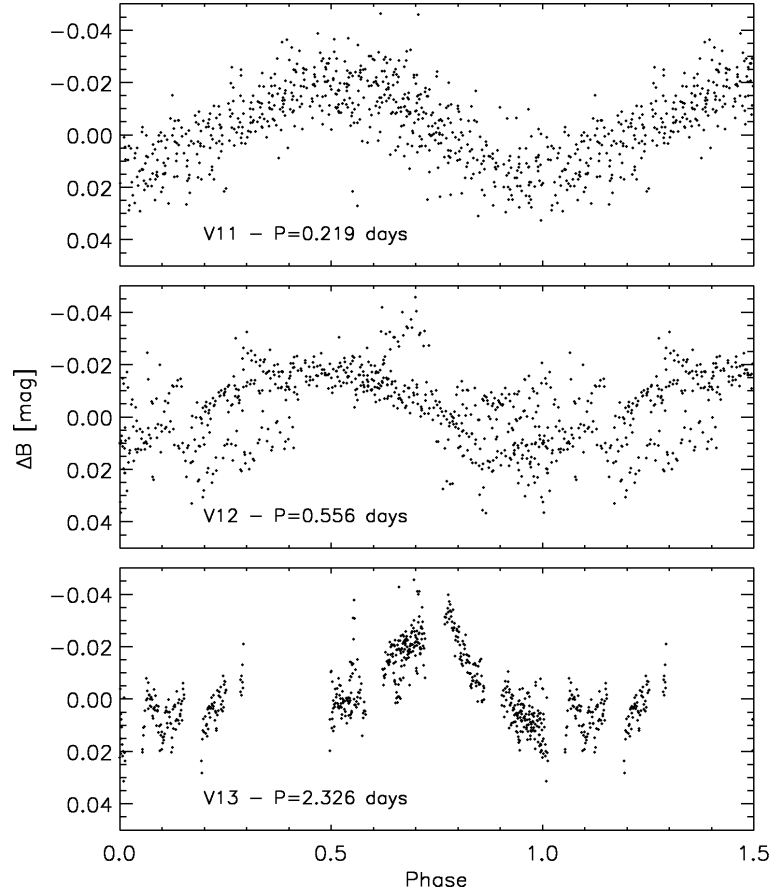


Figure 5.6: Phased light curves for three pulsating stars in the upper part of the main sequence of NGC 371.

plitude spectra of pulsating stars are shown in Fig. 5.5 and phased light curves are shown in Fig. 5.6.

### 5.6.1 Color-magnitude-diagram of NGC 371

We have used the photometry from Zaritsky et al. (2002) to make a  $B$  versus  $B - I$  color-magnitude-diagram of NGC 371 as shown in Fig. 5.7. The center of the cluster was placed on  $\alpha_{2000}, \delta_{2000} = 11^{\text{h}}03^{\text{m}}25^{\text{s}}.0, -72^{\circ}04'40''.0$  and the size was selected as a circle with a radius of  $5'$ . The color-magnitude-diagram shows the upper part of the main sequence, which is almost vertical, and the giant branch. All the identified variable stars which are not eclipsing binaries or Be stars are located on the upper part of the main sequence, which is also where the instability strips for  $\beta$  Cep and SPB stars would be located if the metallicity of the cluster had been larger. Instability analysis of models of hot main-sequence stars of solar metallicity show a group of mostly p-mode pulsators where the longest period is the fundamental radial mode and a second group of cooler stars with mostly g modes and longer periods. The first group can be identified

Table 5.3: Stellar parameters for the pulsating stars in NGC 371. Frequencies ( $\nu$ ) are in c/d, amplitudes ( $A_B$ ) are in mmag, phase differences ( $\phi_I - \phi_B$ ) are in radians and pulsation constants  $Q$  are in d<sup>-1</sup>. The quoted errors on the amplitude ratios and phase differences are based on the error matrix in the least-squares fitting procedure.

ID	$\alpha_{2000}$	$\delta_{2000}$	B [mag]	B-I	$\nu_i$	$\nu$	$A_B$	$A_I/A_B$	$\phi_I - \phi_B$	$Q$
V9	01 03 32.0	-72 05 21	13.72	-0.58	$\nu_1$	1.95	6.89	0.46(7)	-0.73(3)	0.085
					$\nu_2$	2.12	4.64	0.25(10)	-0.34(4)	0.078
V10	01 02 58.9	-72 03 14	15.57	-0.33	$\nu_1$	1.78	12.98	0.68(7)	0.19(2)	0.205
					$\nu_2$	1.70	5.78	1.11(19)	-0.24(2)	0.215
V11	01 04 37.5	-72 09 32	17.75	-0.33	$\nu_1$	4.57	16.70	0.52(11)	-0.03(3)	0.137
V12	01 03 04.2	-72 05 42	15.89	-0.47	$\nu_1$	1.80	12.97	1.00(9)	0.09(1)	0.229
V13	01 03 25.9	-72 03 36	15.79	-0.52	$\nu_1$	0.43	11.94	1.76(10)	0.07(1)	0.958
					$\nu_2$	0.87	9.17	1.57(11)	-0.03(2)	0.474
V14	01 03 29.2	-72 04 21	15.95	-0.54	$\nu_1$	2.85	19.60	0.58(10)	-0.11(2)	0.145
					$\nu_2$	2.40	14.85	1.58(14)	-0.04(2)	0.172
V15	01 03 54.7	-72 06 05	16.24	-0.43	$\nu_1$	3.86	20.99	0.57(8)	-0.01(2)	0.123
					$\nu_2$	1.80	8.65	0.69(20)	0.03(4)	0.264
V16	01 04 02.7	-72 06 21	16.70	-0.31	$\nu_1$	3.33	30.44	0.43(4)	0.00(2)	0.151
					$\nu_2$	0.48	14.86	0.54(13)	-0.04(4)	1.047
V17	01 03 30.4	-72 07 23	16.91		$\nu_1$	3.61	27.71	0.97(6)	-0.02(1)	0.152
					$\nu_2$	2.73	23.52	0.73(6)	0.02(1)	0.202
V18	01 03 16.3	-72 04 55	16.66	-0.43	$\nu_1$	2.18	32.17	0.81(6)	0.03(10)	0.230
V19	01 03 46.9	-72 05 44	17.72	-0.43	$\nu_1$	1.52	63.71	0.87(5)	-0.01(4)	0.412
V20	01 03 26.5	-72 05 25	18.23	-0.29	$\nu_1$	1.94	73.13	0.97(4)	0.03(1)	0.382
V21	01 03 42.4	-72 02 21	18.43	-0.16	$\nu_1$	1.40	35.31	0.90(17)	0.02(3)	0.534
V22	01 03 23.2	-72 00 28	18.51	-0.32	$\nu_1$	0.52	44.84	0.72(11)	-0.15(1)	1.438
V23	01 02 49.5	-72 04 59	18.92	-0.37	$\nu_1$	2.47	48.88	0.93(22)	0.00(4)	0.333
V24	01 03 31.2	-72 05 54	18.70	-0.37	$\nu_1$	0.74	75.45	1.04(6)	-0.01(1)	1.051
V25	01 03 44.9	-72 07 35	19.06	0.03	$\nu_1$	1.35	281.28	0.63(3)	0.02(1)	0.610
V26	01 03 15.3	-72 05 50	19.01	-0.24	$\nu_1$	0.63	183.62	0.47(7)	-0.03(2)	1.307
V27	01 03 24.7	-72 02 49	14.99	-0.53	$\nu_1$	2.52	5.09	1.20(16)	0.02(2)	0.133
V28	01 03 57.0	-72 02 07	15.27	-0.45	$\nu_1$	3.03	10.82	1.10(12)	-0.05(2)	0.121
V29	01 03 31.6	-72 03 54	15.32	-0.56	$\nu_1$	1.69	15.39	0.62(14)	-0.01(3)	0.216
					$\nu_2$	2.04	8.54	0.79(25)	-0.13(6)	0.179
V30	01 03 28.6	-72 03 58	16.59	-0.41	$\nu_1$	1.74	19.77	1.13(16)	0.02(3)	0.288
V31	01 03 39.0	-72 04 34	16.90	-0.46	$\nu_1$	1.30	16.49	1.79(24)	-0.08(2)	0.423
V32	01 03 32.2	-72 06 19	17.28	-0.18	$\nu_1$	1.64	29.46	1.22(10)	0.04(1)	0.336
V33	01 03 22.3	-72 04 08	18.27	-0.09	$\nu_1$	0.79	23.94	1.10(12)	-0.14(2)	0.939
V34	01 02 36.6	-72 02 33	18.97	-0.01	$\nu_1$	1.33	72.25	1.58(17)	-0.01(2)	0.619
V35	01 02 38.2	-72 06 02	19.21	0.11	$\nu_1$	0.38	170.37	0.61(3)	-0.09(1)	2.308
V36	01 03 15.2	-72 04 39	19.01	-0.1	$\nu_1$	1.24	164.74	0.83(6)	-0.01(1)	0.664
					$\nu_2$	0.50	134.43	0.56(12)	-0.04(5)	1.647
V37	01 03 00.1	-72 06 58	19.12	-0.32	$\nu_1$	0.73	250.32	0.60(5)	-0.03(1)	1.202

with the classical  $\beta$  Cep stars (early B-type stars) while the second group can be identified with the SPB stars (mid B-type stars). Models based on revised solar metal abundances and different opacities show that the hot boundary of the SPB instability strip overlaps with the  $\beta$  Cep instability strip (Miglio et al., 2007a,b). At the metallicity of NGC 371, however, no pulsations are excited in the models as already mentioned. Therefore theory cannot be used as a guide in classification. We will come back to this in the next section.

We have used the Padova evolutionary code described in Marigo et al. (2007) to calculate an isochrone for the color-magnitude-diagram of the cluster. The model used solar heavy elements mixture. We adopted a metallicity of  $Z=0.002$  and a  $\log(\text{age})$  of 6.7 from Wisniewski & Bjorkman (2006). The distance modulus was chosen to 18.7 from Crowl et al. (2001) and the reddening to  $E(B - V) = 0.085$  (Larsen et al., 2000).

The isochrone is plotted on top of the color-magnitude-diagram in Fig. 5.7. Here it is seen that the isochrone generally fits the data nicely.

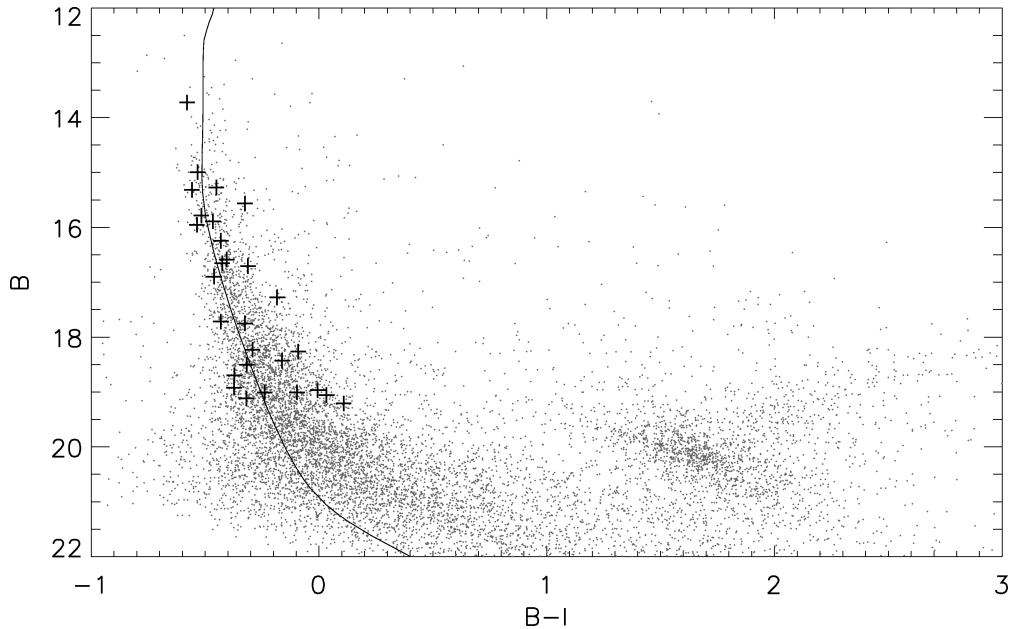


Figure 5.7: Color-magnitude-diagram of NGC 371 with the identified SPB candidates marked. The solid line shows a isochrone fit to the observations.

### 5.6.2 Period Distribution in NGC 371

In the Galaxy,  $\beta$  Cep stars have periods which are consistent with mostly p-mode pulsations. The longest period is that of the fundamental radial mode for which the pulsation constant  $Q \approx 0.033 \text{ d}^{-1}$  (Stankov & Handler, 2005). To classify stars in NGC 371 we need an estimate of  $Q$  for each star:

$$\log Q = \log P + 1/2 \log(M/M_{\odot}) - 3/4 \log(L/L_{\odot}) + 3 \log(T/T_{\odot}),$$

where  $P$  is the period in days,  $M$  the mass,  $L$  the luminosity and  $T$  the effective temperature. Since we do not have data to estimate the masses, luminosities and effective temperatures for individual stars, we use these values of the isochrone shown in Fig. 5.7. The result is shown in Fig. 5.8 together with all the identified periods as a function of  $B$  magnitude. There the mode with the longest period in each star is plotted with large crosses, while the secondary modes with shorter periods are plotted with small diamonds.

In Fig. 5.8 it is seen that all stars have periods that are longer than the fundamental radial periods. We therefore identify all the stars as candidate SPB stars. Classification of the stars as bona fide SPB stars would require more time-series observations to ensure that the periods are correct and exclude other sources of variability, such as close binaries.

If there are  $\beta$  Cep stars in the cluster then we can assume two things about them; That they are generally brighter than the SPB stars and that they have periods shorter than the fundamental radial period. We do not detect any

pulsating stars in this domain than fulfill the detection criteria given in Section 5.3.1 and therefore we do not detect any candidate  $\beta$  Cep stars in NGC 371.

In order to constrain an upper detection limit of  $\beta$  Cep stars in the cluster we measured the highest peak in the amplitude spectrum between 8 and 20 c/d for all the stars brighter than 15.8 in  $B$ . A frequency range from 8 to 20 c/d is in agreement with the frequency range in which the  $\beta$  Cep stars are expected for this cluster (see Fig. 5.8). For the brightest stars we could also have included periods up to 0.4 day, but this gave problems with the  $1/f$  noise in the amplitude spectra of some of the stars.

In Fig. 5.9 we have plotted the amplitude of the highest peaks as a function of magnitude together with the mean  $V$  oscillation amplitude of galactic  $\beta$  Cep stars from Stankov & Handler (2005). It is seen that our detection limit is significantly lower than the mean  $V$  oscillation amplitude of galactic  $\beta$  Cep. If  $\beta$  Cep stars are present in the cluster they have oscillation amplitudes significantly lower than the galactic  $\beta$  Cep stars.

Though we do not detect any candidate  $\beta$  Cep stars some of the stars do show variability between 8 and 20 c/d, but not with a S/N higher than 4 in both filters. In Fig. 5.9 we have marked the peaks which have S/N higher than 3.5 in  $B$  and in Fig. 5.10 we have plotted the amplitude spectrum of one of them. The detection criteria of S/N higher than 4 in both filters is generally conservative and for longer regularly sampled data sets it is too high as the observations in the two filters are independent. But for the present data set it seems as a good indication of pulsation. More photometric data is needed in order to classify these stars as candidate  $\beta$  Cep stars. On the other hand if these stars are  $\beta$  Cep stars they would be very interesting targets as they would have shorter periods and lower oscillation amplitudes compared to the galactic  $\beta$  Cep stars.

Though periods below 0.1 day are not common in  $\beta$  Cep stars they have been seen in the very young cluster NGC 6231 (Balona & Shobbrook, 1983; Arentoft et al., 2001).

### 5.6.3 Amplitude Ratio and Phase Difference

We have also calculated and plotted the amplitude ratios and phase difference between the  $B$  and  $I$  filters (Fig. 5.11) in order to identify any systematic effects that could be compared with theoretical models as in Arentoft et al. (2007) or used for mode identification (Heynderickx et al., 1994). Though we do not find any systematic effects in phase difference versus amplitude ratio within the uncertainties (Fig. 5.11) we do see that the main part of the observed frequencies cluster around an amplitude ratio between 0.5 and 1.0 which is expected for oscillations in  $\beta$  Cep stars with degrees between 0 and 2 (Heynderickx et al., 1994).

The  $I/B$  amplitude ratio can also be used to exclude other causes of the variability than pulsation (e.g. ellipsoidal variables) as the  $I/B$  amplitude ratios are general below unity (see, e.g., Arentoft et al., 2007, and references therein).

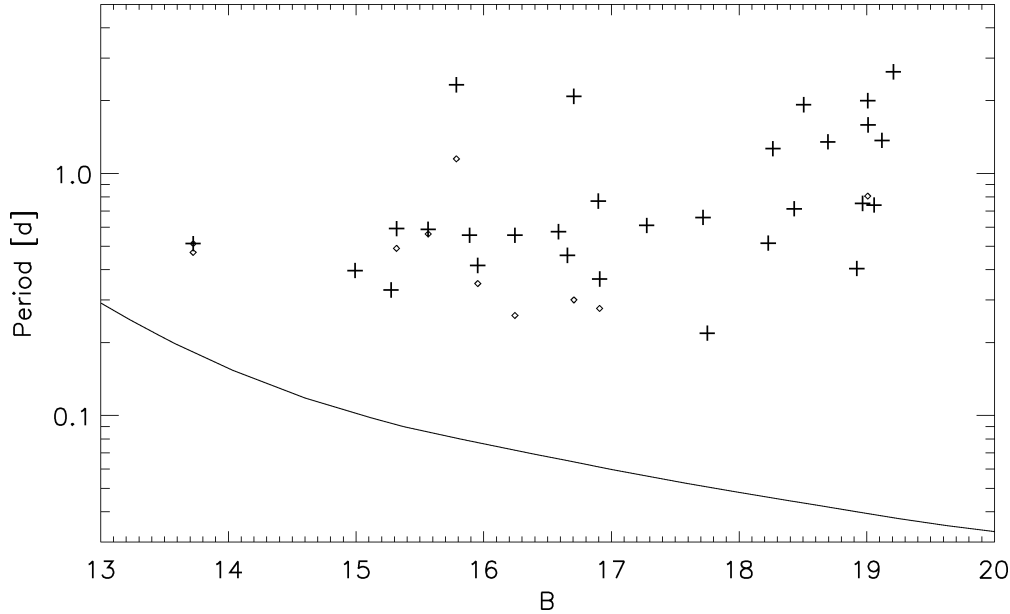


Figure 5.8: Magnitude-period relation for the candidate SPB stars together with the fundamental radial period from the isochrone. The mode with the longest period in each star is plotted with large crosses, while the secondary modes with shorter periods is plotted with small diamonds.

#### 5.6.4 Multimode Pulsation

The last thing to note about the frequencies is that all the multimode pulsators are found among the pulsating stars in the upper part of the main sequence (except for one). One reason for this could be that these stars are brighter, which in general gives a higher S/N, but some of the frequencies that we detect in the stars in the lower part of the main sequence have such a high amplitude that multimode pulsation should have been discovered if it was present (see Table 5.3).

## 5.7 Summary and Conclusions

We have identified 5 eclipsing binaries, 3 periodic Be stars and 29 candidate SPB stars in NGC 371.

The results indicates that excitation of oscillations in SPB stars is more common in low-metallicity environments such as the SMC than predicted by standard stellar models. A possible extension to the standard stellar models to account for this discrepancy could be to include local iron enhancement by diffusion and radiative accelerations (Miglio et al., 2007c).

If there are  $\beta$  Cep stars in the cluster they would generally be brighter than the SPB stars and have periods shorter than the fundamental radial period and we do not detect pulsation in any stars in this domain with an upper limit on the oscillation amplitudes of 5 mmag.

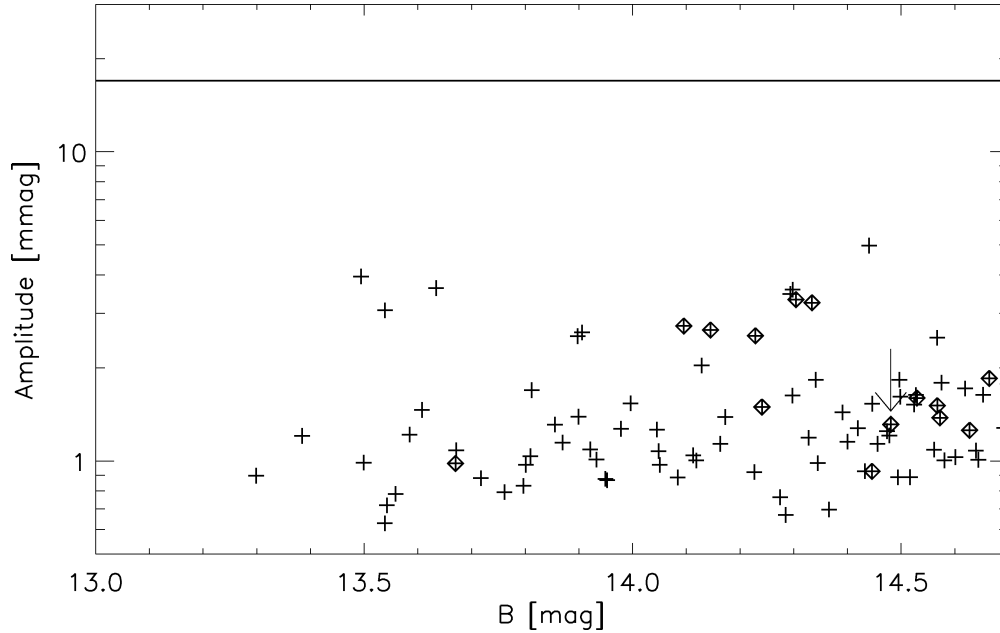


Figure 5.9: Amplitudes of the highest peak as a function of magnitude for the stars brighter than the identified candidate SPB stars. The diamonds mark the peaks with a S/N higher than 3.5. The horizontal line at 17 mmag shows the mean oscillation amplitude of  $\beta$  Cep stars in the Galaxy in  $V$ . The arrow marks the star plotted in Fig. 5.10.

Though it is not possible to calculate a reliable number for the fraction of SPB stars in NGC 371 the absolute number of pulsating stars seems to be high compared to the fraction obtained for the Galaxy by Stankov & Handler (2005).

We see evidence that multimode pulsation is more common in upper part of the main sequence than in the lower.

We have also identified periodic pulsation in 3 stars that were previously identified as Be stars. These stars can be used to study the relation between the Be phenomenon and  $\beta$  Cep and SPB stars in low-metallicity environments.

The results presented here strongly confirm and increase our interest in NGC 371 as an excellent laboratory for  $\beta$  Cep and SPB stars.

## Acknowledgments

We thank the referee Luis Balona for suggesting that we examined the fundamental radial periods of the stars, which helped to improve the paper significantly. We also thank Jørgen Christensen-Dalsgaard for useful suggestions. The Danish Natural Science Research Council and the Instrument Center for Danish Astrophysics (IDA) are acknowledged for financial support. C.K. and F.G. acknowledges financial support from IDA. C.K., T.A., G.D. and F.G. also acknowledges support from the Danish AsteroSeismology Centre.

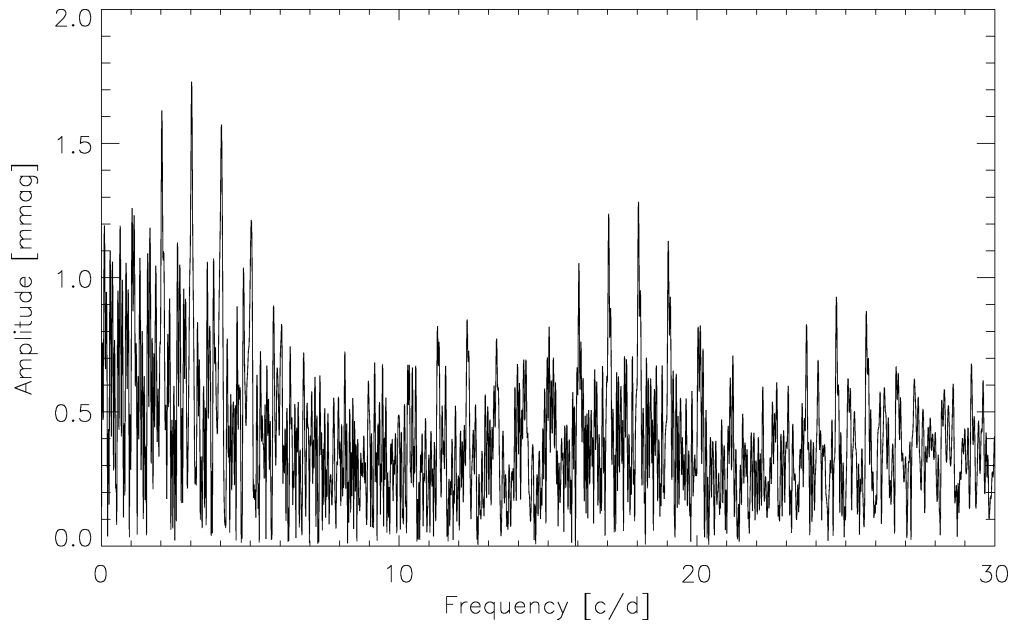


Figure 5.10: Amplitude spectrum in  $B$  of one of the stars showing signs of  $\beta$  Cep variability between 8 and 20 c/d with a S/N below 4.

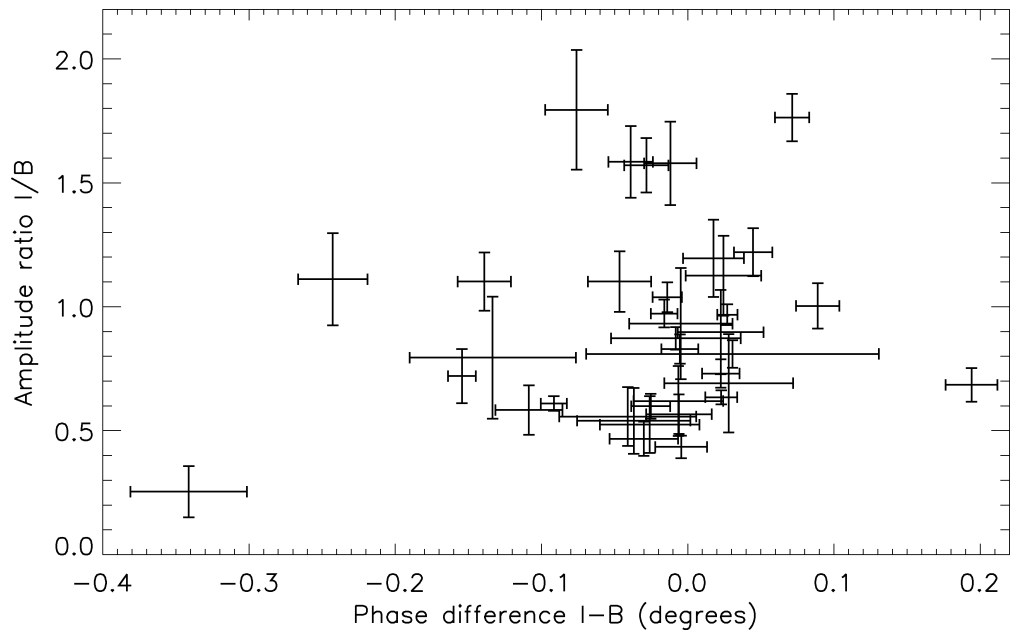


Figure 5.11: Phase difference  $I-B$  versus amplitude ratio  $I/B$  for the candidate SPB stars.



# Chapter 6

## Flare Driven Global Oscillations in the Sun

The paper *Evidence that solar flares drive global oscillations in the Sun* presented in this chapter has been published in:

Karoff & Kjeldsen (2008) Christoffer Karoff, & Hans Kjeldsen, 678, L73, ApJL, 2008

In 1972 Charles Wolff suggested that large solar flares could stimulate free modes of oscillation of the entire Sun, similar to the way the entire Earth is set ringing for several weeks after a major earthquake like the December 2004 Sumatra-Andaman earthquake. In the late seventies these free modes of oscillation of the entire Sun were discovered. The oscillations, which have periods of around 5 minutes, have later been known as p-mode oscillations, as their restoring force is pressure. By comparing observations of p-mode oscillations with theoretical solar models it appeared that the p-mode oscillations were excited by the turbulence in the near surface convection zone immediately beneath the photosphere and not by solar flares. 36 years later Karoff & Kjeldsen (2008) confirmed the original prediction by Wolff (1972). We show that the energy at high frequency in the solar acoustic spectrum is correlated with flares. This indicates that the high-frequency p-mode oscillations are not only excited by the near surface convection zone, but also by solar flares. The discovery was made by comparing frequency/time diagrams of data from the VIRGO instruments on *SOHO* with the solar X-ray flux measured by the *GOES* satellites, which is a good proxy for solar fares.

The discovery could help not just to increase our understanding of solar flares, but also of the solar cycle, which is not fully understood. The discovery might also give solar physicist a possibility to study how global oscillations in the Sun alter the Sun's structure and thus the flare-forming process; all things that could help solar physicist to predict solar activity, which is important in order to predict space weather and understand the effects that solar activity might have on the Earth.

The results in the paper were described in Nature News on 28 March 2008.



# Evidence that solar flares drive global oscillations in the Sun

Christoffer Karoff & Hans Kjeldsen\*

## Abstract

Solar flares are large explosions on the Sun's surface caused by a sudden release of magnetic energy. They are known to cause local short-lived oscillations travelling away from the explosion like water rings. Here we show that the energy in the solar acoustic spectrum is correlated with flares. This means that the flares drive global oscillations in the Sun in the same way that the entire Earth is set ringing for several weeks after a major earthquake such as the 2004 December Sumatra-Andaman one. The correlation between flares and energy in the acoustic spectrum of disk-integrated sunlight is stronger for high-frequency waves than for ordinary p modes which are excited by the turbulence in the near surface convection zone immediately beneath the photosphere.

## 6.1 Introduction

The global 5-minute p-modes oscillations of the Sun have in the last three decades provided us with valuable information about the physics inside the Sun. The oscillations are believed to be excited by the turbulence in the near surface convection zone immediately beneath the photosphere (Gough et al., 1996). Complete reflection is expected to take place only for oscillations with frequencies lower than the solar atmospheric acoustic cut-off (about 5.3 mHz). Oscillations with higher frequencies, which are seen in the Sun up to 9 mHz (sometimes known as high-frequency waves) are only partially reflected and have transmitted components, which propagate upward through the atmosphere (Balmforth & Gough, 1990). While models of near-surface convection can now explain the excitation and damping of the ordinary p modes no consensus has been reached about the details of what drives oscillations with frequencies larger than the acoustic cut-off frequency in the solar atmosphere. Different studies have proposed different models of the high-frequency waves (Balmforth & Gough, 1990; Kumar & Lu, 1991; Jain & Roberts, 1996), but none has explained all the features seen in the observations.

We have used data from the *SOHO* (*Solar and Heliospheric Observatory*) (Fröhlich et al., 1995) and the *GOES* (*Geostationary Operational Environmental Satellite*) (Garcia, 1994) satellites to show that there is a strong correlation

---

\*Department of Physics and Astronomy, University of Aarhus, Ny Munkegade, Building 1520, DK 8000 Aarhus C. E-mail: karoff@phys.au.dk.

between the energy at high frequency in the solar acoustic spectrum and the appearance of solar flares. The correlation suggests that the driving of the high-frequency waves is related to solar flares. Such a driving mechanism is well known from cases in which the entire Earth is set ringing for several weeks after a major earthquake such as the 2004 December Sumatra-Andaman one (Park et al., 2005). In fact it was shown already in 1972 that solar flares could excite free global oscillations in the Sun in the same way large earthquakes excite free global oscillation in the Earth (Wolff, 1972). Since then a few attempts have been made in order to find a correlation between the energy of the low-degree  $p$  modes and flares but none of them have been very successful (Gavryusev & Gavryuseva, 1999; Chaplin et al., 2004; Ambastha & Antia, 2006). Instead flares are found to cause local short-lived high-degree oscillations in the active regions in which they are produced (Kosovichev & Zharkova, 1998).

High-frequency waves were discovered in high-degree observations of the Sun (Libbrecht, 1988), but recently they have also been seen in disk-integrated data such as the BISON radial velocity data (Chaplin et al., 2003a), the GOLF radial velocity data (Jiménez et al., 2005) and the VIRGO intensity data (Jiménez et al., 2005). As the high-frequency waves have the highest S/N in intensity (Jiménez et al., 2005) we have chosen to focus on VIRGO data (green channel) in this study. Fig. 6.1 shows a power-density spectrum of the solar data. Here the high-frequency waves appear clearly from 5.3 mHz up to almost 8 mHz.

## 6.2 Frequency/Time Diagrams

We have calculated frequency/time diagrams of the integrated sunlight in order to evaluate the temporal behaviour of the high-frequency waves. This has been achieved by calculating power spectra of a number of running substrings of a long time series from the VIRGO instrument on SOHO. The power spectra were calculated as least-squares spectra (Lomb, 1976) in order to insure proper treatment of the gaps in the data. We tested different lengths of substrings and found 7.5 days to be the smallest length that we could use and still have enough S/N in the spectra to see the high-frequency waves clearly. In order to keep the rest of the analysis as simple as possible we calculated the spectra with a frequency resolution of  $1 \mu\text{Hz}$ . The power spectra were converted to power-density spectra by multiplying a given power spectrum with the effective length of a given substring, which we calculated as the reciprocal of the area under the spectral window (in power) of the substring (Kjeldsen et al., 2005).

Successive, overlapping substrings were displaced by 18 hr with respect to each other. The procedure yielded 4620 power spectra. The frequency/time diagrams can now be constructed by stacking the power spectra vertically, producing a power diagram with frequency varying along the horizontal axis and time on the vertical axis. In order to enhance the visibility the diagrams were smoothed by a Gaussian point-spread-function having widths of  $33 \mu\text{Hz}$  in frequency and 24 days in time. The widths were chosen to be as small as possible and still allow the structures of the high-frequency waves to appear as clear as possible.

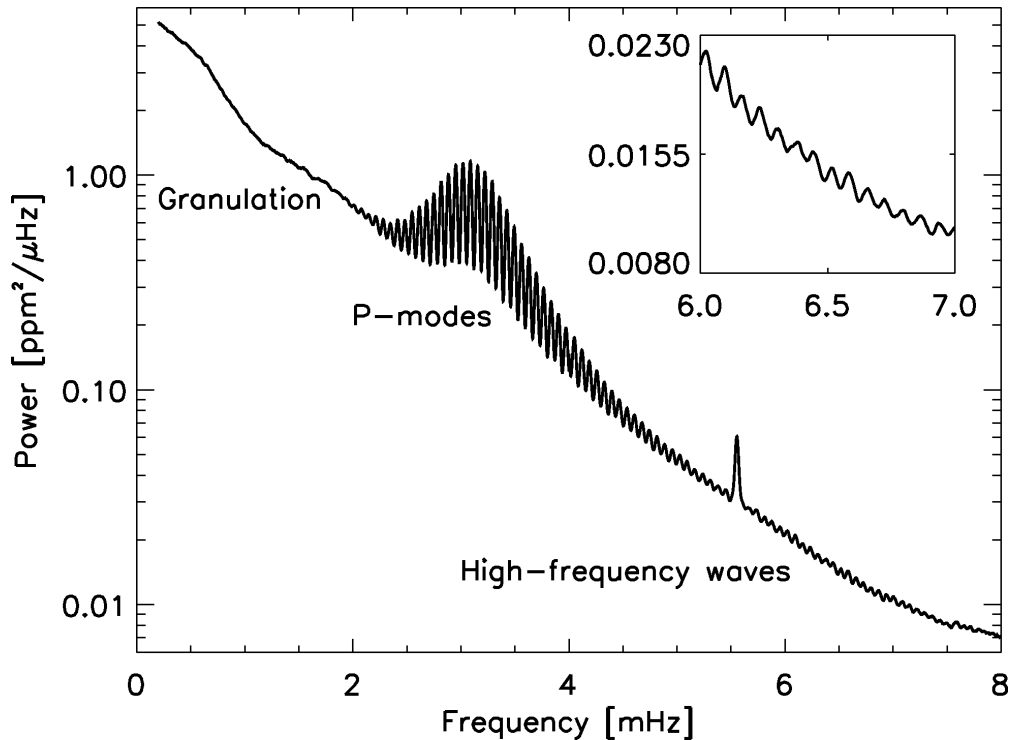


Figure 6.1: Smoothed power-density spectrum of the Sun. The spectrum consists of granulation noise (below 1.8 mHz), acoustic power from completely trapped p modes (between 1.8 and 5.3 mHz), and power from the high-frequency waves (with frequency higher than 5.3 mHz). The peak at 5.55 mHz is an artifact.

As the analyzed VIRGO data have a sampling of 60 s and thus a Nyquist frequency of 8.3 mHz we have chosen to calculate the power spectra up to 8 mHz. There are some gaps in the data set, mainly around the SOHO vacation in the summer of 1998, but when we smooth the diagram interpolation is made of these gaps by the Gaussian point-spread function. As we generally do not think that this interpolation is reliable we have remove the data in the gaps from Figs. 6.2 & 6.3.

The frequency/time diagrams in Fig. 6.2 exhibit a regular pattern of vertical bright lines at low frequency. These indicate the power in the ordinary p modes. But the pattern continues beyond 5.3 mHz, demonstrating that underlying mode structure is present also in the high-frequency waves. The frequency/time diagrams also show a pattern of horizontal lines. It is evident from the middle panel that this pattern is correlated with solar flares. The number and strength of the flares has been represented by the X-ray flux measured in the soft channel (1–8 Å) of the X-ray sensors on the GOES satellites (Garcia, 1994). The X-ray data have been smoothed with a Gaussian running mean of width 25 days in accord with the resolution of the oscillation data. The width was taken to be 25 rather than 24 days as the VIRGO data to some extent have been smoothed

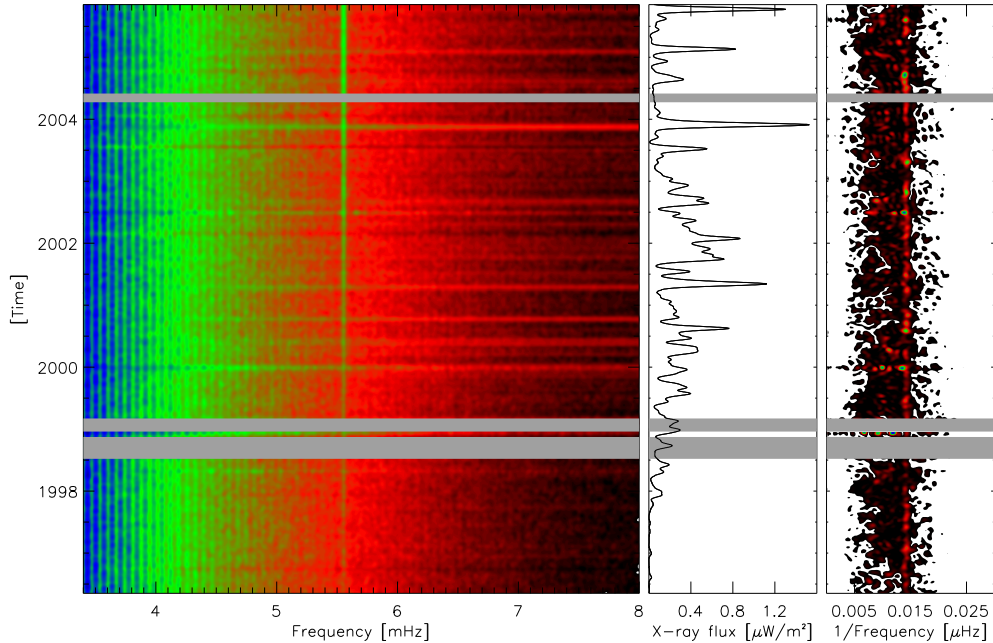


Figure 6.2: Smoothed frequency/time diagram of the Sun from disc-integrated data from the VIRGO instrument on SOHO is shown in the left panel. The clear vertical lines in the left of the image are the p-mode oscillations, and it is evident that these lines continue far beyond 5.3 mHz. The vertical line at 5.55 mHz is an instrumental artifact. The bright horizontal lines are strongly correlated with solar flares, represented by the X-ray flux in the middle panel. These lines are most prominent in the high-frequency region of the spectrum. The right panel shows the amplitude spectra of the individual power-density spectra in the left panel, with a bright line at the frequency separation of the high-frequency waves of  $0.014 \mu\text{Hz}^{-1}$  ( $70 \mu\text{Hz}$ ). The gray regions mark times with no data from SOHO. The color scale is logarithmic.

twice, first by calculating a power spectrum of a substring of length 7.5 days and second by smoothing with a Gaussian point-spread-function of width 24 days in the vertical direction.

### 6.3 Correlation at Different Frequencies

In order to analyze how flares correlate with oscillations at different frequencies we have compared the variation of the total power within  $20 \mu\text{Hz}$  of three different modes (at 3.22, 5.24 and 7.22 mHz). It is seen in Fig. 6.3 that the correlation is strongest for the high-frequency oscillations at 7.22 mHz; at 5.24 the correlation is much weaker and at 3.22 the dominant feature is the well-known slow variation of the dynamo (Chaplin et al., 2003b, and references herein). All three modes have higher power density around 2006 than around 1996, although the power is expected to be the same as both times are close to solar

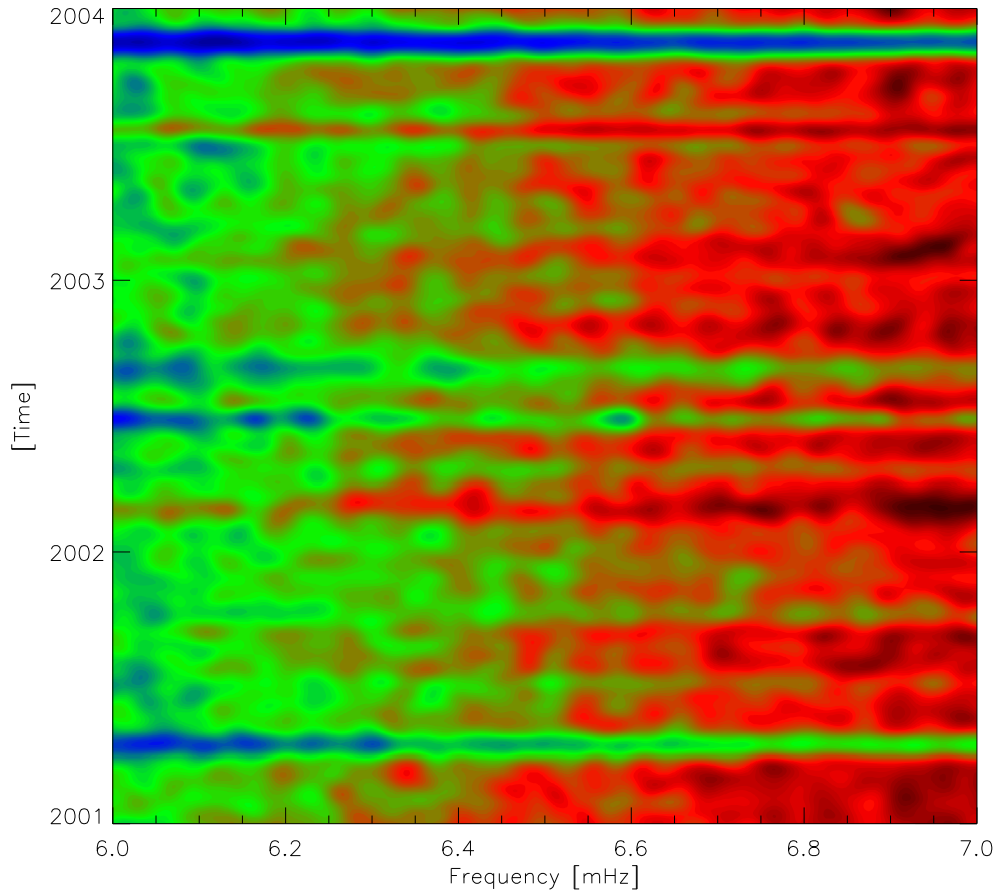


Figure 6.3: A zoom in on Fig. 6.2 where the regularity of the high-frequency waves appears more clearly.

minimum. This trend is also seen in the X-ray flux (the mean power density is higher between 2004 and 2006 than between 1996 and 1998), but as the trend is monochromic increasing it could be an instrumental effect. However, we do not know of such an effect in the instrument.

In Fig. 6.4 we show the general correlation between the power density and X-ray flux independent of the individual modes. In order not to have the correlation dominated by the long period trends we have subtracted a Gaussian running mean with a width of 2 years from both the power density and the X-ray flux. Fig. 6.4 shows that the temporal behavior of the power-density spectrum is more correlated with the temporal behavior of X-ray flares at high frequency than at low frequency.

We do not know the exact excitation mechanism for p modes being excited by flares, however two possible effects may be considered in order to explain and understand the behavior of the high-frequency p-mode power. First of all the observed power of p modes at high-frequency is significantly lower than the power per mode observed at the peak (3 mHz). According to Stein & Nordlund

(2001) one finds the p-mode power to decrease inversely to the fourth power of the frequency (above 3 mHz) simply as a consequence of the granulation power decreasing as  $\nu^{-4}$ . Therefore a single event (such as a flare) that excites a mode will have a larger relative effect at high frequencies because the other excitation sources are much smaller. Related to this one should also note that the high-frequency background (between p modes) shows an increased correlation with flare activity. One may therefore argue that the background noise from granulation correlates with flare activity (as clearly seen in Figs. 6.2 and 6.5) and the increased background transfers more power into the high-frequency modes via the stochastic excitation, which is exactly what is observed. At frequencies around 3 mHz one do not find the background to correlate as strongly (see Fig. 6.5) as at higher frequencies (5–7 mHz).

This may explain why attempts to see a correlation between the energy of the ordinary p modes and flares have not been very successful (Gavryusev & Gavryuseva, 1999; Chaplin et al., 2004; Ambastha & Antia, 2006). Fig. 6.4 shows a steady climb of correlation over the acoustic cut-off frequency, not a sudden jump. This is in agreement with what we expect as the reflectivity of the solar atmosphere is expected to decrease continuously over the acoustic cut-off frequency.

## 6.4 Correlation at High Frequency

The acoustic spectrum contains two parts at high frequency: a background and the acoustic waves. In order to separate these two parts we have performed the same analysis as performed by Jiménez et al. (2005) and calculated amplitude spectra of the individual power-density spectra in the frequency/time diagram. The exponential decay of the power-density spectra were removed before these amplitude spectra were calculated as done by Jiménez et al. (2005). The amplitude spectra as a function of time are shown in the right panel of Fig. 6.2. It is seen that the frequency separation of the high-frequency waves remains constant at 70  $\mu$ Hz throughout the observation independent of solar flares.

## 6.5 Discussion

The correlation we see between the power density of high-frequency wave and the flares is similar to what one would expect from a comet impact. This case was analyzed for the Shoemaker-Levy impact on Jupiter by Gough (1994). In that paper it was also noted that such impacts on the Sun would have the largest response in the high-frequency domain. The discovery presented here will improve our understanding of the flares. An advance here will be provided by the asteroseismic data that we will receive from the *KEPLER* satellite (Borucki et al., 2003). High-frequency waves have been detected in asteroseismic data of the solar-like stars  $\beta$  Hydri and  $\alpha$  Cen A and B (Karoff, 2007), and with the *KEPLER* data we should be able to observe the time variation of the amplitudes of such waves in a large number of solar-like stars,

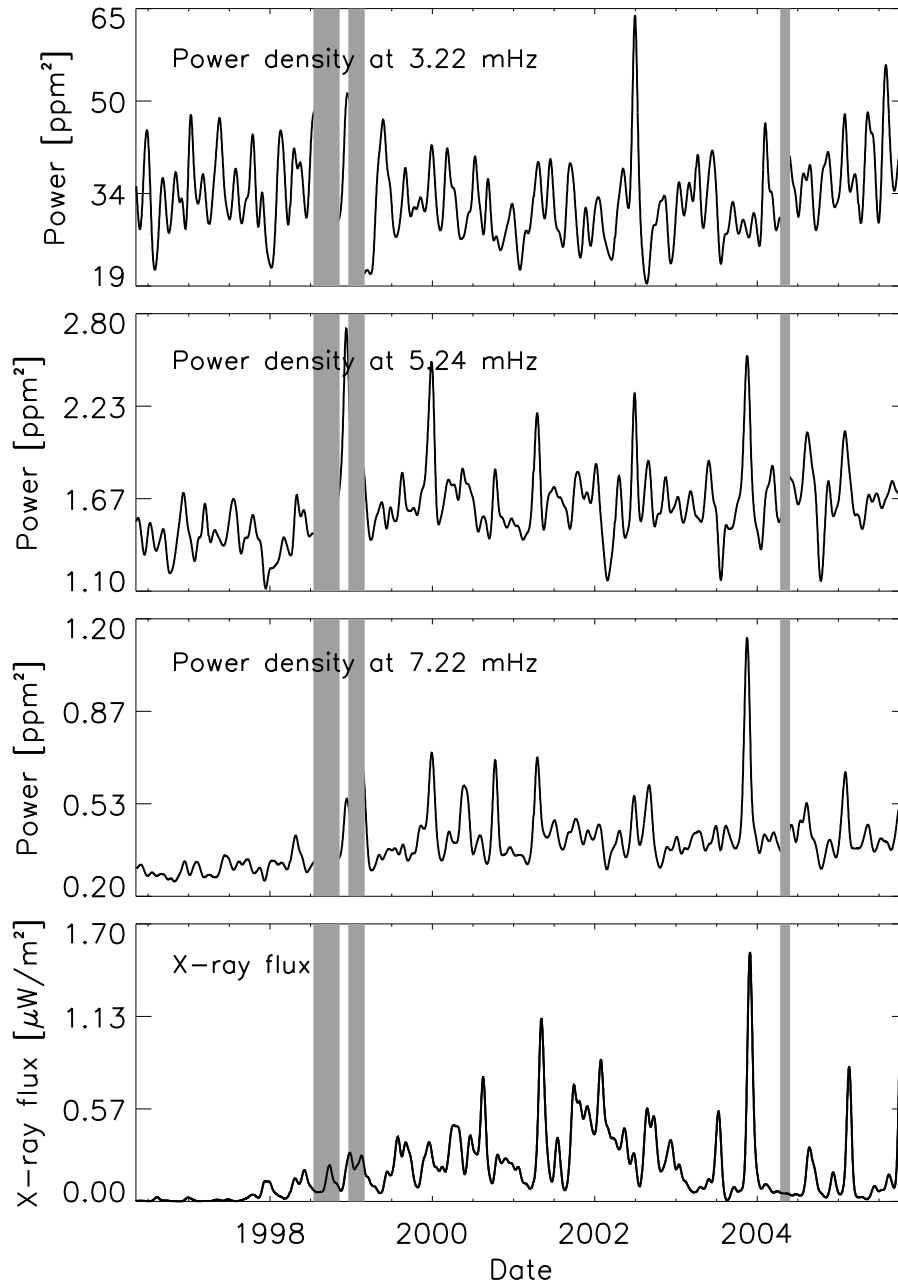


Figure 6.4: The X-ray flux from the Sun (lower panel), total power of the mode at 7.22 mHz (second panel), at 5.24 mHz (third panel) and at 3.22 mHz (top panel). It is evident that the correlation between the total power of the modes and the X-ray flux increases with increasing frequency. The slow change of the total power of the mode at 3.22 mHz is a result for the solar dynamo (Chaplin et al., 2003b, and references herein).

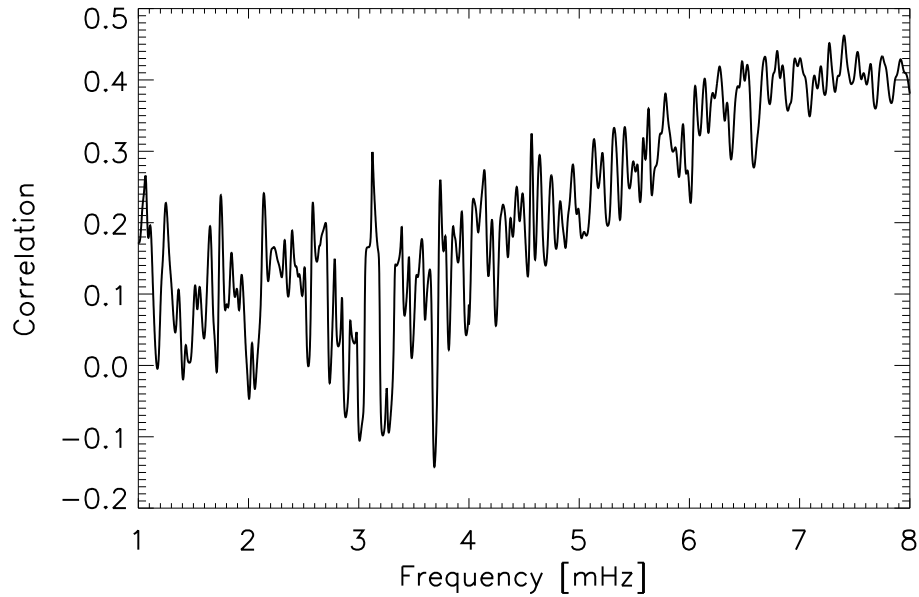


Figure 6.5: Correlation between the power density and the X-ray flux from the Sun as a function of frequency.

perhaps suggesting the presence of flares in those stars. The last outcome could aid our understanding of stellar dynamos.

## Acknowledgements

The authors would like to thank D.O. Gough, J. Christensen-Dalsgaard, T. Bedding and T. Arentoft for comments. The authors acknowledge use of computing resources from the Danish Center for Scientific Computing. CK acknowledges support from the Danish AsteroSeismology Centre and the Instrument Center for Danish Astrophysics. SOHO is a mission of international cooperation between the European Space Agency and NASA. The National Oceanic and Atmospheric Administration operates

# Chapter 7

## High-frequency Modes in Solar-like Stars

The paper *High-frequency modes in solar-like stars* presented in this chapter has been published in:

Karoff (2007) Christoffer Karoff, MNRAS, 381, 1001, 2007

The paper presents the first detection of oscillations with frequencies higher than the atmospheric acoustic cut-off frequency in stars other than the Sun (three Sun-like stars). As the high-frequency modes are believed to be travelling waves in the stellar atmospheres, they have the potential to provide us with knowledge of these atmospheres, i.e. the locations of the acoustic source(s) and the temperature/sound speed profile in these atmospheres.



# High-frequency modes in solar-like stars

Christoffer Karoff\*

## Abstract

p-mode oscillations in solar-like stars are excited by the outer convection zone in these stars and reflected close to the surface. The p modes are trapped inside an acoustic cavity, but the modes only stay trapped up to a given frequency [known as the acoustic cut-off frequency ( $\nu_{ac}$ )] as modes with larger frequencies are generally not reflected at the surface. This means that modes with frequency larger than the acoustic cut-off frequency must be travelling waves. The high-frequency modes may provide information about the physics in the outer layers of the stars and the excitation source and are therefore highly interesting as it is the estimation of these two phenomena that cause some of the largest uncertainties when calculating stellar oscillations.

High-frequency modes have been detected in the Sun, in  $\beta$  Hydri and in  $\alpha$  Cen A and  $\alpha$  Cen B by smoothing the so-called echelle diagram and the large frequency separation as a function of frequency has been estimated. The large frequency separation has been compared with a simple model of the acoustic cavity which suggests that the reflectivity of the photosphere is larger at high frequency than predicted by standard models of the solar atmosphere and that the depth of the excitation source is larger than what has been estimated by other models and might depend on the order  $n$  and degree  $l$  of the modes.

## 7.1 Introduction

Since the first observations of oscillations with frequency above the acoustic cut-off frequency in the Sun (Jefferies et al., 1988; Libbrecht, 1988), different suggestions have been made to locate the nature of these high-frequency modes – known as ‘*mock modes*’ (Kumar et al., 1990), ‘*high-frequency interference peaks*’ (Kumar & Lu, 1991), ‘*pseudo-modes*’ (Roxburgh & Vorontsov, 1995), but the physics behind high-frequency modes is still not clearly understood.

The standard way to obtain a model of the high-frequency modes is to consider a one-dimensional wave equation (Balmforth & Gough, 1990; Kumar et al., 1994):

$$\frac{d^2\psi}{dr^2} + \left[ \frac{\nu^2}{c^2} - V(r) \right] \psi = 0, \quad (7.1)$$

---

\*Department of Physics and Astronomy, University of Aarhus, Ny Munkegade, Building 1520, DK 8000 Aarhus C. E-mail: karoff@phys.au.dk.

where  $\psi$  is the wavefunction and  $V(r)$  is the acoustic potential. A number of studies have used this equation to make a model of the high-frequency modes. Generally, the studies fall in two different categories. Either an excitation source is included on the right-hand

$$\frac{d^2\psi}{dr^2} + \left[ \frac{\nu^2}{c^2} - V(r) \right] \psi = \delta(r - r_0), \quad (7.2)$$

and the acoustic potential is characterized by a step function (Kumar & Lu, 1991; Abrams & Kumar, 1996) or the excitation source is not included, but instead a more realistic model is used for the acoustic potential which includes reflection of the modes at the chromosphere-corona transition (Balmforth & Gough, 1990; Dzhililov et al., 2000). Using these models, different studies have been able to set constraints on the location of the excitation source (Kumar & Lu, 1991), the coronal reflection (Kumar et al., 1994), the solar atmosphere (Dzhililov et al., 2000), the acoustic cut-off frequency (Jiménez, 2006) and give possible explanations of the asymmetries of the line profiles (Roxburgh & Vorontsov, 1995; Abrams & Kumar, 1996).

A third model for the high-frequency modes has been suggested by Jain & Roberts (1996). Here is the reflection of high-frequency modes in the atmosphere caused by a horizontal magnetic field in the chromosphere with an Alfvén speed that is a few magnitudes larger than the sound speed in the low chromosphere. Though this model is able to explain the frequency shifts observed at medium and high degrees, it fails at low degrees where the frequency shifts predicted by the model vanish (Jain & Roberts, 1996) and therefore it is not investigated in this paper, as it will take decades before we can observe medium- and high-degree modes in solar-like stars.

Solar-like oscillations have within recent years been observed in a number of solar-like stars (see Bedding & Kjeldsen, 2006b, for a recent review) and the first signs of high-frequency modes have been reported by Kjeldsen et al. (2005). Compared to observations of high-frequency modes in the Sun, observations in solar-like stars have the disadvantages that the data have a lower signal-to-noise ratio (S/N) and that it is only possible to observe low-degree modes as it is only possible to perform disc-integrated observations of the solar-like stars. Due to the low S/N it is not possible to try to fit a model to the power spectrum or the phase shifts as has been done for the Sun (see e.g. Kumar & Lu, 1991; Kumar, 1994; Jiménez, 2006). Instead the frequency shifts can be used as an input for the models as they can be obtained even at a low S/N.

Kjeldsen et al. (2005) were the first to observe signs of high-frequency modes in another solar-like star – that is,  $\alpha$  Cen B. This was done by smoothing the power spectrum two times with box averages with different widths. In this way, Kjeldsen et al. (2005) could measure the large separation of  $\alpha$  Cen B up to 7 mHz.

High-frequency modes can prove to be very substantial for modelling oscillations in solar-like stars. The reason for this is that high-frequency modes will be more affected by the structure in the surface layer of the star than modes in the ordinary p-mode regime (Christensen-Dalsgaard et al., 1988). Therefore,

Table 7.1: Stellar parameters. Ref 1: Balmforth & Gough (1990) , Ref 2: Di Mauro et al. (2003), Ref 3: Miglio & Montalbán (2005)

Star	M/M <sub>⊙</sub>	R/R <sub>⊙</sub>	T <sub>eff</sub>	$\nu_{ac}$	$\Delta\nu$	Ref.
Sun	1.00	1.00	5777 K	5.3 mHz	135 $\mu$ Hz	1
$\beta$ Hydri	1.14	2.00	5860 K	2.0 mHz	58 $\mu$ Hz	2
$\alpha$ Cen A	1.11	1.22	5810 K	4.0 mHz	107 $\mu$ Hz	3
$\alpha$ Cen B	0.93	0.86	5260 K	6.8 mHz	162 $\mu$ Hz	3

high-frequency modes have the possibility to provide valuable information of these surface layers – for example, sound speed and density profiles in the outer layers. This would be highly valuable to asteroseismology of solar-like stars in general as improper modelling of the surface layers is believed to cause the largest uncertainties in the frequencies of the ordinary p modes (Christensen-Dalsgaard et al., 1988).

Following Kjeldsen et al. (2005) high-frequency modes have been observed in the Sun, in  $\beta$  Hydri and in  $\alpha$  Cen A and  $\alpha$  Cen B by smoothing the power spectrum, but this smoothing has been done in the echelle diagram of the power spectrum instead of in the power spectrum itself.

This paper is arranged as follows. In Section 7.2, the observations used in this paper are discussed as well as the different noise level of the observations. Section 7.3 presents a detailed analysis of the high-frequency modes in the different stars. A description of and comparison to a simple theoretical model is presented in Section 7.4 and concluding remarks are found in Section 7.5.

## 7.2 Data

Four different stars have been analysed in this study. The stars are the Sun,  $\beta$  Hydri and  $\alpha$  Cen A and  $\alpha$  Cen B. For all the four stars the measurements are made from disc-integrated velocity observations.

### 7.2.1 The Sun

This data set is a 805-d series of full-disc velocity observations taken by the Global Oscillations at Low Frequencies (GOLF) instrument on the Solar and Heliospheric Observatory (SOHO) spacecraft (Ulrich et al., 2000; García et al., 2005). The data set has been calibrated as described in García et al. (2005) (The data set is obtained from <http://golfwww.medoc-ias.u-psud.fr/access.html>.) After removing all zero measurements, the noise level in the amplitude spectrum is 0.95 mm s<sup>-1</sup> ! The data set consists of 3477600 non-zero measurements with a sampling of 20 s. This gives a Nyquist frequency of  $\nu_{NY} = \frac{1}{2\delta t} = 25.000$   $\mu$ Hz and a frequency resolution of  $\delta\nu = \frac{1.5}{\Delta T} = 0.02$   $\mu$ Hz (Loumos & Deeming, 1978).

According to Nigam & Kosovichev (1999), high-frequency modes are expected to have a higher S/N in photometry than in velocity, but as only veloc-

ity data are available for the three solar-like stars we have chosen also to use velocity data for the Sun.

### 7.2.2 $\beta$ Hydri

$\beta$  Hydri was observed in 2005 September at the European Southern Observatory in Chile with the use of the High Accuracy Radial velocity Planet Searcher (HARPS) at the La Silla 3.6-m telescope and at the Siding Spring Observatory in Australia with the use of the University College London Echelle Spectrograph (UCLES) at the 3.9-m Anglo-Australian Telescope (AAT) (Bedding et al., 2007). The data set consists of 3957 measurements and the weights have been manipulated in order to downweigh bad data points thereby increasing the S/N in the power spectrum as described by Butler et al. (2004). This has caused a noise level of  $3.2 \text{ cm s}^{-1}$  in the amplitude spectrum at high frequencies.

The Nyquist frequency and the frequency resolution are not well defined for irregular sampled observations (Eyer & Bartholdi, 1999). We have evaluated the Nyquist frequency from a histogram of the time-intervals as in (Eyer & Bartholdi, 1999) and obtained a Nyquist frequency of  $7200 \mu\text{Hz}$ . The frequency resolution was calculated as the full width at half-maximum (FWHM) of the central peak in the window function to  $1.5 \mu\text{Hz}$ .

Here, we have only looked at frequencies below  $2800 \mu\text{Hz}$  as the HARPS data contain a large artificial peak at  $3070 \mu\text{Hz}$  that is due to a periodic error in the guiding system (Bazot et al., 2007).

### 7.2.3 $\alpha$ Cen A

$\alpha$  Cen A was observed in 2001 May with the UV-Visual Echelle Spectrograph (UVES) at the 8.2-m Unit Telescope 2 of the Very Large Telescope (VLT) and UCLES at AAT (Butler et al., 2004). The weights have also been manipulated in this data set and a noise level of  $1.9 \text{ cm s}^{-1}$  has been obtained at high frequencies in the amplitude spectrum. The data set contains 8182 measurements and we obtain a Nyquist frequency of  $26000 \mu\text{Hz}$  and a frequency resolution of  $3.8 \mu\text{Hz}$ .

### 7.2.4 $\alpha$ Cen B

$\alpha$  Cen B was observed in 2003 May with UVES at VLT and UCLES at AAT (Kjeldsen et al., 2005). By manipulating the weights, a noise level of  $1.3 \text{ cm s}^{-1}$  was obtained in the amplitude spectrum at high frequencies. Kjeldsen et al. (2005) were also the first to report signs of high-frequency modes in a solar-like star other than the Sun. The data set contains 5021 measurements and we obtain a Nyquist frequency of  $18000 \mu\text{Hz}$  and a frequency resolution of  $1.6 \mu\text{Hz}$ .

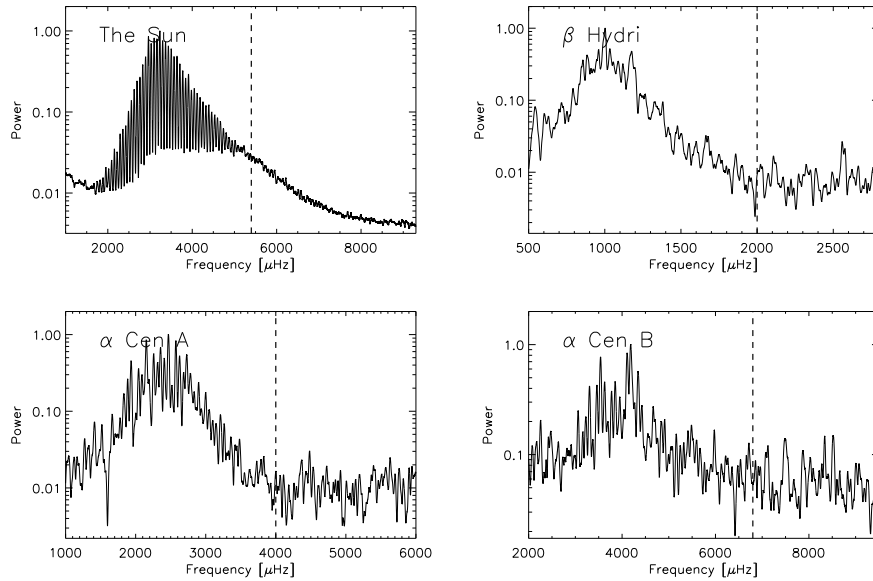


Figure 7.1: Smoothed power spectrum for the Sun,  $\beta$  Hydri,  $\alpha$  Cen A and  $\alpha$  Cen B. All the power spectras have been smoothed with a Gaussian running mean with at width equal to the large separation of the given stars (values are listed in Table 7.1) and normalized to 1 for the highest peak. The dotted lines shown the theoretical calculated acoustic cut-off frequency.

### 7.3 Data Analysis

The power spectra of the four data sets were calculated as a weighted least-squares power spectrum (Lomb 1976; Frandsen et al. 1995). In order to see the high-frequency modes, the four power spectra have been smoothed with a Gaussian running mean, with a width equal to the large separation of the given star (values are listed in Table 7.1). The smoothed power spectra which have all been normalized by setting the highest peak equal to 1 are shown in Fig. 7.1.

In order to quantify when peaks can be associated to high-frequency modes, the acoustic cut-off frequency  $\nu_{ac}$  has been calculated following Kjeldsen & Bedding (1995), and assuming that the derivative of the density scale height is small,  $\nu_{ac}$  will scale as  $c/H$ , where  $c$  is the sound speed and  $H$  is the density scale height expected to scale as  $T/g$ . In this way,  $\nu_{ac}$  is estimated as

$$\nu_{ac} \propto \frac{M}{R^2 \sqrt{T}}, \quad (7.3)$$

where  $M$  is the stellar mass,  $R$  is the radius and  $T$  is the temperature. The acoustic cut-off frequency of the Sun is 5.3 mHz (Balmforth & Gough, 1990). The theoretical calculated acoustic cut-off frequency of the other solar-like stars as well as the mass, radius, effective temperature and large separation is shown in Table 7.1 and marked in Figs 7.1 – 7.4.

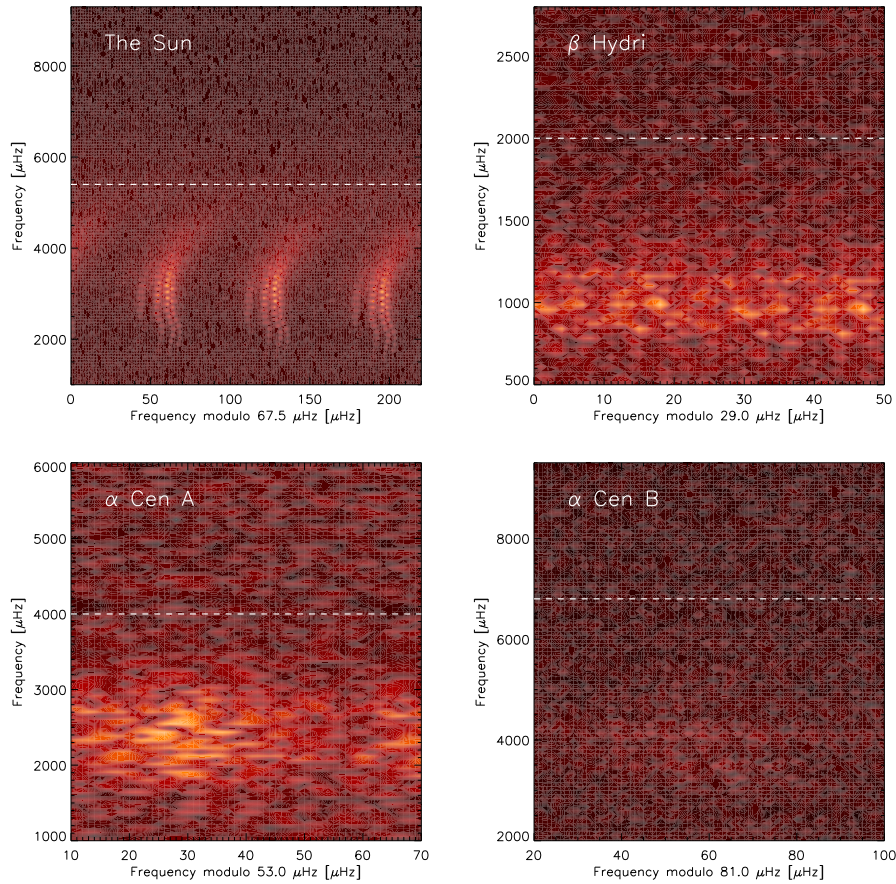


Figure 7.2: Echelle diagram for the Sun,  $\beta$  Hydri,  $\alpha$  Cen A and  $\alpha$  Cen B. The echelle diagrams are made by folding the power spectra with half the large separation. The dotted lines shown the theoretical calculated acoustic cut-off frequency.

Just by looking at the power spectrum in Fig. 7.1 the high-frequency modes are visible in the Sun and to some extent in  $\alpha$  Cen B, but not in  $\alpha$  Cen A and  $\beta$  Hydri.

The visibility of the high-frequency modes increases significantly by averaging a number of power spectra calculated from a number of subsamples of the total time-series (see Jiménez, 2006; García et al., 1998). Though the subsamples can be as short as a few days, it has not been possible to perform this kind of analysis on the three solar-like stars as the entire time-series is needed in order to get high enough S/Ns. We have therefore analysed the high-frequency modes in the echelle diagrams as this kind of analysis could be performed on all four data sets.

The echelle diagrams of half the large separation are produced simply by folding the power spectra with half the large separation as it is shown in Fig. 7.2. The large separations that were used were: Sun – 135  $\mu$ Hz (Kjeldsen et al.,

2005),  $\beta$  Hydri – 58  $\mu\text{Hz}$  (Bedding et al., 2007),  $\alpha$  Cen A – 106  $\mu\text{Hz}$  (Butler et al., 2004) and  $\alpha$  Cen B – 162  $\mu\text{Hz}$  (Kjeldsen et al., 2005).

The reason to produce the echelle diagram for the half large separation is that this will cause the odd and even  $l$  modes to line up in the echelle diagram.

$p$  modes can be found in the echelle diagram where they will line up in vertical lines as the  $p$  modes fulfill the asymptotic relation. In this way  $p$  modes are clearly seen in the echelle diagram for the Sun (Fig. 7.2). The visibility of the  $p$  modes is low for  $\alpha$  Cen A and they are not visible in the echelle diagram for  $\alpha$  Cen B and  $\beta$  Hydri (Fig. 7.2). The low visibility is caused by a relatively low S/N for the  $p$  modes in these stars. In order to see the high-frequency modes, the echelle diagrams have been smoothed with a Gaussian point spread function (PSF). This is a technique that is well known from image manipulation – one increases the contrast in an image by defocusing it. By smoothing the echelle diagrams, the resolution gets lower, but the contrast gets higher. This means that it is not possible to see small frequency separations as, for example, rotation splitting in the smoothed echelle diagrams. Instead it is possible to see structures at low S/Ns as, for example, the high-frequency modes.

The same Gaussian PSF has been used for smoothing all four data sets:

$$PSF(x, x_0, y, y_0) = e^{-\left(\frac{x-x_0}{a}\right)^2 - \left(\frac{y-y_0}{b}\right)^2}, \quad (7.4)$$

where  $a$  and  $b$  are constants that have been set to  $a = \Delta\nu/16$  and  $b = 8$  echelle orders. (The expression ‘echelle order’ refers to one horizontal line in the echelle diagram of the half large separation.) The values of  $a$  and  $b$  were optimized in order to get the highest S/N for the high-frequency modes. Small changes to  $a$  and  $b$  did not change the behaviour of the large frequency separation as a function of frequency.

In order to find peaks in the smoothed echelle diagrams, the same analysis has been applied to all the four data sets. Each echelle order has been normalized by the minimum value in the echelle order. This means that the colour code in Fig. 7.3 gives the S/N in the given echelle order. In this way, it is also possible to see structure in the echelle diagram at high frequencies and, on the other hand, it is possible to see if almost no structure exists – as is the case for the Sun at high frequencies.

The peak amplitude in each echelle order has been found by taking the centroid (centre-of-energy) in a segment of length 40  $\mu\text{Hz}$ . The peaks are easily found in the ordinary  $p$ -mode regime. The peaks in a higher echelle order are found by placing the middle of the segment where the peak was identified in the echelle order just below. This method is free of any individual analysis of the data sets. The peaks found at low frequencies are not reliable, because of the smoothing of the echelle diagram. When the power spectrum is folded with half the large separation, it is assumed that  $l = 0 - 3$  modes fall on top of each other and this is not the case at low frequencies. This is clearly seen in the echelle diagram of the Sun in Fig. 7.2. This means that the method outlined here cannot be used for identifying peaks in the echelle diagram at frequencies lower than the region of the ordinary  $p$  modes, which is anyway not the subject of this paper.

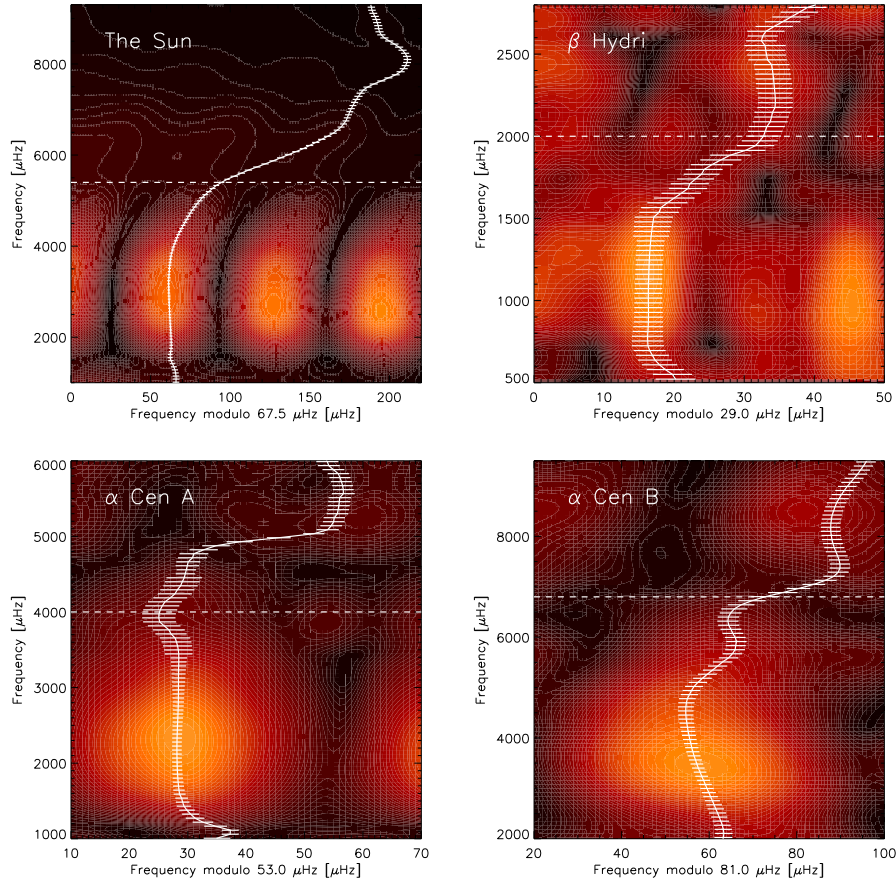


Figure 7.3: PSF folded echelle diagram for the Sun,  $\beta$  Hydri,  $\alpha$  Cen A and  $\alpha$  Cen B. The solid line marks the obtained trend in the echelle diagram which is used for calculating the large separation. The uncertainties are calculated as described in the text. The dotted lines shown the theoretical calculated acoustic cut-off frequency.

Some of the p modes are seen twice in Fig. 7.3 as the range is larger than  $\Delta\nu/2$  on the horizontal axis. This means that p modes are seen more than once in each echelle order. As the peaks move to higher frequencies for higher echelle orders, peaks from the lower echelle order will start appearing in the left-hand side of the images.

The uncertainties have been estimated as

$$\sigma = \sqrt{\frac{N/S\Gamma}{4\pi}}, \quad (7.5)$$

where  $\sigma$  is the uncertainty and  $\Gamma$  is the FWHM of the peak. Though this formulation must be considered as empirical, it is based on the discussion in Libbrecht (1992). An analytical formulation of the uncertainties is not trivial as the power spectra have been folded with a PSF.

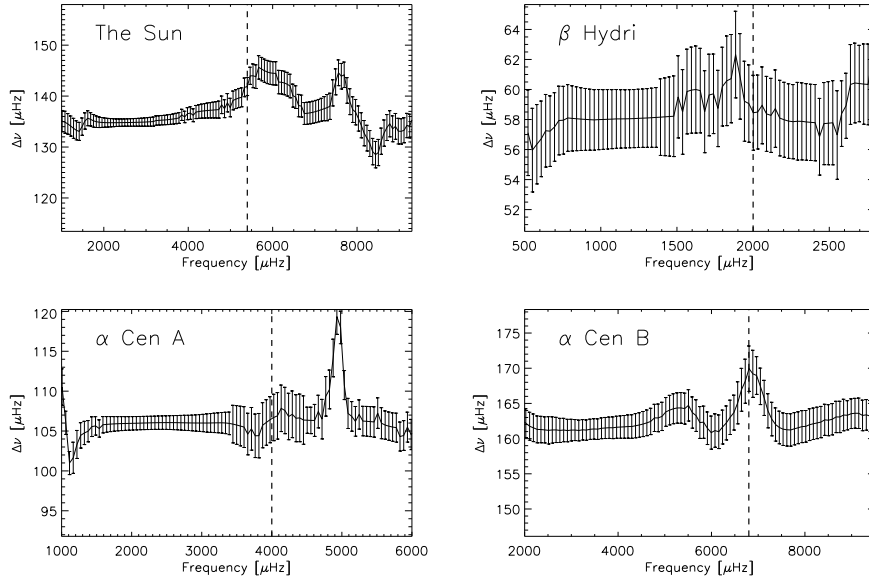


Figure 7.4: The large separation as a function of frequency for the Sun,  $\beta$  Hydri,  $\alpha$  Cen A and  $\alpha$  Cen B. The dotted lines show the theoretical calculated acoustic cut-off frequency.

$\Delta\nu$  for the four stars has been calculated by taking the difference between two peaks in the echelle diagram and multiplying it by 2. Fig. 7.4 shows  $\Delta\nu$  as a function of frequency for the four stars. Here, it is clearly seen that the large separations increase dramatically for frequencies just above the acoustical cut-off frequency. One exception here might be  $\beta$  Hydri where the increase is not significantly within the uncertainties.  $\beta$  Hydri is significantly larger than the other stars; therefore, the peak amplitude of the p modes appears at lower frequency than for the other stars, which might explain why the large separation as a function of frequency is different for  $\beta$  Hydri from the other stars.

## 7.4 Theory

Below we will now compare the observed high-frequency modes to the model developed by Vorontsov et al. (1998). This model is a simplified version of the models analysed by Kumar & Lu (1991); Abrams & Kumar (1996) and Roxburgh & Vorontsov (1995) which means that it shows the same basis features in the power spectrum, but it allows an evaluation of which basis parameters can be extracted from the high-frequency modes. The model consists of a harmonic wave emitted from a source just below the photosphere that suffers multiple reflections at the stellar surface. The observed power spectrum of this simple model is

$$|\psi|^2 = \frac{2 \pm 2\cos(4\pi\nu T_s)}{1 + R(\nu)^2 - 2R(\nu)\cos(4\pi\nu T)}, \quad (7.6)$$

where  $T$  is the acoustic depth of the acoustic cavity,  $T_s$  is acoustic distance between the lower reflection point and the source ( $\Delta T = T - T_s$  equals the acoustic distance from the source to the upper reflection point) and  $R(\nu)$  is the reflection coefficient as a function of frequency. If the source is a monopole, then the sign in the numerator will be a plus sign and a minus for a dipole source.

The reflection coefficient depends on the acoustic potential which can be approximated with a parabolic profile (see Vorontsov et al., 1998, and references herein). This gives a reflection coefficient as a function of frequency as:

$$R(\nu) = \frac{1}{1 + \exp[(\nu^2 - \nu_{ac}^2)/\nu_0^2]}, \quad (7.7)$$

where  $\nu_{ac}$  is the frequency of the maximum value in the parabolic potential profile (roughly equal to the acoustic cut-off frequency) and  $\nu_0$  determines the width of the parabolic barrier.

The free parameters in the model are:  $\Delta T$ , and  $\nu_0$  – that is, the position of the excitation source and the reflection coefficient in the outer layers of the star. The two parameters  $T$  and  $\nu_{ac}$  are not considered as free parameters as observations of ordinary p modes can set relatively tight constraints on these two parameters.  $T$  determines the large separation of the ordinary p modes and  $\nu_{ac}$  can be estimated either by the scaling law relation given by Kjeldsen & Bedding (1995) or by a bivariate analysis (coherence and phase shift) as it is done by Jiménez (2006). Models have therefore only been made with different  $\Delta T$ , and  $\nu_0$ . A comparison of the models to the stars other than the Sun can easily be made just by scaling the acoustic cut-off frequency and the mean large separation.

The large separation can easily be obtained in these noise-free power spectra simply by identifying the highest point in each peak. These large separations are shown as a function of frequency for eight sets of  $\Delta T, \nu_0$  in Fig. 7.5. The other values used in the models are the same as used by Vorontsov et al. (1998) – that is,  $T = 1000$  s,  $\nu_{ac} = 5$  mHz and a dipole source.

Fig. 7.5 shows that the complexity of the structure of the large separation increases as  $\Delta T$  decreases and as  $\nu_0$  increases. The physics behind these causal relations is explained by Vorontsov et al. (1998). When the excitation source is moved outwards (as  $\Delta T$  decreases), the frequency of a global trapped mode needs to be higher for the outermost node to be near the source. Therefore, as  $\Delta T$  is decreased the bumps in Fig. 7.5 will move to higher frequencies. However, at higher frequencies energy leakage due to reduced reflection becomes important; therefore, the amplitudes of the bumps are lowered as the bumps move to higher frequencies. If, on the other hand, the reflectivity is increased at higher frequencies (as  $\nu_0$  increases), the amplitudes of the bumps are increased as energy leakage is reduced. This can be seen in the large-separation plots in Fig. 7.5.

Simulations have been made with both a monopole and a dipole source with the same conclusion as found by Vorontsov et al. (1998) – that is, that the bumps in Fig. 5 will move to higher frequencies when going from a monopole to a dipole source. If one compares Fig. 7.4 to Fig. 7.5, it is seen that the

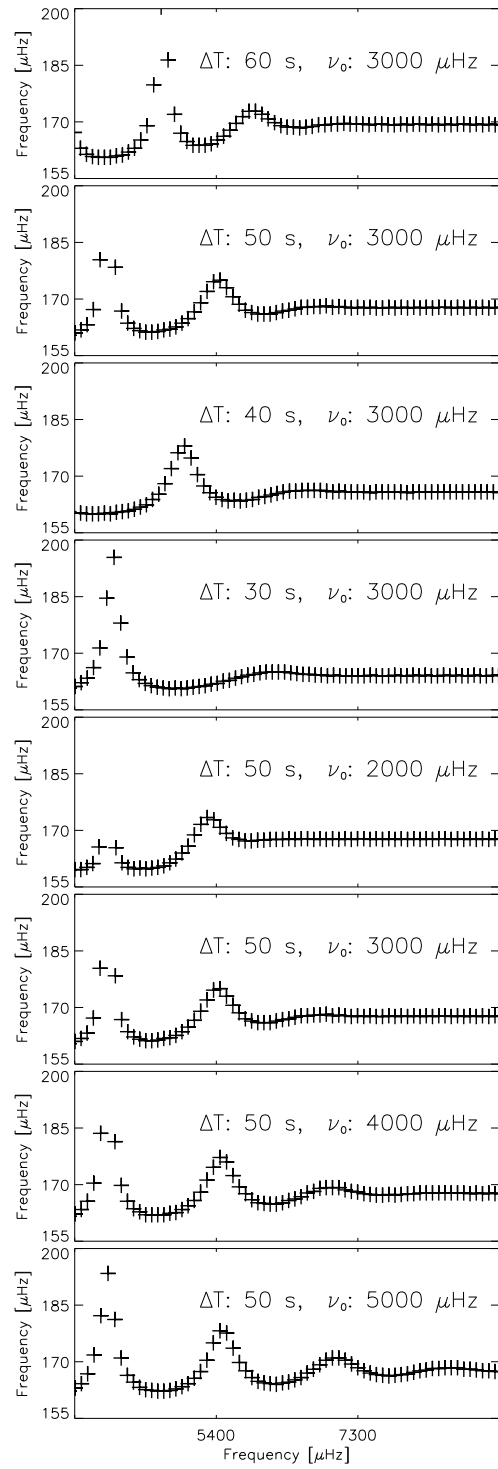


Figure 7.5: Eight different models of the large separation as a function of frequency.  $\Delta T$  and  $\nu_0$  are typed at the top of each plot.

Table 7.2: Estimated depth of the excitation source and width of the reflection

Star	$\Delta T$	$\nu_0$
Sun	$50 \pm 10$ s	$4000 \pm 1000$ $\mu\text{Hz}$
$\alpha$ Cen A	$50 \pm 10$ s	$4000 \pm 1000$ $\mu\text{Hz}$
$\alpha$ Cen B	$50 \pm 10$ s	$3000 \pm 1000$ $\mu\text{Hz}$

observations are in favour of a dipole source, as the bumps generally appear at higher frequencies in the observations than in the simulations.

Looking at Fig. 7.4 bumps are found in the Sun (at 6000 and 7500  $\mu\text{Hz}$ ),  $\alpha$  Cen A (at 4100 and 4900  $\mu\text{Hz}$ ) and  $\alpha$  Cen B (at 5400 and 6800  $\mu\text{Hz}$ ). For the Sun and  $\alpha$  Cen A, the two bumps appear at frequencies higher than  $\nu_{ac}$  for  $\alpha$  Cen B and the second bump appears at the same frequency as  $\nu_{ac}$ . Comparing this with the models in Fig. 7.5 suggests that  $\nu_0$  should have a value of 4000  $\mu\text{Hz}$  or higher in the Sun and  $\alpha$  Cen A. Setting  $\nu_0 = 4000$   $\mu\text{Hz}$  (and  $\nu_{ac} = 5000$   $\mu\text{Hz}$ ) results in a reflection of 0.42 at 5500  $\mu\text{Hz}$  and 0.12 at 7500  $\mu\text{Hz}$ . This contradicts the results by Vorontsov et al. (1998) who propose an upper limit of 0.02 for the reflectivity at 7500  $\mu\text{Hz}$ . For  $\alpha$  Cen B a  $\nu_0$  of 3000  $\mu\text{Hz}$  is found to agree best with the observations as no clear bump appears for frequencies higher than  $\nu_{ac}$ , but only some small curvature at 9000  $\mu\text{Hz}$ . The uncertainty is estimated to  $\pm 1000$   $\mu\text{Hz}$  and is shown together with the estimated values of  $\Delta T$  and  $\nu_0$  in Table 7.2. The estimation is based on the ability of a model to reproduce the observation. The uncertainties are therefore the same for the Sun and the other stars though the S/N is different in the observations. This also means that improving the model could lower the uncertainties significantly.

In  $\beta$  Hydri, a small bump is seen at 1900  $\mu\text{Hz}$ , but it does not appear to be statistically significant.

As two bumps are only seen for a  $\Delta T$  higher than 50 s, we estimate the acoustic depth of the excitation source to  $50 \pm 10$  s for the Sun. By using the sound speed in the outer layers of the Sun from Model S (Christensen-Dalsgaard et al., 1996) this can be converted to a source depth of  $460 \pm 100$  km (below the radius where  $T = T_{\text{eff}}$ ) which is significantly larger than  $140 \pm 60$  km that is found by Kumar (1994). A possible reason for the discrepancy in the estimation of  $\nu_0$  and  $\Delta T$  could be that only low-degree modes are analysed here, whereas Kumar (1994) and Vorontsov et al. (1998) have analysed high-degree modes.

Chaplin et al. (2000b) discuss a number of different estimates of the depth of the excitation source mainly obtained from the asymmetry in the p-mode profile. Depending on the model used, the depth is found to be between 75 and 1500 km (the later value is found when using the first derivatives of  $G_{\Psi}$ ). Evidence is seen that the depth of the excitation source varies with frequency (Chaplin et al., 2000b), but there is no clear evidence that the source depth depends on the degree though the smallest values are found in an analysis of medium- and high-degree modes (Kumar, 1994; Nigam & Kosovichev, 1999).

The Sun shows shape structures in the large separation for frequencies higher than 7200  $\mu\text{Hz}$  (Fig. 7.4). These shape structures are caused by the bump in the echelle diagram at 8000  $\mu\text{Hz}$  (Fig. 7.3). By comparing with the models in

Fig. 7.5, this bump could look like an artefact, but it has not been possible to remove it by re-analysing the data with adjusted parameters. Though the Sun would follow the model predictions much better if the bump is removed and the bump appears in the frequency range with a low S/N in the power spectrum. The same is the case for  $\alpha$  Cen A for frequencies higher than 5000  $\mu\text{Hz}$ . Here, the line in the echelle diagram could also follow the contour at  $x = 40 \mu\text{Hz}$  instead of the contour at 55  $\mu\text{Hz}$ . This would also make  $\alpha$  Cen A follow the model prediction much better, but again this could not be accomplished by re-analysing the data with adjusted parameters.

## 7.5 Discussion

High-frequency modes have been detected in the Sun,  $\beta$  Hydri and  $\alpha$  Cen A and B. By using a simple model of the high-frequency modes that is able to reproduce the main structure in the large separation, it is possible to parametrize the model of the high-frequency modes. Using the model we find that the reflection is higher at high frequency (0.42 at 5500  $\mu\text{Hz}$  and 0.12 at 7500  $\mu\text{Hz}$ ) than what has been found by other studies and that the excitation source is placed deeper in the Sun ( $460 \pm 100$  km) than what has been found by other studies. As most of the other studies have analysed oscillations at lower order  $n$  and higher degree  $l$ , this indicates that the excitation of modes with different  $(n, l)$  does not take place at the same depth.

An analysis of high-frequency modes in solar-like stars has shown to be able to provide two extra parameters in addition to the frequencies of the ordinary p modes to be used in computation of stellar models. The two extra parameters are the depth of the excitation source and the reflectivity of the stellar atmosphere. In this paper, a simplified model has been used for the high-frequency modes where the reflectivity was parametrized with  $\nu_0$ . Of course, future studies should try to compare the high-frequency modes with models using reflectivity profiles calculated from more sophisticated model of the stellar atmosphere and with models using realistic profiles for the excitation source instead of a  $\delta$ -function.

It has been proved in this paper that high-frequency modes can be used in computation of oscillations for solar-like stars. Great advances in our understanding of the effect of the outer layers of the stars on the oscillations can therefore be expected with the successful launch of *COROT* on 2006 December 27 (Baglin et al., 2002) and the launch of *KEPLER* in 2009 (Borucki et al., 2003). These two missions will hopefully provide us with observations of high-frequency modes in a large number of solar-like stars. Here, the high-frequency modes will benefit from being in a frequency range not affected by instrument noise and being observed with photometry (and not with radial velocities as is the case in this paper). According to Nigam & Kosovichev (1999), observing in photometry is expected to be an advancement as the high-frequency modes are expected to have a higher S/N in photometry than in velocity (noise means here stellar noise and not instrument noise).

## **Acknowledgements**

I would like to thank J. Christensen-Dalsgaard, H. Kjeldsen and D. O. Gough for many useful comments on this study. I also acknowledge support from the Instrument Center for Danish Astrophysics.

# Chapter 8

## Mixed Modes in the $\beta$ Hydri

The paper *Combining observations from ground and space: mixed modes in the subgiant  $\beta$  Hydri* presented in this chapter is near submission to MNRAS:

Karoff et al. (2008b) Christoffer Karoff, Hans Bruntt, Hans Kjeldsen, Tim R. Bedding, Derek L. Buzasi, near submission

This paper presents one of the first studies of observations of solar-like oscillations from space. We detect an excess of power around 1 mHz in the acoustic spectrum which could originate from p-mode oscillations. We also model the acoustic spectrum in a way similar to how it was done by Fletcher et al. (2006) on  $\alpha$  Cen A and give an estimate of the mode lifetime.

In the acoustic spectrum we identify two possible mixed modes and suggest that the mode lifetime of these modes is 3 to 5 times longer than for the ordinary p modes.

The appendix gives a detailed introduction to and discussion of two important techniques for data reduction of space-based asteroseismic data: decorrelation of photometric light curves and adjusting of statistical weights.

We are still a bit troubled with the noise in the data and therefore we are as of now not able to completely rule out the possibility that the power excess seen in the data is caused by suborbital noise rather than stellar oscillations. Until we have understood the noise we are only capable of claiming the detection of p-mode candidates.

The important part of this paper for this PhD dissertation is therefore the techniques introduced and discussed in the appendix and the general method for modeling the acoustic spectrum rather than the scientific results of the paper.



## Combining observations from ground and space: mixed modes in the subgiant $\beta$ Hydri

Christoffer Karoff\*, Hans Bruntt<sup>†</sup>, Hans Kjeldsen\*,  
Tim R. Bedding<sup>†</sup>, Derek L. Buzasi<sup>‡</sup>

### Abstract

We present an asteroseismic analysis of the sub-giant  $\beta$  Hydri based on photometric observations with the star tracker on the *WIRE* satellite. The observations consist of 1.6 million images collected during 34 days in 2005.

We combine the data with results from a simultaneous ground-based radial-velocity campaign which has higher S/N, but lower frequency resolution. Most of the modes identified in the radial-velocity campaign are also present in the photometric observations.

Only one of the three modes identified as mixed modes in radial-velocity campaign is clearly visible in the photometric data, but we see two other possible mixed modes that are also in the radial-velocity, but were not mode identified. Assuming that the mixed modes and the ordinary p modes have the same energy supply rate the mixed modes are observed to have mode lifetimes 3 to 5 times longer than the p modes. For the p modes we obtain a mean mode lifetime of  $2.56^{+0.64}_{-0.49}$  days.

Finally, we describe a general technique to correct light curves for instrumental effects, such as stray light and satellite jitter.

## 8.1 Introduction

The observational study of solar-like oscillations (asteroseismology) is entering a golden age. Modern spectrographs on medium-sized to large telescopes can provide time-series radial-velocity observations with a precision around 0.5 m/s for bright stars. To detect the oscillations in integrated light, photometry must be obtained from space to avoid scintillation from the Earth's atmosphere, since the amplitudes of the solar-like oscillations are typically around 10 ppm for stars on the main sequence. While the detection of solar-like oscillations has been done for about a dozen stars with radial-velocity data (see Bedding & Kjeldsen, 2007b, for a recent review), detections with photometry from space include only

---

\*Department of Physics and Astronomy, University of Aarhus, Ny Munkegade, Building 1520, DK 8000 Aarhus C.E-mail: karoff@phys.au.dk

<sup>†</sup>School of Physics, University of Sydney, NSW 2006, Australia

<sup>‡</sup>Department of Physics, US Air Force Academy, Colorado Springs, CO 80840, USA

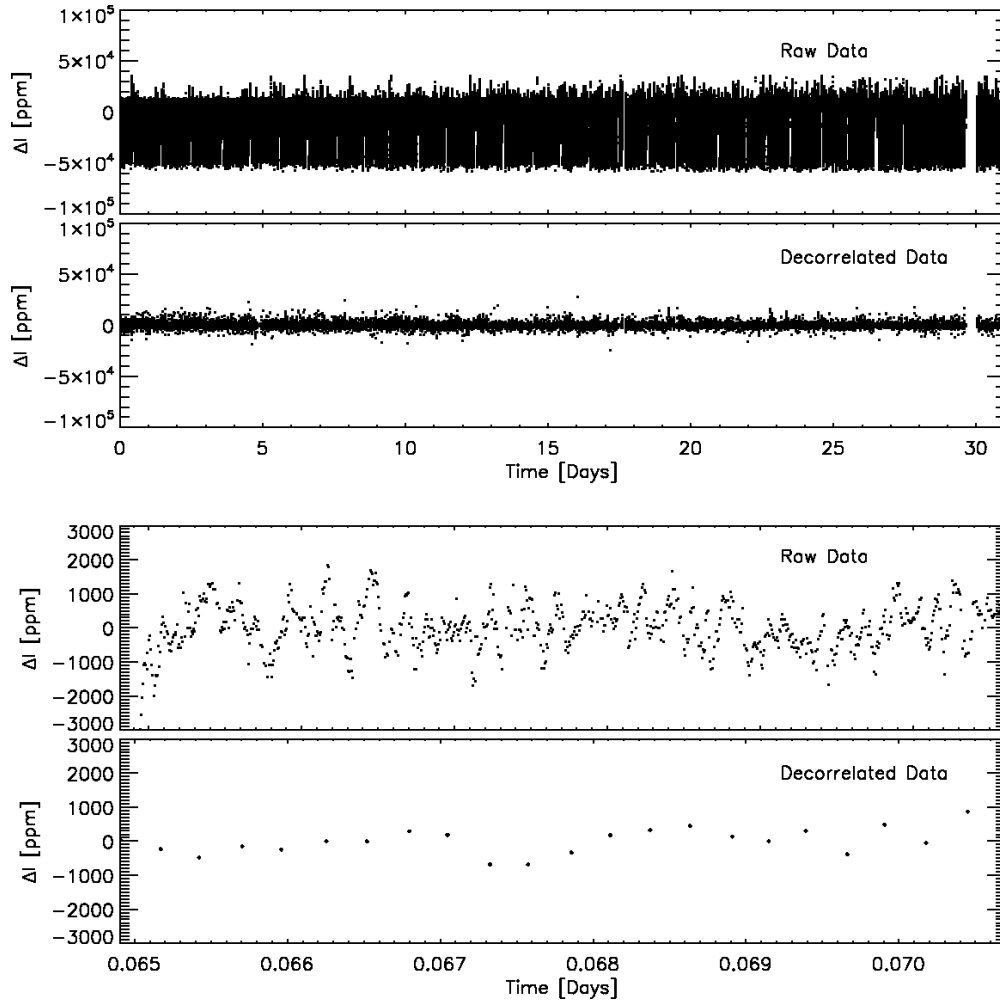


Figure 8.1: The raw and decorrelated time series. The top two panels show the entire data set, while the bottom two show a small part of an orbit not affected by stray light. The orbital noise is clearly seen in the raw data in the top panel, while the short-period noise is clearly seen in the third panel. The decorrelated time series has a RMS noise level of 2 ppt while the raw time series has a RMS noise level of 25 ppt.

a few confirmed examples:  $\alpha$  Cen A (Schou & Buzasi, 2001; Fletcher et al., 2006) and Procyon with the *WIRE* satellite (Bruntt et al., 2005) and HD 49933 with *COROT* (ESA, 2007).

In this paper we demonstrate that asteroseismic observations of solar-like stars with space-based photometry and radial-velocities are complementary. Granulation noise in solar-like stars is about an order of magnitude smaller in radial-velocity than in photometry (Harvey, 1988). Thus, radial-velocity campaigns are preferred as individual modes can be measured with high S/N. However, the duration of radial-velocity campaigns are typically only 1–2 weeks (Bedding & Kjeldsen, 2007b), and as a result the frequency resolution is too low

to accurately measure the effects of finite mode lifetimes and stellar rotation. To study these aspects of stellar astrophysics, long-term space-based photometric observations are needed. This will become possible in the near future with temporal coverage up to a few months with *COROT* (Baglin et al., 2002) and a few years with *KEPLER* (Borucki et al., 2003).

To investigate if this is possible in practice, we collected simultaneous observations of  $\beta$  Hydri comprising dual-site radial-velocity data and photometric observations with the star tracker on the *WIRE* satellite. The results of the ground-based radial-velocity campaign were described by Bedding et al. (2007). The mode identification from that study greatly benefits our analysis of the *WIRE* data.

The paper is arranged as follows: Section 8.2 describes the data and the data reduction including the new correction algorithm. In section 8.3 we analyze the general structure in the power-density spectrum (PDS) and evaluate the amplitudes of the p-modes candidates seen in the photometric data. Section 8.4 describes how we model the PDS. In section 8.5 and 8.6 we discuss the results and present a summary of our study.

## 8.2 Observations and Data Reduction

$\beta$  Hydri was observed for 34 days from August 27 to September 29 in 2005 with the star tracker on the *WIRE* satellite. We collected 1,602,950 images of  $\beta$  Hydri with two images per second. The observations were continuous except for orbital gaps and a short gap at the end of the run. The duty cycle is 27% due to pointing restrictions. In total *WIRE* observed  $\beta$  Hydri for 222.6 hours. The raw light curve is shown in the top panel in Fig. 8.1. The integration time was practically the same as the cadence (0.5 s) as only five  $8 \times 8$  pixels windows are read out from the CCD.

The PSF in the  $8 \times 8$  pixels windows is well sampled, with a FWHM of around 1.8 pixels. The position of the stellar image was calculated by fitting a 2D Gaussian and aperture photometry was performed as described by Bruntt et al. (2005). In this process the central 22 pixels were summed and the background was subtracted.

*WIRE* is in a low Earth Sun-synchronous orbit with a period of 93.3 minutes and a significant fraction of the observations are affected by stray light. The simplest way to solve this problem is to remove all the data points affected by stray light, as done by Bruntt et al. (2005) in their study of Procyon. We did not follow this approach since the duty cycle would be only 10%. Thus, the effective observing time per orbit would be  $\simeq 10$  minutes, which is shorter than the expected oscillation periods in  $\beta$  Hydri.

Instead we used all the data that were available after decorrelation and assignment of point weights. We have developed a general algorithm for the decorrelation, and the lower panels in Fig. 8.1 show the resulting light curve. The algorithm and weight assignment are described in detail in Appendices 8.7.1 and 8.7.2.

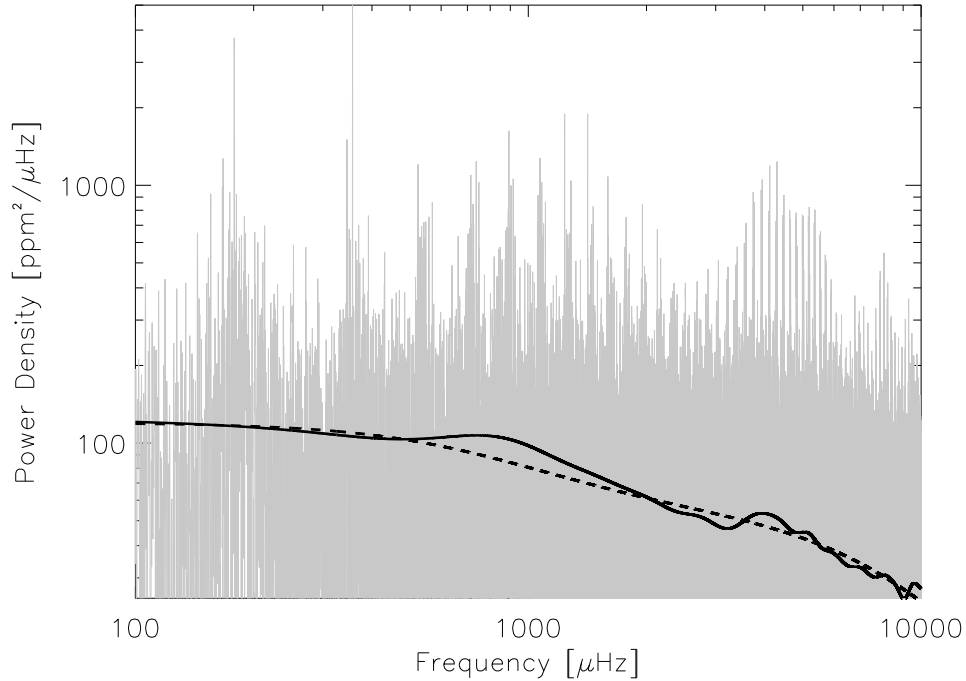


Figure 8.2: The PDS of  $\beta$  Hydri plotted on a log-log scale. The solid line shows the smoothed PDS and the dashed line is the fit to the noise.

### 8.3 Power Excess

The first thing to do with the decorrelated data is to investigate if we see p mode oscillations, – i.e. that we see an excess of the power in the expected frequency range (Fig. 8.2) and to estimate the amplitude of this excess.

In order not to include the power caused by the instrument at the orbital harmonics in the evaluation of the amplitudes, we removed all the power at the orbital harmonic. This was done by cleaning the spectrum at all frequencies intervals:  $\nu = n \cdot \nu_{wire}$  (where  $\nu_{wire}$  equals  $178.5 \mu\text{Hz}$ ). The cleaning was done by iteratively subtracting fitted sinusoids in these frequency intervals (Frandsen et al., 1995). The resulting PDS is shown in Fig. 8.3. Removing the power this way has the effect that we also remove any spectral leakage that could be caused by the power at the orbital harmonics.

Stray light will have more spectra leakage than what is given by the window function as the stray light signal does not have a sinusoidal form. This means that the spectra leakage from e.g. stray light is not perfectly removed simply by removing the power in the power-density spectrum (PDS) at the orbital harmonics.

We have estimated the mode amplitudes of the p-mode candidates by smoothing the PDS following Kjeldsen et al. (2005). This is generally more reliable than measuring the amplitudes of individual modes, which can vary

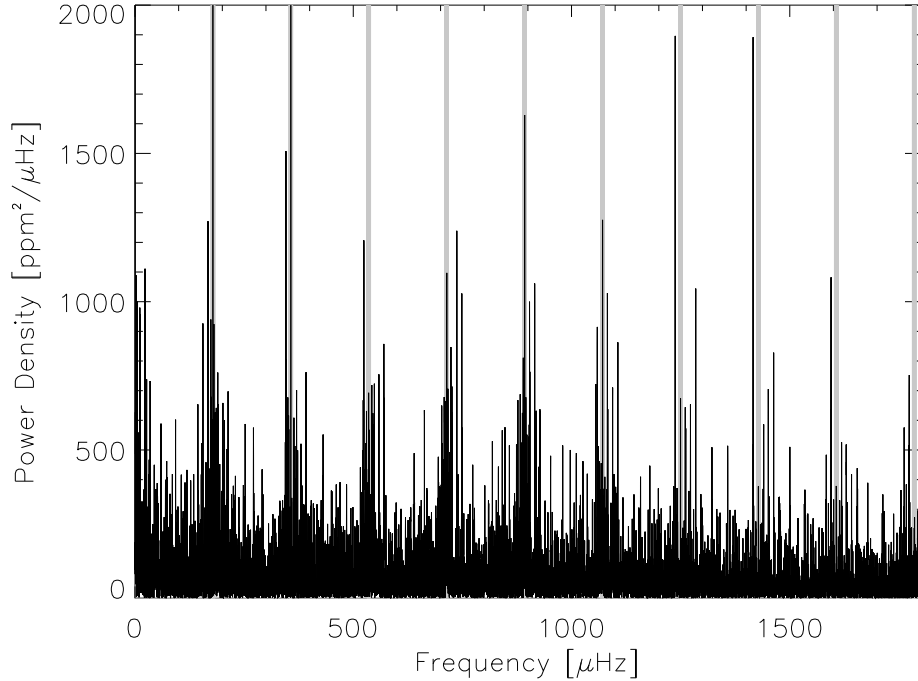


Figure 8.3: Power-density spectrum of  $\beta$  Hydri after decorrelation. The grey regions mark indicate the orbital harmonics of *WIRE*, where spectrum has been cleaned.

significantly because of the stochastic excitation of the oscillations and interference with the noise. We calculated the power spectrum,  $P(\nu)$ , and converted it to the PDS( $\nu$ ). This is done by multiplying the smoothed PDS with the effective observing length, which is the reciprocal of the area under the spectral window,  $W(\nu)$ :

$$PDS(\nu_k) = \frac{A(\nu_k)^2}{\int_0^{\nu_{\text{Nq}}} W(\nu) d\nu}. \quad (8.1)$$

The PDS was then smoothed with a Gaussian running mean with a width of  $224 \mu\text{Hz}$  (equal to four times the large separation of  $\beta$  Hydri).

The smoothed PDS was fitted using a Harvey model (Harvey, 1985) plus white noise (dashed line in Fig. 8.2). We did not include the part of the spectrum where the p-modes are expected to be located (500 to 1700  $\mu\text{Hz}$ ). The amplitude per mode of the p-modes candidates was calculated by first subtracting the Harvey model from the smoothed PDS. Then multiplying this by the large separation of  $57.5 \mu\text{Hz}$  (Bedding et al., 2007) and divided by the number of modes per large separation. For the photometric data we can assume that we observe only  $l = 0, 1$  and  $2$ .

In Fig. 8.4 we show the amplitude per mode as a function of frequency. We obtain a peak amplitude per mode of about 19 ppm, which is somewhat larger

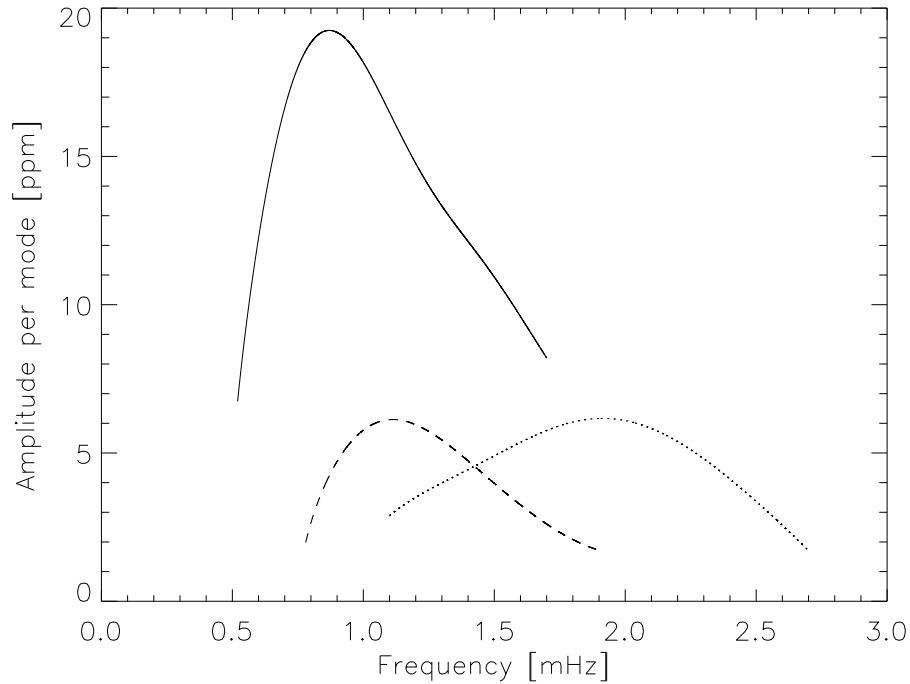


Figure 8.4: Amplitudes per mode as a function of frequency measured from *WIRE* data of three solar-like stars. The solid line is  $\beta$  Hydri, the dashed line Procyon, and the dotted line  $\alpha$  Cen A.

than the semi-empirical prediction by Kjeldsen & Bedding (1995):  $12.7 \pm 1.5$  ppm at  $550 \text{ \AA}$ . We have also evaluated the mode amplitude in Procyon and  $\alpha$  Cen A, and the results are compared to  $\beta$  Hydri in Fig. 8.4. The Procyon data were obtained between March 19 and April 8 2005 and the  $\alpha$  Cen A data were obtained between July 16 and August 4 1999 with *WIRE*. Procyon and  $\alpha$  Cen A both show a peak mode amplitudes around 6 ppm.

The amplitude per mode as a function of frequency is not symmetric and a knee is seen around  $1400 \mu\text{Hz}$ . The same kind of knee is seen in the analysis of the ground-based radial-velocity data (Bedding et al., 2007).

## 8.4 Modelling the Power-Density Spectrum

The frequency resolution in the radial-velocity data (Bedding et al., 2007) is  $\sim 1.2 \mu\text{Hz}$ , measured as the FWHM of the central peak in the window function. This is comparable to the line width caused by the finite mode lifetime. In the photometric light curve the frequency resolution is almost four times higher at  $0.3 \mu\text{Hz}$ . This is high enough that we can put constraints on the lifetime of the modes. To do this we use the precise frequencies from the velocity data and fit a model describing the power spectrum of the photometric light curve.

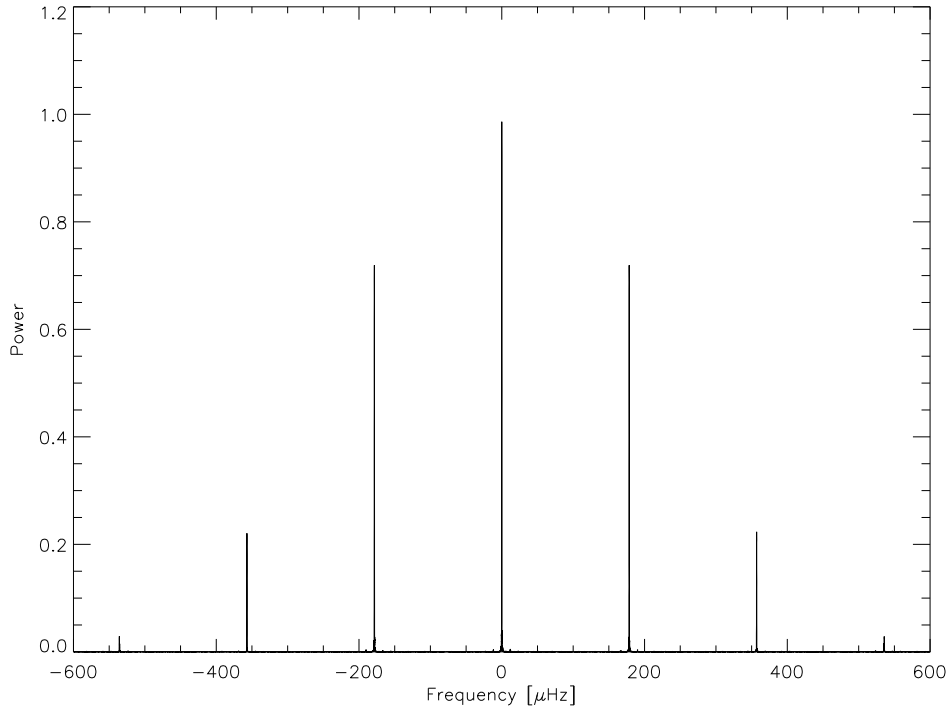


Figure 8.5: The spectral window of the *WIRE* observations of  $\beta$  Hydri. The first and second sidebands are used when modelling the PDS.

Observations of stochastic damped oscillations are seen as a series of peaks describing a Lorentzian profile in the PDS<sup>1</sup>. The frequency, widths and amplitudes of the observed profiles can in principle be used to infer the intrinsic mode amplitude, frequency, lifetime, and rotational splitting. We will extract this information from a global fit of a model to the power spectrum, as was done for *WIRE* observations of  $\alpha$  Cen A by Fletcher et al. (2006). We used the same strategy in order to model modes between 730 and 1310  $\mu\text{Hz}$  (excluding  $\pm 4$   $\mu\text{Hz}$  around the orbital harmonics). The model includes a  $1/f$  background and each frequency in the model is represented by a Lorentzian profile. Each oscillation mode included in the model will produce a number of peaks due to the spectral window and stellar rotation. Following Fletcher et al. (2006), we fit the PDS with a model  $P(\nu)$ :

$$P(\nu) = \frac{B}{\nu} + \sum_{nlmk} \left[ \frac{H_{nlmk}}{1 + \left( \frac{\nu - \nu_{nl} + ms + kw}{\Delta/2} \right)^2} \right], \quad (8.2)$$

<sup>1</sup>This requires that the duration of the observation run is sufficiently long. Simulations show that the Lorentzian profile is clearly seen if  $T_{\text{obs}} > 10 \tau$ , where  $T_{\text{obs}}$  is the observing time and  $\tau$  is the mode lifetime.

where  $B$  is the square of the amplitude of the background,  $\nu_{nl}$  is the central frequency,  $s$  is the rotational splitting,  $w$  is the sideband spacing (178.5  $\mu$ Hz),  $\Delta$  is the width of the Lorentzian profile.  $n, l$  and  $m$  are the radial order, angular degree and azimuthal order, respectively and  $k$  is a variable allowing us to include the first and second sidebands in the spectral window.  $H_{nlmk}$  is the height of each peak in the PDS and can be calculated from the mode amplitude,  $A_{nl}$ , the visibility of the rotation component,  $\epsilon_{nl}$  (Gizon & Solanki, 2003), and the sidebands in the spectral window,  $r_k$  and  $\Delta$ :

$$H_{nlmk} = \frac{A_{nl}^2 \epsilon_{lm} r_k}{\Delta}, \quad (8.3)$$

where  $\epsilon_{nl}$  is:

$$\epsilon_{10}(i) = \cos^2 i, \quad (8.4)$$

$$\epsilon_{1\pm 1}(i) = 1/2 \sin^2 i, \quad (8.5)$$

$$\epsilon_{20}(i) = 1/4 (3 \cos^2 i - 1)^2, \quad (8.6)$$

$$\epsilon_{2\pm 1}(i) = 3/8 \sin^2(2i), \quad (8.7)$$

$$\epsilon_{2\pm 2}(i) = 3/8 \sin^4 i, \quad (8.8)$$

and  $r_k$  is obtained from the spectral window in Fig. 8.5 to:

$$r_0 = 1.0000, \quad (8.9)$$

$$r_{\pm 1} = 0.7186, \quad (8.10)$$

$$r_{\pm 2} = 0.2219. \quad (8.11)$$

The amplitudes  $A_{lm}$  were calculated differently from how it was done by Fletcher et al. (2006) by simply using Eq. 8.3

We used a Powell multi-dimensional hill-climbing minimization algorithm to minimize a simple likelihood function between the observed PDS and the model (Press et al., 1992). Because of the generally low S/N we did not use a logarithmic likelihood function as this would raise the weights of the noise background in the minimization. Instead we used a simple likelihood function given by:

$$LH = \sum_{\nu=\nu_{\min}}^{\nu_{\max}} |PDS(\nu) - M(\nu)|, \quad (8.12)$$

where  $PDS$  is the observed spectrum and  $M$  is the modeled spectrum. We tested other formulations of the likelihood function, but did not find any that performed better than this one.

We did not include the rotation period as a free parameter in the model, since the quality of the data was not good enough to constrain the inclination of the rotation axis. Instead we fixed the inclination to  $45^\circ$  and calculated the rotational splitting based on  $v \sin i$  and the stellar radius to get  $s = 0.36 \mu$ Hz. We used  $v \sin i = 2 \pm 1$  km/s (Dravins et al., 1993) and  $R = 1.814 \pm 0.017 R_\odot$  (North et al., 2007), which was recently measured with the Sydney University Stellar Interferometer. We applied different inclination angles in order to confirm that this only had a negligible effect on the derived mode lifetime.

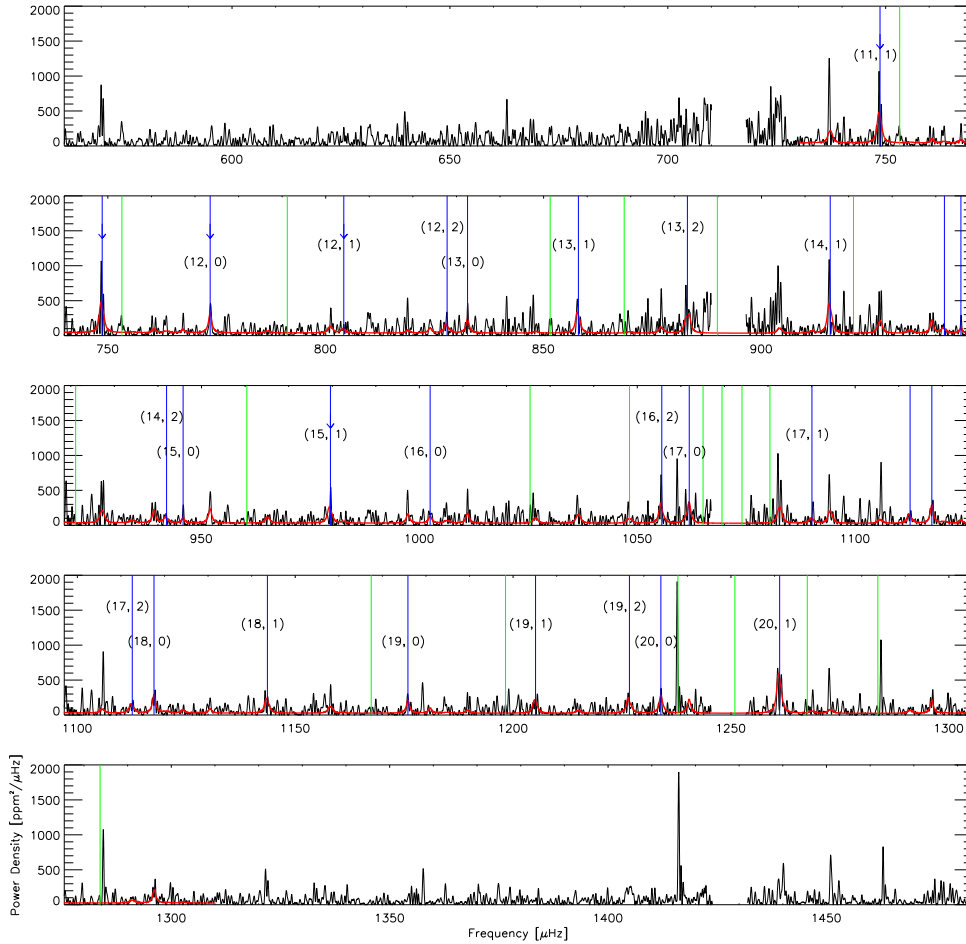


Figure 8.6: The normalized PDS with the model with the maximum likelihood overlaid. The PDS is plotted on three panels with a off-set of  $178.5 \mu\text{Hz}$  so the sidebands in the spectral window lineup vertical. The modes included in the model are marked with a vertical blue line and labeled with  $n, l$ . Modes with S/N higher than 4.9 in the velocity data, but with no mode identification are marked with a green line. These modes were not included in the model.

The mode frequencies are free parameters in the model, but the best fitted model depends on the input frequencies. The reason for this is that we first fit the amplitudes of the frequencies and then adjust the mode frequencies. Therefore if an input mode frequency is shifted with a significant amount compared to the peak in the PDS it will in general be assigned a low amplitude.

As input for the model we used 17 of the 21 mode frequencies with mode identification in Bedding et al. (2007), the last 4 were not visible in the photometric data. Note that we did not include the modes identified as mixed modes in Bedding et al. (2007), since the mode identification is ambiguous.

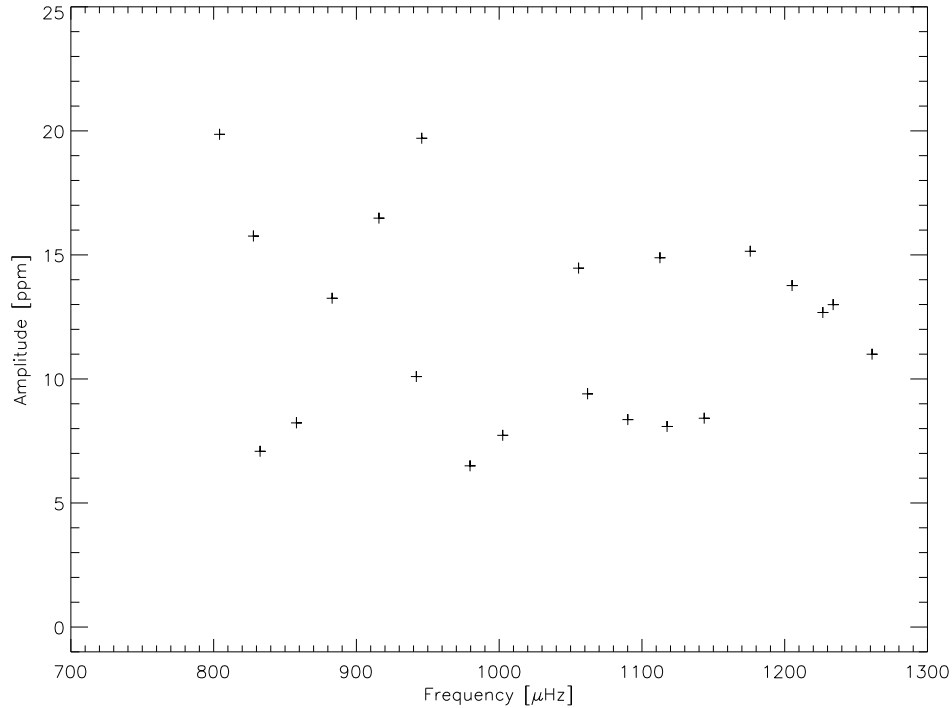


Figure 8.7: Mode amplitudes of the model with the maximum likelihood.

The mode frequencies were adjusted slightly by visually matching them with the photometric PDS. We added another six modes that were clearly visible in the photometric PDS. Their  $l$  values were assigned based on their general alignment with the asymptotic relation (see Fig. 11 in Bedding et al. (2007)).

The initial value of the mode lifetime was  $\tau = 2.32$  d (from Bedding et al. (2007)). We used the same input amplitude for all the modes ( $A = 10$  ppm) and for the input for the background we used the Harvey model fit from Fig. 8.2.

## 8.5 Results and Analysis

The PDS with the best fitted model overlaid is shown in Fig. 8.6. In the following we will discuss the results of the output parameters of this fit. This will include a comparison with the frequencies from the radial-velocity study in Bedding et al. (2007), estimation of the mode lifetime of the modes, analysis of the echelle diagram, and the possible detection of some mixed modes that were not detected in the radial-velocity data.

### 8.5.1 Mode Frequencies

The fitted frequencies and their uncertainties are listed in Table 8.1. The uncertainties on the frequencies are calculated according to Libbrecht (1992), but we

Table 8.1: Mode frequencies. The  $n$  and  $l$  values are obtained from either the Echelle diagram or Bedding et al. (2007)

$n$	$l$	Bedding et al. (2007)	This study	S/N
<b>11</b>	<b>1</b>	–	<b>748.70 ± 0.52 μHz</b>	<b>3.44</b>
11	2	769.62 ± 1.59 μHz	–	–
<b>12</b>	<b>0</b>	–	<b>773.47 ± 0.63 μHz</b>	<b>2.84</b>
<b>12</b>	<b>1</b>	–	<b>804.15 ± 1.50 μHz</b>	<b>1.57</b>
12	2	827.70 ± 1.19 μHz	827.85 ± 1.24 μHz	1.75
13	0	833.72 ± 1.10 μHz	832.54 ± 0.72 μHz	2.52
13	1	857.54 ± 0.86 μHz	857.99 ± 0.57 μHz	3.09
13	2	883.38 ± 0.94 μHz	883.00 ± 0.94 μHz	2.07
14	0	889.87 ± 1.45 μHz	–	–
14	1	913.11 ± 0.89 μHz	915.78 ± 0.48 μHz	3.75
14	2	940.33 ± 0.95 μHz	941.98 ± 1.51 μHz	1.57
15	0	945.64 ± 1.13 μHz	945.76 ± 1.23 μHz	1.75
<b>15</b>	<b>1</b>	–	<b>979.58 ± 0.61 μHz</b>	<b>2.92</b>
15	2	998.95 ± 0.90 μHz	–	–
16	0	1004.21 ± 0.85 μHz	1002.47 ± 0.95 μHz	2.06
16	1	1033.52 ± 0.86 μHz	–	–
16	2	1056.74 ± 0.87 μHz	1055.62 ± 1.06 μHz	1.93
17	0	1062.06 ± 1.27 μHz	1061.92 ± 0.57 μHz	3.10
17	1	1086.45 ± 0.93 μHz	1090.08 ± 1.08 μHz	1.90
17	2	1114.77 ± 1.49 μHz	1112.60 ± 1.02 μHz	1.97
18	0	1118.93 ± 0.87 μHz	1117.60 ± 0.55 μHz	3.23
18	1	1146.69 ± 0.95 μHz	1143.62 ± 0.59 μHz	2.99
18	2	1171.61 ± 0.97 μHz	–	–
19	0	1176.48 ± 0.87 μHz	1175.87 ± 0.63 μHz	2.82
19	1	1203.52 ± 1.04 μHz	1205.16 ± 0.61 μHz	2.91
<b>19</b>	<b>2</b>	–	<b>1226.70 ± 0.72 μHz</b>	<b>2.54</b>
<b>20</b>	<b>0</b>	–	<b>1233.91 ± 0.57 μHz</b>	<b>3.12</b>
20	1	1262.20 ± 2.66 μHz	1261.17 ± 0.39 μHz	5.02

have replaced the observing length  $T$  with the effective observing length, which is proportional to the reciprocal of the area of under the spectral window.

It is seen that the modes generally have low S/N, and the photometry data alone does not justify statistical significant detection of them. This is why we need the complementary analysis of the radial-velocity data, so we can have a secure detection of the oscillation modes with high S/N before fitting a model to the PDS of the photometry data.

One way to show the mode frequencies is by plotting them in an echelle diagram. Here we have the mode frequencies on the ordinate and the frequencies modulo the large separation on the abscissa as shown in Fig. 8.9.

The largest scatter appears for  $l = 1$  modes, whereas the  $l = 0$  and 2 modes show a very good agreement. A possible explanation for this could be that

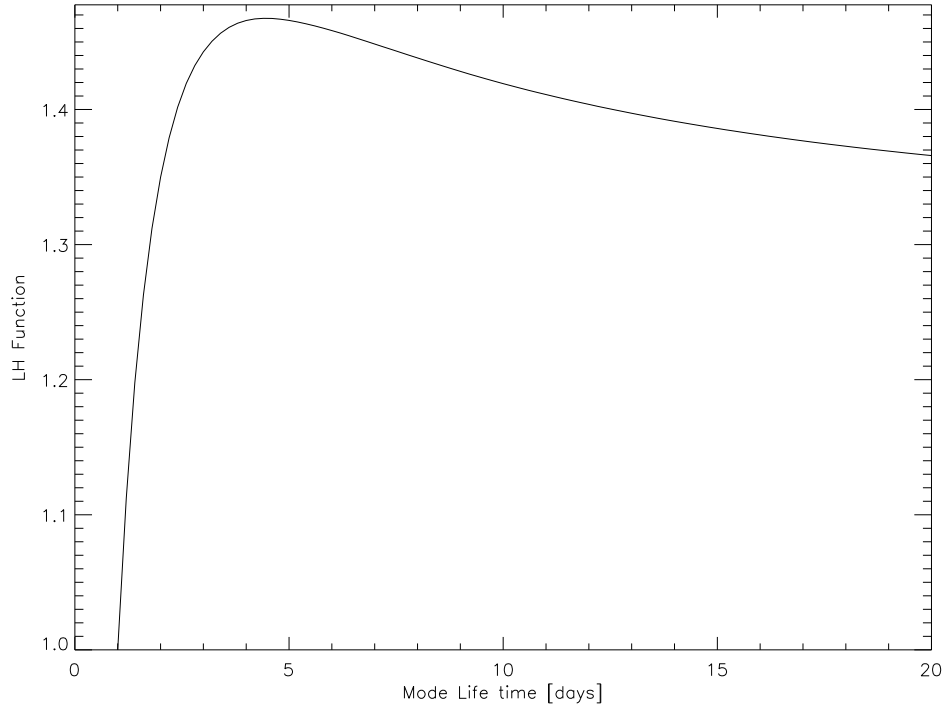


Figure 8.8: Likelihood function as a function of mode lifetime. The likelihood function has been normalised by the minimum value. The obtained value of the mode lifetime is  $4.2^{+5.8}_{-2.0}$  days.

the  $l = 1$  modes in  $\beta$  Hydri are affected by avoided crossings of these modes (Bedding et al., 2007).

The amplitudes of the fitted modes are shown in Fig. 8.7. It is seen that the amplitudes in Fig. 8.7 are generally lower than the ones in Fig. 8.4. We believe that this reflects the fact that it has not been possible to remove all the frequency leakage from the orbital harmonics (we have therefore used a mean value of 13.5 ppm obtained in Fig. 8.7 in the analysis in Section. 3.2.2).

### 8.5.2 Mode Lifetime

We obtain a mean line width of  $0.88^{+0.79}_{-0.51}$   $\mu\text{Hz}$ . This is equal to a mode lifetime of  $4.2^{+5.8}_{-2.0}$  days. The result is in agreement with the result from Bedding et al. (2007) who obtain a mode lifetime of  $2.32^{+0.64}_{-0.51}$  days, though the uncertainties are significant larger in the result from the *WIRE* data. As the two results are independent they can be combined to get  $\tau = 2.56^{+0.64}_{-0.49}$  days.

The uncertainty is estimated by evaluating the likelihood function as a function of mode lifetime in Fig. 8.8. In this way the lower and upper boundary of the mode lifetime is found where the likelihood function is half the peak value.

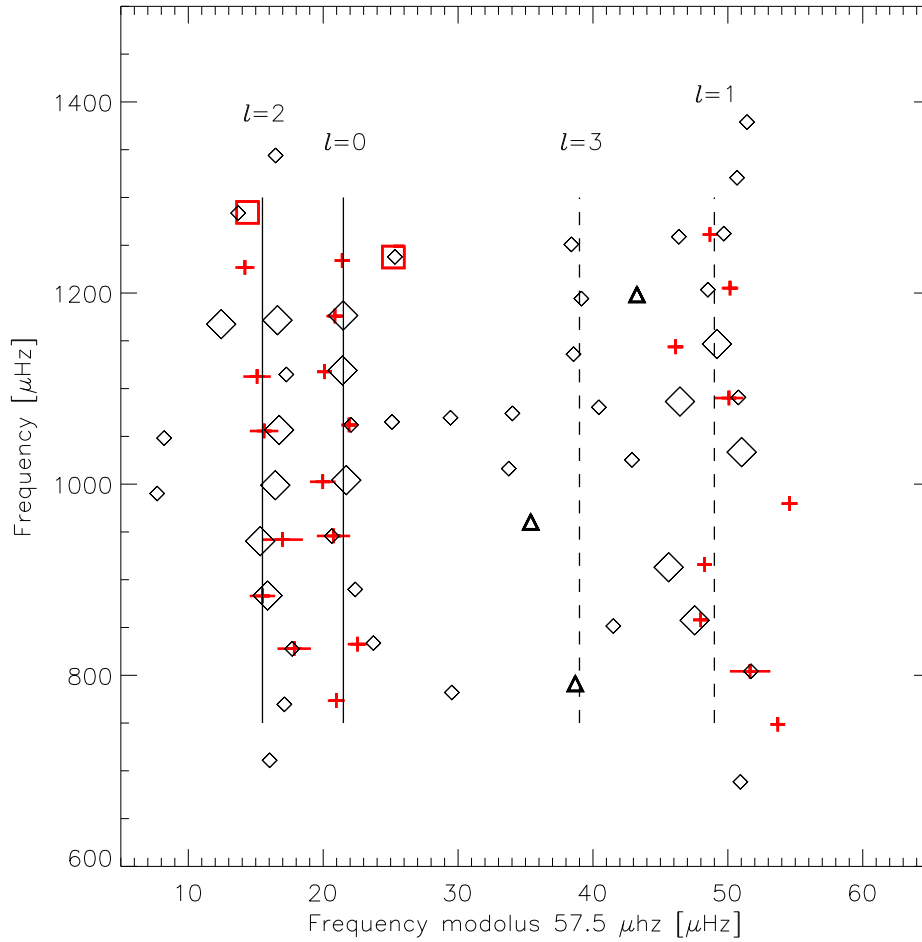


Figure 8.9: Echelle diagram of  $\beta$  Hydri from velocity and photometry measurements. The diamonds are from the velocity observations in Bedding et al. (2007), the crosses are from the observations in this study. The triangles are the modes identified as mixed modes in Bedding et al. (2007) and the squares are the modes we identify as possible mixed modes. The horizontal line in the crosses represents the error bars.

### 8.5.3 Echelle Diagram and Avoided Crossings

In Fig. 8.9 we show the frequencies from Bedding et al. (2007) and those obtained in the current study in an echelle diagram. The red crosses are the frequencies obtained in this study (the horizontal lines show the uncertainties), the diamonds are the mode frequencies from Bedding et al. (2007). Frequencies with S/N larger than 7 have large diamonds and frequencies with S/N lower than 7 have small. The 17 fitted frequencies in common with Bedding et al. (2007) generally agree within the uncertainties. The 6 new frequencies we observed in the *WIRE* PDS follow the general trend in the echelle diagram, which

gives some support that they are intrinsic to  $\beta$  Hydri.

Some of the peaks in the PDS that were not included in the model could potentially be oscillations. We have compared the location of these peaks with the low S/N peaks from Bedding et al. (2007) (i.e. peaks without identification of  $l$ ). Firstly, we see that only one of the three modes identified as mixed modes ( $f = 1198.26 \mu\text{Hz}$ ) in Bedding et al. (2007) is clearly visible in the photometry data. Secondly, we see that the two highest peaks in the photometry data (1237.65 and 1284.43  $\mu\text{Hz}$ ) are also visible in the velocity data, but they have low S/N. These two peaks could be mixed modes.

It is remarkable that only one of the three modes identified as mixed modes in Bedding et al. (2007) is clearly visible in the photometry data as these three modes all have high S/N in the radial-velocity data. In fact these three modes are all among the 5 modes with the highest S/N in the radial-velocity data. We have therefore calculated the PDS of the 14 days of WIRE data the overlap exactly with the radial-velocity data in order to see if these modes had higher visibility here. This was not the case.

Mixed modes are expected to have significantly longer mode lifetime than the ordinary p modes, as the mixed modes will have both g- and p-mode character (Osaki, 1975). If the mixed modes have significant longer mode lifetimes they will be unresolved in the velocity data. In the *WIRE* photometry data the mode amplitudes would be larger than the ordinary p modes. These characteristics of mixed modes are in agreement with what we have observed. To our knowledge no general theoretical estimate of the ratio between the lifetime of the mixed modes and the p modes are available in the literature. Though models of  $\eta$  Boo suggest that mixed modes should have mode lifetimes up to 5 times longer than the p modes (Christensen-Dalsgaard, private communication).

These possible mixed modes could be due to some artifacts of the data reduction. We checked if the oscillation signal is coherent. That was done by cutting the time series into three substrings of 11 days and analyzing the PDS around the frequencies of the modes in the three substrings. The modes were present in all the three substrings, i.e. the modes are coherent and gives some support that they are intrinsic to  $\beta$  Hydri. The lifetime of the modes can be evaluated from the amplitude ratio between the ordinary p modes and the mixed modes as the power of the modes is proportional to the mode lifetime (Eq. 8.3). This is valid if we assume that the different modes have the same energy supply rate. If the peaks at  $f = 1237.65$  and  $1284.43 \mu\text{Hz}$  are indeed mixed modes, then their lifetimes will be 3 to 5 times longer than that of the ordinary p modes as they have amplitudes 3-5 times higher than the ordinary p modes. This is in agreement with the theoretical estimate.

## 8.6 Summary

We have analyzed high-precision photometry data from the *WIRE* satellite on the sub-giant  $\beta$  Hydri. The raw data is affected by stray light and we developed a general algorithm to correct light curves for systematic instrumental noise. We used it to improve data from the star tracker on the *WIRE* satellite, which

allowed us to extract new information from the peaks that could be due to p-mode oscillations.

The long temporal coverage of 34 days means the frequency resolution is high enough that we can estimate the lifetime of the p-mode candidates. We used accurate frequencies from a two-site radial-velocity campaign (Bedding et al., 2007) as input to a model to fit the power spectrum. We modelled the power-density spectrum in order to obtain mode frequencies, amplitudes and lifetimes of the p-mode candidates. This method should work in principle, but the S/N ratio in the *WIRE* data is too poor ( $2 - 3\sigma$ ) to improve on the mode lifetime.

We find evidence of two mixed modes with lifetimes 3 to 5 times longer than that of the ordinary p modes candidates.

## Acknowledgments

We would like to thank Torben Arentoft, Jørgen Christensen-Dalsgaard, Poul Erik Nissen and Dennis Stello for their useful remarks. CK acknowledges support from the Danish AsteroSeismology Centre and the Instrument Center for Danish Astrophysics. HB was supported by the Australian Research Council.

## 8.7 Appendix

### 8.7.1 Decorrelation of Photometric Light Curves

The idea behind the algorithm is to find a correction to the photometry as a function of any instrumental variable, e.g. the change in position of the stellar image due to satellite jitter. The correction is defined as the distance-weighted mean of the photometry as a function of jitter. Using the value of the jitter, measured on the CCD in  $x$  and  $y$ , the correction to data point  $i$  is given as:

$$\delta p(i) = \frac{\sum_j w(i, j) \cdot p(j)}{\sum_j w(i, j)}, \quad (8.13)$$

where  $p(j)$  is the measured relative intensity of the star for data point  $j$ , and  $w(i, j)$  are the weights. These depend on the distance and are defined as:

$$w(i, j) = \frac{1}{1 + (x_i - x_j)^a + (y_i - y_j)^a}, \quad (8.14)$$

where  $x, y$  are the measured jitter at a given time and  $a$  is an even integer. If  $a$  is small – i.e. 4, then the algorithm uses as many data points as possible. If  $a$  is large – i.e. 30, then the algorithm will only use the data points which are a small distance from the data point to be corrected.

If the number of measurements is small, it is important not to include the corrected data point in the calculation. We therefore rewrite Eq. 8.13 as follows:

$$\delta p(i) = \frac{\sum_j w(i, j) \cdot p(j) - p(i)}{\sum_j w(i, j) - 1}. \quad (8.15)$$

We tested several different ways of defining the weights as a function of the distance, e.g. by including more terms. We found good results when including a linear term in the calculation of the weights, i.e.  $x = x/b$  and  $y = y/b$  and using  $a = 12$ .

The algorithm can be used to decorrelate a given time-series for any number of parameters because the weights can easily be defined as a function of an arbitrary number of parameters:

$$w(i, j) = f[x_1(i), x_1(j), x_2(i), x_2(j), \dots, x_n(i), x_n(j)]. \quad (8.16)$$

In this way we can rewrite Eq. 8.14:

$$w(i, j) = \frac{1}{1 + \sum_n [x_n(i) - x_n(j)]^a}. \quad (8.17)$$

A large number of different decorrelation sequences were tested in order to optimize the S/N of the oscillations in  $\beta$  Hydri. Basically, we wanted to decorrelate for satellite jitter and for stray light. When correcting for jitter we used the position of the star on the CCD and to correct for the stray light we used the orbital phase. By inspecting the raw light curve it was seen that the stray light varies not only with orbit phase, but also from orbit to orbit. We therefore also used the orbit number for decorrelating for stray light.

The first thing we tried was to decorrelate for all four parameters ( $x$ ,  $y$ , orbit phase and orbit number) at the same time, but the result was not successful as the different parameters are not independent.

The light curve has a clear periodicity of around 10 s (see Fig. 8.1) which must be instrumental. We could recognize some of this periodicity in the time series of the jitter, but no simple correlation was found. Since the amplitude of this short period noise is quite high we tried to decorrelate for this first. This was done by using the  $x$  and  $y$  jitter as correlation parameter, but since the light curve showed some long period ( $> 5$  h) structure we also used the observation time as a correlation parameter. The linear term  $b$  was set as high as 20,000 s. Using the time in the decorrelation has the same effect as applying a high-pass filter to the data – i.e. decorrelating with  $b = 20,000$  s has the same effect as running a soft high-pass filter at 51  $\mu$ Hz. For the  $x$  and  $y$  jitter the linear term  $b$  was set to 0.01 pixels.

The next step was to decorrelate against stray light. This was done by using the orbital phase and the orbit number as decorrelation parameters – i.e. as  $x$  and  $y$ . Here the linear term  $b$  was set to 0.01 for orbit phase and 5 for orbit number. These values were found by optimizing the S/N of the oscillations within a reasonable frequency range. If the linear term for the orbit number is too low ( $< 1$  orbit) all signal is removed from the light curve, but if term is too high ( $> 10$  orbits) the decorrelation will not work. The linear term for the orbit phase is restricted by the resolution of the orbit phase – i.e. how many data points with a sufficiently small photon noise level are available in each phase element. On the other hand, the term needs to be small enough to resolve any stray light changes within each orbit.

We made a number of simulations in order to confirm that decorrelating the data in this way does not lower the amplitudes of the stellar oscillation and the simulation showed that the amplitudes were not suppressed.

With about 1.6 million data points, the computing times are long when decorrelating the data and when calculating power spectra. We therefore rebinned the data. Rebinning the data has no effect on the subsequent analysis, as long as the sampling is a few times higher than the periods we are interested in. For this reason, the decorrelation for the high frequency periodic noise was done in the original data, while the decorrelation for stray light and the rest of the analysis was done for the binned data. The binning was made with a 20 s sampling resulting in 33,452 data points.

The decorrelation was able to remove the main part of the stray light and short periodic noise, but some signature of the orbit is still present. The noise in the light curve increases at certain phases of the orbit and this causes an higher noise level in the power spectrum. Thus, we must assign weights to each data point, as we will describe in the following.

### 8.7.2 Adjusting Statistical Weights

We used statistical weights when calculating the power spectrum following Frandsen et al. (1995). The weights were calculated as  $w_i = 1/\sigma_i^2$ , where  $\sigma_i$  is the uncertainty of data point  $i$ . It is therefore important that the  $\sigma_i$  reflect the true uncertainties.

We have evaluated different ways to obtain the uncertainties: based on the quality of the Gaussian fit to the PSF, the background level, and the running mean RMS scatter. In the end, we estimated the uncertainty assigned to a given data point as the RMS of all the (non-binned) data points separated by less than 60 s.

We have checked whether the uncertainties reflect the noise in the time series. By removing all stellar signal in the light curve and assuming that the residuals  $r_i$  in the time series are caused by instrumental noise. We then assume that the ratio between the residuals and the assigned uncertainty  $|r_i/\sigma_i|$  has a Gaussian distribution and we down weighted all data points that do not follow a Gaussian-distribution. This is the same approach used by Butler et al. (2004).

To check which data points follow a Gaussian-distribution, a cumulative histogram was made of the ratio  $|r_i/\sigma_i|$ . This histogram was then fitted with a cumulative Gaussian distribution of the form:

$$F(x) = c_1 \left[ 1 + \operatorname{erf} \left( \frac{x - c_2}{c_3} \right) \right], \quad (8.18)$$

where  $c_1$ ,  $c_2$  and  $c_3$  are constants and erf is the error function:

$$\operatorname{erf}(x) = \frac{2}{\sqrt{\pi}} \int_0^x e^{-t^2} dt. \quad (8.19)$$

In Fig. 8.10 it is seen that for low values of the ratio  $|r_i/\sigma_i|$  the distribution follows a Gaussian distribution. However, there is a tail at high values due

to noisy data points. These data points were down weighted by making a polynomial fit  $f$  of low degree to the difference between the ratio  $|r_i/\sigma_i|$  and the Gaussian fit to this ratio (see Fig. 8.10). The fit  $f$  was forced to have a maximum of 1, and the function falls off at high values of the ratio  $|r_i/\sigma_i|$ . New weights were assigned to the data points according to:

$$w_i = (f_i/\sigma_i)^2. \quad (8.20)$$

Most of the noisy data points that were down weighted with this approach were affected by stray light. The reason is that the variance of the data is significantly larger in this part of the orbit than in the rest of the data. Around 5% of the data are so heavily down weighted that they are not used in the rest of the analysis and these are all among the data that show strong signs of stray light.

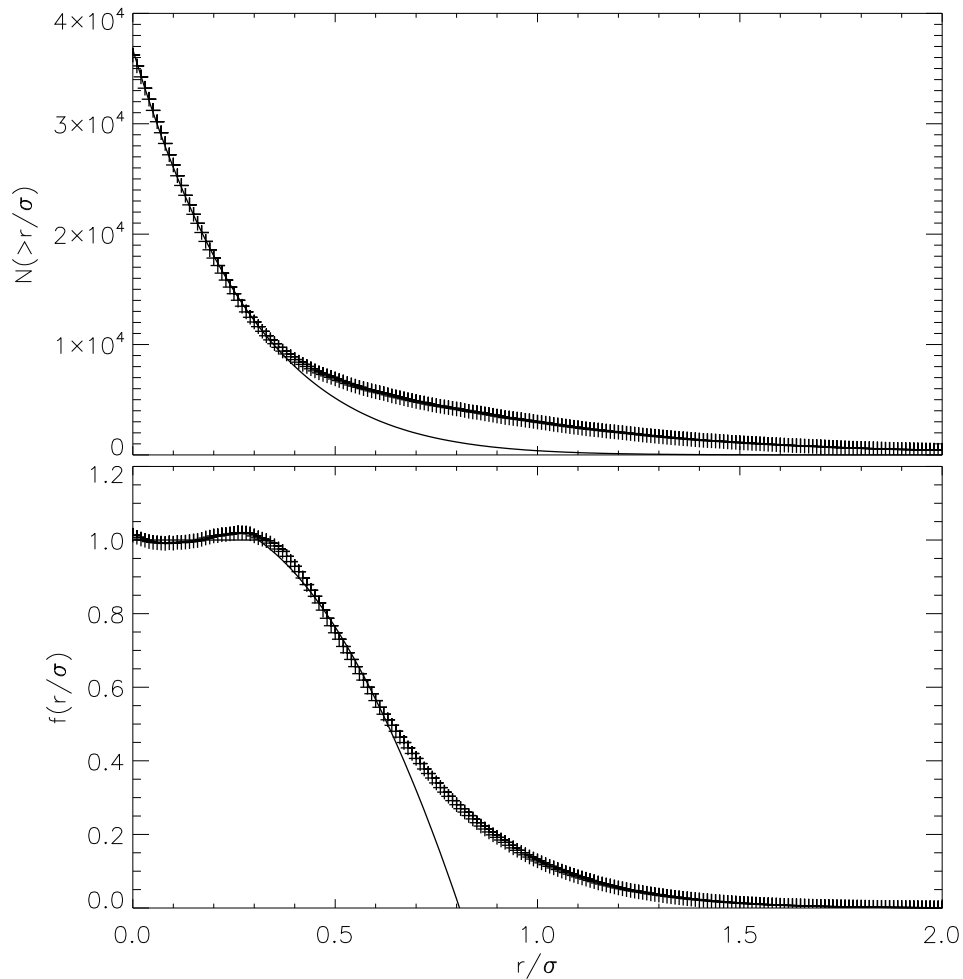


Figure 8.10: Upper panel: Cumulative histograms of the ratio  $|r/\sigma|$ . The crosses show the observations and the solid curve shows the result expected from Gaussian-distributed noise. Lower panel: The crosses show the ratio between the two curves in the upper panel – i.e. the observed and expected cumulative noise histograms. The solid curve is a polynomial fit to the crosses. The weights in the data set were adjusted by multiplying them with the solid curve.



# Conclusions

This dissertation presents a general review of the current status of observational asteroseismology and five papers which present independent researches in observational helio- and asteroseismology. In this conclusion we want to highlight the four most significant results obtained in this PhD project.

## **Evidence that Solar Flares Drive Global Oscillations in the Sun**

The discovery of a strong correlation between the energy at high frequency in the solar acoustic spectrum and flares is the most significant achievement in this PhD project. The correlation suggests that solar flares drive global oscillations in the Sun, though we are still left with a lot of open questions such as: How is the energy delivered from the flares to the oscillations?

As noted by Karoff & Kjeldsen (2008) it might also be possible to use the technique to detect flares on other stars by use of asteroseismology. This could teach us how the number and strength of flares on other stars vary with stellar type and also if and how the number and strength of flares follow the stellar cycles. The last question is interesting as a large part of the largest flares observed by *SOHO* has been observed around solar minimum, which we do not understand.

The discovery by Karoff & Kjeldsen (2008) was made by analyzing disk-integrated photometry data from *SOHO* with a wavelet-like technique. This technique was written from scratch in order to ensure proper treatment of data gaps and proper normalization of the amplitudes. After having proven its usefulness the technique can now be improved in order to include some of the same features as the conventional wavelet analyses.

## **Discovery of High-frequency Modes in Solar-like Stars**

It was shown by Karoff (2007) that the Sun is not the only solar-like star that has oscillations with frequencies higher than the atmospheric acoustic cut-off frequency. This means that the oscillation signals that we detect in solar-like stars not only consist of completely trapped p modes, but also of waves traveling in the stellar atmospheres. These high-frequency modes may provide us with information about the physics in the outer layers of the stars.

Also, the discovery by Karoff & Kjeldsen (2008) that the high-frequency modes in the Sun are correlated with flares has provided a new goal for the

study of high-frequency modes in solar-like stars, i.e. detection of flare driven waves in solar-like stars.

### **Discovery of 29 Candidate SPB Stars in a Low-metallicity Cluster**

Our discovery of 29 candidate SPB stars in the SMC is not the first discovery of extra-galactic candidate SPB stars. Kołaczkowski et al. (2006) reported the discovery of 92 candidate  $\beta$  Cep stars in the LMC and 6 in the SMC and 59 candidate  $\beta$  Cep stars in the LMC and 11 in the SMC. These stars were mostly multi-periodic. But these candidates were all found by looking at all bright stars in the two galaxies. We identified the 29 candidate SPB stars by looking only at a single cluster, so if a significant fraction of the 29 candidates turn out to be bona fide SPB stars, then the discovery suggests that the fraction of SPB stars in NGC 371 is comparable to or larger than what is seen in the Galaxy. As SPB stars are not believed to be present in low-metallicity environments this suggests one of two things: Either the metallicity of NGC 371 is higher than the general metallicity of the SMC, or SPB stars are present in low-metallicity environments. The last thing could be explained by including local iron enhancement by diffusion and radiative accelerations (Miglio et al., 2007c) in the models of SPB stars.

### **Development of Techniques for Data Reduction of Space-based Asteroseismic Data**

A new method for data reduction of space-based asteroseismic data has been developed. The method uses the two algorithms described in Karoff et al. (2008b), i.e. distance-weighted mean decorrelation and adjustment of statistical weights. This new method has a number of advantages over other methods for reduction of space-based asteroseismic data. For example it does not throw away any data points and it does not use the measurements themselves to correct the measurements. We therefore expect that future space-based asteroseismic missions could benefit from using this reduction method.

# Bibliography

- Abrams, D., & Kumar, P. 1996, ApJ, 472, 882
- Aerts, C., Thoul, A., Daszyńska, J., Scuflaire, R., Waelkens, C., Dupret, M. A., Niemczura, E., & Noels, A. 2003, Science, 300, 1926
- Aerts, C., et al. 2006, ApJ, 642, L165
- Aerts, C., et al. 2006, ApJ, 642, 470
- Aigrain, S., Gilmore, G., Favata, F., & Carpano, S. 2003, Scientific Frontiers in Research on Extrasolar Planets, 294, 441
- Aizenman, M., Smeyers, P., & Weigert, A. 1977, A&A, 58, 41
- Alard, C. 2000, A&AS, 144, 363
- Ambastha, A., & Antia, H. M. 2006, Sol. Phys., 238, 219
- Anders, E., & Grevesse, N. 1989, Geochim. Cosmochim. Acta, 53, 197
- Anderson, E. R., Duvall, T. L., Jr., & Jefferies, S. M. 1990, ApJ, 364, 699
- Arentoft, T., Sterken, C., Knudsen, M. R., Freyhammer, L. M., Duerbeck, H. W., Pompei, E., Delahodde, C. E., & Clasen, J. W. 2001, A&A, 380, 599
- Arentoft, T., et al. 2007, A&A, 465, 965
- Asplund, M., Grevesse, N., & Sauval, A. J. 2005, Cosmic Abundances as Records of Stellar Evolution and Nucleosynthesis, 336, 25
- Arentoft et al. 2008, ApJ, near submission
- Baglin, A., Auvergne, M., Barge, P., Buey, J.-T., Catala, C., Michel, E., Weiss, W., & *COROT* Team 2002, ESA SP-485: Stellar Structure and Habitable Planet Finding, 17
- Bahcall, J. N., Basu, S., Pinsonneault, M., & Serenelli, A. M. 2005, ApJ, 618, 1049
- Baliunas, S. L., et al. 1995, ApJ, 438, 269
- Ballai, I. 2007, Sol. Phys., 246, 177

- Ballot, J., García, R. A., & Lambert, P. 2006, MNRAS, 369, 1281
- Balmforth, N. J., & Gough, D. O. 1990, ApJ, 362, 256
- Balona, L. A., & Shobbrook, R. R. 1983, MNRAS, 205, 309
- Barban, C., et al. 2007, A&A, 468, 1033
- Baudin, F., Appourchaux, T., Boumier, P., Kuschnig, R., Leibacher, J. W., & Matthews, J. M. 2008, A&A, 478, 461
- Basu, S., & Antia, H. M. 2008, Phys. Rep., 457, 217
- Bazot, M., Bouchy, F., Kjeldsen, H., Charpinet, S., Laymand, M., & Vauclair, S. 2007, A&A, 470, 295
- Bedding, T. R., Kjeldsen, H., Butler, R. P., McCarthy, C., Marcy, G. W., O'Toole, S. J., Tinney, C. G., & Wright, J. T. 2004, ApJ, 614, 380
- Bedding, T. R., et al. 2005, A&A, 432, L43
- Bedding, T. R., & Kjeldsen, H. 2006, Memorie della Societa Astronomica Italiana, 77, 384
- Bedding, T., & Kjeldsen, H. 2006, Proceedings of SOHO 18/GONG 2006/HELAS I, Beyond the spherical Sun, 624,
- Bedding, T. R., & Kjeldsen, H. 2007, American Institute of Physics Conference Series, 948, 117
- Bedding, T. R., & Kjeldsen, H. 2007, Communications in Asteroseismology, 150, 106
- Bedding, T. R., et al. 2007, ApJ, 663, 1315
- Berdyugina, S. V. 2005, Living Reviews in Solar Physics, 2, 8
- Bertin, E., & Arnouts, S. 1996, A&AS, 117, 393
- Bordé, P., Rouan, D., & Léger, A. 2003, A&A, 405, 1137
- Borucki, W. J., et al. 2003, Proceedings of the SPIE, 4854, 129
- Bouchy, F., & Carrier, F. 2002, A&A, 390, 205
- Bouchy, F., Schmitt, J., Bertaux, J.-L., & Connes, P. 2002, IAU Colloq. 185: Radial and Nonradial Pulsations as Probes of Stellar Physics, 259, 472
- Breger, M., et al. 1993, A&A, 271, 482
- Breger, M. 2000, Delta Scuti and Related Stars, 210, 3
- Brewer, B. J., Bedding, T. R., Kjeldsen, H., & Stello, D. 2007, ApJ, 654, 551
- Brookes, J. R., Isaak, G. R., & van der Raay, H. B. 1978, MNRAS, 185, 1

- Brown, T. M., & Christensen-Dalsgaard, J. 1990, *ApJ*, 349, 667
- Brown, T. M. 2003, *ApJ*, 593, L125
- Bruntt, H. 2002, Ph.D. Dissertation
- Bruntt, H., et al. 2004, *A&A*, 425, 683
- Bruntt, H., Kjeldsen, H., Buzasi, D. L., & Bedding, T. R. 2005, *ApJ*, 633, 440
- Bruntt, H., et al. 2007, *A&A*, 461, 619
- Butler, R. P., Marcy, G. W., Williams, E., McCarthy, C., Dosanjh, P., & Vogt, S. S. 1996, *PASP*, 108, 500
- Butler, R. P., Bedding, T. R., Kjeldsen, H., McCarthy, C., O'Toole, S. J., Tinney, C. G., Marcy, G. W., & Wright, J. T. 2004, *ApJ*, 600, L75
- Buzasi, D., Catanzarite, J., Laher, R., Conrow, T., Shupe, D., Gautier, T. N., III, Kreidl, T., & Everett, D. 2000, *ApJ*, 532, L133
- Buzasi, D. L. 2004, *ESA SP-538: Stellar Structure and Habitable Planet Finding*, 205
- Buzasi, D. L., et al. 2005, *ApJ*, 619, 1072
- Carrier, F., Bouchy, F., & Eggenberger, P. 2003, *Asteroseismology Across the HR Diagram*, 311
- Carrier, F., & Bourban, G. 2003, *A&A*, 406, L23
- Carrier, F., Eggenberger, P., D'Alessandro, A., & Weber, L. 2005, *New Astronomy*, 10, 315
- Carrier, F., Eggenberger, P., & Bouchy, F. 2005, *A&A*, 434, 1085
- Carrier, F., & Eggenberger, P. 2006, *A&A*, 450, 695
- Chaplin, W. J., Elsworth, Y., Howe, R., Isaak, G. R., McLeod, C. P., Miller, B. A., & New, R. 1995, 4. *SOHO Workshop Helioseismology*, Vol. 2, p. 335 - 339, 2, 335
- Chaplin, W. J., Elsworth, Y., Isaak, G. R., Miller, B. A., & New, R. 2000, *MNRAS*, 313, 32
- Chaplin, W. J., Appourchaux, T., Elsworth, Y., Isaak, G. R., Miller, B. A., & New, R. 2000, *MNRAS*, 314, 75
- Chaplin, W. J., Elsworth, Y., Isaak, G. R., Marchenkov, K. I., Miller, B. A., & New, R. 2003, *GONG+ 2002. Local and Global Helioseismology: the Present and Future*, 517, 247
- Chaplin, W. J., Elsworth, Y., Isaak, G. R., Miller, B. A., New, R., & Toutain, T. 2003, *ApJ*, 582, L115

- Chaplin, W. J., Dumbill, A. M., Elsworth, Y. P., Isaak, G. R., McLeod, C. P., Miller, B. A., New, R., & Pintér, B. 2004, *Sol. Phys.*, 220, 307
- Chaplin, W. J., Elsworth, Y., Miller, B. A., Verner, G. A., & New, R. 2007, *ApJ*, 659, 1749
- Charbonneau, P. 2005, *Living Reviews in Solar Physics*, 2, 2
- Charpinet, S., Fontaine, G., Brassard, P., & Dorman, B. 1996, *ApJ*, 471, L103
- Charpinet, S., Fontaine, G., Brassard, P., Chayer, P., Rogers, F. J., Iglesias, C. A., & Dorman, B. 1997, *ApJ*, 483, L123
- Christensen-Dalsgaard, J., Dilke, F. W. W., & Gough, D. O. 1974, *MNRAS*, 169, 429
- Christensen-Dalsgaard, J., Gough, D. O., 1979, in *Lecture Notes in Physics 125, Nonradial and Nonlinear Stellar Pulsation*, ed. H. A. Hill & W. A. Dziem-bowski (Heidelberg: Springer), 184
- Christensen-Dalsgaard, J., & Frandsen, S. 1983, *Sol. Phys.*, 82, 469
- Christensen-Dalsgaard, J., Dappen, W., & Lebreton, Y. 1988, *Nature*, 336, 634
- Christensen-Dalsgaard, J. 1989, *MNRAS*, 239, 977
- Christensen-Dalsgaard, J., Bedding, T. R., & Kjeldsen, H. 1995, *ApJ*, 443, L29
- Christensen-Dalsgaard, J., et al. 1996, *Science*, 272, 1286
- Christensen-Dalsgaard, J., 2003, 'Lecture Notes on Stellar Oscillations. Fifth Edition', lecture notes, University of Aarhus.
- Christensen-Dalsgaard, J., & Kjeldsen, H. 2004, *Nature*, 430, 29
- Christensen-Dalsgaard, J., 2008, 'Stellar Structure and Evolution Sixth Edition Fourth Printing', lecture notes, University of Aarhus.
- Claudi, R. U., et al. 2005, *A&A*, 429, L17
- Cox, A. N., Morgan, S. M., Rogers, F. J., & Iglesias, C. A. 1992, *ApJ*, 393, 272
- Crowl, H. H., Sarajedini, A., Piatti, A. E., Geisler, D., Bica, E., Clariá, J. J., & Santos, J. F. C., Jr. 2001, *AJ*, 122, 220
- Cuypers, J., Aerts, C., Buzasi, D., Catanzarite, J., Conrow, T., & Laher, R. 2002, *A&A*, 392, 599
- De Cat, P., Briquet, M., Daszyńska-Daszkiewicz, J., Dupret, M. A., de Ridder, J., Scuflaire, R., & Aerts, C. 2005, *A&A*, 432, 1013
- De Cat, P., et al. 2007, *A&A*, 463, 243
- De Ridder, J., Arentoft, T., & Kjeldsen, H. 2006, *MNRAS*, 365, 595

- Dekker, H., D’Odorico, S., Kaufer, A., Delabre, B., & Kotzlowski, H. 2000, Proc. SPIE, 4008, 534
- Deleuil, M., Moutou, C., Deeg, H., Meunier, C., Surace, C., Guterman, P., Almenara, J. M., Alonso, R., Barge, P., Bouchy, F., Erikson, A., Leger, A., Loeillet, B., Ollivier, M., Pont, F., Rauer, H., Rouan, D., & Queloz, D. 2006, ESA SP-1306: The *COROT* Mission, 341
- Deubner, F.-L. 1995, GONG 1994. Helio- and Astro-Seismology from the Earth and Space, 76, 303
- Di Mauro, M. P., Christensen-Dalsgaard, J., & Paternò, L. 2003, Ap&SS, 284, 229
- Dintrans, B., Brandenburg, A., Nordlund, Å., & Stein, R. F. 2005, A&A, 438, 365
- Dravins, D., Lindegren, L., Nordlund, A., & Vandenberg, D. A. 1993, ApJ, 403, 385
- Drummond, R., Vandenbussche, B., Aerts, C., De Oliveira Fialho, F., & Auvergne, M. 2006, PASP, 118, 874
- Dupret, M.-A., De Ridder, J., De Cat, P., Aerts, C., Scufflaire, R., Noels, A., & Thoul, A. 2003, A&A, 398, 677
- Duvall, T. L., Jr., & Harvey, J. W. 1986, NATO ASIC Proc. 169: Seismology of the Sun and the Distant Stars, 105
- Dzhalilov, N. S., Staude, J., & Arlt, K. 2000, A&A, 361, 1127
- Eggenberger, P., Carrier, F., Bouchy, F., & Blecha, A. 2004, A&A, 422, 247
- Endl, M., Cochran, W. D., Hatzes, A. P., & Wittenmyer, R. A. 2005, Revista Mexicana de Astronomia y Astrofisica Conference Series, 23, 64
- European Space Agency, *COROT Surprises A Year After Launch*, press release from [http://www.esa.int/esaCP/SEMFOC2MDAF\\_index\\_0.html](http://www.esa.int/esaCP/SEMFOC2MDAF_index_0.html), 2007
- Eyer, L., & Bartholdi, P. 1999, A&AS, 135, 1
- Fahlman, G. G., & Ulrych, T. J. 1982, MNRAS, 199, 53
- Fletcher, S. T., Chaplin, W. J., & Elsworth, Y. 2003, MNRAS, 346, 825
- Fletcher, S. T., Chaplin, W. J., & Elsworth, Y. 2004, Sol. Phys., 220, 361
- Fletcher, S. T., Chaplin, W. J., Elsworth, Y., Schou, J., & Buzasi, D. 2006, MNRAS, 371, 935
- Fletcher, S. T., Chaplin, W. J., Elsworth, Y., & New, R. 2008, ArXiv e-prints, 803, arXiv:0803.3033
- Fossat, E., et al. 1999, A&A, 343, 608

- Frandsen, S., Jones, A., Kjeldsen, H., Viskum, M., Hjorth, J., Andersen, N. H., & Thomsen, B. 1995, *A&A*, 301, 123
- Frandsen, S., & Lindberg, B. 2000, *The Third MONS Workshop: Science Preparation and Target Selection*, 163
- Frandsen, S., et al. 2007, *A&A*, 475, 991
- Fröhlich, C., et al. 1995, *Sol. Phys.*, 162, 101
- Frohlich, C., et al. 1997, *Sol. Phys.*, 170, 1
- García, H. A. 1994, *Sol. Phys.*, 154, 275
- García, R. A., et al. 1998, *ApJ*, 504, L51
- García, R. A., et al. 2005, *A&A*, 442, 385
- García, R. A., Lambert, P., Ballot, J., Pires, S., Nghiem, P. A. P., Turck-Chièze, S. & Matthews, J. M. 2006, submitted to *A&A*
- García, R. A., Turck-Chièze, S., Jiménez-Reyes, S. J., Ballot, J., Pallé, P. L., Eff-Darwich, A., Mathur, S., & Provost, J. 2007, *Science*, 316, 1591
- García, R. A., et al. 2008, *ArXiv e-prints*, 802, arXiv:0802.4296
- Gauss, C. F. 1866, *Carl Friedrich Gauss Werke*, 3, 265
- Gavryusev, V. G., & Gavryuseva, E. A. 1999, *MNRAS*, 303, L63
- Gilliland, R. L., et al. 1993, *AJ*, 106, 2441
- Gizon, L., & Solanki, S. K. 2003, *ApJ*, 589, 1009
- Gizon, L., & Solanki, S. K. 2004, *Sol. Phys.*, 220, 169
- Gizon, L., & Birch, A. C. 2005, *Living Reviews in Solar Physics*, 2, 6
- Gough, D. O. 1981, *MNRAS*, 196, 731
- Gough, D. O. 1990, *Progress of Seismology of the Sun and Stars*, 367, 283
- Gough, D. O. 1994, *MNRAS*, 269, L17
- Gough, D. O., et al. 1996, *Science*, 272, 1296
- Grevesse, N., & Noels, A. 1993, *Physica Scripta Volume T*, 47, 133
- Grevesse, N., & Sauval, A. J. 1998, *Space Science Reviews*, 85, 161
- Guenther, D. B. 1991, *ApJ*, 375, 352
- Guenther, D. B. 2004, *ApJ*, 612, 454
- Guenther, D. B., et al. 2005, *ApJ*, 635, 547

- Guenther, D. B., et al. 2007, *Communications in Asteroseismology*, 151, 5
- Handler, G. 2003, *Baltic Astronomy*, 12, 243
- Hartman, J. D., Bakos, G., Stanek, K. Z., & Noyes, R. W. 2004, *AJ*, 128, 1761
- Hartman, J. D., Stanek, K. Z., Gaudi, B. S., Holman, M. J., & McLeod, B. A. 2005, *AJ*, 130, 2241
- Harvey, J. 1985, *Future Missions in Solar, Heliospheric and Space Plasma Physics*, 199
- Harvey, J. W. 1988, *Advances in Helio- and Asteroseismology*, 123, 497
- Harvey, J. W., Duvall, T. L., Jr., Jefferies, S. M., & Pomerantz, M. A. 1993, *GONG 1992. Seismic Investigation of the Sun and Stars*, 42, 111
- Hatzes, A. P., Guenther, E., Kürster, M., & McArthur, B. 2003, *Earths: DARWIN/TPF and the Search for Extrasolar Terrestrial Planets*, 539, 441
- Heynderickx, D., Waelkens, C., & Smeyers, P. 1994, *A&A Suppl.*, 105, 447
- Houdek, G., Balmforth, N. J., Christensen-Dalsgaard, J., & Gough, D. O. 1999, *A&A*, 351, 582
- Houdek, G., et al. 2001, *MNRAS*, 327, 483
- Houdek, G., & Gough, D. O. 2007, *MNRAS*, 375, 861
- Högbom, J. A. 1974, *A&AS*, 15, 417
- Jain, R., & Roberts, B. 1996, *ApJ*, 456, 399
- Jefferies, S. M., Pomerantz, M. A., Duvall, T. L., Jr., Harvey, J. W., & Jaksha, D. B. 1988, *ESA SP-286: Seismology of the Sun and Sun-Like Stars*, 279
- Jiménez, A., Jiménez-Reyes, S. J., & García, R. A. 2005, *ApJ*, 623, 1215
- Jiménez, A. 2006, *ApJ*, 646, 1398
- Jorden, P. R., Deltorn, J.-M., & Oates, A. P. 1994, *Proc. SPIE*, 2198, 836
- Kabath, P., Eigmüller, P., Erikson, A., Hedelt, P., Rauer, H., Titz, R., Wiese, T., & Karoff, C. 2007, *AJ*, 134, 1560
- Kabath, P., Eigmüller, P., Erikson, A., Hedelt, P., Kirste S., von Paris, P., Rauer, H., Renner, S., Titz, R., Wiese, T., Karoff, C. 2008, *AJ*, near submission
- Kallinger, T., et al. 2008, *A&A*, 478, 497
- Kallinger, T., et al. 2008, *Communications in Asteroseismology*, 153, 84
- Kambe, E., et al. 2008, *PASJ*, 60, 45

- Kane, S. R., Collier Cameron, A., Horne, K., James, D., Lister, T. A., Pollacco, D. L., Street, R. A., & Tsapras, Y. 2004, MNRAS, 353, 689
- Kane, S. R., Lister, T. A., Collier Cameron, A., Horne, K., James, D., Pollacco, D. L., Street, R. A., & Tsapras, Y. 2005, MNRAS, 362, 117
- Kane, S. R., Collier Cameron, A., Horne, K., James, D., Lister, T. A., Pollacco, D. L., Street, R. A., & Tsapras, Y. 2005, MNRAS, 364, 1091
- Karoff, C., Master Thesis, University of Aarhus, 2005
- Karoff, C., Pedersen, M. S. S., & Jensen, H. R. 2005, DTU
- Karoff, C., Arentoft, T., & Kjeldsen, H. 2006a, Astronomical Society of the Pacific Conference Series, 349, 393
- Karoff, C., Rauer, H., Erikson, A., & Voss, H. 2006b, Astronomical Society of the Pacific Conference Series, 349, 261
- Karoff, C., et al. 2007, AJ, 134, 766
- Karoff, C. 2007, MNRAS, 381, 1001
- Karoff, C., Arentoft, T., Glowienka, L., Coutures, C., Nielsen, T. B., Dogan, G., Grundahl, F., & Kjeldsen, H. 2008, MNRAS, 386, 1085
- Karoff, C., & Kjeldsen, H. 2008, ApJ, 678, L73
- Karoff, C., Bruntt, H., Kjeldsen, H., Bedding, T. R., Buzasi, D. L. 2008b, near submission
- Kawaler, S. D., Sekii, T., & Gough, D. 1999, ApJ, 516, 349
- Keller, C. U., Schüssler, M., Vögler, A., & Zakharov, V. 2004, ApJ, 607, L59
- Kholopov, P. N., et al. 1998, in Combined General Catalogue of Variable Stars, 4.1 Ed (II/214A)
- King, H., et al. 2006, Communications in Asteroseismology, 148, 28
- Kjeldsen, H., & Frandsen, S. 1992, PASP, 104, 413
- Kjeldsen, H., & Baade, D. 1994, Pulsation; Rotation; and Mass Loss in Early-Type Stars, 162, 29
- Kjeldsen, H., & Bedding, T. R. 1995, A&A, 293, 87
- Kjeldsen, H., Bedding, T. R., Viskum, M., & Frandsen, S. 1995, AJ, 109, 1313
- Kjeldsen, H., et al. 2005, ApJ, 635, 1281
- Kjeldsen, H., & Bedding, T. R. 2007, IAU Symposium, 239, 130
- Kjeldsen et al. 2008, ApJ, accepted

- Kjeldsen, H. & Bedding, T. R. 2025, Living Reviews Solar Physics, to be submitted
- Kołaczkowski, Z., et al. 2004, IAU Colloq. 193: Variable Stars in the Local Group, 310, 225
- Kołaczkowski, Z., et al. 2006, Memorie della Societa Astronomica Italiana, 77, 336
- Kosovichev, A. G., & Zharkova, V. V. 1998, Nature, 393, 317
- Kumar, P., Duvall, T. L., Jr., Harvey, J. W., Jefferies, S. M., Pomerantz, M. A., & Thompson, M. J. 1990, Progress of Seismology of the Sun and Stars, 367, 87
- Kumar, P., & Lu, E. 1991, ApJ, 375, L35
- Kumar, P. 1994, ApJ, 428, 827
- Kumar, P., Fardal, M. A., Jefferies, S. M., Duvall, T. L., Jr., Harvey, J. W., & Pomerantz, M. A. 1994, ApJ, 422, L29
- Kurtz, D. W. 2004, Sol. Phys., 220, 123
- Lambert, P., Pires, S., Ballot, J., García, R. A., Starck, J.-L., & Turck-Chièze, S. 2006, A&A, 454, 1021
- Larsen, S. S., Clausen, J. V., & Storm, J. 2000, A&A, 364, 455
- Lenz, P., & Breger, M. 2005, Communications in Asteroseismology, 146, 53
- Li, C.-H., et al. 2008, Nature, 452, 610
- Libbrecht, K. G. 1988, ApJ, 334, 510
- Libbrecht, K. G. 1992, ApJ, 387, 712
- Lomb, N. R. 1976, Ap&SS, 39, 447
- Loumos, G. L., & Deeming, T. J. 1978, Ap&SS, 56, 285
- Maeder, A., Grebel, E. K., & Mermilliod, J.-C. 1999, A&A, 346, 459
- Marchenko, S. V. 2008, A&A, 479, 845
- Marigo, P., Girardi, L., Bressan, A., Groenewegen, M. A. T., Silva, L., & Granato, G. L. 2007, ArXiv e-prints, 711, arXiv:0711.4922
- Martić, M., Lebrun, J.-C., Appourchaux, T., & Korzennik, S. G. 2004, A&A, 418, 295
- Martić, M., et al. 1999, A&A, 351, 993

- Matthews, J. M., Kusching, R., Guenther, D. B., Walker, G. A. H., Moffat, A. F. J., Rucinski, S. M., Sasselov, D., & Weiss, W. W. 2004, *Nature*, 430, 51
- Matthews, J. M. 2007, *Communications in Asteroseismology*, 150, 333
- Metcalf, T. S., Dziembowski, W. A., Judge, P. G., & Snow, M. 2007, *MNRAS*, 379, L16
- Miglio, A., & Montalbán, J. 2005, *A&A*, 441, 615
- Miglio, A., Montalbán, J., & Dupret, M.-A. 2007a, *MNRAS*, 375, L21
- Miglio, A., Montalbán, J., & Dupret, M.-A. 2007b, *Communications in Asteroseismology*, 151, 48
- Miglio, A., Bourge, P.-O., Montalbán, J., & Dupret, M.-A. 2007c, *Communications in Asteroseismology*, 150, 209
- Mochejska, B. J., Stanek, K. Z., Sasselov, D. D., & Szentgyorgyi, A. H. 2002, *AJ*, 123, 3460
- Monet, D., et al. 1998, *The PMM USNO-A2.0 Catalog. (1998)*
- Monteiro, M. J. P. F. G., Christensen-Dalsgaard, J., & Thompson, M. J. 1994, *A&A*, 283, 247
- Moore, D. R., & Weiss, N. O. 1973, *Journal of Fluid Mechanics*, 58, 289
- Moreira, O., Appourchaux, T., Berthomieu, G., & Toutain, T. 2005, *MNRAS*, 357, 191
- Moreton, G. E., & Ramsey, H. E. 1960, *PASP*, 72, 357
- Mosser, B., et al. 2005, *A&A*, 431, L13
- Mosser, B., et al. 2008, *A&A*, 478, 197
- Muller, R. 1988, *Advances in Space Research*, 8, 159
- Müller, D. A. N., Steiner, O., Schlichenmaier, R., & Brandt, P. N. 2001, *Sol. Phys.*, 203, 211
- Nigam, R., & Kosovichev, A. G. 1999, *ApJ*, 510, L149
- Nordlund, A., Spruit, H. C., Ludwig, H.-G., & Trampedach, R. 1997, *A&A*, 328, 229
- North, J. R., et al. 2007, *MNRAS*, 380, L80
- Osaki, J. 1975, *PASJ*, 27, 237
- Pamyatnykh, A. A. 1999, *Acta Astronomica*, 49, 119

- Pamyatnykh, A. A. & Ziomek, W. 2007, *Communications in Asteroseismology*, 150, 207
- Park, J., et al. 2005, *Science*, 308, 1139
- Pietrinferni, A., Cassisi, S., Salaris, M., & Castelli, F. 2004, *ApJ*, 612, 168
- Pigulski, A., & Kołaczkowski, Z. 2002, *A&A*, 388, 88
- Pigulski, A. 2006, *Astrophysics of Variable Stars*, 349, 137
- Pijpers, F. P. 2003, *A&A*, 400, 241
- Pijpers, F. P., Teixeira, T. C., Garcia, P. J., Cunha, M. S., Monteiro, M. J. P. F. G., & Christensen-Dalsgaard, J. 2003, *A&A*, 406, L15
- Poretti, E., Buzasi, D., Laher, R., Catanzarite, J., & Conrow, T. 2002, *A&A*, 382, 157
- Press, W. H., Teukolsky, S. A., Vetterling, W. T., & Flannery, B. P. 1992, Cambridge: University Press, —c1992, 2nd ed.,
- Rauer, H., Eislöffel, J., Erikson, A., Guenther, E., Hatzes, A. P., Michaelis, H., & Voss, H. 2004, *PASP*, 116, 38
- Rast, M. P. 2003, *ApJ*, 597, 1200
- Reegen, P. 2004, *IAU Symposium*, 224, 791
- Reegen, P., et al. 2006, *MNRAS*, 281
- Régulo, C., & Roca Cortés, T. 2005, *A&A*, 444, L5
- Retter, A., Bedding, T. R., Buzasi, D. L., Kjeldsen, H., & Kiss, L. L. 2003, *ApJ*, 591, L151
- Roberts, D. H., Lehar, J., & Dreher, J. W. 1987, *AJ*, 93, 968
- Roca Cortés, T., Jiménez, A., Pallé, P. L., Golf, T., & VIRGO Teams 1999, *ESA SP-448: Magnetic Fields and Solar Processes*, 135
- Rowe, J. F., et al. 2006, *Communications in Asteroseismology*, 148, 34
- Roxburgh, I. W., & Vorontsov, S. V. 1995, *MNRAS*, 272, 850
- Rupprecht, G., et al. 2004, *Proc. SPIE*, 5492, 148
- Saio, H., et al. 2006, *ApJ*, 650, 1111
- Samadi, R., Houdek, G., Goupil, M.-J., Lebreton, Y., & Baglin, A. 2002, *ESA SP-485: Stellar Structure and Habitable Planet Finding*, 87
- Samadi, R., Georgobiani, D., Trampedach, R., Goupil, M. J., Stein, R. F., & Nordlund, Å. 2007, *A&A*, 463, 297

- Scargle, J. D. 1982, *ApJ*, 263, 835
- Schou, J., Christensen-Dalsgaard, J., & Thompson, M. J. 1994, *ApJ*, 433, 389
- Schou, J., & Buzasi, D. L. 2001, *ESA SP-464: SOHO 10/GONG 2000 Workshop: Helio- and Asteroseismology at the Dawn of the Millennium*, 10, 391
- Schwarzenberg-Czerny, A. 1996, *ApJ*, 460, L107
- Soriano, M., Vauclair, S., Vauclair, G., & Laymand, M. 2007, *A&A*, 471, 885
- Stankov, A., & Handler, G. 2005, *ApJS*, 158, 193
- Stein, R. F., & Nordlund, Å. 2001, *ApJ*, 546, 585
- Stello, D., et al. 2007, *MNRAS*, 377, 584
- Stello, D., Bruntt, H., Preston, H., & Buzasi, D. 2008, *ApJ*, 674, L53
- Stetson, P. B. 1987, *PASP*, 99, 19
- Stetson, P. B. 1996, *PASP*, 108, 851
- Söderhjelm, S., & Dischler, J. 2005, *A&A*, 442, 1003
- Tamuz, O., Mazeh, T., & Zucker, S. 2005, *MNRAS*, 356, 146
- Tarrant, N. J., Chaplin, W. J., Elsworth, Y., Spreckley, S. A., & Stevens, I. R. 2007, *ArXiv e-prints*, 706, arXiv:0706.3346
- Tassoul, M. 1980, *ApJS*, 43, 469
- Toutain, T., & Appourchaux, T. 1994, *A&A*, 289, 649
- Udry, S., & Santos, N. C. 2007, *ARA&A*, 45, 397
- Ulrich, R. K., et al. 2000, *A&A*, 364, 799
- Valdes, F. G., Campusano, L. E., Velasquez, J. D., & Stetson, P. B. 1995, *PASP*, 107, 1119
- Vázquez Ramió, H., Régulo, C., & Roca Cortés, T. 2005, *A&A*, 443, L11
- Vorontsov, S. V., Jefferies, S. M., Duval, T. L., Jr., & Harvey, J. W. 1998, *MNRAS*, 298, 464
- Voss, H. 2006, PhD dissertation
- Walker, G., et al. 2003, *PASP*, 115, 1023
- Walker, G. A. H., et al. 2005, *ApJ*, 623, L145
- Walker, G. A. H. 2007, *ArXiv e-prints*, 711, arXiv:0711.0706
- Weiss, W. W. 2008, *Communications in Asteroseismology*, 152, 6

Wilson, O. C. 1978, ApJ, 226, 379

Wisniewski, J. P., & Bjorkman, K. S. 2006, ApJ, 652, 458

Wolff, C. L. 1972, ApJ, 176, 833

Zaritsky, D., Harris, J., Thompson, I. B., Grebel, E. K., & Massey, P. 2002,  
AJ, 123, 855